Semiconducting Materials Based on Donor/Acceptor Units for Optoelectronic Applications

Teng Teng

To cite this version:

Teng Teng. Semiconducting Materials Based on Donor/Acceptor Units for Optoelectronic Applications. Material chemistry. Sorbonne Université, 2018. English. NNT : 2018SORUS452 . tel-02966419

HAL Id: tel-02966419
https://theses.hal.science/tel-02966419v1

Submitted on 14 Oct 2020

Sorbonne Université

Ecole doctorale Physique et Chimie des Matériaux (ED397)

Institut Parisien de Chimie Moléculaire (CNRS-UMR8232)

Semiconducting Materials Based on Donor/Acceptor Units for Optoelectronic Applications

Par Teng TENG

Thèse de doctorat de Chimie

Dirigée par Dr. David KREHER et Dr. Fabrice MATHEVET

Présentée et soutenue publiquement le 12 octobre 2018

Devant un jury composé de:

Dr. Chantal ANDRAUD	Directeur de Recherche CNRS Université de Lyon	Rapporteur
Dr. Philippe BLANCHARD	Directeur de Recherche CNRS Université d'Angers	Rapporteur
Prof. Anna PROUST	Professeur Sorbonne Université	Examinateur
Dr. Stéphane MERY	Chargé de Recherche CNRS Université de Strasbourg	Examinateur
Dr. David KREHER	Maître de Conference (HDR) Sorbonne Université	Directeur de thèse
Dr. Fabrice MATHEVET	Chargé de Recherche CNRS Sorbonne Université	Co-Encadrant

Glossary

DMF	N,N-Dimethylformamide
DCM	Dichloromethane
THF	Tetrahydrofuran
PE	Petroleum Ether
PPh_3	Triphenylphosphine
EHA	2-Ethyl-1-hexylamine
NBS	N-Bromosuccinide
OTS	Octadecyltrichlorosilane
Brine	Saturated sodium chloride solution
TMS	Tetramethylsilane
Ar	Argon
NMR	Nuclear Magnetic Resonance
UV	Ultra-Violet
DSC	Differential Scanning Calorimetry
POM	Polarized Optical Microscopy
OFET	Organic Field Effect Transistor
OLET	Organic Light Emitting Field Effect Transistor
OLED	Organic Light Emitting Diodes
OPV	Organic Photovoltaics
LCD	Liquid-crystal display
AFM	Atomic-Forced Microscopy
XRD	X-ray diffraction
TOF	Time of flight
BC	Bottom-Contact
TC	Top-Contact
MO	Molecular Orbital theory
HOMO	Highest Occupied Molecular Orbital
LUMO	Lowest Unoccupied Molecular Orbital
n-type	Negative-type (electron-conducting)
p-type	Positive-type (hole-conducting)

nm	nanometer
LC	Liquid Crystal
M	Mesophase
Iso	Isotropic phase
Cr	Crystalline phase
Sm	Smectic phase
Nem	Nematic phase
Lam	Lamellar mesophase (hearafter specifical definition in this thesis)
LamA	Smectic A-like lamellar mesophase
HRMS	High-resolution mass spectrometer

Content

Glossary **3**

Content **5**

Chapter 1 Introduction **9**

1.1 Organic semiconductors **11**

1.1.1 π-conjugated materials 11

1.1.1.1 π-conjugated polymers 13

1.1.1.2 π-conjugated small molecules 14

1.1.2 Application of organic semiconductors 14

1.1.2.1 OLEDs 15

1.1.2.2 OPVs 16

1.1.2.3 OFETs 18

1.1.3 Charge carrier mobility characterization methods 22

1.1.3.1 OFET 23

1.1.3.2 Time of flight (TOF) 24

1.2 Liquid crystals **25**

1.2.1 Generalities 25

1.2.2 Liquid crystals general classification 26

1.2.2.1 Different types of mesogens 26

1.2.2.2 Different types of mesophases 27

1.2.3 Liquid crystalline semiconductors 33

1.2.4 Liquid crystalline fluorescent materials 34

1.2.5 OLETs 35

1.2.6 Liquid crystalline materials characterization methods 38

1.2.6.1 Polarizing microscope 38

1.2.6.2 Differential scanning calorimetry 39

1.2.6.3 X-ray diffraction 40

1.3 Narrow bandgap materials **42**

1.3.1 Generalities 42

1.3.2 Design and synthesis of narrow bandgap materials 42

1.3.2.1 Synthetic Approaches 42

1.3.2.2 Rational Design for Different Applications 44

1.3.3 State of the art 45

1.3.3.1 OPVs 45

1.3.3.2 Ambipolar OFETs 49

1.4 Aim of work **54**

Chapter 2 Synthesis and Characterization of Liquid Crystal Fluorescent Derivatives 57

2.1 Synthesis 59

2.1.1 Synthesis of precursory building blocks 59

2.1.2 Synthesis of target calamitic C10-PBT and C6-PBT 60

2.2 Photophysical properties (absorption and emission) 61

2.2.1 Absorption and emission of C10-PBT 61

2.2.2 Absorption and Emission of C6-PBT 64

2.3 Mesomorphic properties 65

2.3.1 DSC and POM of C10-PBT 66

2.3.2 DSC and POM of C6-PBT 67

2.4 Self-organization study (X-ray diffraction and Atomic force microscopy) 69

2.4.1 X-ray diffraction (XRD) 69

2.4.1.1 XRD of C10-PBT 70

2.4.1.2 XRD of C6-PBT 71

2.4.2 Atomic force microscopy (AFM) 72

2.5 Electronic properties and HOMO/LUMO energy levels 73

2.6 Charge Transport Properties 76

2.6.1 Field-effect transistor measurements 76

2.6.2 Temperature-dependent time-of-flight measurements 77

2.7 Conclusions 78

2.8 Experimental 79

2.8.1 Materials and methods 79

2.8.2 Synthesis 80

2.8.2.1 Synthesis of precursory building blocks 80

2.8.2.2 Synthesis of C10-PBT and C6-PBT 81

2.8.3 AFM sample preparation 82

2.8.4 OFET sample preparation and configurations 82

2.8.5 TOF sample preparation and configurations 83

2.8.6 Dipole Moments Calculations 83

Chapter 3 Synthesis and Characterization of Liquid Crystal Fluorescent Dyad and Triad 85

3.1 Synthesis 87

3.1.1 Synthesis of precursory building blocks 87

3.1.1.1 Synthesis of 4,4'-(benzo[c][1,2,5]thiadiazole-4,7-diyl)diphenol (BTP) 87

3.1.1.2 Synthesis of benzo[4,5]thieno[2,3-d]thiophene (BTBT) 88

3.1.2 Synthesis of triad BPB 88

3.1.3 Synthesis of dyad BP 89
3.2 Photophysical properties (absorption and emission)....................91
3.2.1 Photophysical properties of building block molecules 91
3.2.2 Absorption and Emission of triad BPB....................92
3.2.2 Absorption and Emission of dyad BP....................93
3.3 Mesomorphic properties 94
3.3.1 DSC and POM of triad BPB 94
3.3.2 DSC and POM of dyad BP....................96
3.4 Self-organization study (X-ray diffraction and Atomic force microscopy) 98
3.4.1 XRD of BPB 98
3.4.2 XRD of BP....................99
3.4.3 AFM of BPB and BP 101
3.5 Charge Transport Properties....................102
3.6 Conclusions....................103
3.7 Experimental 104
3.7.1 Materials and methods....................104
3.7.2 Synthesis 105
3.7.2.1 Synthesis of precursory building blocks (terthiophene and perylene building blocks) 105
3.7.2.2 Synthesis of BPB....................108
3.7.2.3 Synthesis of BP 109
3.7.3 TOF configurations....................109

Chapter 4 Narrow Bandgap Molecules Based on Naphthalene and Thiophene 111
4.1 Synthesis 113
4.1.1 Synthesis of precursory building blocks 113
4.1.2 Synthesis of OTP....................114
4.1.3 Synthesis of PTC 115
4.2 Photophysical properties (absorption and emission)....................117
4.2.1 Absorption of OTP 117
4.2.2 Absorption and emission of PTC....................117
4.3 Electronic properties and HOMO/LUMO energy levels....................118
4.3.1 OTP....................118
4.3.2 PTC....................120
4.4 Thermal behavior....................121
4.5 Thin film morphology study (Atomic force microscopy) 123
4.6 Charge Transport Properties Study (OFET) 124
4.6.1 Charge Transport Properties Study of OTP 124
4.6.2 Charge Transport Properties Study of PTC....................126

4.7 Conclusion **127**
4.8 Experimental **127**
4.8.1 Materials and methods 127
4.8.2 Synthesis 128
4.8.2.1 Synthesis of building blocks 128
4.8.2.3 Synthesis of PTC 131
4.8.3 OFET sample preparation and configurations 133

Conclusions and Perspectives **135**

References **141**

Chapter 1 Introduction

1.1 Organic semiconductors

In the past century, semiconductors are well known in a great variety of applications, for example, in computers, telephones, displays, etc., so that they are practically necessary in our daily life. A semiconductor material has an electrical conductivity value falling between that of a conductor such as aluminum, silver etc. and an insulator, such as wood, paper. Generally speaking, a material possessing a conductivity of about10^{-8}-10^{3} $\mathrm{Scm^{-1}}$ is considered as a semiconductor [1] .

The discovery of ‘organic semiconductors’ dates back to 1948 [2]. But in 1977, high conductivity in polyacetylene was reported by Heeger, MacDiarmid, Shirakawa et al. they won the Nobel Prize in Chemistry for ‘The discovery and development of conductive polymers’ in 2000 [3]. Since then, the development of organic semiconductors and their potential industrial applications has been an important topic in materials science.

Compared to conventional inorganic materials, organic semiconductors possess a lot of essential advantages that make them competitive alternatives for applications in electronics and photonics: (a) low cost synthesis; (b) easy manufacture of thin film devices by vacuum evaporation/sublimation or solution cast or printing technologies; (c) deposition of large area organic thin films on low-cost substrates such as glass, plastic, or metal foils etc [4,5] .

Such organic semiconductors are particularly attractive for three main applications: organic field-effect transistors (OFETs), light-emitting diodes (OLEDs) and photovoltaic cells (OPVs).

1.1.1 π-conjugated materials

What is a π-conjugated compound? The term ‘conjugated’ was coined in 1899 by the German chemist Johannes Thiele. Generally speaking, a conjugated system such as conjugated alkenes and α,β-unsaturated carbonyl compounds is a system of connected p-orbitals with delocalized electrons in molecules which are conventionally represented as having alternating single and multiple bonds conjugated systems: thus it may lower the overall energy of the molecule and give increased stability to the conjugated system [6] . The compound may be cyclic, acyclic, linear or mixed.

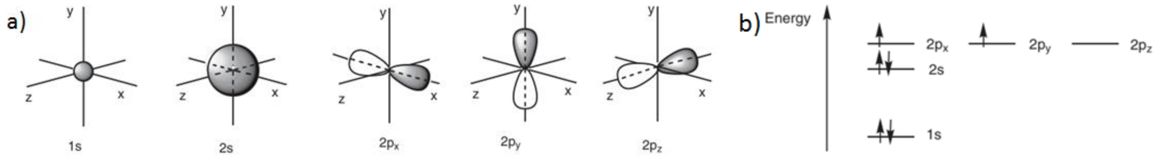

Figure 1.1 a) Atomic orbitals; b) Energy levels of atomic orbitals [6] .

According to the Valence Bond (VB) theory, the electronic configuration for carbon is $1s^22s^22p_x^12p_y^1$ (*Figure 1.1*). The use of these three orbitals in bonding explains the shape of an alkene, for example ethene ($H_2C{=}CH_2$).

In the double bond, the 2s orbital mixes with the two 2p orbitals ($2p_x$, $2p_z$) to form three equal energy hybridized sp^2 orbitals. The energy of the remaining single $2p_y$ orbital is slightly higher than the hybridized orbitals. Each sp^2 hybridized carbon uses three sp^2 hybridized orbitals to form three σ bonds (*Figure 1.2*). The remaining $2p_y$ track overlaps with the adjacent $2p_y$ track, forming a π bond and a π* bond. In this case, the π electrons do not belong to a single bond or atom but rather to a group of atoms.

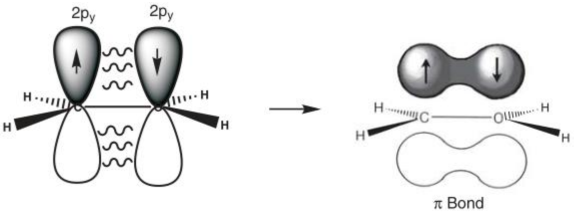

Figure 1.2 Formation of a π bond [6].

The molecular orbital of ethene is shown at *Figure 1.3*. Based on the frontier molecular orbitals theory, for the ethene orbital energy diagram, the Highest Occupied Molecular Orbital (HOMO) is π_{CC} and the Lowest Unoccupied Molecular Orbital (LUMO) is π^*_{CC}. The bandgap between HOMO and LUMO is significant and depends on the materials. For example, the bandgap of semiconductors usually is less than 4.0 eV while for insulators that is more than 4.0 eV.

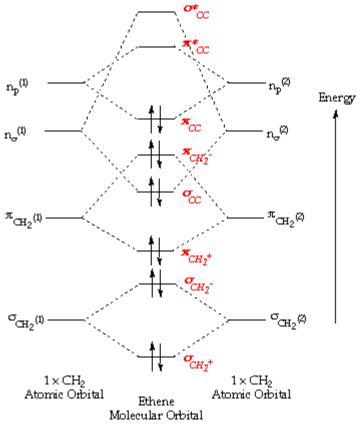

Figure 1.3 Molecular orbital of ethene.

In addition to their electronic properties, such materials are interesting as they play a structural role and allow charge transport, which is one of the essential step in device configuration, either holes (p-type), electrons (n-type) or both (ambipolar). *Figure 1.4* shows several chemical structures of p-type, n-type and ambipolar molecules.

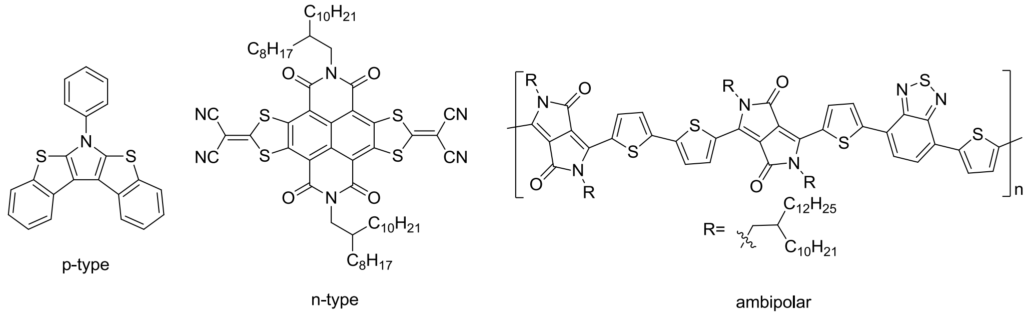

Figure 1.4 Chemical structures of p-type [7]*, n-type* [8] *and ambipolar molecules and polymers* [9]*.*

The concept of π-conjugation is extendable to many other compounds, such as there are several well known examples: pentacene, rubrene, C8-BTBT, phthalocyanine etc. as small molecules and polyacetylene, polypyrrole, poly(3-alkylthiophene), poly(p-phenylene vinylene) etc. as polymers (*Figure 1.5*).

Although there is no precise definition of small molecules and polymers, generally a material with well-defined molecular weight is classified as 'small molecule', compared to the multiple dispersed polymers being classified as 'polymers' [10].

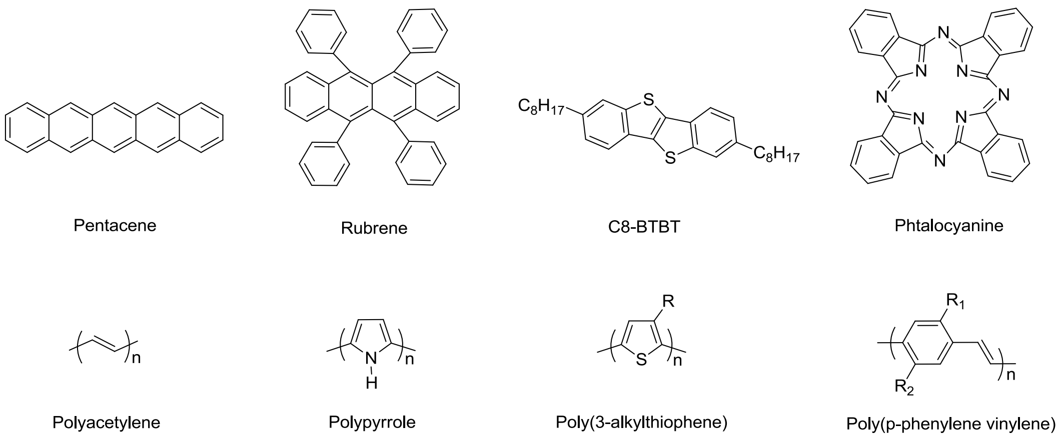

Figure 1.5 Chemical structure of typical small conjugated molecules and polymers.

1.1.1.1 π-conjugated polymers

Due to pretty good electronic and optoelectronic properties, π-conjugated polymers are no doubt one of the most suitable candidates for electronic devices. Polymers possess obvious advantanges. Firstly, polymers have good solution-processabilities. Through solution-processing techniques, for example drop-casting, spin-coating, dip-coating, and ink-printing, polymers can be easily prepared onto a range of desirable substrates. Moreover, polymers possess good flexibility. This made them promising materials for flexible devices such as folding displays, electronic papers, with large area.

Seveal disadvantages can not be ignored. It is also well-known that polymers are difficult to arrange into ordered structure which is very important for charge transport. Usually alkyl groups can be introduced into the molecular structures so that their solubilities may be improved. Nevertheless, the stability of polymers is reduced as the solubility is increased.

In polymer based devices, there are often two pathways to allow charge transport: intrachain transport and interchain transport [10] (*Figure 1.6*). It is worth to mentioning that normally the speed of intrachain transport is much faster than that of interchain.

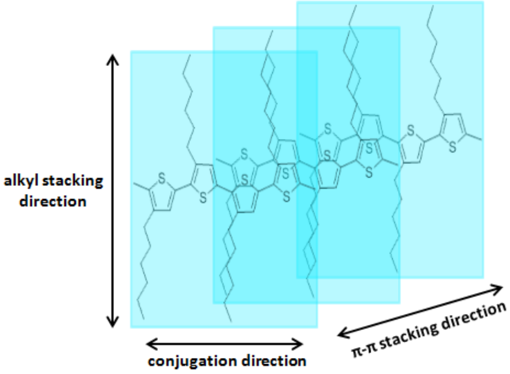

Figure 1.6 Charge transport mechanisms in polymer films (using P3HT for illustration): Intrachain transport, along the π-conjugation direction and interchain transport, along the π-stacking direction.

1.1.1.2 π-conjugated small molecules

It is obviously clear that small molecules present advantages and disadvantages as well.

On the one hand, in comparison with polymers, small molecules are very easy to purify and easily form crystalline films to fabricate the desired high performance devices. In addition, they have well defined chemical structures so that they possess reproducible properties. It explains why the π-conjugated small molecules are reported to show excellent electronic or optical properties [10].

On the other hand, since the synthetic route has to be carried out step-by-step, it can be costly as well as the evaporation process itself, although in some cases small molecules can be easily processed in solution like the polymers (for example, after introducing solubilizing long alkyl chains) [6].

1.1.2 Application of organic semiconductors

As we talked previously, the development of organic semiconductors has been expanding to three main applications: organic light-emitting diodes (OLEDs), organic photovoltaic cells (OPVs) and organic field-effect transistors (OFETs). The flexible, thin and cost-efficient devices are promised to bring innovation to our daily lives, which apprently makes the research in this area so attacktive. In this context, we will review the structure of some usual devices, before to present the reported devices with high performance in the past decade and the important factors that affect device's performance as well.

1.1.2.1 OLEDs

Organic light-emitting diode (OLED), is a device with a film of organic compound as emissive electroluminescent layer, which emits light in response to an electric current. OLEDs are more and more used in displays as a promising approach to replace conventional liquid crystal displays or flat panel displays. In 1987, Eastman Kodak's physical chemists Ching W. Tang and Steven Van Slyke reported the first OLED device based on tris(8-quinolinolato)aluminum (Alq3) [11]. With a drive voltage of ca. 10 V, the external quantum yield reached 1%. This indicates the practical value of organic photoelectric materials in this area. Then, in 1990, Burroughes and his co-authors built the first OLED with conjugated polymer PPV as emissive layer [13]. Based on structure, OLED can be divided into two types: simple layer structure (2-3 layers) and complex layer structure (5-6 layers). *Figure 1.7* shows various OLED configurations.

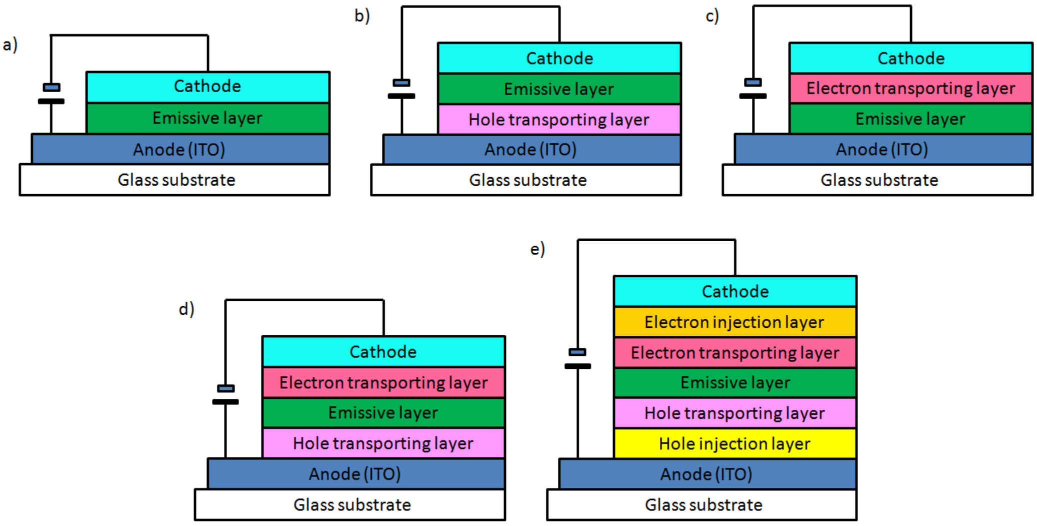

Figure 1.7 Schematic representations of various OLED configurations.

Moreover, in the past decades, three generations of OLED were reported based on different types of electroluminescence mechanisms. In general, the most important part of a device architecture is the emissive layer which transforms excitons into light. There are two types of excitons: singlets and triplets, and the singlet and triplet excitons are generally formed in a 1:3 ratio. The first generation emitters only use singlet excitons, taking the advantage of fluorescence materials, so that this first generation OLED cannot in theory present a EQE (external quantum yield) higher than 5%. In order to improve the performance of OLED, an effective way is consequently to utilize triplet excitons. The seond generation is phosphorescence emitters which posess transition from the excited triplet states (T_1) to the singlet ground state (S_0). Finally, more recently, TADF emitters is the third generation of OLED materials, this time transformation of triplet excitons into singlet excitons can be followed by light emission [14,15]. *Figure 1.8* illustrates the molecular structures of such three different types of materials in OLEDs.

For expansion of OLED use, there are several issues to be resolved, among them blue OLED is one of the most important. As a result, most recent OLED material designing focused on high-efficiency and long-life blue light emitters. Recent efforts to develop high-efficiency blue-light emitters have made encouraging progress. The traditional fluorescent blue OLEDs have an EQE of <10%, while triplet-triplet fluorescence (TTF) OLEDs are about 15%, and phosphorescent and TADF OLEDs have exceeded 20%.

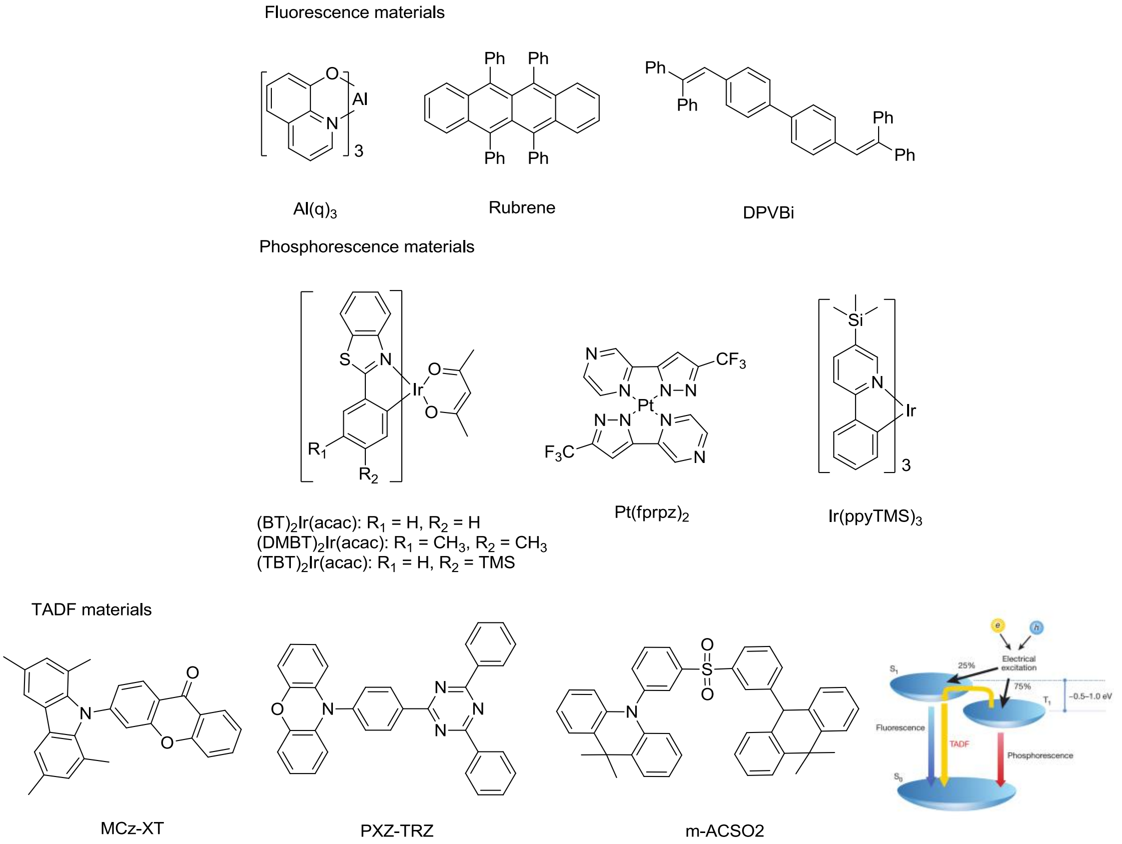

Figure 1.8 Molecular structures of fluorescence materials [16]*, phosphorescence materials* [17,18,19] *and TADF materials* [20,21].

1.1.2.2 OPVs

In order to solve the problem of the depletion of traditional energy sources, many research groups around the world are committed to the development and application of new energy sources. Due to the large energy source and no pollution, solar energy has become the most concerned direction of new energy research. Therefore, because of its advantages such as low cost, no pollution, cleanliness and safety, solar cells have been rapidly developed in recent years.

Based on the device configuration, OPV can be divided into three type: single layer, multilayer and bulk-heterojunction, as shown in *Figure 1.9*.

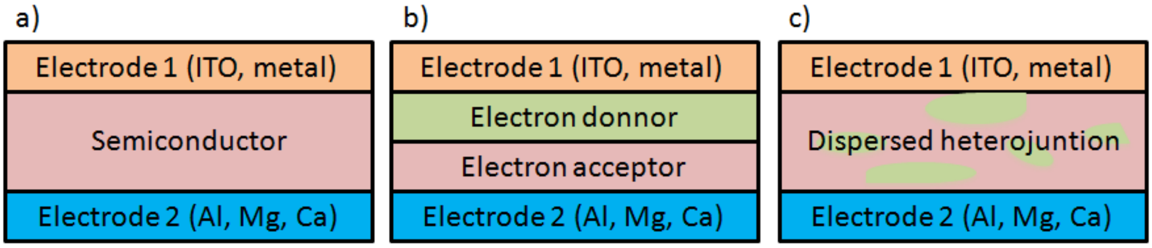

Figure 1.9 Structure of organic solar cell: a) single layer; b) multilayer; c) bulk-heterojunction.

Single layer organic solar cells (*Figure 1.9 a*) are the simplest form of organic solar cells. This kind of OPV is composed of two metal conductive layers, the high work function indium tin oxide (ITO) and low work function such as aluminum, magnesium, and calcium, sandwiched an organic electronic material layer. In fact, single layer organic solar cells work poorly because their quantum efficiency is very low at less than 1% and their energy conversion efficiency is less than 0.1%. The main reason is that the electric field between the two electrodes is not enough to make the excitation. When separated, the electrons recombine more with the hole than reach the electrode.

In order to solve the problem of single layer organic solar cells, multilayer organic solar cells have been developed. This type of battery has two layers of different materials between the electrodes. These two materials have different electron affinity and ionization energy, so the electrostatic force is generated at the interface between the two layers. The materials used in these two layers need to be as large as possible so that the local electric field is large enough to separate the excitons and is more effective than single-layer solar cells. This structure is also called planar heterojunction.

In bulk heterojunction solar cells, electron donors and acceptors are mixed to form a film. The length of each donor or acceptor area is as close as the exciton diffusion length, and most of the excitons generated in the donor or acceptor can reach the interface between the two substances and be effectively separated. Electrons migrate to the acceptor area and gradually reach the electrode and the holes are pulled in the opposite direction and collected by the other electrode. The illustration of bulk heterojunction solar cell and an example are given in *Figure 1.10*.

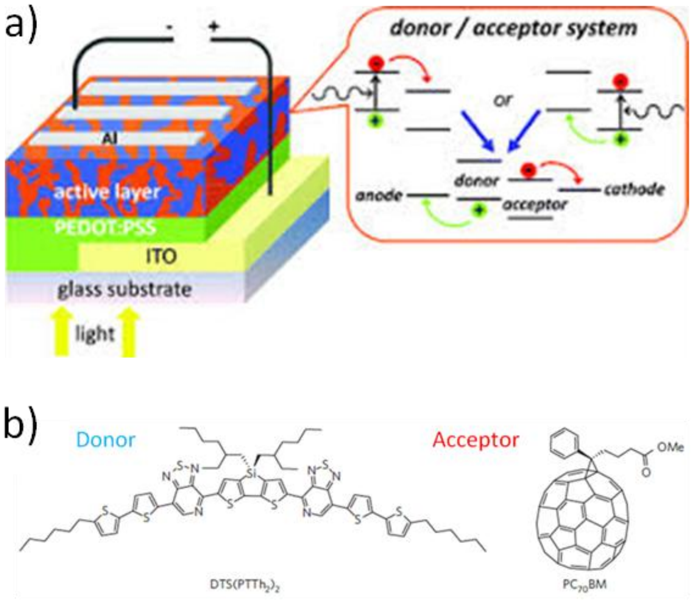

Figure 1.10 a) Schematic illustration of a bulk heterojunction solar cell. Left side: typical device architecture; right side: energy scheme illustrating the charge separation process at the donor/acceptor interface. [22]*, d) Molecular structures of DTS(PTTh$_2$)$_2$ and PC$_{70}$BM* [23].

The most important parameter for evaluating the performance of OPV is efficiency. The maximum efficiency η is expressed as

$$\eta = J_{\mathrm{SC}} \times V_{\mathrm{OC}} \times FF/\text{incident light energy}$$

where J_{SC} is the current density at a voltage of 0V (short circuit current density), V_{OC} is voltage at the current density of 0 mA cm^{-2} (open circuit voltage), and *FF* is the fill factor---the area of an inscribed square divided by ($J_{\mathrm{SC}} \times V_{\mathrm{OC}}$) [24]. For the purpose of obtaining higher conversion rates, increasing J_{SC}, V_{OC}, and *FF* is necessary. To increase J_{SC}, several ways can be listed: absorbance, the rate of photo-generated charge separation, and inhibition of the recombination of holes and electrons. V_{OC} is correlated with the energy gap between the HOMO of a p-type semiconductor and the LUMO of an n-type semiconductor. In order to increase V_{OC}, the p-type semiconductor materials with a deep HOMO level and n-type semiconductor materials with a shallow LUMO level are required obviously. For the *FF*, it is strongly related to the resistance of a PV cell. There are many ways to effectively increase the FF value, such as using a high carrier mobility material in the active layer, reducing the resistance at the interface of each layer, increasing the parallel resistance of PV equivalent circuits etc [24]. By the way of designing appropriate material, OPV is expected to achieve high conversion efficiency.

1.1.2.3 OFETs

In 1986, Tsumura group reported the first organic field-effect transistors (OFETs), applying polythiophene as semiconductor layer materials [25]. This opened up OFETs research areas although the device's mobility was low.

OFETs is a three-terminal switching device that regulates the source (S)-drain (D) current between the electrodes through the gate (G) voltage and it mainly consists of substrate, organic semiconductor layer, dielectric layer, gate electrode and source-drain electrode. According to the relative positions of the electrode and the semiconductor layer, the OFETs can be divided into four structures (see *Figure 1.11*) bottom gate top electrode (BGTC), bottom gate bottom electrode (BGBC), top gate top electrode (TGTC) and top gate bottom electrode (TGBC). In general, p-type materials use bottom-gate OFETs structures while ambipolar or n-type materials use top-gate OFETs structure since the gate electrode and the dielectric layer have a certain protective effect on the semi-conductor active layer and can prevent air in a certain extent.

The key parameters for evaluating the performance of OFETs include mobility (μ), current on/off ratio (I_{on}/I_{off}), and threshold voltage (V_T). Among them, mobility is the most important parameter. Organic semiconductor layers are the core components of OFETs. It is very significant to design and synthesize high-performance organic semiconductor materials. There are three types of OFETs based on their carrier transmission: the first type is p-type OFETs with positive charge (hole) as the main carrier. The electron ionization energy of the organic semiconductor materials is close to the Fermi energy level of the metal electrode, so that the holes can be efficiently injected into the highest occupied orbital (HOMO) of the material. The second type uses negative charges (electron) as the main carrier of the n-type OFETs. The electron affinity of the molecule is close to the Fermi level of the metal electrode and the electrons can be efficiently injected into the material’s lowest unoccupied orbital (LUMO). The third category is namely ambipolar OFETs as well as the organic semiconductor material can transmit both holes and electrons.

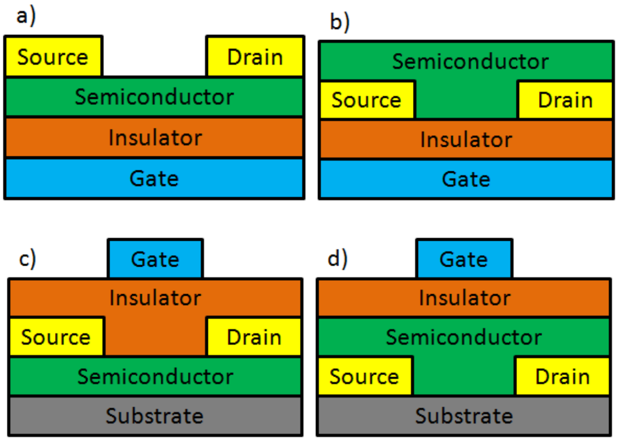

Figure 1.11 Conventional OFETs device structures: a) BGTC; b) BGBC; c) TGTC; d) TGBC.

As explained before, organic semiconductor materials can be classified into two types: organic small molecules, and polymer materials. In this context, we will review the different types of polymers and small-molecule materials published in the past decade.

Polymer OFETs Materials

Diketopyrrolopyrrole (DPP) is a red dye widely used in the printing and dyeing industry. In 2008, Winnewisser et al. reported a OFETs based on polymer BBTDPP1 for the first time. The hole and electron mobility reached 0.1 and 0.09 $cm^2 V^{-1} s^{-1}$, respectively [26]. In 2012, Yu Gui, Liu Yunxi and others synthesized a copolymer PDAPP-TVT. The introduction of double bonds prolonged the conjugation of the polymer, and its hole mobility was as high as 8.2 $cm^2 V^{-1} s^{-1}$, which was the best result at that time [27].

Isoindigo (IID), an isomer of the ancient dye indigo, is widely used in OFETs polymers due to its strong electron-withdrawing ability, simple synthesis, and good chemical tunability. Most of the polymers are p-type materials, only a few are ambipolar materials. Since Pei Jian et al. first introduced this unit into OFETs, many new polymers have been synthesized [28]. The hole mobility of these two polymers IIDDT and IIDT reached 0.019 and 0.79 $cm^2 V^{-1} s^{-1}$, respectively.

Through the way of inserting a strong electron-withdrawing unit tricyclic benzodifurandione into isoindigo, a new monomer BDOPV (benzodifurandione-based oligo (p-phenylene vinylene) was obtained. It is very easy to do chemical modification on benzene ring or an intermediate triple ring of BDOPV such as replacing carbon atoms with nitrogen atoms, then a series of derivatives of BDOPV are obtained. Compared to IID polymers, the LUMO level of BDOPV polymers are generally below -3.8 eV, which is easier for the injection of electrons. Most of BDOPV polymers are n-type materials or ambipolar materials [29].

Naphthalimide (NDI) and phthalimide (PDI) are common aromatic imides. Because of their strong electron-withdrawing properties, the LUMO levels are generally lower than -3.8 eV. This kind of materials are usually n-type or ambipolar material. In 2016, Cho et al. introduced a 18 carbon fluorinated alkyl long chain into the nitrogen atoms of naphthalimide central core to form the two types of polymers PNDIF-T2 and PNDIF-TVT. After annealing, the maximum electron mobility of PNDIF-T2 and PNDIF-TVT were 6.5 and 5.64 $cm^2 V^{-1} s^{-1}$, respectively. This performance was greatly improved compared to those polymer with common alkyl chain, thus indicating the side chain can significantly change the structure of the molecular aggregation state, so that achieving the purpose of improving the mobility.

To sum up, the mobility in p-type materials is as high as 36.3 $cm^2 V^{-1} s^{-1}$ [30], the mobility in n-type materials is as high as 8.5 $cm^2 V^{-1} s^{-1}$ [31], and the mobility of holes in ambipolar materials reached 8.84 $cm^2 V^{-1} s^{-1}$, the electron mobility reaches a maximum of 4.34 $cm^2 V^{-1} s^{-1}$ [32] (see *Figure 1.12*). Compared to p-type materials, both n-type and ambipolar materials are lagging behind. This is due to the few types of acceptor units that strongly accept electrons. Therefore, designing and synthesizing new acceptor units is an important task in this field.

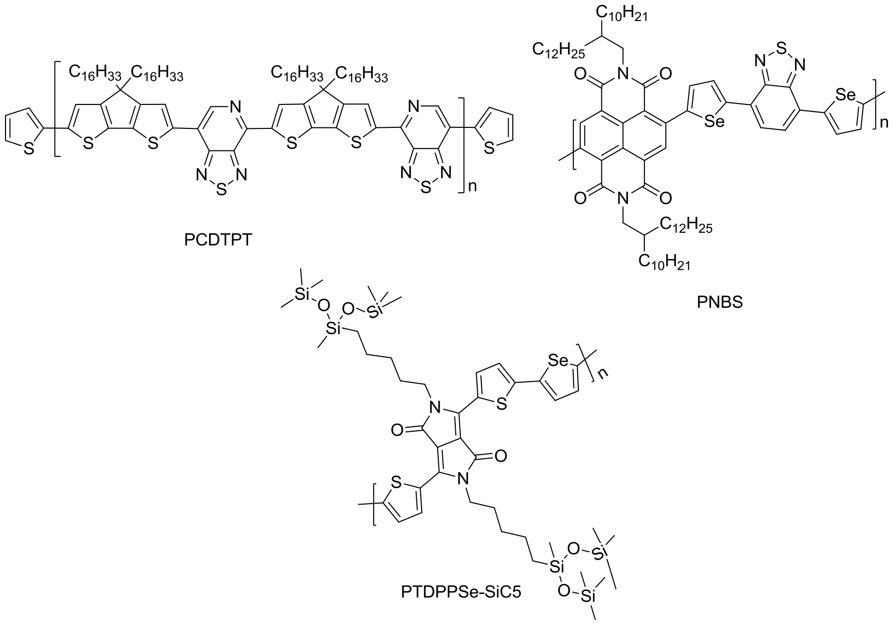

PCDTPT

PNBS

PTDPPSe-SiC5

Figure 1.12 Chemical structures of several typical polymer OFETs materials.

Small Molecule OFETs Materials

Molecules with an extended π-conjugated system are promising to obtain high mobility [33]. Nevertheless, the solubility of such materials in organic solvents is poor due to strong π–π interactions. In the past two decades, material research of OFETs was focused on both high mobility and increased solubility in common organic solvents. Several ways were performed to improve the solubility such as incorporating long alkyl chains, a bulky moiety or an asymmetric molecular shape around the molecularaxis [34]. Many differents small-molecules including p-channel and n-channel OFET materials with good solubility have been reported, such as DH4T, C8-BTBT [35], PTCDI-C13 [36], TIPS-Pentacene [37], as shown in *Figure 1.13*. Through a solution process to fabricate OFETs with these small molecules, a high mobilitiy over 1 $cm^2 V^{-1} s^{-1}$ can be reached.

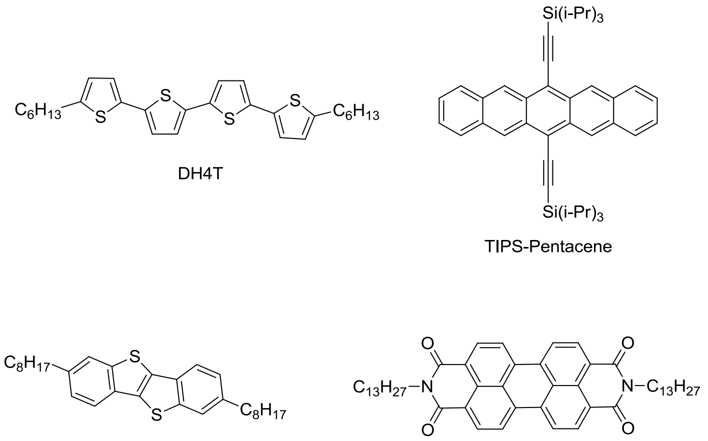

DH4T

TIPS-Pentacene

C_8-BTBT

PTCDI-C13

Figure 1.13 Chemical structures of small-molecule materials.

There are two main problems that need to be solved in this research area. Firstly, the performance from device to device varies greatly in large-scale circuits due to the random recrystallization of the small molecules on the OFETs substrate during the solvent evaporation, which lead to poor uniformity and surface morphology of films. Secondly, the melting point of soluble small molecules is considerably decreased after chemically modification with long alkyl chains so that these materials obviously have thermal durability issues. For example, the melting point of BTBT [38] is 200 °C while for the BTBT derivatives (with dialkyl chains) it is reduced to 100 °C [35]. It is very important to design a molecule that could satisfy both requirements the solubility in solvents and the melting point [34].

1.1.3 Charge carrier mobility characterization methods

In the previous chapters, we presented several important applications of organic semiconductor materials. Amoung these applications, the inherent charge transport properties of the material must be determined. A key parameter for characterizing organic semiconductor materials is the charge mobility μ.

In general, transportation can be described as a diffusion process without any external potential:

$$\langle x^2 \rangle = nDt$$

where $<x^2>$ is the mean-square displacement of the charges, D is the diffusion coefficient, t is the time, and n represents an integer number equal to 2, 4, or 6 for one-,two-, and three-dimensional (1D, 2D, and 3D) systems, respectively. The charge mobility μ is related to the diffusion coefficient via the Einstein-Smoluchowski equation:

$$\mu = \frac{eD}{k_B T}$$

where k_B is the Boltzmann constant, e is the electron charge.When an external electric field is applied, the charge carriers will begin to drift. The ratio of the mobility and the velocity of the charge (v) to the magnitude of the applied electric field (F) can be described: the unit of carrier mobility is then expressed in cm^2/Vs.

$$\mu = \mathrm{v/F}$$

Most importantly, diffusion is the local displacement of the charge near the average position, while drift causes the displacement of the average position. This is why drift is more representative to determine the migration of charge through organic semiconductors.

There are several ways to determine the charge mobility in an organic semiconductor by experiment [39, 40, 41], for example, time of flight (TOF), organic field effect transistor (OFET), space charge limited current (SCLC or 'diode') and pulsed radiation time resolved microwave conductivity (PR-TRMC). Our work involves TOF and OFET measurements and they are presented below.

1.1.3.1 OFET

Different types of device structures have been described in the previous Paragraph 1.1.2.3.

As mentioned before, when a positive or negative source-gate bias is applied, electrons or holes accumulate at the interface between the semiconductor and the dielectric, respectively, and the source-drain current (I_{SD}) increases: this is called an 'on' status of transistor.

The carrier mobility in linear and saturated states can be extracted from standard MOSFET equations [42]:

$$(I_{SD})_{lin} = (W/L)\mu_{FET}C_i(V_{SG} - V_T - V_{SD}/2)V_{SD}$$

$$(I_{SD})_{sat} = (W/2L)\mu_{FET}C_i(V_{SG} - V_T)^2$$

where μ_{FET} is the field effect carrier mobility of the semiconductor (the average drift velocity per unit electric field), W and L are the transistor channel width and length, respectively, C_i the capacitance per unit area of the dielectric and V_T the threshold voltage [43].

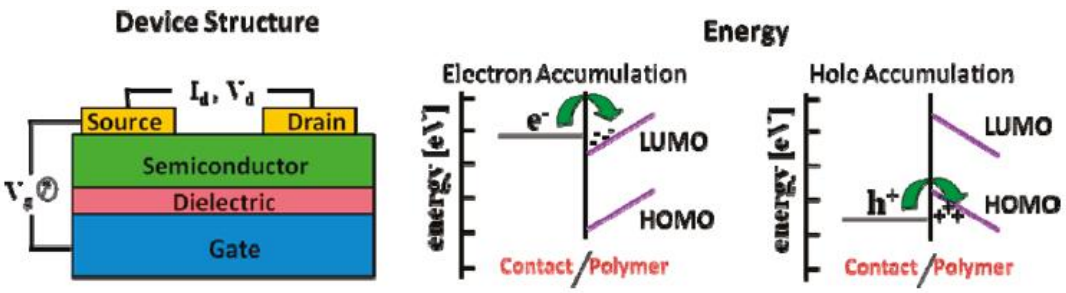

Figure 1.14 Structure and materials of bottom-gate top-contact OFET along with the energy levels of the contact-semiconductor materials where charge accumulation takes place [44].

Figure 1.14 shows a schematic structure of a bottom-gate top-contact OTFT. In this device, negligible source-drain current (I_{SD} = 0 A) flows when the gate voltage is zero (V_G = 0 V) independently of the bias applied between the source and the drain contacts (V_{SD}). When a gate field ($V_G \neq 0$ V) is applied, the device turns on ($I_{SD} \neq 0$ A), which induces charge carriers in the semiconductor at the interface with the dielectric layer. Transistor performance is evaluated from the output and transmission current-voltage curves, where key parameters such as field effect mobility (μ), current on/off ratio (I_{on}/I_{off}), threshold voltage (V_T) and subthreshold swing (S) are measured [44] (*Figure 1.15*).

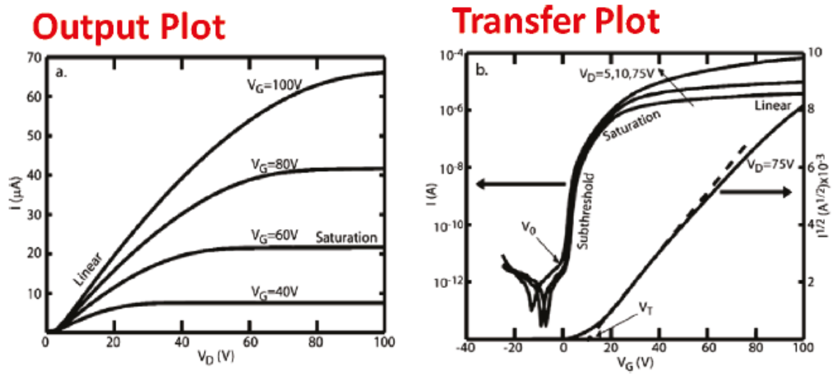

Figure 1.15 Output plot of the source-drain current versus the source-drain voltage at given VG values and transfer plot of the source-drain current [44].

By increasing the V_{SD} amplitude, the current increases linearly until it is saturated. It is worth noting that the field-effect mobility in organic semiconductors typically depends on the gate voltage, which indicates that larger V_{SG} result in higher density of free (or moving) charge carriers at the dielectric-semiconductor interface leading to increased field effect mobility [45].

1.1.3.2 Time of flight (TOF)

TOF is a technology that is ideal for measuring the transport properties of organic semiconductors with low mobility [41]. Leblanc and Kepler have achieved the first charge mobility measurement of organic semiconductors by this technology [46, 47].

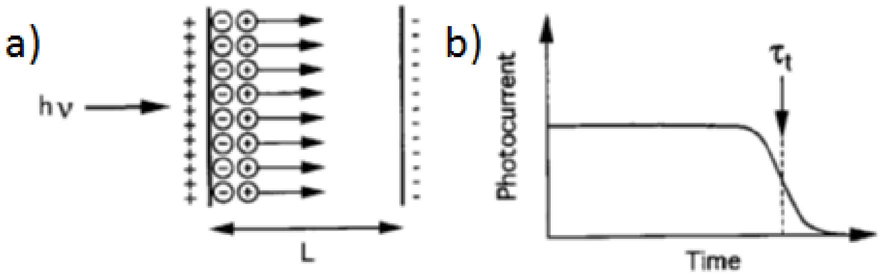

Figure 1.16 Principle of the time of flight measurement. a) schematic view of the carrier generation and transport;b) resulting time dependent current [41].

The sample consists of an organic film or crystal sandwiched between two conducting electrodes. The electrode is usually composed of a transparent conductor such as indium-doped tin oxide (ITO), but a translucent metal electrode is also often used. The material is illuminated with a short laser pulse in close proximity to one of the electrodes to create a hole-electron pair. *Figure 1.16 a* shows the principle, the photogenerated charge migrates through the material to the second electrode by applying the polarity of the bias voltage and driving the electric field in the range of 10^4-10^6 V/cm. This charge transfer gives the current recorded in the external circuit. The current is constant and then the time t of the electrode drops to zero after the charge sheet arrives. The time is related to mobility:

$$\tau_t = \frac{L}{\mu F} = \frac{L^2}{\mu V}$$

Where L is the distance between the electrodes, F is the electric field in the organic layer, and V is the external voltage on the sample.

Under ideal conditions, the signal shows a step shape (*Figure 1.16 b*), and the decay of the current corresponds to the arrival of the charged sheet. However, in practical situations, charge transfer is much more complicated from the front electrode to the back electrode. Diffusion and capture are two important features that occur in TOF experiments: therefore this technique requires high purity work and flawless samples.

1.2 Liquid crystals

1.2.1 Generalities

Since the beginning of 1888, Friedrich Reinitzer studying the physicochemical properties of various cholesterol derivatives (ie, cholesteric liquid crystal materials), liquid crystal materials have entered the field of researchers and attracted more and more attention. Then, in 1922, G. Friedel proposed that liquid crystals are intermediate between anisotropic crystals and isotropic liquid (*Figure 1.17*).

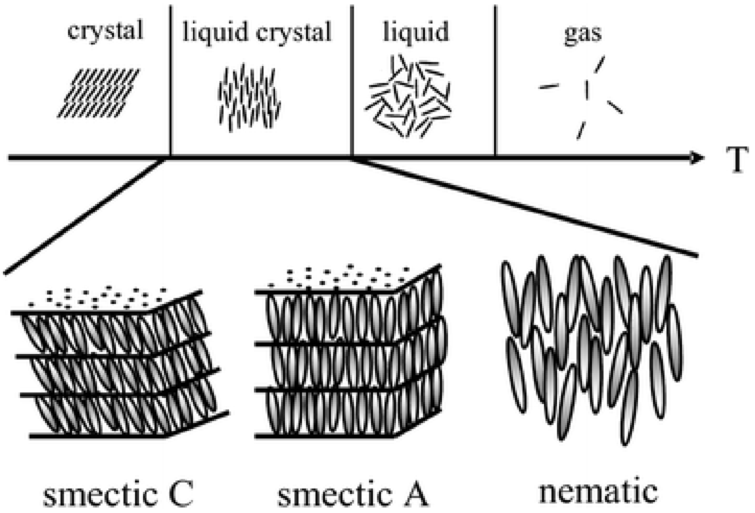

Figure 1.17 A common phase sequence on material's thermal behavior and the structures of nematic, smetic A, C [48].

More precisely, the liquid crystal state is defined as the real state between the classical crystalline solid state and isotropic liquid. Liquid crystalline phase, also known as 'mesophase', is now one of the main research fields of soft materials. Their macroscopic behavior depends on the molecular properties of their constituents: mesomorphic and liquid parts (usually alkyl chains). In addition, the type of liquid crystalline phase is usually determined by the shape anisotropy of these mesogens.

Based on the nature of the system, liquid crystals can be classified into two types: lyotropic liquid crystals [49] and thermotropic liquid crystals. Lyotropic liquid crystal, liquid crystalline polycrystalline phenomena produced by the interaction between one or more solvents and amphiphilic molecules. Regarding thermotropic liquid crystals, the phase continuity is obtained by changing the temperature. Under special circumstances, these processes can also be combined to obtain amphotropic liquid [50].

In this work, we only focus on thermotropic compounds.

1.2.2 Liquid crystals general classification

There are different ways to classify liquid crystals. For example, we can separate them based on the molecular molar mass of the starting materials, leading to liquid crystal polymer materials and liquid crystal small molecule materials (*Figure 1.18*).

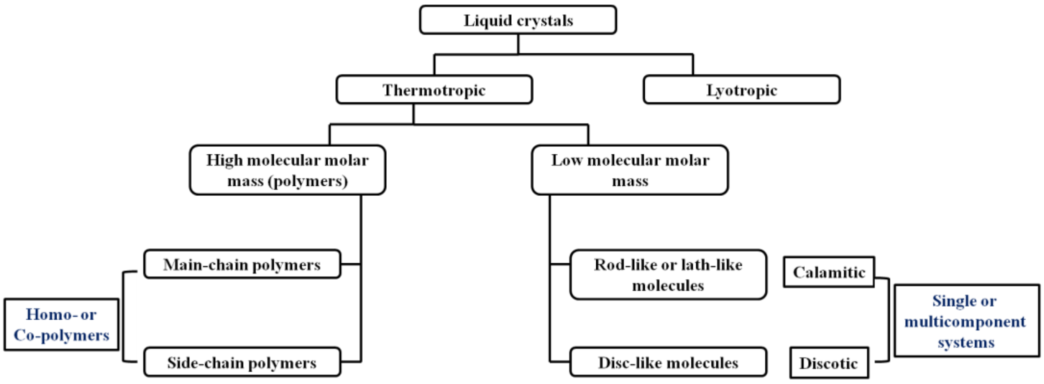

Figure 1.18 Schematic representation of the classifications of liquid crystals.

As our study involves only small molecules, we will focus only on this family of materials in the following parts.

Small molecules are classified according to their shapes and well-defined molecular structures, which are directly related to the molecular structure of mesomorphic compounds. Therefore, here we will introduce only two types of liquid crystal classifications involving small molecules, based on the shape of the starting material or the thermal behavior of the material (mesophase classification).

1.2.2.1 Different types of mesogens

Molecules that show the liquid crystal phase are called mesogens. For molecules showing the LC phase, it is usually necessary to have rigidity and anisotropy (ie longer in one direction than the other). A liquid crystal mesogen is composed of a rigid part and a flexible part. The classification of mesogen is depending on the shape of rigid aromatic core. For calamitic type mesogens, their orientation is along the long axis. Disk-like mesogens are also known, and these orientations are in their short-axis direction. In addition to small molecules, polymers can also form LC phases. Besides calamitic and discotic, there are two other shapes of molecules reported. *Figure 1.19* shows the different shapes of mesogens.

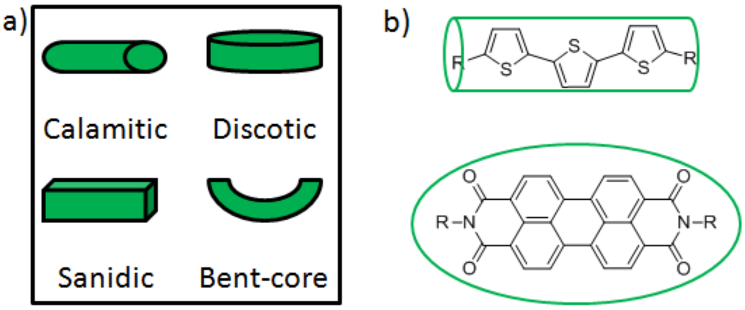

Figure 1.19 a) Different shapes of mesogens; b) Examples of calamitic and discotic molecules.

Figure 1.20 illustrates the representation of discotic and calamitic liquid crystalline materials. Charge transport properties are indeed different depending on the shape of mesogens. Obviously, for discotic mesogens, one dimensional charge transport is favored along the column while for calamic mesogens the two dimentional charge transport is favored within the layers.

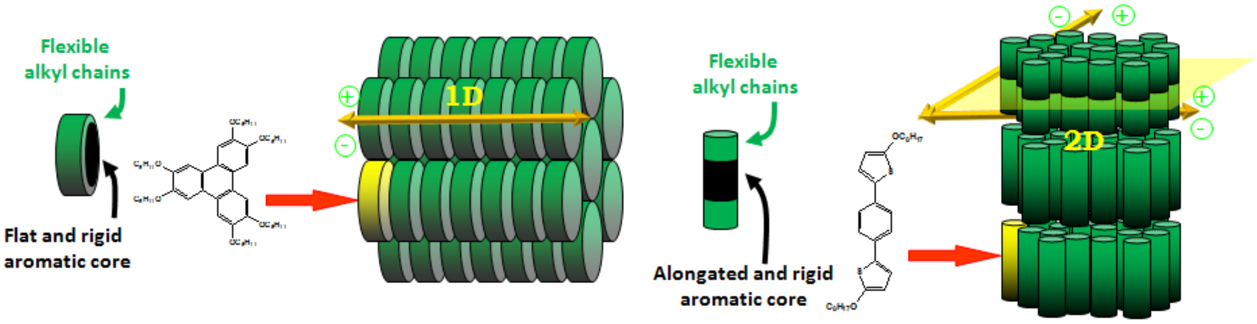

Figure 1.20 Schematic representation of discotic and calamitic liquid crystalline materials.

1.2.2.2 Different types of mesophases

Various liquid crystal phases, also called mesophases, can be characterized by the type of ordering that exists. The positional order whether the molecules are arranged in any ordered lattice and the orientation order whether or not the molecules mainly point in the same direction can be distinguished. Furthermore the order can be short-range (only between molecules close to each other) or distant (extended to larger, sometimes macroscopic sizes). Most thermotropic liquid crystals will have an isotropic phase at high temperatures. That is, heating will eventually drive them into the traditional liquid phase, which is characterized by random and isotropic molecular sorting (with little or no long range order) and fluid-like flow behavior. The order of liquid crystal phases is extensive on the molecular scale. This sequence extends to the entire domain size, which can be on the order of micrometers, but does not generally extend to the macroscopic scale that often occurs in classical crystalline solids.

There are many mesophases, and the essential ones are shown in *Figure 1.21*.

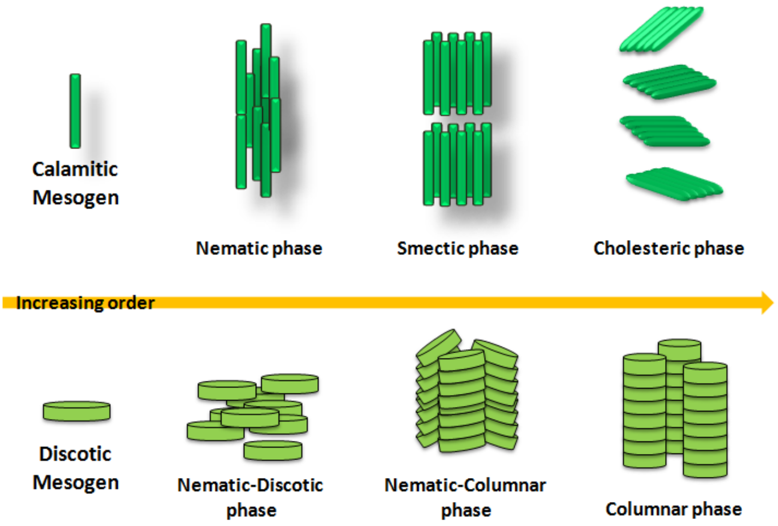

Figure 1.21 Commn mesophases of small molecular liquid crystals.

For calamitic shape molecules, the phases can be described depending on the degree of order, going from nematic phases to smectic phases which means the molecules are organized in lamellar systems. Discotic compounds possess different mesophase as well. They can form two types of nematic phase and columnar phase. The molecules are organized in column systems.

Some common mesophases, including nematic, smectic A-C, columnar phases will be exhibited in this part.

Nematic phases

The nematic phase is one of the most common LC phases. Its distinguishing feature is that the molecules have no positional order, but they do have long-range orientation ordering. Therefore, in each domain the molecules flow and are randomly distributed in the liquid, but they all point in the same direction (*Figure 1.22*).

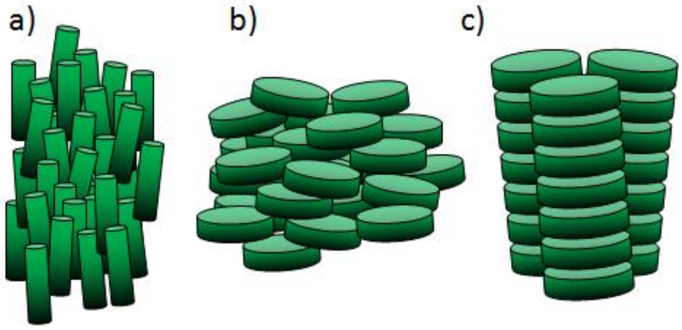

Figure 1.22 Schematic representation of the nematic mesophase in the case of the a) calamitic; b) and c) discotic mesogens.

The typical schlieren textures observed by polarized optical microscopy for nematic phases are shown in *Figure 1.23*.

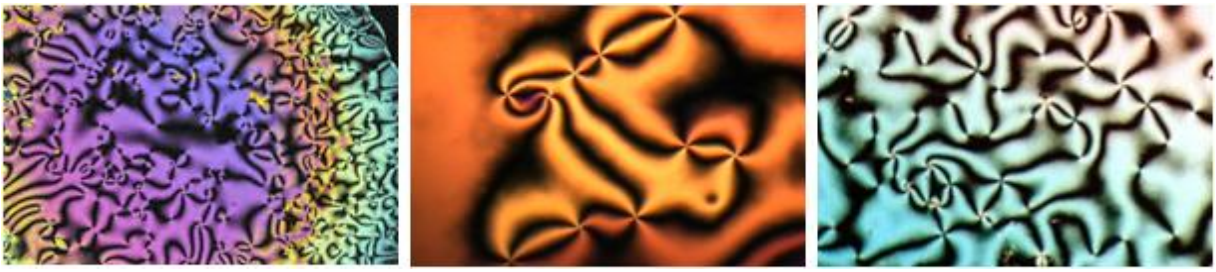

Figure 1.23 Schlieren textures of nematic phases [52].

Chiral molecules (ie, those with no internal planes of symmetry) can produce a special chiral nematic phase, often referred to as the cholesterol phase, because it was first observed with cholesterol derivatives. This phase shows the distortion of the molecule perpendicular to the director with the molecular axis parallel to the director. The limited twist angle between adjacent molecules is due to their asymmetric stacking, which results in a longer chiral sequence. The molecules have a positional order in the layered structure (as in other layered phases), where the molecules are tilted at a limited angle with respect to the layer normal. Chirality causes a limited azimuthal distortion from one layer to the next, creating a helical twist of the molecular axis along the layer normal (*Figure 1.24*).

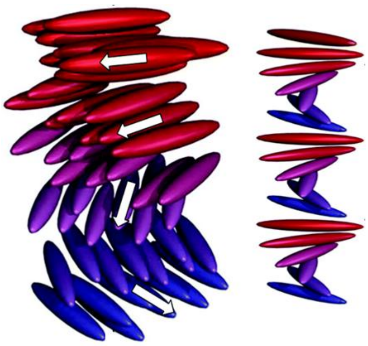

Figure 1.24 Schematic representation of the organization of chiral nematic mesogens.

The typical optical textures observed by polarized optical microscopy for chiral nematic phases are given in *Figure 1.25*.

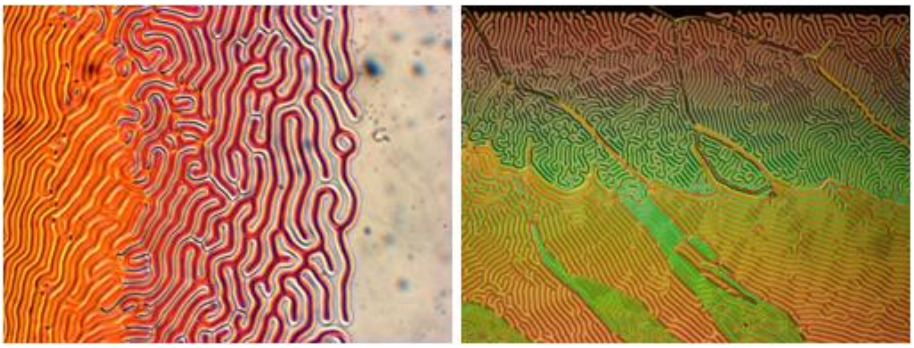

Figure 1.25 Some cholesteric textures of chiral nematic phase [52].

Smectic phases

The smectic phase is another different mesophase of the liquid crystal state. In the smectic state, the molecules maintain the general orientation sequence of the nematic phase and positional order are organized in layers or planes. The motion of the molecules is confined within these planes, and it can be observed that separate planes flow through each other. An increasing in the order means that the smectic state is more ‘solid-like’ than the nematic.

Smectic liquid crystals have a wide range of variations, ranging from low-ordered smectic phases to highly ordered smectic phases. According to its historical sequence of discovery, it is often referred to as SmA, SmB, SmC, etc., and is characterized by the layered structure of liquid crystal molecules [51]. Each smectic phase, however, has a different molecular orientation and alignment in a smectic layer. In the smectic A (SmA) phase (*Figure 1.26 a*), the molecular orientation is parallel to the normal to the layer and a uniaxial phase is formed, whereas in the smectic C (SmC) phase (*Figure 1.26 c*), the molecules are inclined at an average angle θ to the normal layer. The smectic B (SmB) (*Figure 1.26 b*) which derive from the smectic A, smectic I (SmI) (*Figure 1.26 d*) and smectic F (SmF) (*Figure 1.26 e*) which derive from the smectic C phases, are other smectic phases characterized by a positional order within the layer. In these highly ordered phases, the molecules are arranged hexagonally within the layers.

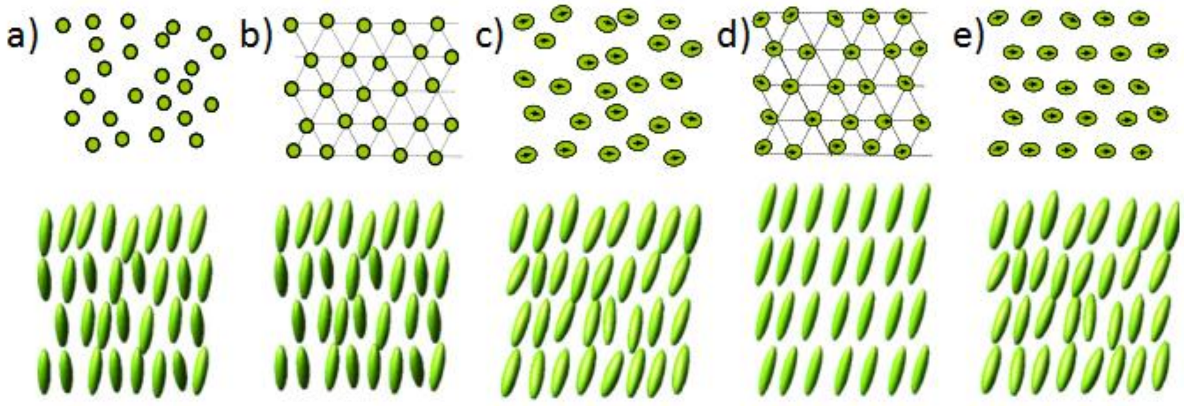

Figure 1.26 Schematic representation of the organizations of the mesogens in a) Smectic A; b) Smectic B; c) Smectic C; d) Smectic I and e) Smectic F mesophases.[51]

In general, when a smectic sample is placed between two glass slides, these layers will distort and slide to each other to adjust the surface condition and maintain its thickness. The distortions of these layers produce smectic optical properties (focal conic structures). Typical optical textures formed by smectics are shown in *Figure 1.27*.

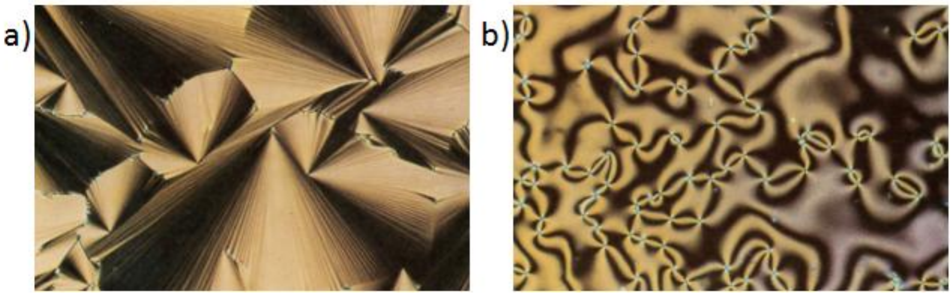

Figure 1.27 Typical focal conic textures of a) Smectic A phase and b) Smectic C phase.[52]

Several smectic phases have been recognized, but we will introduce the two major conventional SmA-C in this chapter.

SmA

Both the director and the optical axis of the smectic SmA are perpendicular to the smectic plane, but the orientation sequence is not optimal (*Figure 1.28*).

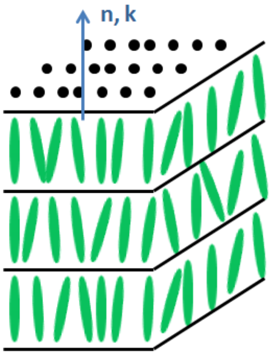

Figure 1.28 Structure model of smectic A phase.

The repeating order is d, which is equivalent to the interval between the smectic layers. That is, the length of the mesophase can be described by the sequence parameters of the smectic layer:

$$\delta = < \frac{3\cos^2 \vartheta_i - 1}{2} \cos(\frac{2\pi}{d} z_i) > \qquad 1.1$$

The smectic layer spacing can be estimated by X-ray small angle scanning using Bragg reflection:

$$n\lambda = 2d \sin\theta \qquad 1.2$$

n is the scattering coefficient, λ is the X-ray wavelength, d is the repeating period, and θ is the scattering angle. For the fluid smectic phase, the first diffraction peak can be observed in the smectic except for some amphoteric molecules and intermediate sugars. The X-ray scattering pattern is proportional to the Fourier transform of the electron intensities, so we can deduce that the actual smectic layer is not an optimal layer (which will lead to scattering and reflection phenomena) and the center of mass is sinusoidal.

Figure 1.29 shows that the SmA layer has the following possible arrangements: (a) The monolayer has a thickness d equal to the length L of the molecule ; (b) Bilayer, d≈2L; (c) Crossed molecular arrangement, L< d< 2L.

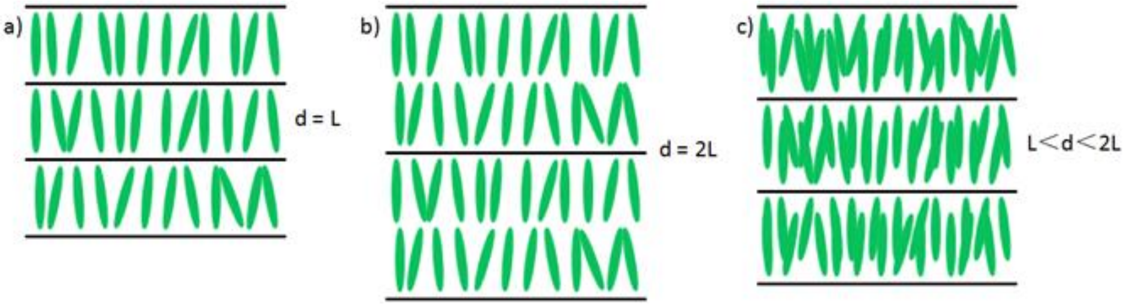

Figure 1.29 Possible arrangement of SmA layers.

SmC

The SmC phase is one-dimensionally ordered, and the difference from SmA is that the director has a certain tilt angle with respect to the near-plane. The tilt angle of a single molecule can be represented by the vector θ and the tilt azimuth φ. The average numerator of the total molecules gives:

$$\theta = < \theta_i \begin{pmatrix} \cos\varphi_i \\ \sin\varphi_i \end{pmatrix} > \qquad 1.3$$

The magnitude of the tilt angle θ is determined by dynamic thermodynamic factors such as temperature and pressure, but the tilt direction cannot be predicted so far. If the molecule is chiral, the tilt of the director is not only related to the physical properties but also to the texture.

Figure 1.30 depicts the basic structure of SmC. The tilt angle θ is a parameter related to temperature, increasing as the temperature decreasing. In the range of low temperature SmC phase, the tilt angle of pure material is $\theta \approx 25^o$--35^o. The condition of θ >45 has not been observed.

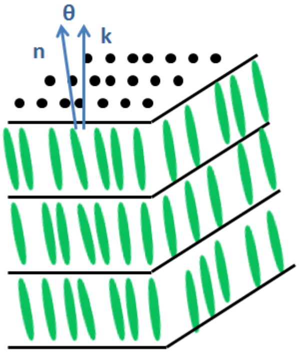

Figure 1.30 Structure model of smectic C phase.

SmB

Unlike SmA and SmC phases, SmB is a hexagonal phase. In fact, the molecules are arranged perpendicular to the plane of the layer, and the middle layer has a hexagon of long axes, thereby maintaining the rotation and positional sequence as well as the intra-layer flexibility. This is clearly shown in *Figure 1.31*, the rod-shaped molecules pack tightly into hexagons without staggering and tilting interlayer, but each molecule is free to rotate.

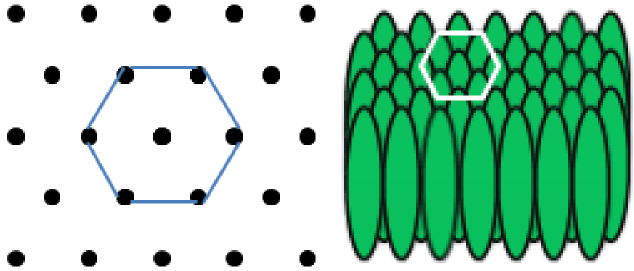

Figure 1.31 Structure model of smectic B phase.

A typical X-ray image of the SmB pattern is a picture with a sharp outer ring and a defined inner circle. DSC can detect the SmB transition by having a relatively large chirp signal with a value of 4-8 KJ/mol.

In general, the arrangement order is from smectic phase A to C and then B. We can distinguish these three phases according to their arrangement, director axis and stratification type. [53, 54]

1.2.3 Liquid crystalline semiconductors

It is difficult to design and synthesize molecules with high carrier mobility, excellent solution processing and high flexibility. In general, the dense molecular structure in molecular crystals helps to increase the carrier mobility. For example, some aromatic molecules have a carrier mobility up to 1 $cm^2\ V^{-1}\ s^{-1}$. However, accurate control of the crystal growth process is essential for obtaining high-quality crystal films. At the same time, solution processability requires weak intermolecular interactions. Nevertheless, such weak intermolecular interactions may lead to the formation of amorphous structural materials and exhibit low carrier mobility [55]. Indeed, the carrier mobility in the amorphous organic semiconductor is in the range of 10^{-7}-10^{-4} $cm^2\ V^{-1}\ s^{-1}$ [56].

One of the methods to solve the above mentioned problems is to use the properties of liquid crystals. Based on weak intermolecular interactions, dynamic anisotropic nanostructures have been constructed in the liquid crystal phase, and the use of nanostructures can achieve various electrical and optical enhancements [57]. The smectic or columnar liquid crystals have a highly ordered molecular packing structure similar to that of crystals, which contributes greatly to carriers transport. Moreover, most liquid crystal molecules have an alkyl chain so that they are soluble in organic solvents, while the thermal movement of the alkyl chain also contributes to the flexibility of the mesogenic structure [55].

In the 1990s, liquid crystal materials entered the field of organic semiconductor materials. Although these materials are easy to make uniform thin films and it is easy to control their molecular orientation (in a self-assembled manner), they have received little attention for a long time. But more recently, liquid crystals have been reported as organic transistor materials in the 2000s [58].

Garnier et al. reported an OFET based on dialkyl oligothiophene derivative, the alkyl chain attached to the oligothiophene affected the solubility of the molecular layer and the molecular assembly. The dihexyl-tetrathiophene exhibiting a liquid crystal phase, the OFETs was fabricated by spinning at high temperatures [59, 60]. Later, Phillips and coworkers reported thiophene-ethynyl-trithiophene derivatives as liquid crystal organic semiconductors and successfully manufactured OFETs [61]. Funahashi et al. studied the performance of an OFET prepared with a liquid crystal material phenyltrithiophene derivative (3-TTP-Ph-5), the mobility is as high as 10^{-2} cm^{2} V^{-1} s^{-1} [62].

Subsequently, there have been many reports on OFETs prepared from thin films of liquid crystal materials including dithienylnaphthalene [63], hexabenzoxazolone [64], bis-(5'-hexylthiophene-2'-yl)-2,6-Anthracene [65], and dialkyl-BTBT derivatives [66]. *Figure 1.32* shows the chemical structures of typical liquid crystalline semiconductors.

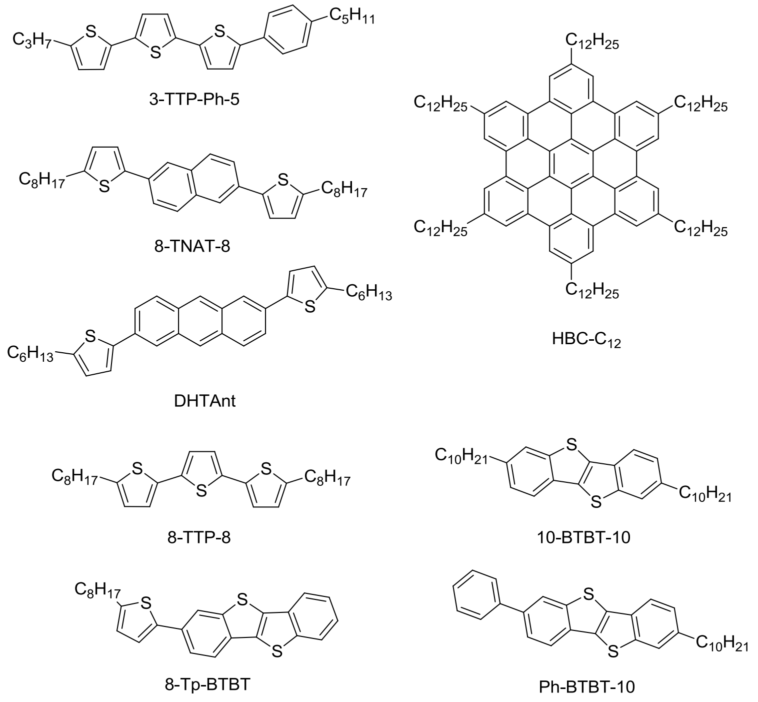

Figure 1.32 Chemical structures of typical liquid crystalline materials for organic transistors.

1.2.4 Liquid crystalline fluorescent materials

Among various liquid crystals, fluorescent liquid crystal materials have received more and more attention [67, 68, 69, 70]. The combination of the internal luminescence and self-assembly properties of the liquid crystal phase is important for optoelectronic applications such as anisotropic light-emitting diodes and liquid crystal displays [71, 72, 73]. Fluorescent liquid crystals can emit linear or circularly polarized light [68, 74, 75], which can be used to build illumination and alignment layers in liquid crystal optical displays, thus avoiding the use of polarizers and absorbing filters. The color and brightness of the light emitted by the liquid crystal light emitter can be controlled by an external field, which may lead to the development of an easily tuneable electrochromic and optical switching system. This approach simplifies device design and significantly increases device brightness, contrast, efficiency, and viewing angle [76, 77, 78].

Although the prospects for high emission efficiency liquid chromatography are promising, its synthesis is difficult to handle. In the mesophase, especially those mesophases formed by discotic molecules [79], the chromophoric mesogens are conventionally wrapped and subjected to strong mutual interactions, which are usually extinguished by the formation of harmful substances such as stimulating agents and exciplexes [80, 81, 82]. The accumulation of sacrificial molecules usually enhances the luminescence, thus making the synthesis of highly efficient fluorescent LCs a daunting task [78]. As examples, *Figure 1.33* shows the chemical structures of fluorescent liquid crystals.

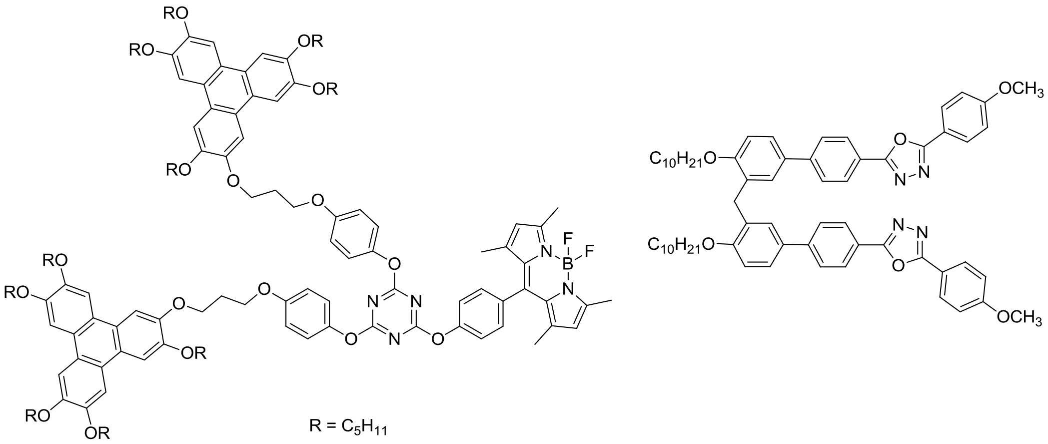

Figure 1.33 Chemical structures of liquid crystalline fluorescent materials [83, 84].

1.2.5 OLETs

In recent years, a new class of organic optoelectronic devices, organic light emitting transistors (OLETs), combines the switching functions of the OFETs and the light emitting functions of OLEDs, and shows great promise in the fields of optical communication, flat panel display, solid state lighting, and lasers [85] (*Figure 1.34*). In addition, different from the vertical structure of OLEDs, OLETs is a planar structure of the light-emitting device, which provides a new perspective and system for the study of carrier injection, transmission and composite luminescence and other physical processes.

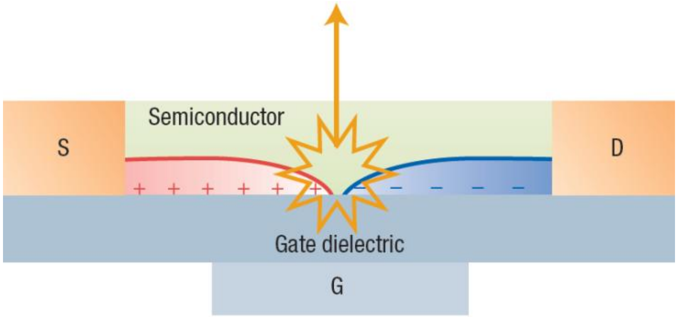

Figure 1.34 Scheme of a light emitting transistors [85].

According to the transmission properties of OLETs, they can be classified into unipolar OLETs, bipolar OLETs, and heterojunction OLETs. Based on the relative positions of the source and drain electrodes, OLETs can be divided into planar OLETs and vertical OLETs.

Unipolar OLETs

There is only one type of carrier (mainly hole-based) in the unipolar OLETs channel, and the other type of carrier is injected from the electrode into the organic semiconductor layer in a tunneling manner. Its emission position is only limited near the electrode.

In 2003, Hepp et al. reported the first unipolar OLET. They deposited a polycrystalline organic tetracene layer as a carrier transport layer and a light-emitting layer under high vacuum conditions. A P-type field effect characteristic was observed and the light emission position was observed near the drain of the device [86].

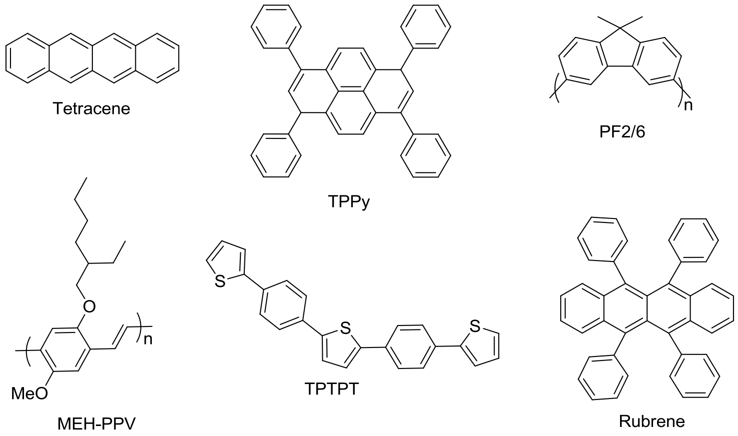

Figure 1.35 Chemical structures of typical materials for unipolar OLETs.

Ambipolar OLETs

Ambipolar OLETs refer to the preparation of OLETs using an ambipolar organic semiconductor material as the active layer of the transistor. Ambipolar OLETs can control the transfer of electrons and holes in the channel by adjusting the gate voltage and the source-drain voltage, thereby making holes and the electrons meet in the channel to form excitons and emit light. According to organic semiconductor materials used in ambipolar OLETs, they can be classified into three types: single crystal ambipolar OLETs, polymer ambipolar OLETs, and small organic molecules ambipolar OLETs.

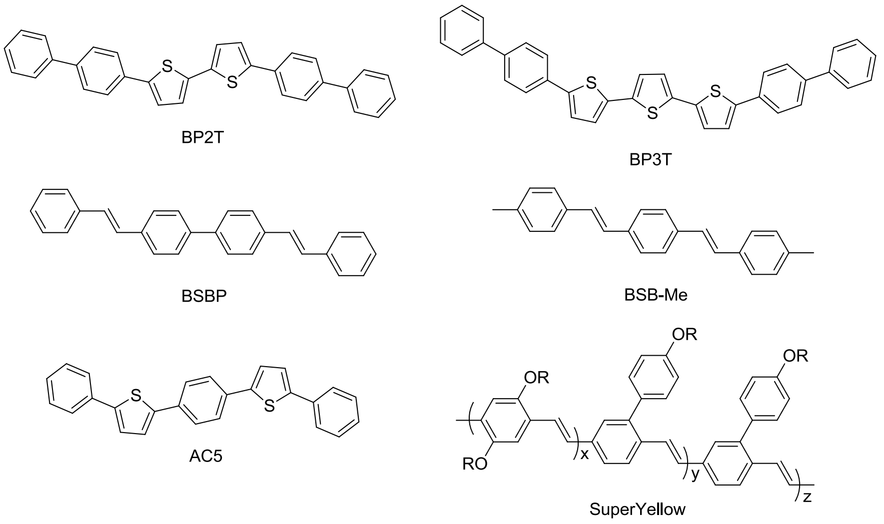

Figure 1.36 Chemical structures of typical materials for ambipolar OLETs.

PN heterojunction OLETs

The organic semiconducting layer in the PN heterojunction OLETs is formed by a combination of a n-type organic semiconductor material and a p-type organic semiconductor material, which can realize the simultaneous propagation of electrons and holes in the channel.

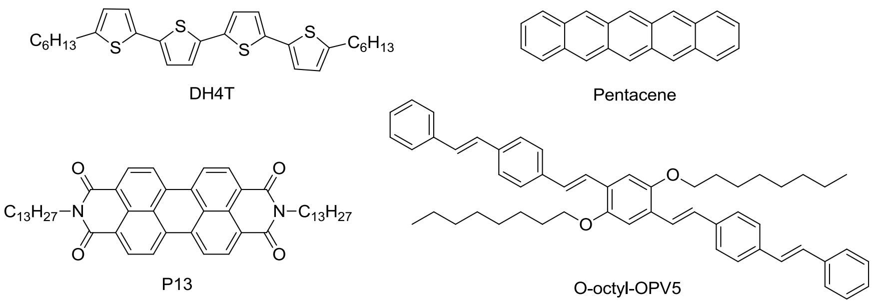

Figure 1.37 Chemical structures of typical materials for PN heterojunction OLETs.

AC grid pressure type OLETs

The above types of OLETs are DC gated OLETs. The characteristic of AC gated OLETs is to apply AC voltage to the gate. It is a new way of operation of the device. This method effectively promote the injection of electrons and holes from the source and drain electrodes into the active layer of the OLETs, and the luminous intensity of the device changes with the change of the frequency of the AC voltage.

Vertical structure OLETs

At present, most of the reported OLETs device structures are based on traditional planar structures.

Recently, Vertical structure OLETs have attracted attention from researchers because of their low operating voltage, high operating frequency, high current density, and wide light emitting area, including electrostatically-induced OLETs, metal-insulator-semiconductor-type OLETs (MIS-OLETs), and vertical field-effect OLETs.

1.2.6 Liquid crystalline materials characterization methods

There are several methods for determining liquid crystal properties and their phase transitions by different techniques. Our work involves polarizing microscope (POM), differential scanning calorimetry (DSC) and X-ray diffraction (XRD) measurements, which are the most common ones and are described below.

1.2.6.1 Polarizing microscope

The characteristic of a polarizing microscope is to change the ordinary light into polarized light for microscopic examination, in order to identify whether a matter is monorefractory (isotropic) or birefringent (anisotropic).

When light passes through a matter, if the nature and approach of the light does not change due to the direction of illumination, the matter is optically ‘isotropic’, also known as single refraction, such as ordinary gases, liquids, and amorphous solid. On contrary, if light passes through another matter, the speed, refractive index, absorbency, and vibration of the light are different depending on the direction of illumination. This matter is optically ‘anisotropic’, also known as birefringent. It occurs for crystals, fibers,liquid crystals.

The polarizing microscope has two polarizers, one called ‘polarizer’ between the light source and the object to be inspected; the other one is called ‘analyzer’ between the objective lens and the eyepiece. If the vibration directions of the polarizer and the analyzer are parallel to each other, that is, in the case of ‘parallel detection’, the field of view is the brightest. Conversely, if the two are perpendicular to each other, thus, in the case of ‘orthogonal misalignment’, the field of view is completely dark. If the two are tilted, the field of view indicates a moderate degree of brightness.

Figure 1.38 shows the principle of a POM system. In the case of orthogonality, the field of view is dark. If the sample being examined is optically isotropic (single-refractor), the field of view is still dark no matter how the stage is rotated. If the material to be inspected contains a birefringent matter, this part will emit light. This is because the linearly polarized light emitted from the polarizer enters the birefringent matter, and two kinds of linearly polarized light whose vibration directions are perpendicular to each other are generated. When the light passes through the birefringent materials, the vibration directions of the two polarized lights are different depending on the type of the materials.

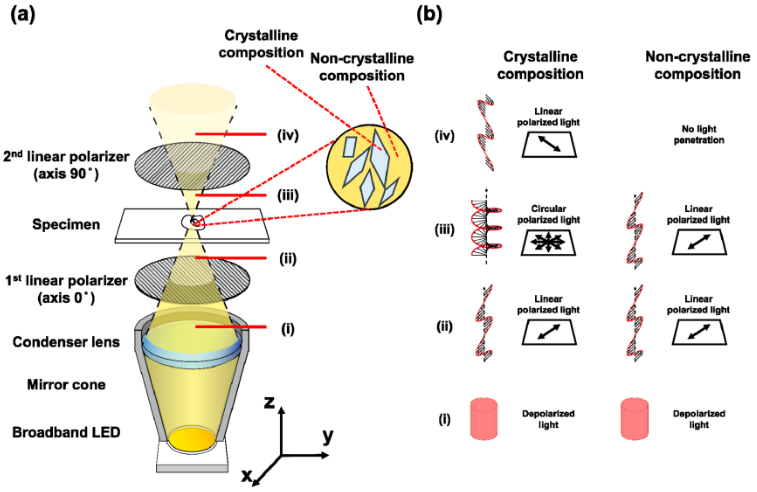

Figure 1.38 The a) schematic and b) principle of a polarization microscopy system [87].

In the case of liquid crystals, different liquid crystal phases exhibit different characteristic patterns. *Figure 1.39* shows several liquid crystal phases texture under POM.

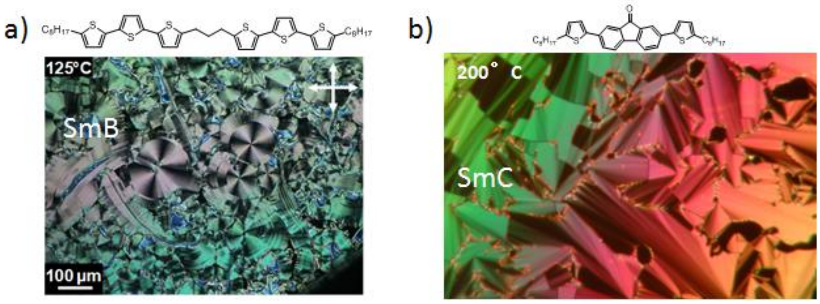

Figure 1.39 a) SmB; b) SmC phases texture under POM [88,89].

1.2.6.2 Differential scanning calorimetry

Differential scanning calorimetry (DSC) is a thermal analysis technique in which the difference in heat required to increase the sample and reference temperature as a function of temperature is measured. The sample and reference are maintained at nearly the same temperature throughout the experiment. Typically, a temperature program is designed for DSC analysis that causes the rack temperature to increase linearly over time.

The basic principle of this technique is that when a sample undergoes a phase change, more or less heat is required to flow to it than the reference to keep the two at the same temperature. Whether there must be less or more heat flowing to the sample depends on whether the process is exothermic or endothermic. For instance, when a solid sample melts into a liquid state, more heat is required to flow into the sample to increase its temperature at the same rate as the reference. This is due to the fact that the sample absorbs heat as it undergoes an endothermic phase change from solid to liquid. On parallel, when the sample undergoes an exothermic process (for example crystallization) less heat is required to raise the sample temperature. The differential scanning calorimeter is capable of measuring the amount of heat absorbed or released during this transition by observing the difference in heat flow between the sample and the reference [90, 91, 92].

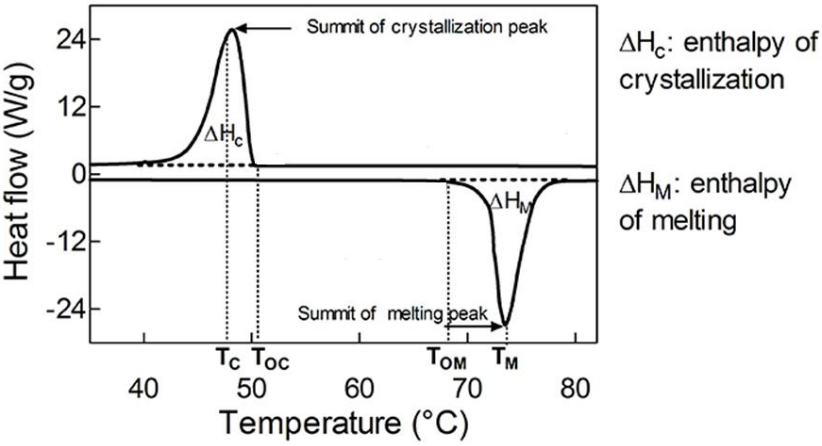

Figure 1.40 Schematic diagram of a thermogram [93].

The x axis of the differential scanning calorimetry curve is temperature or time, and the y axis is the rate at which the sample absorbs heat and exotherms, also known as heat flow rate (*Figure 1.40*). The peak area can be calculated by the following formula:

$$\Delta H = KA$$

where H is a phase transition, K is a calorimetry constant, and A is the area of the peak. Different instruments have different calorimetric parameters, and the calorimetry constant of the instrument can be determined by standard samples [91].

DSC is widely used to study liquid crystals. As the temperature increases, substances with liquid crystal properties undergo a series of phase transitions from solid state to isotropic liquids. For high-precision scanning calorimetry, the phase transition enthalpy of each phase change can be measured, and the phase transition can be studied by observation of the phase state.

1.2.6.3 X-ray diffraction

X-ray diffraction (XRD) is mainly used for phase analysis and crystal structure determination, and all the information it acquires is based on the structure of the material. X-ray diffraction is generally classified into single crystal X-ray diffraction and multiple crystalline powder X-ray diffraction.

Each crystalline material has its own unique chemical composition and crystal structure. There are no two materials, their unit cell size, particle type and their arrangement in the unit cell are completely consistent. Therefore, when X-rays are diffracted by the crystal, each of the crystalline materials has its own unique diffraction pattern, and its characteristics can be characterized by the respective diffraction crystal plane spacing d and the relative intensity I/I_1 of the diffraction line. In physics, Bragg's law gives the angles for coherent and incoherent scattering from a crystal lattice:

$$2d\sin\theta = n\lambda$$

where θ is the scattering angle, n is a positive integer, λ is the wavelength of the incident wave.

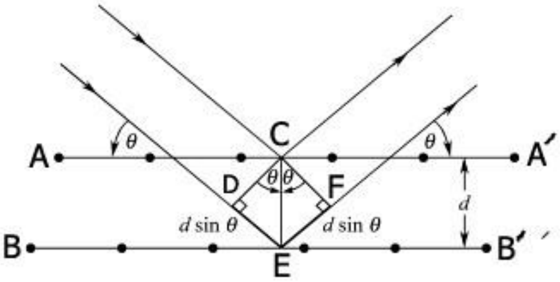

Figure 1.41 Principle of X-ray diffraction [94].

For crystal materials, when the crystal to be measured is at a different angle from the incident beam, those crystal planes satisfying the Bragg diffraction are detected, which are diffraction peaks with different diffraction intensities on the X-ray diffraction (XRD) spectrum. For amorphous materials, X-ray diffraction (XRD) patterns of amorphous materials are diffuse scattering peaks due to the absence of long-range ordering of atomic arrangements in crystal structures and short-range ordering in several atomic ranges. *Figure 1.42* shows the X-ray diffraction spectrum of different materials.

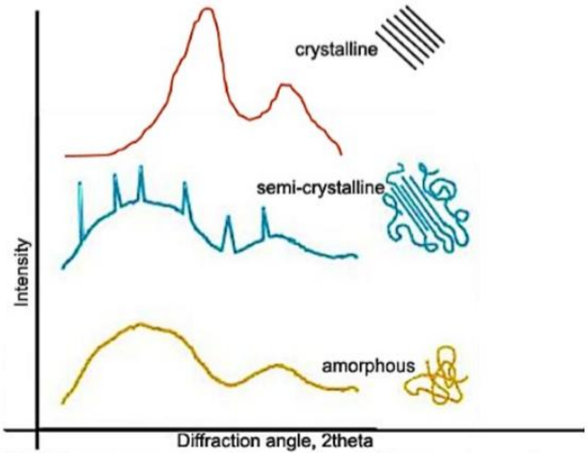

Figure 1.42 X-ray diffraction spectrum of crystalline, semi-crystalline and amorphous material [94].

1.3 Narrow bandgap materials

1.3.1 Generalities

One of the major advantages of organic semiconductor materials is that the properties such as optical bandgaps, tunable energy levels, and desired electronic properties can be adjusted by changing the structure. For example, conjugated polymers/small molecules with narrow optical band gaps can be designed. In this context, narrow bandgap materials (including polymers and small molecules), which are absorbing in the near-infrared range and usually have a band gap of less than 1.3 eV, are particularly attractive for organic photovoltaics (OPVs) and ambipolar organic field-effect transistors (OFETs) applications [4].

The physical properties of this type of material are very interesting because of its smaller energy gap. For instance, these narrow bandgap materials' electronic orbitals are much more closely overlapping and the π electrons are easier to delocalize [95]. In addition, in such materials the charge separation is more efficient. This may lead to i) larger dielectric constant, ii) stronger dipole moment, and iii) lower exciton binding energy [96]. Therefore, photophysical and charge transfer of narrow bandgap polymers/molecules is quite unique in organic semiconductors.

This kind of material is an interesting series of semiconductor materials and led to sort out many exciting breakthroughs in the field of organic electronics applications. The small bandgap makes it easy to inject electrons into LUMO and holes into HOMO, and the strong polarity of the molecules makes both negative and positive charges transfer efficiently. Therefore, such materials exhibit both p-type and n-type charge-transfer properties, which has great promise for the manufacture of bipolar field effect transistors. In addition, this type of material has a relatively small optical bandgap energy utilizing near-infrared photons, which is extremely advantageous for the preparation of OPVs [4].

1.3.2 Design and synthesis of narrow bandgap materials

1.3.2.1 Synthetic Approaches

In general, there are two design approaches for preparing narrow bandgap polymers: i) stabilizing the quinoid resonance structure and ii) utilizing donor-acceptor interactions [97, 98, 99, 100].

On the one hand, the *Figure 1.43* shows few strategies to synthesize polymers. The first way is to stabilize the quinoid resonance structure. Generally speaking, quinoid and aromatic are two resonant structures that any conjugated polymer possessed (see in *Figure 1.43 a*). Although the quinoid form has a smaller bandgap than the aromatic form, it is less energetically unstable since the use of a quinoid structure requires the loss of aromaticity and the loss of stable energy. Studies have shown that one way to stabilize the quinoid form can be achieved by condensing another aromatic ring with the polymer backbone [97]. *Figure 1.43 b* shows that when a thiophene ring is converted from aromatic form to quinoid form in a polymer molecule, the benzene ring fused to the thiophene ring providing a large aromatic resonance stabilization energy. Therefore, poly(isathianapthene) is the first well-known narrow band gap polymer with a bandgap as low as 1 eV. The result indicates that when the conjugated backbone of the polymer is composed of alternating sequences of fluorene and aromatic units, the bandgap adjustment can be achieved [101].

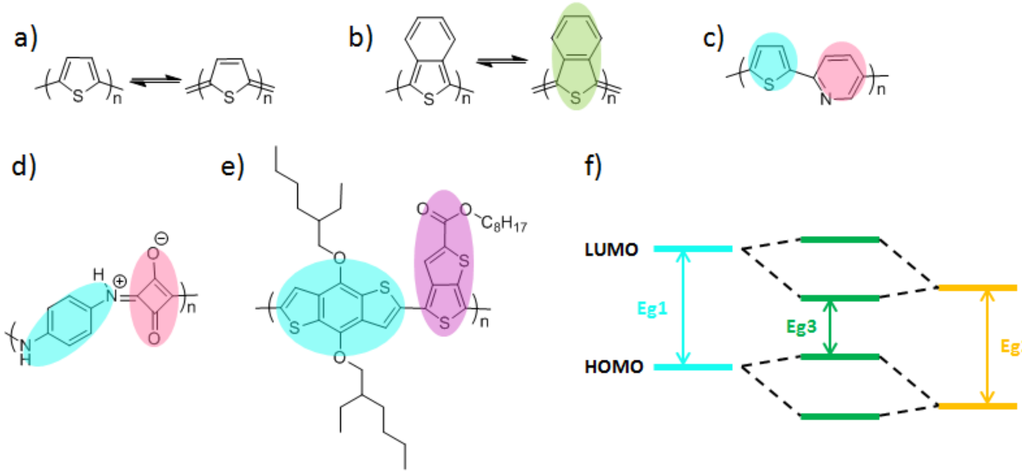

Figure 1.43 Strategies to make polymers. a) Aromatic (left) and quinoid (right) resonance structures of polythiophene; b) Stabilization of the quinoid resonance structure (green color); c) Donor−acceptor copolymer made by Yamamoto (blue part is donor and red part is acceptor); d) Donor−acceptor copolymer made by Havinga; e) Modern synthetic approach that combines both methods (purple part is electron-accepting and can stabilize the quinoid resonance structure); f) Simplified mechanism of bandgap lowering by donor−acceptor interaction.[4]

The second approach is utilizing donor-acceptor interactions. As shown in *Figure 1.1 c*, this method is using alternating electron donating (D) and electron withdrawing (A) units to adjust the band gap of the polymer. Yamamoto et al. conducted the earliest research on Donor-Acceptor polymers [102]. Afterwards, Havinga et al. synthesized a polymer with a bandgap below 0.5 eV through a condensation reaction, further validating this concept [103] (*Figure 1.43 d*). The simple mechanism was given in *Figure 1.43 f*. After polymerization, the HOMO of the electron donating (D) units interacted with the HOMO of the electron withdrawing (A) units, giving two new HOMOs. At the same time, the LUMO of the donor also interacted with the LUMO of acceptor to produce two new LUMOs. The redistribution of electrons into the polymer's new hybrid orbit results in an increase in the HOMO level and a decrease in the LUMO level, which narrows the optical band gap [4].

On the other hand and on parallel, narrow bandgap organic semiconductor small molecule materials show great application prospects in the field of optoelectronic applications and have attracted extensive attention of researchers as well. The approach for synthesizing narrow bandgap small molecules is similar to that of polymers. Donor-acceptor (D-A) or quinoid (Q) approaches have been successfully utilized for the design of high-performance small molecule organic materials [104, 105]. In general, donors and acceptors reacted through palladium-catalyzed stille or suzuki cross-coupling reactions to obtain narrow bandgap molecules [4]. *Figure 1.44* exhibits few examples of narrow bandgap small molecules utilizing donor-acceptor interactions (blue part is donor and red part is acceptor). However, controling and decreasing the gap within small molecules can be more difficult than narrow bandgap polymers. The solution is to use very strong donor or acceptor units so that to achieve near-IR absorbing/emitting abilities [4].

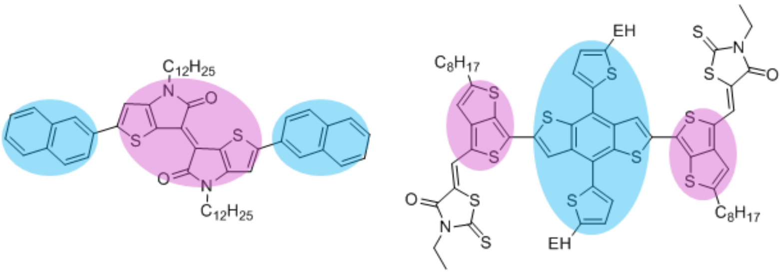

Figure 1.44 Strategies to make small molecules utilizing donor-acceptor interactions (blue part is donor and red part is acceptor).

1.3.2.2 Rational Design for Different Applications

Generally, several hybrid heterocycles such as thiophene, bithiophene, thieno[3,2-b]thiophene, cyclopentadithiophene (CPD), dithienosilole (DTS), naphtho[2,1-b:3,4-b']-dithiophene (NDT), benzodithiophene (BDT) and thiophene-phenylene-thiophene (TPT) are well-known as electron-donating units. Meanwhile, 2,1,3-benzothiadiazole (BT), 4,7-dithien-2-yl-2,1,3-benzothiadiazole (DTBT), diketopyrrolopyrrole(DPP), thieno[3,4-c]pyrrole-4,6-dione (TPD), naphthalene diimide, benzobisthiadiazole (BBT), thieno[3,4-b]thiophene (TT) and thieno[3,4-b]pyrazine (TP) are usually utilized as electron-withdrawing units [106]. The methods of synthesizing either polymers or small molecules often follow palladium-catalyzed cross-coupling reactions. By modifying building blocks, it is possible to design new materials for different applications.

There are similarities and differences for various types of applications of low band gap polymers.

For solar cells, in order to achieve effective exciton dissociation at the donor-acceptor interface, the bandgap of the polymer in the range of 1.2-1.6 eV is more easier to achieving high optoelectronics, so that, the HOMO should be higher than -5.2 eV and LUMO is less than -3.7 eV [107, 108]. In addition, good film morphology and high charge carrier mobility are also essential for high performance OPVs. To achieve this goal, it is necessary to use moderate electron donating and electron withdrawing units with good planar and π-π stacking. For example, BDT, BT, and ester/carbonyl substituted TT units [109].

For bipolar field effect transistors, the most important is to increase the mobility of electrons and holes. Unlike organic solar cells, the materials of bipolar field-effect transistors require relatively shallow HOMO and deep LUMO levels [110]. In general, LUMO levels can be reduced with very strong electron-withdrawing groups such as BBT in order to increase electron affinity and improve electron transport. Moreover, there are many other factors that need to be considered to achieve high performance, such as device interface design, film morphology, molecular stacking and so on.

1.3.3 State of the art

1.3.3.1 OPVs

Polymers

For the molecular design of high-efficiency photovoltaic molecules, several key factors in designing highly efficient conjugated polymer donors are the realization of narrow bandgap (E_g) and broad absorption, relatively low lower-lying HOMO level and higher hole mobility. To achieve the above objectives, the following three strategies can be used: i) D-A copolymerization for narrower E_g and lower HOMO; ii) substitution of lower order HOMO with electron withdrawing group and iii) two-dimensional conjugation for wider Absorption and higher hole mobility. At the same time, increasing the planarity of the main chain and less steric hindrance of the side chains can enhance the π-π stacking to achieve high hole mobility. In addition, the molecular weight of the polymers also affect their photovoltaic properties. In order to obtain highly efficient photovoltaic polymer materials, researchers should try to increase the molecular weight while maintaining solubility [111].

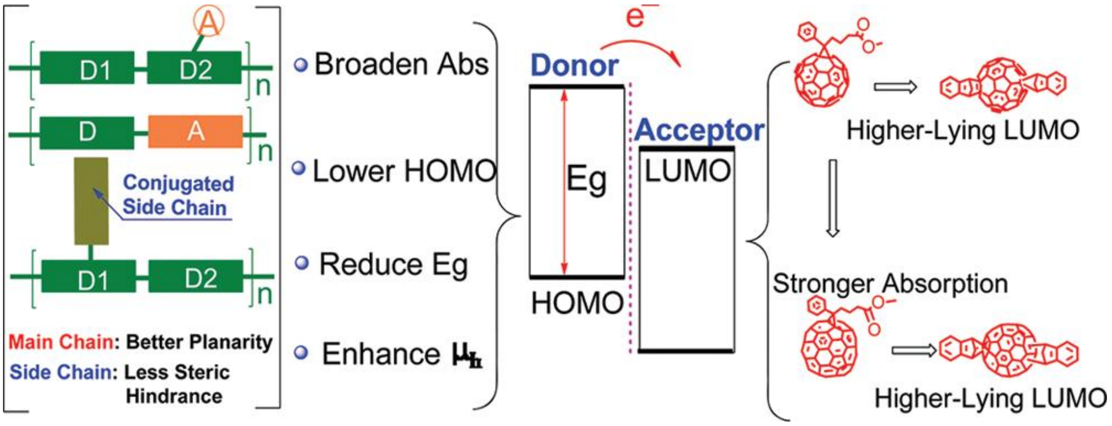

Figure 1.45 Strategies to make high-efficiency photovoltaic molecules [111].

In 2009, Yu et al. introduced thieno[3,4-b]thiophene structural units into the OPV field for the first time, and thieno[3,4-b]thiophene stabilized the quinoid structure to reduce the band gap. When the TT unit was combined with planar BDT unit to form the PTB series polymers, ~50% enhancement in J_{SC} and PCE (from 4% to~6%) was obtained [112]. This serie of materials has inspired a great deal of research over the past decade. Studies have found that D-A polymers, especially fluorinated polymers, show higher dielectric constants and lower exciton binding energy [113]. In 2015, Tang et al. reported a polymer through incorporating the 2-(2-ethylhexyl)-thienyl group into the BDT unit. The device exhibited a high PCE of 10.1% with a J_{sc} of 19.47 mA/cm^2 and V_{OC} of 0.775 V [114]. *Figure 1.46* shows the chemical structures of some representative low-band gap polymers based on thieno[3,4-b]thiophene.

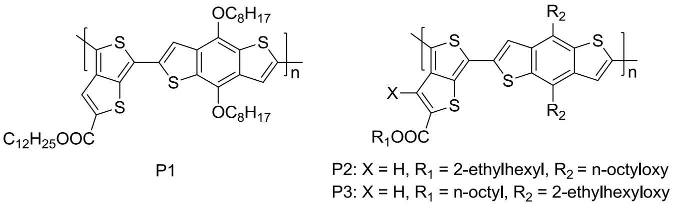

Figure 1.46 Chemical structures of some representative low-band gap polymers based on thieno[3,4-b]thiophene.

Reducing the band gap below 1.5 eV is very significant for OPV. *Figure 1.47* shows the chemical structures of some representative low-band gap infrared polymers based on Benzothia-diazole. Brabec et al. reported the first high performance polymers P4 based on alternating strongly electron-donating CPD units and electron-withdrawing BT units with a bandgap of ~1.4 eV and a moderate PCE of 3.5% was achieved [115]. Later, the same group found that replacing the bridged carbon atoms between two thiophenes into silicon atoms can improve the efficiency of the device significantly. The P5 based device attained a PCE of 5%, a J_{sc} equal to 15.2 mA/cm^2, V_{OC} of 580 mV, and FF of 57% [116]. Yang et al. designed a new polymer P6 of 1.38 eV by replacing the BT unit to strongly electron-withdrawing difluorobenzothiadiazole unit. This polymer shows excellent performance in bulk-heterojunction solar cells with power conversion efficiencies reaching 8.0% and a good V_{OC} of ~0.7 V [117].

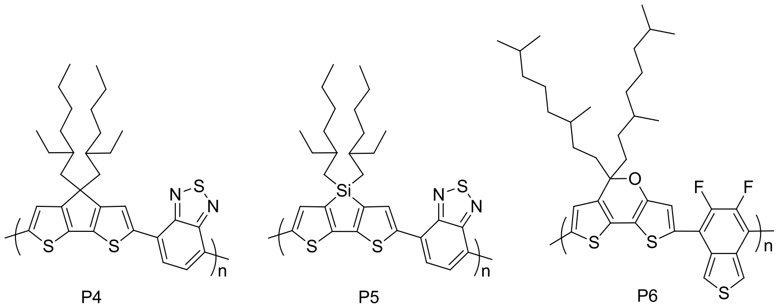

Figure 1.47 The chemical structures of some representative low-band gap infrared polymers based on Bbenzothiadiazole.

Besides thieno[3,4-b]thiophene and benzothiadizole, diketopyrrolopyrrole and isoindigo are important building block for polymers as well [118, 119, 120, 121, 122, 123, 124].

Small Molecules

One of the most important factors limiting the performance of organic solar cells is the mismatch of the absorption spectrum of the organic material and the solar spectrum. This is why, as counterpart of polymers, small-molecule photovoltaic materials have attracted more and more attention, and relevant research results have been published [125, 126, 127, 128, 129, 130]. As we mentioned before, donor-acceptor (D-A) approaches has been successfully utilized for the design of narrow bandgap small molecules. Different combinations can be obtained from a given donor (D) and acceptor (A), resulting in several defined structures, namely D-A, A-D-A, D-A-D, D-A-D-A-D etc (see *Figure 1.48*).

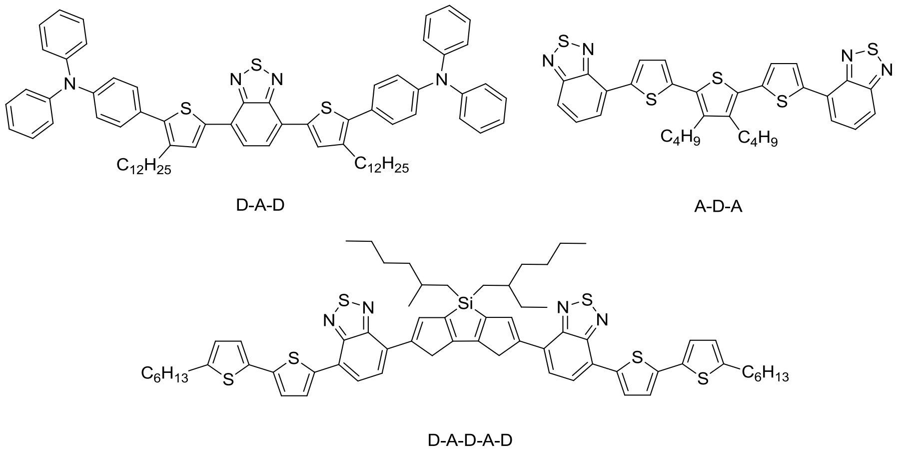

D-A-D

A-D-A

D-A-D-A-D

Figure 1.48 The chemical structures of D-A-D, A-D-A, D-A-D-A-D type molecules.

Diketopyrrolopyrrole (DPP), which present the advantages of planar conjugated structure, high extinction coefficient, strong photochemical stability and strong electron acceptability, is widely used in narrow bandgap materials [131, 132]. Nguyen et al. reported a D-A-D type small molecule M1 with DPP as a core unit [133] (*Figure 1.49*). By adjusting the donor/acceptor ratio, different results can be obtained. Among them, when the donor/acceptor ratio was 70:30, the solar cell exhibited an optimum PCE of 2.33%, with the Voc was 0.67V, the *Jsc* was 8.42, and the FF was 0.45. It is worth noting that this small molecule M1 may not be thermally stable. Later, this group further synthesized another small molecule M2 containing DPP [134] (*Figure 1.49*). The bandgap of this molecule is 1.5 eV. A 3.0% PCE was obtained with *Jsc* of 9.2 mA/cm^2, Voc of 0.75 V, and FF of 44%, which is the best PCE for solution-processed small molecule solar cells at that time.

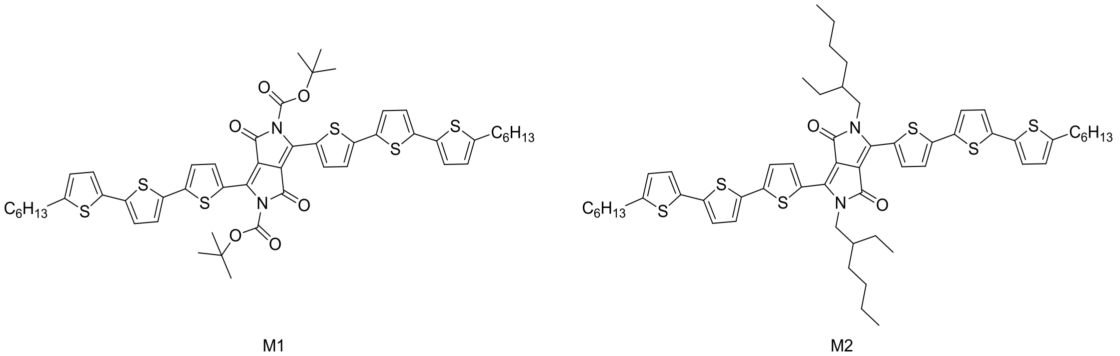

M1

M2

Figure 1.49 The chemical structures of M1 and M2.

As mentioned earlier, Isoindigo is another type of building block commonly used for narrow bandgap materials. Similar to DPP, Isoindigo has a strong electron-absorbing ability, a low HOMO level and a large planar structure [135, 136, 137, 138]. Roncali et al. reported on an indigo-based small molecule of D-A-D type with a band gap of 1.48 eV, but photovoltaic devices showed very poor performance (PCE = 0.01%) [136]. Later, Yang et al. reported another narrow bandgap small molecule M3 based on isoindigo. By introducing thieno[3,2-b]thiophene (TT) units, this small molecule shows a narrow bandgap of 1.5 eV. Photovoltaic devices exhibited a preliminary PCE of 1.41%, Voc of 0.72V, *Jsc* of 6.03 mA/cm^2, and FF of 32.5% [137]. In 2015, Cabanetos group reported two acetylene-bridged D-A-D type small molecules involving triphenylamine or N-phenylcarbazole as donor blocks (D) and thienoisoindigo as the acceptor unit (A). Among them, the triphenylamine-terminated molecule M4 resulted in highest power conversion efficiency of 2.20%, which is the highest reported value of the thienoisoindigo-based material [139] (*Figure 1.50*).

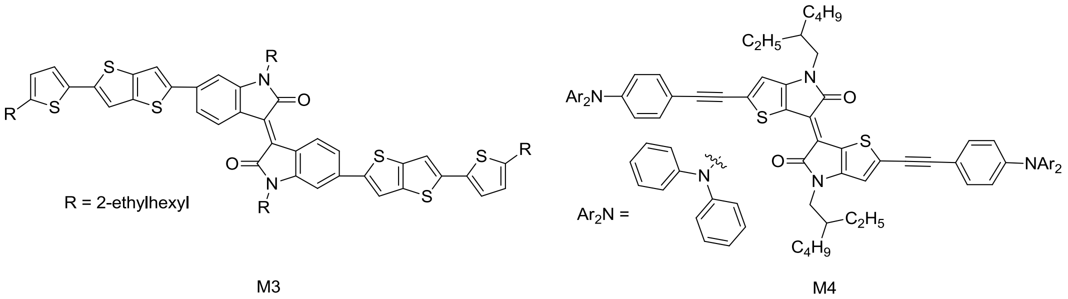

Figure 1.50 The chemical structures of M3 and M4.

Another class of dyes that are widely used in OPV materials is squaraines. Compared with other dyes, squaraine dyes have many advantages such as easy synthesis, a variety of possible structural motifs, strong photochemical and photophysical stability, and a very high absorption coefficient [140]. In 2014, Zhao et al. designed and synthesized two squaraine dyes, with indoline and 1,2,3,4-tetrahydroquinoline as capping agents, respectively (*Figure 1.51*). Among them, the small molecule M5 with dihydroquinone as the capping agent exhibits a low band gap of 1.43 eV and a wide absorption band in the Vis-NIR region of 550-850 nm, thus making the solution processed organic solar cell impressive *Jsc* is up to 11.03 mA/cm^2 and the excellent PCE is 4.29% [141].

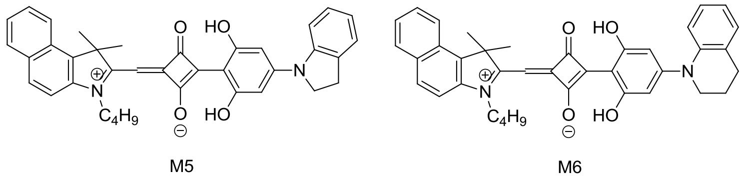

Figure 1.51 The chemical structures of M5 and M6.

Bordipyrromethane (BODIPY) is another class of dyes worth mentioning. It has good chemical and photochemical stability, a high extinction coefficient, and optical properties that can be easily changed by chemical conversion, and are therefore used in BHJ solar cells [142, 143, 144]. Yao et al. designed and synthesized three small molecules based on BODIPY in 2014. The absorption band of these small molecules extends to 880-900 nm. The *Jsc* values for devices based on these molecular are 6.80 mA/cm^2, 7.62 mA/cm^2, and 11.28 mA/cm^2, respectively. The highest PCE is 3.13% [145]. Narrow bandgap small molecules M8 based on BODIPY have also been used as acceptor in BHJ OSCs (*Figure 1.52*). Thayumanavan group reported two A-D-A type molecules with terminal BODIPY moieties with bandgap about 1.5 eV. The deep LUMO level and good visible absorption of these molecules led to their use as acceptors in bulk heterojunction solar cells, with a device efficiency as high as 1.51%. The result shows the potential application of BODIPY-based acceptor materials in OSC [146].

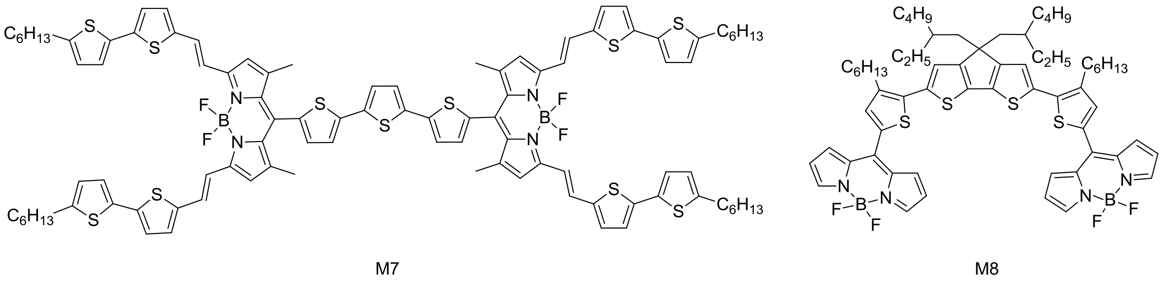

Figure 1.52 The chemical structures of M7 and M8.

1.3.3.2 Ambipolar OFETs

Ambipolar field effect transistors, which have the ability to transport holes and electrons, are easier to handle in circuits, and are therefore more widely used in various electronic devices [147]. Theoretically, in order to stabilize hole transport, semiconductor materials need to have a HOMO level below -5.0 eV, while the LUMO level needs to be close to or below -4.0 eV to stabilize electron transport.[51] Moreover, in general, the same metal (ie, Au) is used as a source electrode and a drain electrode in the preparation of the OFET, which requires that the energy gap between the HOMO and the LUMO of the organic semiconductor material cannot be too large, otherwise a charge injection failure occurs [148, 149].

In this context, narrow bandgap molecules were developed, both at small molecule and polymer level.

Polymer-Based Ambipolar Field Effect Transistors.

Since thiophene-flanked DPP units have been introduced into the transistor field, many DPP-based polymers have been reported to be successfully applied to p-type and ambipolar field effect transistors [150]. Very high hole mobility of up to 10.5 $cm^2 V^{-1} s^{-1}$ in the saturation regime, high on/off current ratio $\geq 10^6$ were obtained by Zhao and coworkers [151]. Sonar et al. reported the design and synthesis of a solution-processable ambipolar polymer semiconductor P8, the polymer having a small optical bandgap of ~1.1 eV and a deep LUMO level of -4.0 eV, exhibiting high hole and electron mobility of 0.35 $cm^2 V^{-1} s^{-1}$ and 0.40 $cm^2 V^{-1} s^{-1}$, respectively, after annealing at 200 °C [152] (*Figure 1.53*).

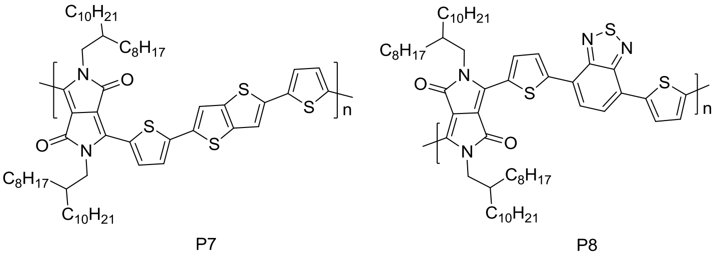

Figure 1.53 The chemical structures of polymers P7 and P8.

In 2013, Oh group reported as well a series of polymers based on diketopyrrolopyrrole-selenophene with hybrid siloxane-solubilizing groups to improve ambipolar performance (*Figure 1.54*). The best polymer P9 exhibites a HOMO of -5.10 eV, a LUMO of -3.49 eV and high hole and electron mobilities of 8.84 and 4.34 cm^2 V^{-1} s^{-1}, respectively, were obtained. These are the highest hole and electron mobilities for organic polymer based ambipolar field effect transistors that have been reported at that time [153]. The result indicates that the method of hybridizing side chains to improve the performance of narrow bandgap polymers for OFETs has good prospects, which brings new ideas to molecular design [3].

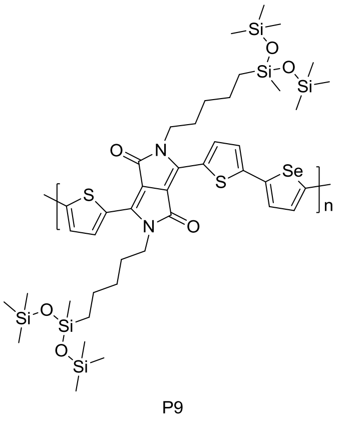

Figure 1.54 The chemical structures of polymer P9.

In addition, two isoindigobased conjugated polymers P10 and P11 designed and synthesized in 2012 by Liu, Pei and coworkers were observed to posess ambipolar transport behavior for the first time (*Figure 1.55*). Through the way of silanization on isoindigo units, the LUMO level of the polymer effectively reduced to -3.9 eV and significantly increased the electron mobility from 10^{-2} to 0.43 cm^2 V^{-1} s^{-1} while maintaining high hole mobility up to 1.85 cm^2 V^{-1} s^{-1} for OFETs devices [154]. Since the device is manufactured under ambient conditions, the polymer has good stability to moisture and oxygen.

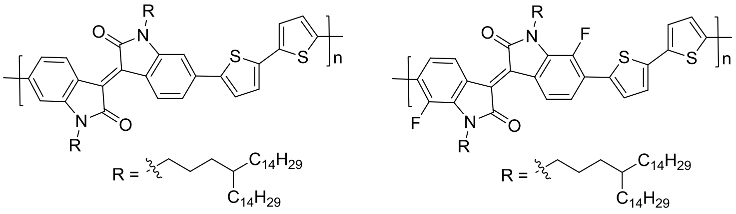

P10 P11

Figure 1.55 The chemical structures of polymer P10 and P11.

The same year, Wudl et al. reported an ultranarrow bandgap polymer P12 by using a very strong electron-accepting benzobisthiadiazole unit (*Figure 1.56*). This polymer has a deep LUMO calculated from the onset reduction potential, which was –3.80 eV, whereas the HOMO value of -4.36 eV was determined from the difference between the LUMO and the optical bandgap, therefore the optical bandgap as small as ~0.6 eV. This semi-conducting polymer exhibits nearly balanced hole and electron mobilities as high as 1.0 and 0.7 cm^2 V^{-1} s^{-1}, respectively [155].

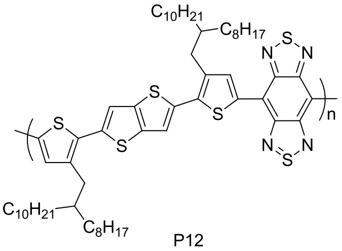

P12

Figure 1.56 The chemical structures of polymer P12.

Small Molecule-Based Ambipolar Field-Effect Transistors.

As described above, conjugated polymers with a narrow bandgap have been extensively studied in OFETs, but ambipolar small molecules also attracted great attention in this field, as illustrated with few examples.

In 2008, Nguyen et al. synthesized two new oligothiophene derivatives M9 and M10 bearing a diketopyrrolopyrrole core and their use in solution-processed organic field effect transistors are reported (*Figure 1.57*). Depending on the type of alkyl substituent and the film annealing temperature, changes in grain size and layer spacing were observed using atomic force microscopy and X-ray diffraction, respectively. These changes in film morphology and layer spacing result in magnitude differences in field-effect mobility. The field-effect mobility of the annealed films was 0.02 and 0.01 cm^2 V^{-1} s^{-1}, respectively. This was the first demonstration of DPP-based small molecules in FET applications. Moreover, multiple substitution sites allow adjustment of solubility, resulting in ease of processing, and control of thermal properties and inter-molecular spacing in the solid state. These features support the use of DPP as a universal platform for designing new organic small molecule semiconductors for electronic applications [156].

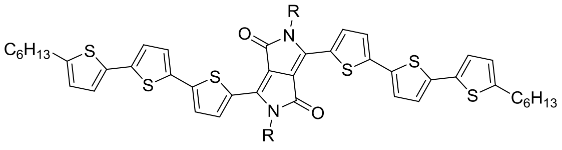

M9 R = C_6H_{13}
M10 R = $C_{12}H_{25}$

Figure 1.57 The structure of small molecules M9 and M10.

Cho, Kim and co-workers reported also a solution-processable narrow band gap small molecule M11 consisting of an electron-rich thiophene-dithienothiazole-thiophene unit and an electron-deficient diketopyrrolopyrrole (DPP) unit (*Figure 1.58*). The primary device has bipolar transmission characteristics with a hole mobility of 7.3 × 10^{-5} cm^2 V^{-1} s^{-1} and an electron mobility of 1.6 × 10^{-5} cm^2 V^{-1} s^{-1}. Thermal annealing at 110 ° C resulted in a significant increase in the carrier mobility, and the hole and electron mobility were 3.7 × 10^{-3} and 5.1 × 10^{-4} cm^2 V^{-1} s^{-1}, respectively. As expected, the increase in the performance of OFET is strongly correlated with the enhanced crystalline nanostructures in the semiconductor film by heat treatment. This is the first report demonstrating that solution-processable small molecules can be applied in both ambipolar transistors and nonvolatile memory devices [157].

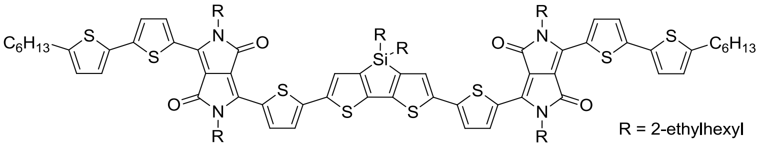

M11

Figure 1.58 The structure of small molecule M11.

Two novel dicyanovinylene-substituted DPP-oligothiophene semiconductors, M12 and M13 have been designed and synthesized by Ortiz et al. (*Figure 1.59*). In these materials, the combination of an extended oligothiophene conjugated skeleton with the strong electron-withdrawing DPP-dicyanovinylene groups results in semiconductors exhibiting ambipolar TFT response with reasonably balanced electron and hole mobilities of up to 0.16 cm^2 V^{-1} s^{-1} and 0.02 cm^2 V^{-1} s^{-1}, respectively. Furtherrnore, no thermal annealing of the semiconductors is necessary to afford high mobility, making it an ideal candidate for low-cost fabrication of devices on inexpensive plastic foils [158].

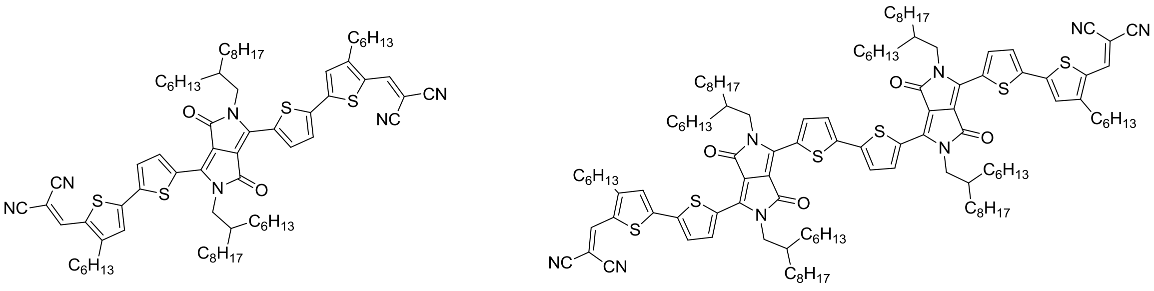

M12 M13

Figure 1.59 The structure of small molecules M12 and M13.

Recently, a series of acceptor-donor-acceptor (A-D-A) type small molecules (*Figure 1.60*) based on an oligothiophene-phenylene core was studied by Woo, Cho and coworkers in 2018. A flexible OFET array with solvent-vapor-annealed M15 was successfully fabricated on a PEN substrate. These OFET devices exhibited a hole mobility of 0.15 $cm^2 V^{-1} s^{-1}$, an electron mobility of 0.05 $cm^2 V^{-1} s^{-1}$, an on-off current ratio of ~10^5, and excellent mechanical stability even after 300 bending cycles [159].

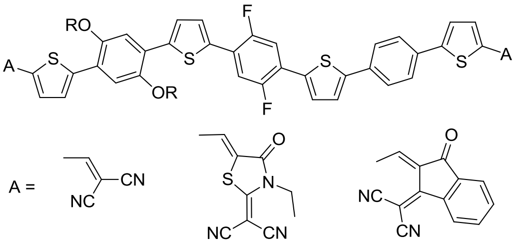

M14 M15 M16

Figure 1.60 The structure of small molecules M14, M15 and M16.

Conclusion

The above sections present the state-of-the-art liquid crystal materials and narrow bandgap materials used in organic electronics and photonics, such as OPVs, OLEDs and OFETs. The key to achieving high performance is the rational design of new donor and acceptor components and there are many similarities between OPVs, OLEDs and OFETs during the design process. In other words, people working in different fields can learn from each other. For instance, donor and acceptor units suitable for the design of OPVs can also be considered for the design of transistor materials. This is why in the following chapters, we will introduce three family of new semiconducting materials based on different donor and acceptor units.

1.4 Aim of work

The last couple years, we have developed and studied in our group at the Polymer Chemistry team a series of liquid crystalline polymeric and molecular architectures based on different π-conjugated mesogens. *Figure 1.61* shows some of these mesogenic materials such as a) polythiophenes grafted with a triphenylene discotic or perylene side groups presenting lamello-columnar structures [160, 161, 162] or b) linear dyad and triad molecular architectures based on calamitic terthiophene moieties and perylene units presenting multi-lamellar structures [163].

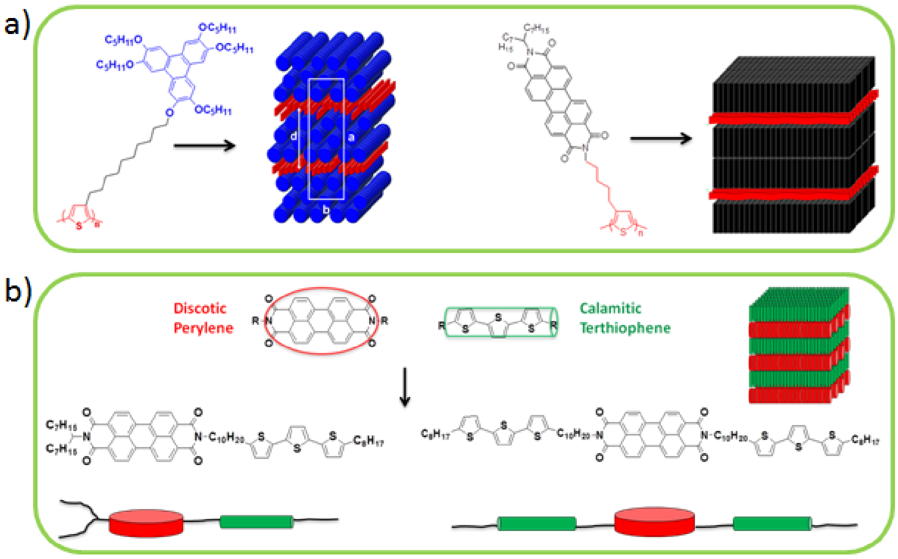

Figure 1.61 Schematic representation of some liquid crystalline small molecules and polymers already prepared in our group.

In this work, during my PhD, we were interested in designing and synthesizing novel self-organized semiconducting materials based on donor/acceptor architectures presenting additional functionalities, such as high luminescence or narrow bandgap properties.

More precisely, in the next chapter (Chapter 2), we will deal with the elaboration of a new series of highly fluorescent liquid crystalline homologues based on a calamitic (rod-like) architecture, presenting a Donor-Acceptor-Donor (D-A-D) π-conjugated core end-capped by two alkyl chains (*Figure 1.62 a*). This amphipathic structure should favor the nano-segregation of the incompatible parts of the molecules and induce a lamellar organization in which both aromatic cores and alkyl chains are arranged in alternating separate sublayers (*Figure 1.62 b*). In addition, this self-organization will lead to anisotropic materials that should present two-dimensional charge transport properties favored within the layers and specific luminescence properties.

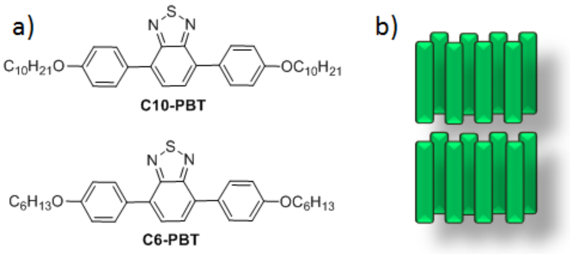

Figure 1.62 a) Chemical structures of fluorescent D-A-D compounds based on benzothiadiazole acceptor moities; b) Schematic representation of the expected lamellar organization.

In the third chapter, we propose to design and study a family of liquid crystal fluorescent dyad and triad architectures based on the fluorescent calamitic derivative described in the previous paragraphe as central highly emissive core and and higly conductive derivatives such as benzo[4,5]thieno[2,3-d]thiophene (BTBT) as side groups. The chemical structures of the derivatives are given in *Figure 1.63*. the objective of this work is to try to obtain multi-lamellar materials with both high charge transport and high fluorescence properties. In this chapter, we will detail the design and synthesis of the materials and we will also study their photophysical, thermal, structural and charge transport properties by UV-visible spectrum (UV), Polarized Optical Microscopy (POM) Differential Scanning Colorimetry (DSC), X-ray diffraction and Time of Flight (TOF) technique, respectively.

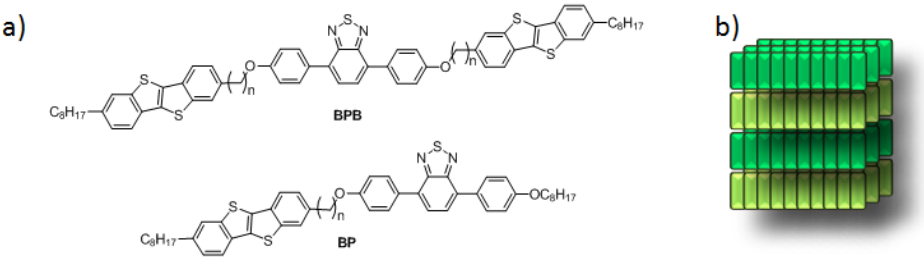

Figure 1.63 a) Chemical structures of the linear dyad and triad architectures based on fluorescent benzothiadiazole derivative and BTBT units; b) Schematic representation of the ideal multi-lamellar organization expected with these materials.

In the fourth chapter, we propose to design and study two novel narrow bandgap molecules based on a central naphthalene diimide core, functionalized with different thiophene-based π-conjugated entities. The chemical structures of the derivatives are detailed in *Figure 1.64*. Based on their extended D-A π-conjugated systems, these molecules should present interesting optical or charge transport properties such as near-IR range absorption or ambipolar behavior. In this chapter, we will describe the design and the synthesis of the materials and we will investigate their photophysical, thermal and structural properties by UV, DSC, POM, X-ray diffraction and AFM. Moreover, the charge carier mobility of these derivatives will be also discussed.

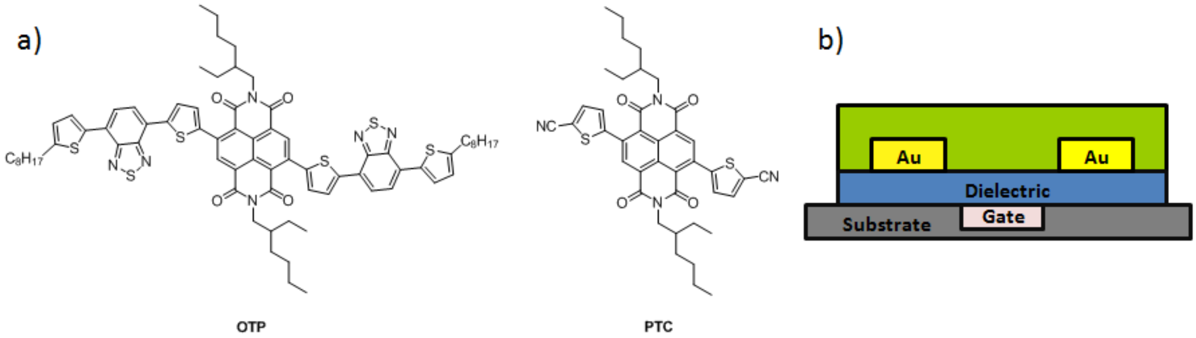

Figure 1.64 a) Chemical structures of marrow bandgap moleculars based on naphthalene and thiophene; b) OFET device structure.

Finally, we will conclude this work and we will give some perspectives based on the new design guiding provided by this study and which should be taken into account for the future development of high emissive self-organized materials and new narrow bandgap molecules for applications in optoelectronics such as light-emitting devices (OLEDs and OLETs) and photovoltaic cells (OPV).

Chapter 2 Synthesis and Characterization of Liquid Crystal Fluorescent Derivatives

In this chapter, we will study two liquid crystalline fluorescent homologues **C10-PBT** and **C6-PBT** (*Figure 2.1*), based on a calamitic architecture. For this series, the conjugated part has been designed as a Donor-Acceptor-Donor structure (D-A-D) with O-alkylphenyl groups as donor units and benzothiadiazole unit as acceptor core. The benzothiadiazole is one of the most widely used moities in photoluminescent compounds [164] and in organic electronics applications. Its derivatives have several desired characteristics for its uses in the field of optoelectronics such as electron withdrawing ability for the elaboration of compounds exhibiting negative charge carrier transport properties and effective fluorescent properties [165]. In addition, they can form well-ordered crystal structures because they are strongly polarized, and therefore they can induce strong intramolecular interactions. As a remark, these two compounds differ only from the length of the alkyl chains grafted on both extremities of the conjugated core. These molecules were inspired from previous work. In what follows, we will describe and discuss the synthesis, photophysical, mesomorphic and electronic properties of those molecules. In addition, the self-organization properties in bulk and the film morphology will be also detailed, before charge transport properties are investigated.

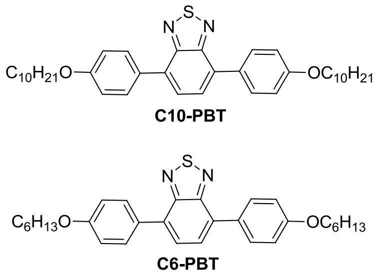

Figure 2.1 Chemical structures of D-A-D compounds based on benzothiadiazole acceptor moities.

2.1 Synthesis

2.1.1 Synthesis of precursory building blocks

For the synthesis of these two compounds, three precursors were prepared: tributyl(4-(decyloxy)phenyl)stannane (**2C**, n=10), tributyl(4-(hexyloxy)phenyl)stannane (**2C,** n=6) and 4,7-dibromobenzo[c][1,2,5]thiadiazole (**2E**). The synthetic route of these precursory building blocks is given in *Figure 2.2*.

The first step is the preparation of the intermediate building blocks **2B**. This building block is prepared from the commercially available 4-bromophenol **2A**, which is first converted into its O-alkylphenyl derivatives by a Williamson etherification reaction **2B** in very good yields. **2B** derivatives are finally converted into their stannane derivatives to lead to the building blocks **2C** by the reaction of the tributyltin chloride on the lithiated intermediate of **2B**. The second step is the preparation of the precursor **2E**. This building block is prepared from the commercially available benzothiadiazole **2D**, which is treated with bromine to give the targeted derivative **2E** in a good yield about 60%.

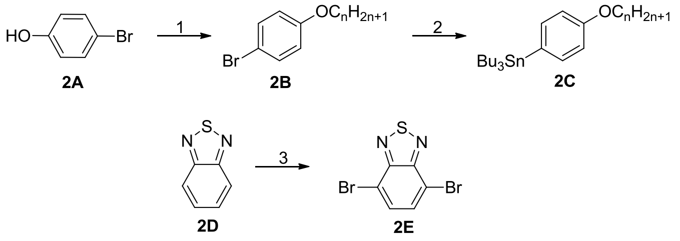

Figure 2.2 Synthetic route of precursors. Conditions: 1)1-bromodecane or 1-bromohexane, K_2CO_3, acetone, reflux, 48 h, 90%; 2) n-BuLi, -78 °C, 1h; $ClSnBu_3$, -78 °C, 30min; THF, RT, 12h, 73%; 3) bromine, HBr (48%), reflux, 6h, 60%.

2.1.2 Synthesis of target calamitic C10-PBT and C6-PBT

The synthetic route toward **C10-PBT** and **C6-PBT** is given in *Figure 2.3*. The synthesis is carried out by a Stille coupling between either tributyl(4-(decyloxy)phenyl)stannane (**2C$_a$**, n=10) or tributyl(4-(hexyloxy)phenyl)stannane (**2C$_b$**, n=6) and 4,7-dibromobenzo[c][1,2,5]thiadiazole (**2E**). All the compounds are well soluble in common organic solvents, and they can be purified via column chromatography using dichloromethane:petroleum ether (1:2 v/v) as the eluent and characterized by the conventional methods (NMR, Elementary analysis, HRMS).

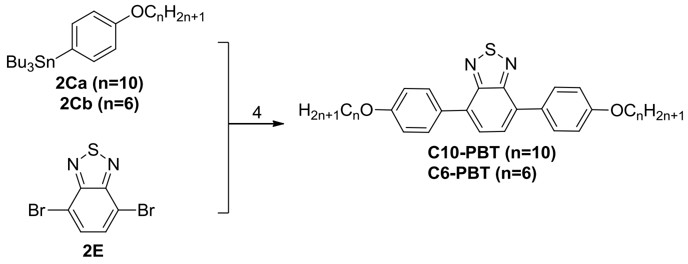

*Figure 2.3 Synthetic route of the **C10-PBT** and **C6-PBT**. Conditions: 4) $Pd(PPh_3)_4$, DMF, 110 °C, 24h, **C10-PBT** 42%, **C6-PBT** 46%.*

Figure 2.4 shows a typical NMR spectra of **C10-PBT**. The symmetrical structure of these derivatives leads to an easy spectrum interpretation showing for example in the aromatic part one singlet corresponding to the two protons of benzothiadiazole unit, and a simple doublet of doublet associated to the 8 protons of para-substituted benzene rings.

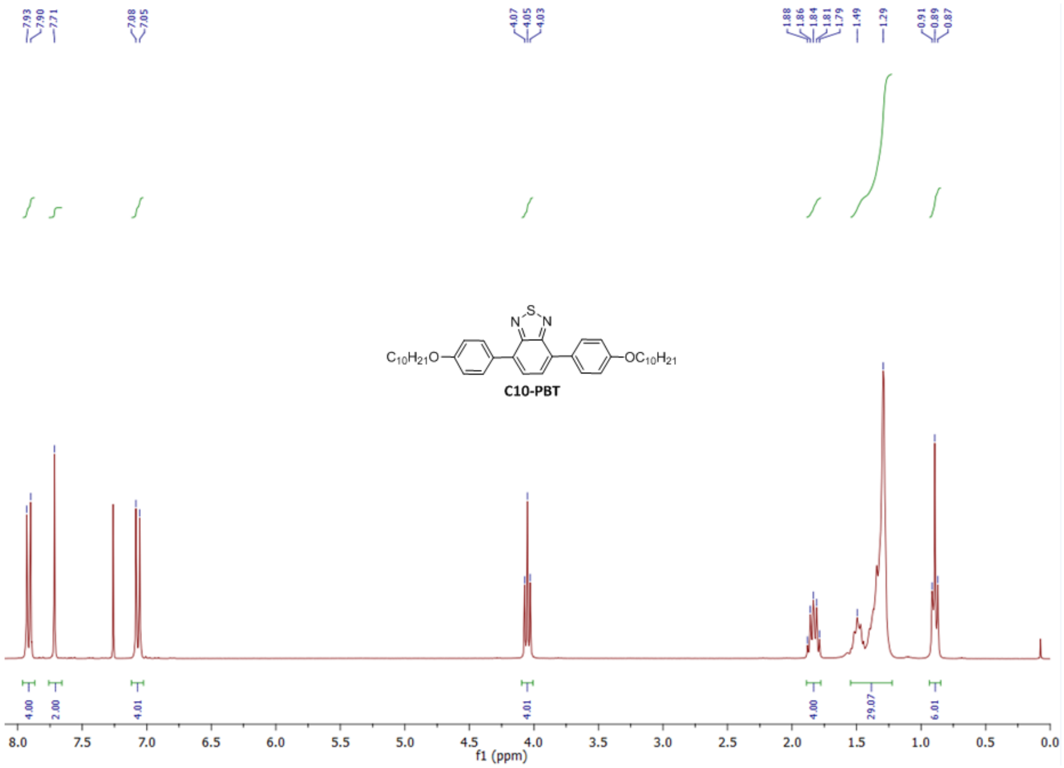

Figure 2.4 The NMR spectrum of the ***C10-PBT****.*

2.2 Photophysical properties (absorption and emission)

For the study of absorption and emission properties, low concentration solutions (ca. 10^{-5} M) were used and the measurements were performed at room temperature. In this condition, these molecules can be considered as adequately isolated, i.e. the aggregation and the intermolecular interactions can be neglected. The film samples were fabricated by spin-coating 3000 r/min at room temperature (1% w in chloroform).

2.2.1 Absorption and emission of C10-PBT

The absorption and emission spectra of **C10-PBT** in chloroform solution are shown in *Figure 2.5*. More precisely, in solution the **C10-PBT** molecules show two absorption bands: a π-π* transition in the 230-320 nm range and an intramolecular charge transfer band in the 330-500 nm range consistent with the D-A-D structure of the derivative. This compound is strongly fluorescent in chloroform solution and the photoluminescence (PL) spectrum displays an emission with a maximum peak at 550 nm and a very high photoluminescent quantum yield around 89%.

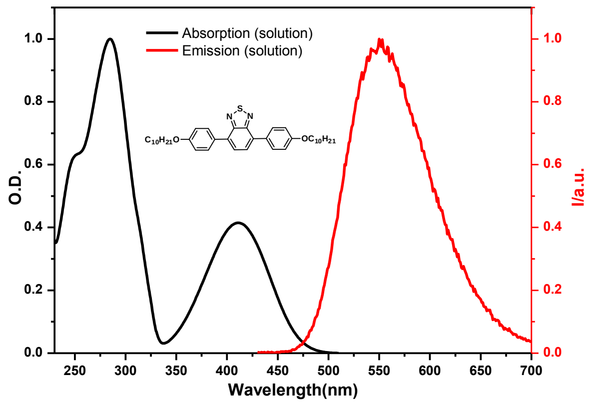

*Figure 2.5 UV/Vis absorption and emission spectra of **C10-PBT** in $CHCl_3$ solution.*

Due to the charge transfer character of the low energy absorption band of **C10-PBT**, we investigated the absorption and emission properties in different solvents (polar and apolar) to study the solvatochromic effects. The effect of solvent polarity is reported in *Figure 2.6*. All the solutions were prepared at low concentration (10^{-6}) M in order to limit the potential aggregation effects.

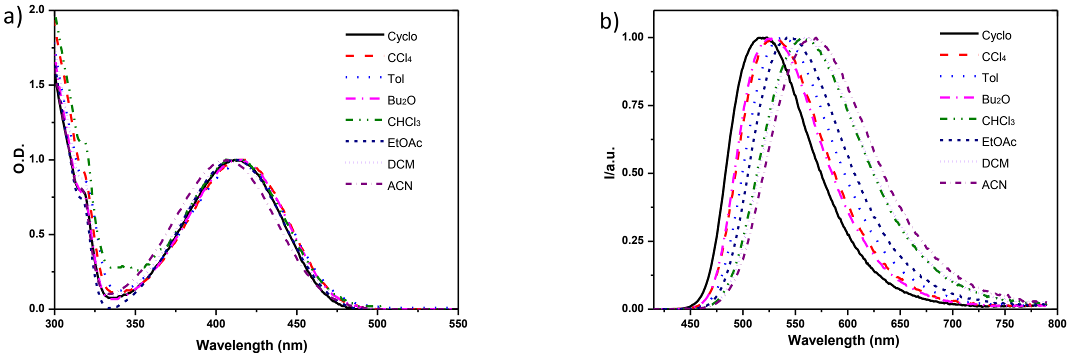

*Figure 2.6 a) Absorption spectra of **C10-PBT** measured at room temperature in different solvents; b) Fluorescence spectra of C-10PBT at room temperature measured in different solvents (Cyclo: cyclohexane, CCl_4: tetrachloromethane, Tol: toluene, Bu_2O: dibutylether, $CHCl_3$: chloroform, EtOAc: ethyl acetate, DCM: dichloromethane, ACN: acetonitrile).*

The absorption spectra of **C10-PBT** shows slight changes, with a maximum moving from 409 to 411 nm for the intramolecular charge transfer band for instance. However, we can observe a significant solvatochromic shift of the fluorescence spectrum maxima from 523 nm in cyclohexane to 566 nm in acetonitrile. The red shift of fluorescent spectra with the solvent polarity indicates the high polarity of the excited state in comparison with its ground state. This compound presents high PLQY in most of solvents with a maximum of 100% in very apolar solvent such as cyclohexane. The absorption maximum wavelengths λ_{abs}, emission maximum wavelengths λ_{em}, photoluminescence quantum yields φ_f, fluorescence lifetimes τ_f in different solvents are given in *Table 2.1*.

C10-PBT				
Solvent	λ_{abs}	λ_{em}	Φ_f	τ_f
Cyclo	409	523	1	8.64
$CHCl_4$	411.5	530		
Tol	413.5	537	0.83	8.57
Bu_2O	412.5	531	0.88	9.5
$CHCl_3$	415	557	0.89	11.48
EtOAc	413.5	544		
DCM	414.5	564	0.77	11.36
ACN	411.5	566		

Absorption maximum wavelengths λ_{abs} (nm), emission maximum wavelengths λ_{em} (nm), photoluminescence quantum yields φ_f, fluorescence lifetimes τ_f (ns).

*Table 2.1 Photophysical properties of **C10-PBT** in different solvents.*

In addition, the Bilot-Kawski-Bakshiev formalism [167, 168, 169] was used to estimate experimentally the ground state dipole moment and a value of 2.7 Debye was calculated for **C10-PBT** (see Paragraph 2.8.6 for calculation details), indicating a negligeable dipole moment in the ground state. The excited state dipole moment was also estimated by using the Lippert-Mataga formalism [167, 168, 169]. In comparison with the ground state, a higher value of 17.7 Debye was then calculated for **C10-PBT**. Thus, the singlet excited state exhibits a larger dipole moment than that of the ground state due to the intramolecular charge transfer character of the excited state [170].

In solid state, the absorption spectra of this compound is blue-shifted relative to the solution spectra (about 21 nm). This result suggests the formation of π-stacked aggregates in the solid state (*Figure 2.7 a*). For the emission properties, the photoluminescence (PL) spectrum in film exhibits a blue shifted emission with maxima at 542 nm, while the solution displays an emission with a maximum peak at 550 nm. The Stokes shift has a remarkably large value of 6363 and 6943 cm^{-1} in chloroform solution and in film respectively.

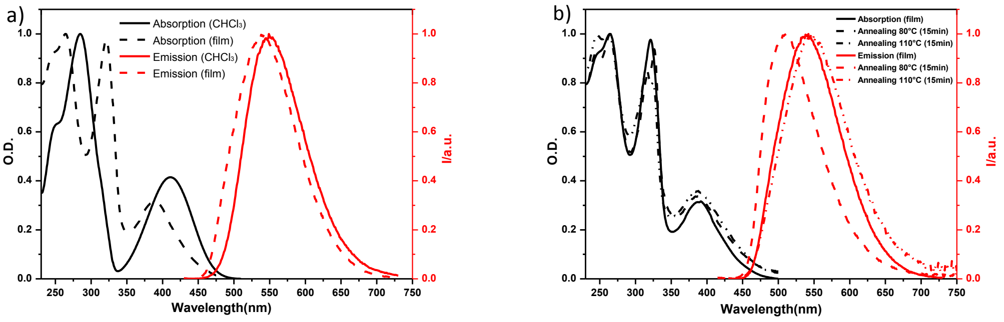

*Figure 2.7 a) UV/Vis absorption and Emission of **C10-PBT** in solution and film; b) UV/Vis absorption and Emission of **C10-PBT** in film before and after annealing.*

We also investigated the absorption and emission spectra in solide state after annealing at different temperature. The absorption spectra of **C10-PBT** in film before and after annealing is shown in *Figure 2.7 b*. Upon annealing at 80°C, a slight increase of the absorption bands is observed accompanied by a slight blue shift of the lowest transition in energy. The peak to peak ratio between the S_0-S_1 and S_0-S_2

decreases. After annealing at 110°C, we observe a shift back to the lowest transition to its original point with a change in the shape of the S_0-S_2 band. In terms of the emission spectra, upon annealing at 80 °C, the initial emission at 548 nm is blue shifted toward 510 nm. This induces also an increase of the PLQY from 67 % to 88 %. Annealing at 110 °C results in a red shift bringing back the emission to the original point with a decrease of the PLQY (from 88 % to 57 %). The change of emission spectra and the increase of PLQY suggest that after annealing at 80 °C, there is a modification of the molecular packing.

2.2.2 Absorption and Emission of C6-PBT

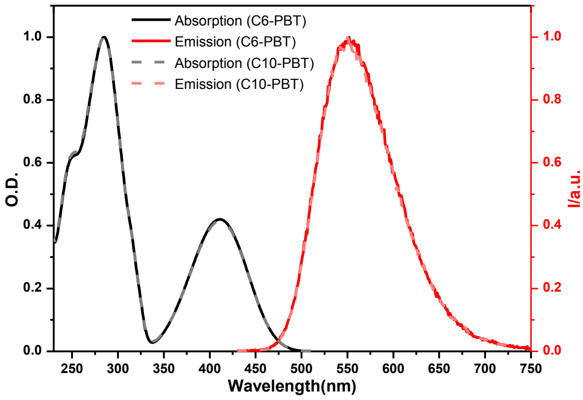

Figure 2.8 UV/Vis absorption and Emission spectra of ***C6-PBT*** *and* ***C10-PBT*** *in* $CHCl_3$ *solution.*

The absorption and emission spectra of **C6-PBT** in solution are shown in *Figure 2.8*. As expected, and based on the molecule structure of these two compounds, differing only from the length of alkyl chains, it is no wonder that both the absorption spectra and emission peaks of compound **C6-PBT** and **C10-PBT** are very similar in chloroform solution (see *Table 2.2*).

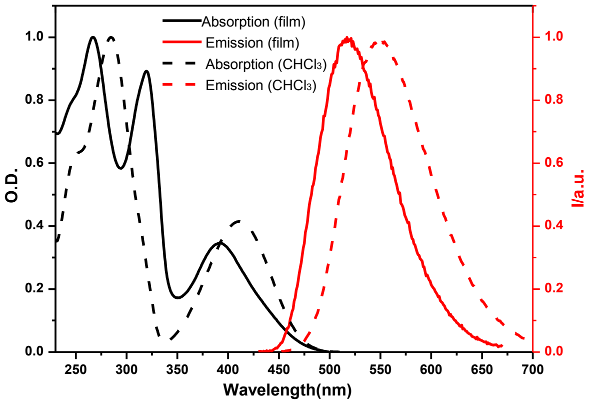

Figure 2.9 UV/Vis absorption and emission of ***C6-PBT*** *in film.*

On the contrary, *Figure 2.9* shows the absorption and emission spectra of **C6-PBT** in film. It can be observed that the emission maximum exhibits a larger blue shifted (about 33 nm) with maxima at 517 nm in film. The Stokes shift for compound **C6-PBT** is 140 nm and 126 nm in chloroform solution and in film respectively.

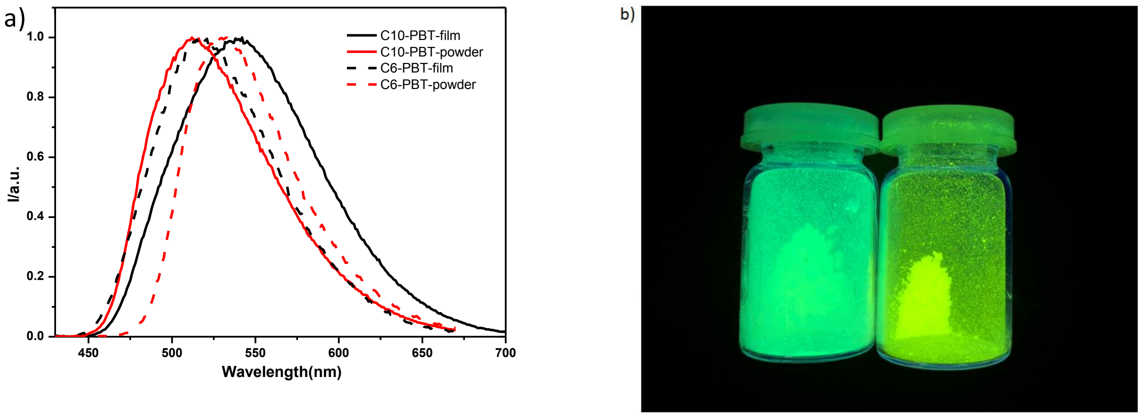

*Figure 2.10 a) Emission spectra of **C10-PBT** and **C6-PBT** in film and powder; b) Fluorescence under UV (365 nm) of compound **C10-PBT** (left) and **C6-PBT** (right).*

Compared with the **C10-PBT**, for the compound **C6-PBT** there is a slight difference in color in the solid powder and film (see *Figure 2.10*). The color difference of the two materials in the solid state probably originates from a difference in ‘packing’ of the molecules linked to the different chain lengths.

The photophysical parameters of these compounds **C10-PBT** and **C6-PBT** at room temperature are summarized in *Table 2.2.*

	solution			film			powder
Compound	λ_{abs}/nm		λ_{em}/nm	λ_{abs}/nm		λ_{em}/nm	λ_{em}/nm
C10-PBT	285	411	550	320	390	542	513
C6-PBT	285	410	550	319	392	518	530

*Table 2.2 Photophysical parameters of the compounds **C10-PBT** and **C6-PBT** at room temperature.*

2.3 Mesomorphic properties

The mesomorphic properties of **C10-PBT** and **C6-PBT** were investigated by Polarized-light Optical Microscopy (POM) and Differential Scanning Calorimetry (DSC) on heating and cooling cycles. All the samples for POM were prepared on cleaned or octadecyltrichlorosilane (OTS) treated glass sides, and all the photographs were captured upon cooling from their isotropic phases.

2.3.1 DSC and POM of C10-PBT

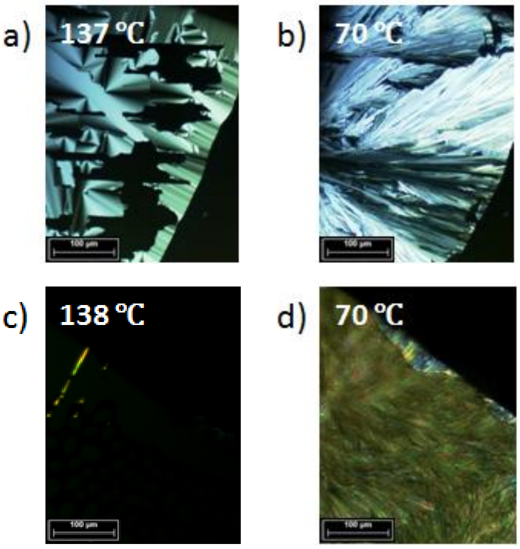

Figure 2.11 POM microphotographs (under crossed polarizer) of ***C10-PBT****. POM microphotographs obtained upon cooling: a-b) the optical textures of* ***C10-PBT*** *at 137 °C and 70 °C respectively on clean glass substrates; c-d) the optical textures of* ***C10-PBT*** *at 138 °C and 70 °C respectively on OTS treated glass substrates.*

The POM photographs of **C10-PBT** on clean glass substrates and on OTS treated glass substrates are given in *Figure 2.11*.

Under POM with crossed polarizers, the compound **C10-PBT** appeared as a birefringent yellow powder which melted on heating at around 105 °C to give a birefringent viscous phase. On further heating, this viscous phase transformed at around 145 °C into an isotropic fluid phase presenting no birefringence which can be attributed to the isotropic phase. Upon cooling, a birefringent fan-shape focal-conic texture from isotropic phase appears at around 137 °C (*Figure 2.11 a*) indicating the presence of a smectic phase. On further cooling, the transition from the lamellar mesophase to crystal phase was clearly observed at around 70 °C (*Figure 2.11 b*) and the crystal phase texture was then maintained unchanged until room temperature.

In order to investigate more precisely the mesophase nature, the same study was performed on OTS treated glass substrates (*Figure 2.11 c-d*). On cooling from the isotropic state, a mainly homeotropic texture (black) was observed with some very small residual focal-conic domains indicating the presence of an untilted lamellar mesophase (smectic A). On further cooling, these homeotropic domains can be maintained until 70 °C which corresponds to the transition from liquid crystal to crystal phase (*Figure 2.11 d*). Then upon cooling, the crystal texture also maintains unchanged until room temperature.

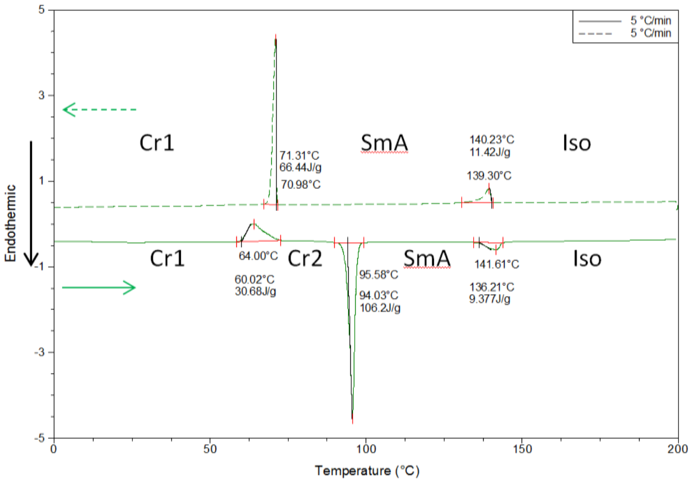

*Figure 2.12 DSC thermogram of **C10-PBT**.*

The DSC traces of **C10-PBT** on third heating and third cooling recorded with a rate of 5 °C/min present several transitions. On heating until 200 °C, we can observe two endothermic peaks: at 94 °C (ΔH = 106.2 Jg^{-1}) and 136 °C (ΔH = 9.4 Jg^{-1}) corresponding to the melting point of the crystalline phase to the liquid crystal phase and the isotropization of the material, respectively. On cooling, from the isotropic state, the first transition at 140 °C associated to a small enthalpy (ΔH = 11.4 Jg^{-1}) is consistent with the appearance of the birefrigent texture of liquid crystal phase observed on cooling by POM. Upon further cooling, the second transition at 71 °C associated with a higher enthalpy (ΔH = 66.4 Jg^{-1}) is attributed to the transition to the crystalline phase. Interestingly, during heating, we can observe an exothermic peak at 60 °C (ΔH = 30.7 Jg^{-1}), attributed to a possible reorganization of the molecular packing of the crystal phase obtained on cooling (Cr1) to another crystalline phase (Cr2).

Based on DSC and POM studies, the polymorphism can be refined and the following phase sequence Iso→LamA→ Cr1 can be proposed (on cooling). A summary of the mesomorphic properties of **C10-PBT** is presented in *Table 2.3*.

		T(°C)	**ΔH(J g^{-1})**	**Transition**	**T(°C)**	**ΔH(J g^{-1})**	**Transition**	**T(°C)**	**ΔH(J g^{-1})**	**Transition**
C10-PBT	**Heating**	60	30.7	Cr1→Cr2	94	106.2	Cr2→SmA	136	9.4	SmA→Iso
	Cooling	-	-	-	71	66.4	SmA→Cr1	140	11.4	Iso→SmA
Crystalline phase (Cr), Smectic A phase (SmA), Isotropic liquid phase (Iso).										

*Table 2.3 Phase transition temperatures and enthalpy changes of **C10-PBT**.*

2.3.2 DSC and POM of C6-PBT

The POM photographs of **C6-PBT** on clean glass substrates and on OTS treated glass substrates are given in *Figure 2.13*.

Under POM, the compound **C6-PBT** appeared as a birefringent yellow powder which melted at around 85 °C to give a clearly birefringent viscous phase. On further heating, this phase transformed to a non-birefringent isotropic phase at around 155 °C. Then on cooling from previous isotropic phase, a first birefringent texture of **C6-PBT** appears around 153 °C under crossed polarizers consistently with the first transition observed by DSC. The schlieren texture observed (*Figure 2.13 a*) indicates the formation of a nematic phase. On further cooling, the transition from the nematic phase to lamellar mesophase was clearly observed at around 150 °C *(Figure 2.13 b*) with the appearence of a focal-conic texture. Then upon cooling, the crystalline phase was observed at 82 °C (*Figure 2.13 c*). When the compound is cooled until 38 °C, the texture color changed, indicating the possible presence of another phase transition consistently with DSC measurements (*Figure 2.13 d*). Then, this texture is maintained unchanged until room temperature.

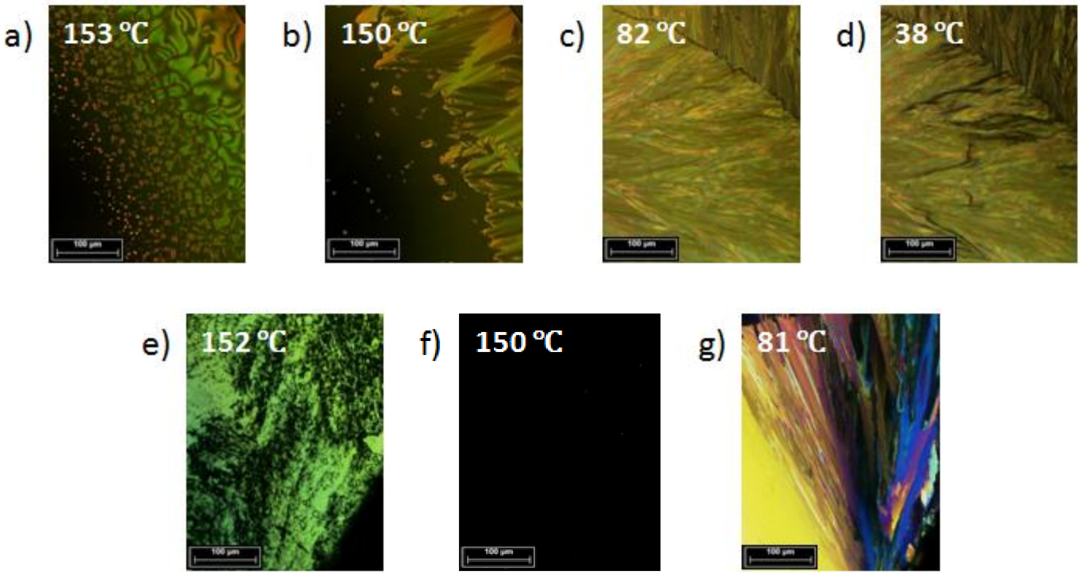

Figure 2.13 POM microphotographs (under crossed polarizer) of ***C6-PBT****. POM microphotographs obtained upon cooling: a-d) the optical textures of* ***C6-PBT*** *at 153 °C, 150 °C, 82 °C and 38 °C respectively on clean glass substrates; e-g) the optical textures of* ***C6-PBT*** *at 153 °C, 150 °C and 81 °C respectively on OTS treated glass substrates.*

The POM study was also performed on OTS treated glass substrates (*Figure 2.13 e-g*). On cooling from the isotropic state, the birefringent schlieren texture reappeared at around 153 °C (*Figure 2.13 e*). Then, on cooling at 150 °C, the POM microphotograph shows a homeotropic texture (black), corresponding to the presence of smectic A mesophase (*Figure 2.13 f*). On further cooling, the black domains transform to give a birefringent crystalline texture at around 81 °C (*Figure 2.13 g*).

The DSC traces of **C6-PBT** on heating and cooling recorded with a rate of 5 °C/min (*Figure 2.14*) present a rich polymorphism with several reversible transitions. On heating until 180 °C, four endothermic peaks at 85 °C, 97 °C, 151 °C and 153 °C are observed with enthalpy values (ΔH) around 8.2 Jg^{-1}, 78.7 Jg^{-1}, 2.7 Jg^{-1} and 2.0 Jg^{-1}, respectively. In the absence of additional transitions at higher temperature, the last peak at 153 °C can be attributed to the transition to the isotropic phase consistently with POM observation. On cooling, reversible transitions are observed and the thermogram presents four exothermic peaks at 153 °C ($\Delta H = 2.8\ Jg^{-1}$), 150 °C ($\Delta H = 1.8\ Jg^{-1}$), 80 °C ($\Delta H = 46.0\ Jg^{-1}$) and 41 °C ($\Delta H = 21.9\ Jg^{-1}$). On cooling from the isotropic phase, the first transition at

153 °C associated with a small transition enthalpy is consistent with the appearance on a very small range of temperature of nematic phase (Nem) observed by POM. On further cooling, the second transition at 150 °C indicates the presence of a more ordered mesophase such as a lamellar smectic A phase (SmA). Then, the third transition at 80 °C associated with a large enthalpy value can be attributed to the transition to the crystal phase Cr3. Finally, the last broad peak observed at 41 °C could be attributed to the transition from the crystal phase (Cr3) to another crystalline phase (Cr1) not clearly observed by POM. Therefore, on cooling from isotropic phase, the phase sequence of **C6-PBT** can be described as Iso→Nem→SmA→Cr3→Cr1.

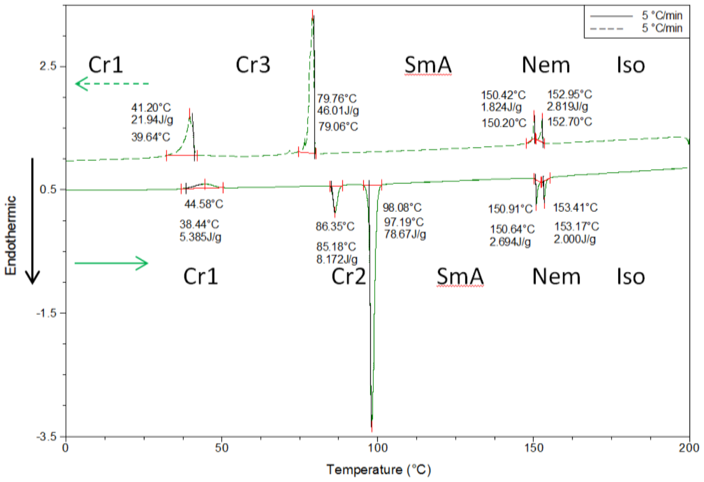

Figure 2.14 DSC thermogram of C6-PBT.

A summary of the the mesomorphic properties of **C6-PBT** are reported in *Table 2.4*.

		T(°C)	**ΔH(J g^{-1})**	**Transition**	**T(°C)**	**ΔH(J g^{-1})**	**Transition**	**T(°C)**	**ΔH(J g^{-1})**	**Transition**	**T(°C)**	**ΔH(J g^{-1})**	**Transition**
C6-PBT	**Heating**	85	8.2	Cr1→Cr2	97	78.7	Cr2→SmA	151	2.7	SmA→Nem	153	2.0	Nem→Iso
	Cooling	41	21.9	Cr2→Cr1	80	46.0	SmA→Cr2	150	1.8	Nem→SmA	153	2.8	Iso→Nem
Crystalline phase (Cr), Smectic A phase (SmA), Nemetic phase (Nem), Isotropic liquid phase (Iso).													

*Table 2.4 Phase transition temperatures and enthalpy changes of **C6-PBT**.*

2.4 Self-organization study (X-ray diffraction and Atomic force microscopy)

The self-organization properties of **C10-PBT** and **C6-PBT** were analyzed by X-ray diffraction (XRD) and Atomic force microscopy (AFM).

2.4.1 X-ray diffraction (XRD)

To assess the unambiguous mesophases formation and probe the effects of the intimate structural modifications onto the mesophase temperatures ranges, **C10-PBT** and **C6-PBT** compounds were studied by temperature dependent X-ray diffraction (TDXRD). The measurements were carried out in collaboration with Dr. Benoit Heinrich at Institut de Physique et de Chimie des Matériaux de Strasbourg (IPCMS).

2.4.1.1 XRD of C10-PBT

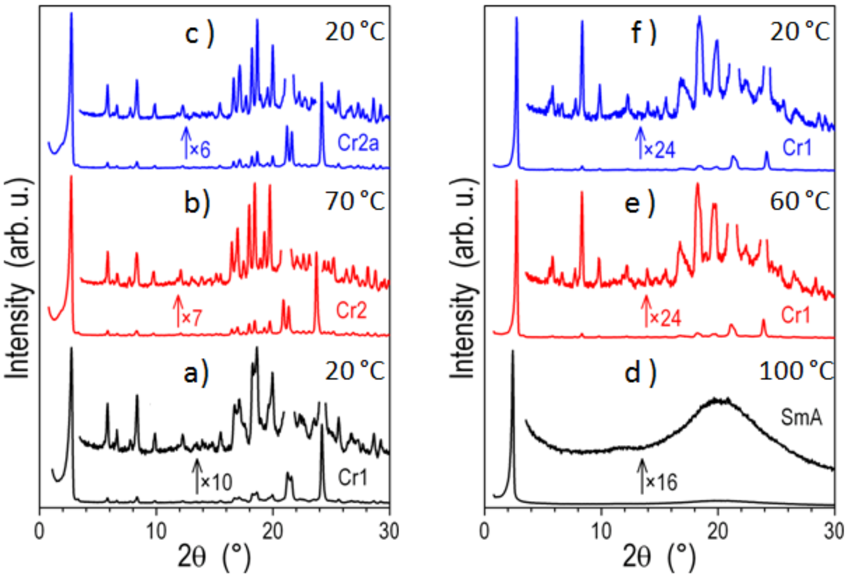

Figure 2.15 XRD patterns of ***C10-PBT****. a) at 20 °C (pristine); b) at 70 °C; c) at 20 °C; d) at 100 °C; e) at 60 °C; f) at 20 °C.*

The *Figure 2.15* shows the typical X-ray diffraction patterns of the **C10-PBT** recorded at different temperatures such as 20 °C pristine (Cr1), 70 °C (Cr2) on heating and 20 °C on cooling. The pristine state pattern at 20 °C (*Figure 2.15 a*) shows a lot of very sharp reflections, indicating a well-developed three-dimensional lattice (Cr1). Two reflections in a small angle region with a d-spacing ratio of 1:2 show that the molecules are arranged in a lamellar fashion in pristine crystalline phase. The X-ray diffraction also demonstrates that the exothermic peak in heating DSC curves of **C10-PBT** (at 66°C, ΔH =35 Jg^{-1}) is a transition from an initial crystal phase Cr1 to a second crystal phase Cr2. The reverse transition is not observed on cooling from the Cr2 phase and this phase is maintained on cooling to room temperature (*Figure 2.15 b, c*). In contrast, the phase Cr1 is directly re-obtained on cooling from the SmA phase (*Figure 2.15 d, e* and *f*).

The *Figure 2.16* shows the typical X-ray patterns of the **C10-PBT** recorded at 100 °C in the smectic A phase and a model of the lamellar organization.

The pattern in the liquid crystal state at 100 °C presents a sharp reflection in the small-angle region and one diffuse halos in the wide-angle region (*Figure 2.15 a*). The small-angle reflection indicates that the molecules are arranged in a lamellar fashion and they can be assigned to (001) reflections. The repeat distances d associated with the first reflection can be calculated in using the Bragg's law:

$$\lambda=2d \sin\theta$$

where λ is the wavelength of incident X-ray and θ is the angle incidence. The corresponding layer spacing at about 36.3 Å, is consistent with the length of the molecule determined by modeling (38 Å). In the wide-angle region, the very broad halo centered at 4.5 Å (h_{mes}+h_{ch}) indicates the molten state of the alkyl chains and the average distance of the aromatic cores in the layers. This X-ray pattern is typical of a disordered smectic A mesophase as suggested by POM and DSC studies.

Based on these results we can propose a schematic representation of **C10-PBT** molecular arrangement in the smectic A mesophase as displayed in *Figure 2.15 b*, in which both aromatic cores (mes) and alkyl chains (ch) are arranged in separate layers alternating along the normal to the layers.

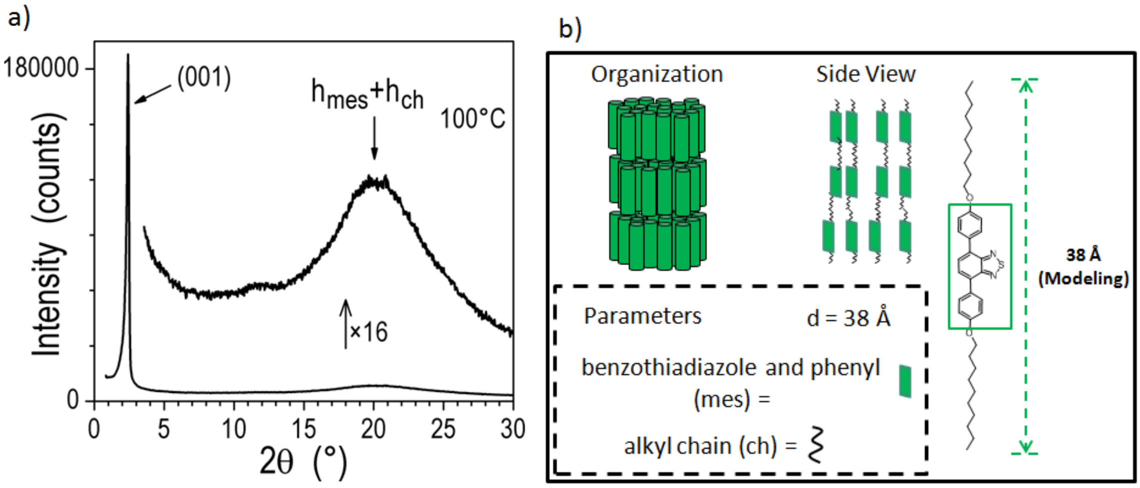

*Figure 2.16 a) X-ray diffraction patterns of **C10-PBT** 100 °C on heating; b) Schematic representation of the lamellar organization of **C10-PBT** in SmA mesophase and lattice parameters.*

2.4.1.2 XRD of C6-PBT

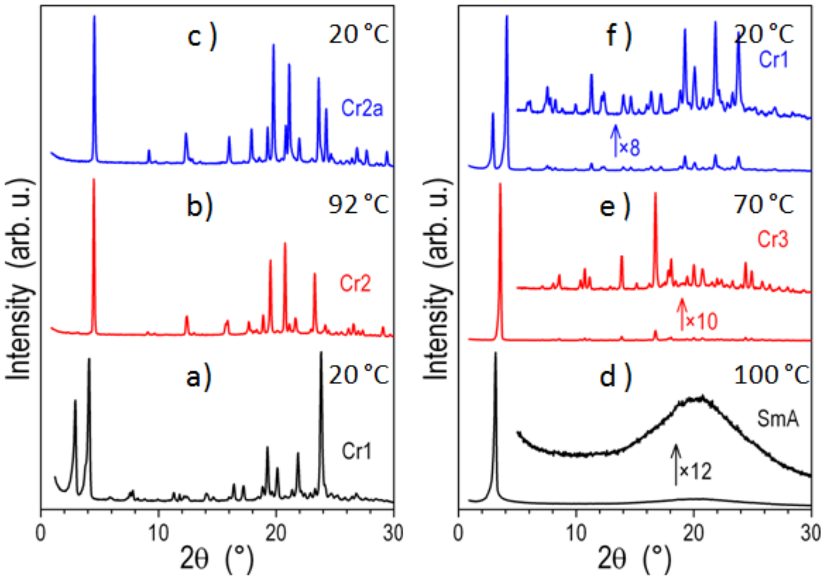

*Figure 2.17 XRD patterns of **C6-PBT**. a) at 20 °C (pristine); b) at 92 °C; c) at 20 °C; d) at 100 °C; e) at 70 °C; f) at 20 °C.*

Similar X-ray diffraction characterizations were performed on **C6-PBT** and *Figure 2.17* shows the typical patterns obtained at different temperatures. In full accordance between SAXS and DSC, the crystalline phase behavior of **C6-PBT** is very similar to the one of **C10-PBT**, except that an additional intermediate crystal phase Cr3 is observed on cooling from the SmA phase, prior to the reappearance of the initial Cr1 phase.

The *Figure 2.18* gives the X-ray diffraction of **C6-PBT** recorded at 100 °C in the smectic A phase and a model of the lamellar organization.

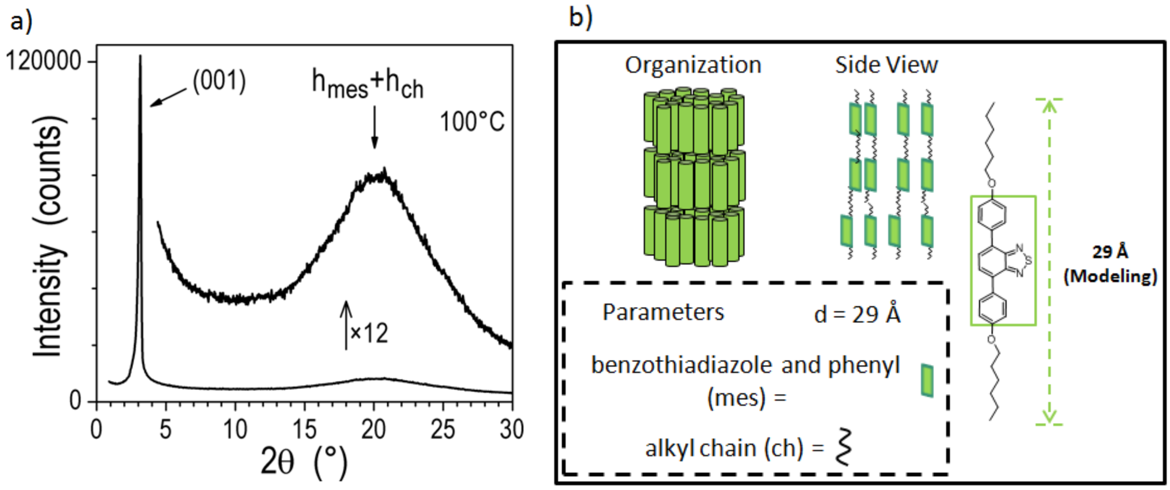

*Figure 2.18 a) X-ray diffraction patterns of **C6-PBT** 100 °C on heating; b) Schematic representation of the smectic A organization and the lattice parameter.*

In the same way as for **C10-PBT**, the liquid crystal state pattern at 100 °C of **C6-PBT** presents a reflection in the small-angle indicating that the molecules are arranged in a lamellar fashion and, in the wide-angle region, a very broad halo centered at 4.5 Å (h_{ch}) indicating the molten state of the aliphatic chains and the average distance of the aromatic core. This X-ray pattern is typical of disordered smectic A mesophase in which both aromatic cores and alkyl chains are arranged in alternating separate layers.

Based on these results we can propose a schematic representation of **C6-PBT** molecular arrangement in the smectic A mesophase as displayed in *Figure 2.18 b*.

2.4.2 Atomic force microscopy (AFM)

The morphology of **C10-PBT** thin films were studied by tapping mode Atomic Force Microscopy (AFM) at the Institut des NanoSciences de Paris (INSP) in collaboration with the Dr. Emmanuelle Lacaze and Ms Xiao Liu (PhD IPCM/INSP).

Samples of **C10-PBT** were prepared either by drop casting of a chloroform solution of material (0.1 % w/w) on a cleaned octadecyltrichlorosilane (OTS) treated substrate at room temperature or by melting processing [171] between OTS treated wafer and cover glass from isotropic state.

The AFM topography images of **C10-PBT** thin films are given in *Figure 2.19* and show clear nanostructured films with terraces indicating extended flat lamellae oriented parallel to the OTS substrates. The heights of the terraces determined from topography images (*Figure 2.19 b*) are about 4 nm or multiples of 4 nm, which are consistent with the **C10-PBT** molecular length around 38 Å and the ‘periodicity’ of the lamellar arrangement of molecules (*Figure 2.19 c*) determined by X-ray diffraction.

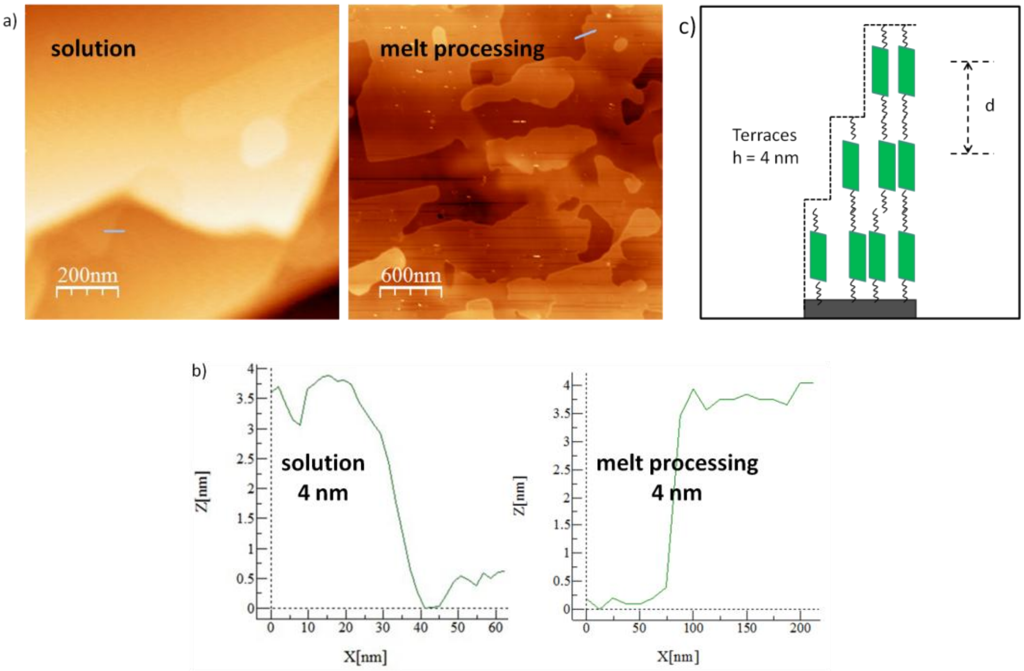

Figure 2.19 The AFM images of ***C10-PBT*** *thin film on OTS substrate: a) Topography; b) Terrace step profile of film determined from topography image; c) Schematic representation of film terrace structure of* ***C10-PBT****.*

2.5 Electronic properties and HOMO/LUMO energy levels

The electrochemical behaviors of **C10-PBT** were studied using cyclic voltammetry. All the experiments were carried out at room temperature in chloroform solutions (concentrations around 10^{-3} M, $n\text{-}Bu_4NPF_6$ 0.5 M being added as supporting electrolyte), at a scan rate of 100 V s^{-1}, with Pt as the working and counter electrodes and Ag/AgCl electrode (saturated KCl) as the reference electrode. Note that oxidation and reduction potentials were determined as an average value between each anodic and corresponding cathodic potentials: $E_{1/2}^{red/ox} = ½ (E_{pa} + E_{pc})$.

The *Figure 2.20* presents the voltammogram of **C10-PBT**. It shows on one hand two well-separated chemically reversible one-electron reduction waves at -0.94 V and -1.39 V (vs Ag/AgCl) corresponding to the formation of the radical anion and dianion characteristic of the benzothiadiazole acceptor moiety. But the first reduction where is not revesible electrochemically. On the other hand, two reversible one-electron oxidation waves corresponding to the phenyl donnor moiety radical cation at 1.35 V and 1.54 V (vs Ag/AgCl).

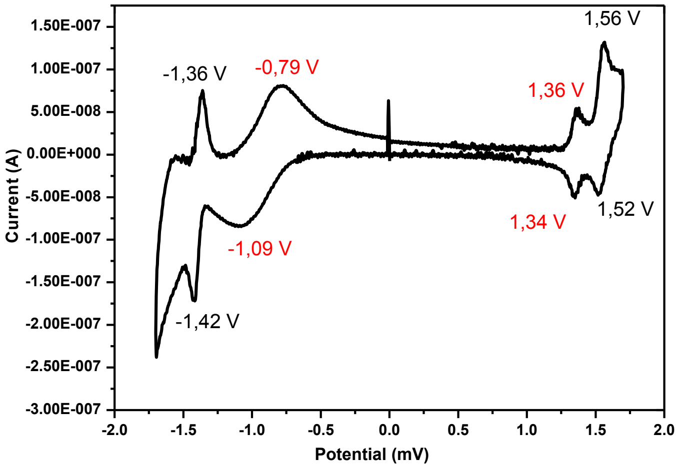

Figure 2.20 Cyclic voltammetry of ***C10-PBT****, in chloroform solution of n-Bu$_4$NPF$_6$ (c (n-Bu$_4$NPF$_6$) = 0.05 M, c (C10-PBT) = ca. 10^{-3} M, 0.05 V/s, room temperature).*

Based on these redox potential values summarized in the *Table 2.5*, the HOMO and LUMO energies of **C10-PBT** were estimated (see *Table 2.6*) after using Fc as a calibrant to be measured first in the same experimental conditions, $E_{1/2}^{ox}$(vs Fc) and $E_{1/2}^{red}$ (vs Fc) are the first potentials values for oxidation and reduction of the studied material relative to the Fc/Fc$^+$ internal standard.

Compound	**$E_{1/2}^{red2}$ (V/Fc/Fc$^+$)**	**$E_{1/2}^{red1}$ (V/Fc/Fc$^+$)**	**$E_{1/2}^{ox1}$ (V/Fc/Fc$^+$)**	**$E_{1/2}^{ox1}$ (V/Fc/Fc$^+$)**
C10-PBT	-1.92	-1.47	0.82	1.01

Table 2.5 Redox potentials of ***C10-PBT*** *measured in solution cyclic voltammetry: $E_{1/2}^{Fc}$ = 0.53 V vs Ag/AgCl * waves overlapped.*

The optical band gap $E_g^{UV\text{-}Vis}$, expressed in electronvolts, depends on the incident photon wavelength by means of a Planck - Einstein relation:

$$E=h\nu=hc/\lambda$$

where h is the Planck constant, ν is the wave frequency and c is the speed of light in vacuum. Since the absorption spectrum reveals information on electronic transition, the onset of absorption can be considered as the band gap of the compound. *Figure 2.21* shows the determination of band gap form UV-vis spectrum of **C10-PBT**. The optical band gap $E_g^{UV\text{-}Vis}$ about -2.62 eV is close to electrochemical band gap about -2.29 eV. As these two compounds have very similiar absorption spectra in solution, the optical band gap of **C6-PBT** can also be evaluated about -2.62 eV.

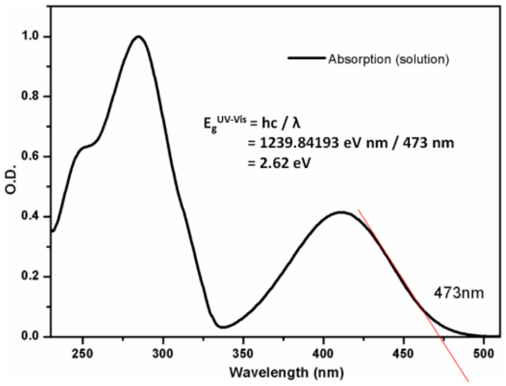

Figure 2.21 Determination of band gap from UV-vis spectrum of C10-PBT.

The values of HOMO/LUMO energies and the band gap of **C10-PBT** are summarized in *Table 2.6*.

Compound	**E^{HOMO} (eV)**	**E^{LUMO} (eV)**	**E_g^{CV} (eV)**	**$E_g^{UV\text{-}Vis}$ (eV)**
C10-PBT	-5.62	-3.30	2.29	2.62

*Table 2.6 HOMO/LUMO values of **C10-PBT**.*

We also investigated the HOMO levels of **C10-PBT** and **C6-PBT** in solid state (thin films) by photoelectron spectroscopy (see *Figure 2.22*). These both compounds have the same value of HOMO level at -6.1 eV, which is a little different with the value determined by cyclic voltammetry.

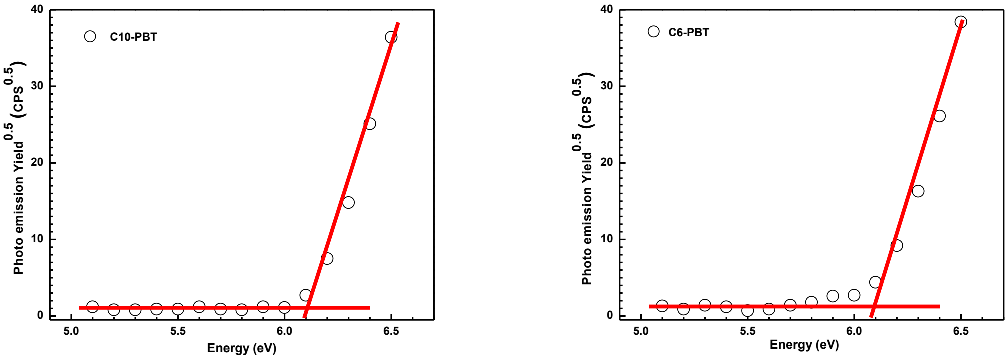

*Figure 2.22 Photoelectron spectroscopy of **C10-PBT** and **C6-PBT**.*

In addition, to better understand the nature of the electronic states of **C10-PBT** and **C6-PBT**, the ground-state geometries were optimized using density functional theory (DFT) at the B3LYP/6-31G* level. The calculation was performed by replacing alkyl chains with methyl groups for simplicity. As shown in *Figure 2.23*, the electronic spatial distribution of the HOMO is mainly distributed over the benzothiadiathole and phenyl moieties, while that the LUMO is competely localized over the benzothiadiathole moiety. This indicates a charge-transfer character for these D-A-D-type compounds.

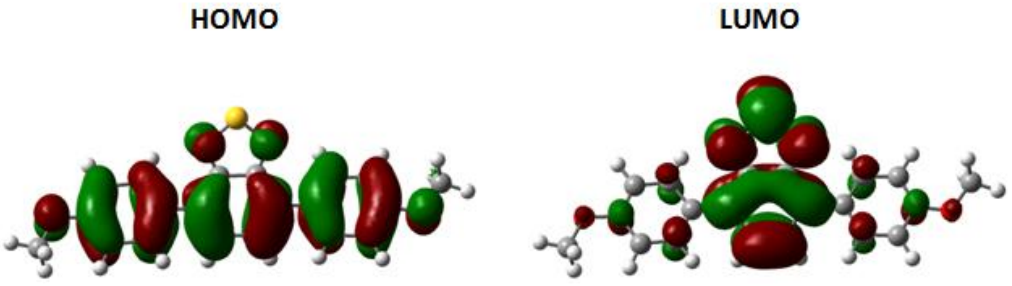

*Figure 2.23 The HOMO and LUMO of **C10-PBT** calculated at the B3LYP/6-31G* level. The alkyl chains have been replaced with methyl groups in the calculation.*

The calculated HOMO/LUMO values of the energy optimized structures are listed in *Table 2.7*. The theoretically predicted LUMO energy levels are about 1 eV higher than the electrochemical value whereas the HOMO energy levels match better. The higher LUMO values than those estimated experimentally may be related with various effects such as conformation and solvation which were not taken into account during DFT calculations.

Comound	E^{HOMO} (eV)	E^{LUMO} (eV)	E_g^{Cal} (eV)
C10-PBT	-5.27	-2.23	3.04

*Table 2.7 Summary of DFT derived HOMO and LUMO energies of **C10-PBT**.*

2.6 Charge Transport Properties

The charge transport properties of **C10-PBT** material were studied by two methods. The charge carrier mobility of thin film prepared by thermal evaporation was evaluated in field effect transistor (OFET) configuration at room temperature. At the same time, the charge carrier mobility was measured by temperature-dependent time-of-flight (TOF) technique in the mesophase. These measurements were carried out at Ewha University (Korea) and at Kyushu University (OPERA, Japan), in collaboration with the Dr. P. Sleczkowskt and the Prof. J.-C. Ribierre. The devices fabrication is described in the experimental part Paragraph 2.8.4 and Paragraph 2.8.5.

2.6.1 Field-effect transistor measurements

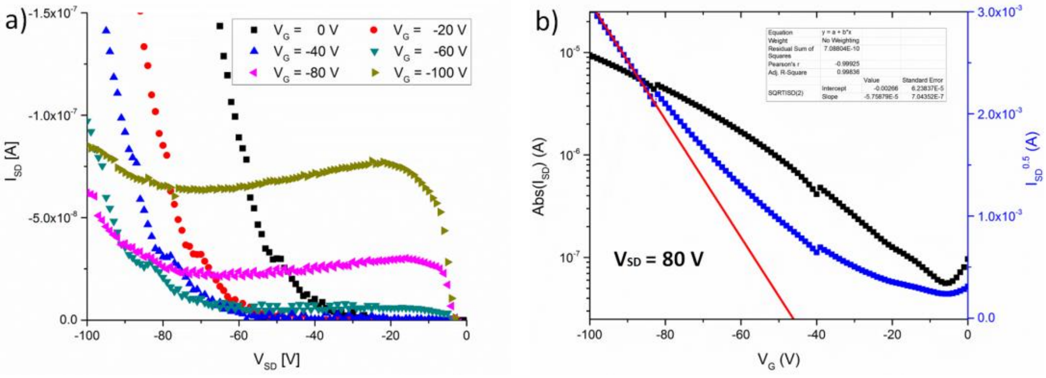

*Figure 2.24 Output and transfer characteristics for holes of **C10-PBT** (OFET).*

The charge transport properties of **C-10PBT** were investigated in OFET configuration (bottom gate BG and top contacts TC). Evaporated thin films were prepared on silanized silicone substrates treated with octadecyltrichlorosilane (OTS) and were annealed at 80 °C (1 h) before gold electrode deposition. The output and transfer characteristics are given in *Figure 2.24.*

The data of OFET devices prepared with **C-10PBT** are given in *Table 2.8*. In particular, a field effect can be observed for VG ≥ 60V and a hole mobility of 3 x 10^{-3} $cm^2\,V^{-1}\,s^{-1}$ can be calculated from the transfer curve.

Compound	Configuration	Annealing	Gate surface	Hole mobility($cm^2V^{-1}s^{-1}$)	Threshold voltage (V)	I_{on}/I_{off} ratio
C10-PBT	BC	N	OTS	3×10^{-3}	-47	5×10^2

*Table 2.8 OFET performances of **C10-PBT**.*

Note that this mobility value is probably underestimated due to the large difference of the gold electrode work function (-5.1 eV) and the HOMO energy level of **C-10PBT** (-6.1 eV). This difference could also explain the poor quality of the OFET electrical characteristics and the low reproducibility of the measurements.

2.6.2 Temperature-dependent time-of-flight measurements

The bulk charge transport properties of **C10-PBT** was characterized by conventional TOF technique: 9 μm thick **C10-PBT** films (sandwiched between two ITO electrodes) were excited by laser nanosecond pulses at 337 nm, where the sample strongly absorbs light. The *Figure 2.25* shows typical transient photocurrents obtained in the SmA mosophase at 115 °C for hole and electron transport.

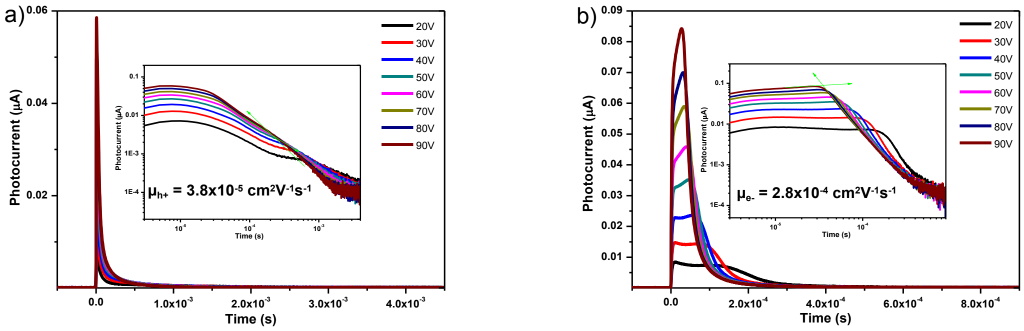

*Figure 2.25 Transient photocurrent curves recorded on cooling in a bulk **C10-PBT** sample in the SmA phase at **115** °C (a) hole mobility; (b) electron mobility.*

The hole/electron mobility (μ) is calculated using the standard equation $\mu = d / \tau E$, where d is the film thickness, E is the magnitude of the applied electric field, and τ is the transmission time. A plateau region with a well-defined inflection point is typically present in the TOF signal, which defines the propagation time τ of the charge carrier packet. As shown in the inset of *Figure 2.25*, clear transit times can be measured for hole and electron carriers from the intersection of an extrapolation of the plateau and the tangent to the tail of the transient curves in the double logarithmic scale, as described by Scher and Montroll first[172]. As a result, the hole mobility was determined to be equal to 3.8 x 10^{-5} cm^2 V^{-1} s^{-1} and electron mobility 2.8 x 10^{-4} cm^2 V^{-1} s^{-1}.

2.7 Conclusions

In this chapter, a family consisting of two liquid crystalline fluorescent compounds **C10-PBT** and **C6-PBT**, based on a D-A-D structure with O-alkylphenyl donor groups and a benzothiadiazole acceptor core, were designed, synthesized and characterized.

The photophysical study showed that these derivatives can present very high luminescence properties with PLQYs in solution as high as 100% for an emission wavelength about 530 nm in apolar solvent. The **C10-PBT** exhibits also unusual very high properties in solid state with a PLQY about 90% in neat film.

Both compounds present liquid crystalline properties on heating and cooling as demonstrated by DSC and POM. The reversible mesophases were investigated by XRD. The structural study confirms that these compounds exhibit mainly a lamellar organization (smectic A mesophase) in which both aromatic D-A-D cores and laterale O-alkyl chains are arranged in separated layers alternating along the normal to the layers.

The film morphology study by AFM showed clearly nanostructured thin films with terraces structures and evidenced that it is possible to orient layers of these fluorescent molecules parallel to the substrate surface. This is a promising property in the domain of organic transistors where 2D orientation is one of the key parameters for the fabrication of high performance transistors.

Finally, the charge transport properties of **C10-PBT** were investigated by field-effect transistor and temperature-dependent time-of-flight measurements. As a preliminary results, a hole mobility about 3 x 10^{-3} cm^2 V^{-1} s^{-1} in crystal state was observed in OFET configuration for **C10-PBT**. TOF measurements in the liquid crystal SmA phase of the same compound show an ambipolar charge transport with a hole and electron mobility about 3.8 x 10^{-5} cm^2 V^{-1} s^{-1} and 2.8 x 10^{-4} cm^2 V^{-1} s^{-1}, respectively.

To conclude, this family of self-organized, orientable and highly fluorescent semiconductors can be considered as interesting and promising candidates in the field of optoelectronics as for example for the fabrication of organic light-emitting devices such as light-emitting diodes or transistors (OLEDs/OLETs).

2.8 Experimental

2.8.1 Materials and methods

The starting materials, 4-bromophenol, 1-bromodecane, potassium carbonate, sodium hydroxide, magnesium sulfate ($MgSO_4$), n-BuLi, tributyltinchloride, benzothiadiazole, hydrobromic acid (48%), bromine, tetrakis(triphenylphosphine)palladium(0) were purchased from Aldrich, Alfa and Acros or TCI and used without any further purification. The solvents, acetone, ether, tetrahydrofuran, ethanol, dimethylformamide, dichloromethane and petroleum ether were purchased from VWR Chemicals. The solvents for recrystallization and precipitation were purchased from Aldrich or distilled before using. The solvents for spectroscopic studies were of spectroscopic grade. Column chromatography was performed on silica gel.

^{1}H- and ^{13}C NMR spectra were recorded on Bruker AC 300 and 400 spectrometers (300 MHz and 400 MHz) using the signal of Tetramethylsilane (TMS) or the carbon signal of the deuterated solvents as internal standard, and the chemical shift are reported in ppm. Abbreviations used for splitting patterns are s = singlet, d = doublet, t = triplet, q = quintet, m = multiplet. The UV/Vis spectra were taken on a spectrometer Varian Cary 300 scan spectrometer using 100 mm quarts cuvette, and the fluorescence spectrum were recorded on a Varian Cary Eclipse spectrofluorimeter. The PLQY measurements in films were performed using an integrating sphere system coupled with a photonic multichannel analyser (Hamamatsu Photonics C9920–02, PMA-11) under a flowing nitrogen atmosphere. The transient photoluminescence decay characteristics of the solution samples were recorded using a fluorescence lifetime measurement system (C11367-03(Quantaurus-Tau), Hamamatsu Photonics). DSC measurement was performed on an Instrument DSC Q2000 V24.4 Build 116, using the Module DSC Standard Cell RC. Phase transitions (POM) were examined by a Leica microscope of Linkam TMS 94 with a Linkam LTS temperature-controlled hot stage and Nikon LWD 0.65 camera. The elementary analysis was performed at the Service de Microanalyse ICSN-CNRS (France) and at Service Central d'Analyse isa (France). AFM images were recorded on a Digital Instrument, DI3100 in tapping mode to analyze the surface density of the samples at INSP- Sorbonne University (France). The SAXS measurement was carried out at the Institut de Physique et de Chimie des Matériaux de Strasbourg (IPCMS) and the patterns were obtained with a transmission Guinier-like geometry. A linear focalized monochromatic Cu Kα1 beam (λ = 1.5405 Å) was obtained using a sealed-tube generator (600 W) equipped with a bent quartz monochromator. In all cases, the crude powder was filled in Lindemann capillaries of 1 mm diameter and 10 µm wall-thickness. The diffraction patterns were recorded with a curved Inel CPS120 counter gas-filled detector linked to a data acquisition computer (periodicities up to 90 Å) and on image plates scanned by STORM 820 from Molecular Dynamics with 50 µm resolution (periodicities up to 120 Å). The sample temperature was controlled within ± 0.01 °C and typical exposure times were of 6 h.

2.8.2 Synthesis

2.8.2.1 Synthesis of precursory building blocks

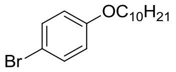

Chemical Formula: $C_{16}H_{25}BrO$
Molecular Weight: 313.273
2B

1-bromo-4-(decyloxy)benzene (2B$_{a}$, n=10): A mixture of 4-bromophenol (5 g, 28 mmol), 1-bromodecane (6.38 g, 28 mmol), potassium carbonate (3.98 g, 28 mmol) was dissolved in 15 mL of acetone, then heated under refluxed for 48 h. After cooling to room temperature, the mixture was poured into water and then extracted with diethyl ether. The combined organic phases were washed with 10 % sodium hydroxide, followed by water, and dried over $MgSO_4$. After the solvent was removed by evaporation, the desired product was obtained as colorless oil by distillization. Yield, 8.1 g, 90%. NMR δH (ppm) (300 MHz, $CDCl_3$) 7.34 (d, 2H), 6.75 (d, 2H), 3.91 (t, 2H), 1.76 (quint, 2H), 1.21-1.44 (14H), 0.89 (t, 3H). **1-bromo-4-(hexyloxy)benzene (2B$_{b}$, n=6)** was synthesized by the similar procedure, except that 1-bromohexane (4.62 g, 28 mmol) was used instead of 1-bromodecane, and obtained as colorless oil. Yield, 5.9 g, 83%. NMR δH (ppm) (300 MHz, $CDCl_3$) 7,24 (d, 2H), 6,64 (d, 2H), 3,77 (t, 2H), 1,64 (t, 2H), 1,23 (m, 6H), 0,79 (t, 3H).

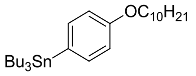

Chemical Formula: $C_{28}H_{52}OSn$
Molecular Weight: 523.422
2C

Tributyl(4-(decyloxy)phenyl)stannane (2C$_{a}$, n=10): 1B (n=10) 1-bromo-4-(decyloxy)benzene (**2B$_{a}$, n=10**) (5 g, 16 mmol) was dissolved in 30 mL of dry THF and cooled to -78 °C. n-BuLi (10 ml, 1.6 M solution in hexane) was added under argon and stirred for 30 min, then 5.2 g of tributyltinchloride (16 mmol) in 20 mL of dry THF was added to the solution in dropwise. The temperature was slowly raised overnight to room temperature. The reaction mixture was quenched with water and extracted with diethyl ether. The organic phases were dried over $MgSO_4$. After the solvent was removed by evaporation, the desired product was obtained as colorless oil by distillization. Yield, 7.36g, 87.6%. NMR δH (ppm) (300 MHz, $CDCl_3$) 7.34 (d, 2H), 6.90 (d, 2H), 3.95 (t, 2H), 1.77 (q, 2H), 0.86-1.58 (44H). **Tributyl(4-(hexyloxy)phenyl)stannane (2C$_{b}$, n=6)** (4.1 g, 16 mmol) was synthesized by the similar procedure, except that 1-bromo-4-(hexyloxy)benzene **(2B$_{b}$, n=6)** was used instead of 1-bromo-4-(decyloxy)benzene (**2B$_{a}$, n=10**), and obtained as colorless oil. Yield, 6.0 g, 80%. NMR δH (ppm) (300 MHz, $CDCl_3$) 7,35 (d, 2H), 6,90 (d, 2H), 3,92 (p, 2H), 1,61 (m, 45H), 1,28 (4H), 1,01 (23H).

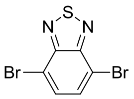

Chemical Formula: $C_6H_2Br_2N_2S$
Molecular Weight: 293.966
2E

4,7-dibromobenzo[c][1,2,5]thiadiazole (2E): Benzothiadiazole (2 g, 14.7 mmol) was added to HBr (30 mL, 48%) and stirred under a normal atmosphere. To this mixture, a solution of molecular bromine (2 mL, 74.5 mmol) in HBr (25 mL, 48%) was added and the mixture was heated under reflux for 6 h. The reaction was quenched by addition of ice and washing the aqueous mixture with $NaHSO_3$ to remove the unreacted bromine. The product precipitated as small off-white crystals which were then filtered and collected. Recrystallisation from ethanol yielded the desired product as long needle-like, pale yellow crystals which were dried under vacuum overnight at 50°C. Yield, 2.38 g, 55%. NMR δH (ppm) (300 MHz, $CDCl_3$) 7.73 (s, 2H).

2.8.2.2 Synthesis of C10-PBT and C6-PBT

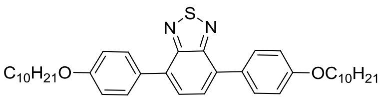

Chemical Formula: $C_{38}H_{52}N_2O_2S$
Molecular Weight: 600.897
C10-PBT

C10-PBT: 4,7-dibromobenzo[c][1,2,5]thiadiazole (**2E**, 1.41 g, 4.8 mmol) and Tributyl(4-(decyloxy)phenyl)stannane (**$2C_a$, n=10**, 5.03 g, 9.6 mmol) were dissolved in anhydrous DMF (60 mL) in a round-bottom flask under argon, and a catalytic amount of $Pd(PPh_3)_4$ was added into the flask. Then the reaction mixture was refluxed for 48 h at 150 °C. After cooling to room temperature, the mixture was washed with water then extracted with dichloromethane. The organic phases were dried over $MgSO_4$. The solvent was evaporated, and the crude product was purified via column chromatography using dichloromethane:petroleum ether = 1:2 by volume as the eluent to afford C10-PBT as a green solid (1.2 g). Yield, 42%. NMR δH (ppm) (400 MHz, $CDCl_3$) 7.90 (d, 4H), 7.71 (s, 2H), 7.03 (d, 4H), 4.03 (t, 4H), 1.84 (m, 4H), 1.29-1.49 (m, 28H), 0.89 (s, 6H) ; δC (ppm) (100 MHz, $CDCl_3$) 159.91, 154.83, 132.94, 130.91, 130.37, 128.82, 127.93, 115.25, 68.73, 32.48, 30.15, 29.99, 29.95, 29.90, 26.65, 23.26, 14.69. Elementary analysis: Calcd for $C_{38}H_{52}N_2O_2S$: C 75.95, H 8.72, N 4.66; Found C 75.79, H 8.60, N 4.42. HRMS: $C_{38}H_{52}N_2O_2S+Na^+$: 623.3642, Found: 623.3644.

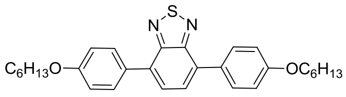

Chemical Formula: $C_{30}H_{36}N_2O_2S$
Molecular Weight: 488.684
C6-PBT

C6-PBT were synthesized by the similar procedure as **C10-PBT** with **$2C_b$** (**n = 6**) with a yield of 46%. NMR δH (ppm) (400 MHz, $CDCl_3$) 7.90 (d, 4H), 7.72 (s, 2H), 7.08 (d, 4H), 4.05 (t, 4H), 1.83 (p, 4H), 1.36 (m, 12H), 0.94 (t, 6H); δC (ppm) (100 MHz, $CDCl_3$) 160.02, 154.77, 132.80, 130.97, 130.79, 127.84, 127.93, 115.05, 68.83, 32.15, 29.77, 26.32, 23.18, 14.39. Elementary analysis: Calcd for $C_{30}H_{36}N_2O_2S$: C 73.73, H 7.43, N 5.73; Found C 73.35, H 7.07, N 5.90. HRMS: $C_{30}H_{36}N_2O_2S+Na^+$: 511.2390, Found: 511.2400.

2.8.3 AFM sample preparation

Preparation of organic crystalline layer by drop casting method: one drop of **C10-PBT** solution ($CHCl_3$, 0.1 % w/w) was deposited on the surface of OTS treated substrate at room temperature. The sample was used directly after the solvent evaporated.

Preparation of organic crystalline layer by melt-processing method: processing of the crystalline thin layer was carried out in several steps. Firstly, a small amount of the material was heated up in the isotropic liquid phase, to fill out, by capillary action, the empty space separating a cover glass and a silicon (or fused silica) wafer. The cover glass, placed on top, was previously treated with a self-assembled monolayer of octadecyltrichlorosilane (OTS), in order to reduce its adherence with the final organic film. Second step consists in a slow cooling down to room temperature, in order to obtain a crystalline film. A polarized optical microscope (POM) was used to monitor the process. In the last step, the weakly adhering OTS-treated cover glass was removed, leaving crystalline organic thin film of 100 to 150 nm thickness.

2.8.4 OFET sample preparation and configurations

The **C10-PBT** films were prepared by thermal evaporation onto OTS-treated silicon wafer. The thickness of films varies from 50 to 70 nm as evaluated by profilometer. The samples were studied after annealing (80 °C for 2 hours in vacuum). For thermal evaporation, the product was used directly without further purification or treatment. The deposition rate used was 0.5 Å/s and the thickness was fixed as 50 nm. The annealing was effected in glove-box for 2 hours at 80 °C .

The substrates were sonicated in acetone and isopropanol and then placed in a piranha solution to remove the residues of organic materials and to induce OH groups in the vicinity of the surface. After rinsing the substrates again in isopropanol and tried by nitrogen flow. Then they were cleaned in a UV cleaner during 20 minutes. For the preparation of the OTS-treated substrates, the silanization was carried out in a 3 mm OTS (Octadecyltrichlorosilane) solution of dry hexane for 90 min. All solvents were purchased from Sigma Aldrich and were used without further purification.

Gold top-contact source and drain electrodes were deposited through a shadow mask by evaporation. The channel lengths are 40 µm respectively and the channel width is always 1.6 cm.

OFET characteristics were measured using a double channel source meter unit (Keithley 2600) and all the tests were realized in glove-box. All the field effect mobilities were calculated on the saturation regime.

2.8.5 TOF sample preparation and configurations

In this chapter, the TOF measurement were performed in the basic configuration, CGL was not used. The standard liquid crystal cell was purchased from Instec Inc. with gap thickness of 9 µm and transparent electrodes of indium tin oxide (ITO). Compound **C10-PBT** powder was placed near the hole of the cell and heated to an isotropic state. The sample then flows into the cell by capillary force and the film is cooled down before using.

The sample was mounted in the TOF setup using hot stage (Instec HCS302). Sample was excited by nanosecond pulses from N_2 laser at 337 nm, where the sample strongly absorbs light and a repetition rate of 1.8 Hz. The excitation of the sample results in a transient photocurrent signal that is amplified and then recorded by a Tektronix TDS 5034 350 MHz digital oscilloscope.

2.8.6 Dipole Moments Calculations

By employing the simplest quantum-mechanical second order perturbation theory, Bilot and Kawski have obtained expressions for solvent spectral shift given by:

$$\nu_a - \nu_f = m^1(\varepsilon, n) + constant \quad \textbf{(1)}$$

$$\nu_a + \nu_f = -m^2[f(\varepsilon, n) + 2g(n)] + constant \quad \textbf{(2)}$$

where ν_a is the absorption maximum and ν_f is the fluorescence maximum, both in wavenumber. ε is the permittivity and n is the refractive index. m^1 and m^2 represent the slope plotting relation **(1)** and **(2)** using Bakshiev polarity function f(ε, n) and Kawski-Chamma-Viallet polarity function g (n):

$$f(\varepsilon, \mathrm{n}) = \frac{2n^2+1}{n^2+2}\left(\frac{\varepsilon-1}{\varepsilon+2} - \frac{n^2-1}{n^2+2}\right) \quad \textbf{(3)}$$

$$\mathrm{g(n)} = \frac{3}{2}\left(\frac{n^4-1}{(\mathrm{n}+2)}\right) \quad \textbf{(4)}$$

Following the Onsager theory, m^1 and m^2 can be expressed as following

$$m^1 = \frac{2(\mu_e-\mu_g)^2}{hca^3} \quad \textbf{(5)}$$

$$m^2 = \frac{2({\mu_e}^2-{\mu_g}^2)}{hca^3} \quad \textbf{(6)}$$

where h is the Planck constant ($h = 6.63 \cdot 10^{-34}$ Js), c is the velocity of light in vacuum ($c = 3 \cdot 10^8$ ms^{-1}) and a is the Onsager's radius with μ_g the ground state dipole moment and μ_e the excited state dipole moment. Therefore the ground state dipole moment can be found by using the following equation

$$\mu_g = \frac{m^2-m^1}{2}\left(\frac{hca^3}{2m^1}\right)^{1/2} \quad \textbf{(7)}$$

In this equation, the Onsager radius a is calculated using the equation **(8)**

$$\mathrm{a} = \left(\frac{3\mathrm{M}}{4\pi\delta \mathrm{N}_A}\right)^{1/3} \quad \textbf{(8)}$$

where δ is the density (δ = 0.905 for **C-10PBT**, the value were calculated according to procedures described in the literature[173]), M is the molecular weight (600.9 g.mol^{-1}) and N_A is the Avogadro's constant (6.022*10^{23} mol^{-1}). The Onsager radius a is thus equal to 6.41 Å. In addition to these calculations from Bilot and Kawski, Lippert and Mataga proposed the following equation to determine the excited state dipole moment μ_e

$$\nu_a - \nu_f = m^3\Delta f' + constant \quad \textbf{(9)}$$

with $\Delta f'$ and m^3 defined as following:

$$\Delta f' = \frac{\varepsilon - 1}{2\varepsilon + 1} - \frac{n^2 - 1}{2(2n^2 + 1)} \quad \textbf{(10)}$$

$$m^3 = \frac{2(\mu_e - \mu_g)^2}{hca^3} \quad \textbf{(11)}$$

The plotting of **(1)**, **(2)** and **(9)** for **C10-PBT** is represented in *Figure 2.25*.

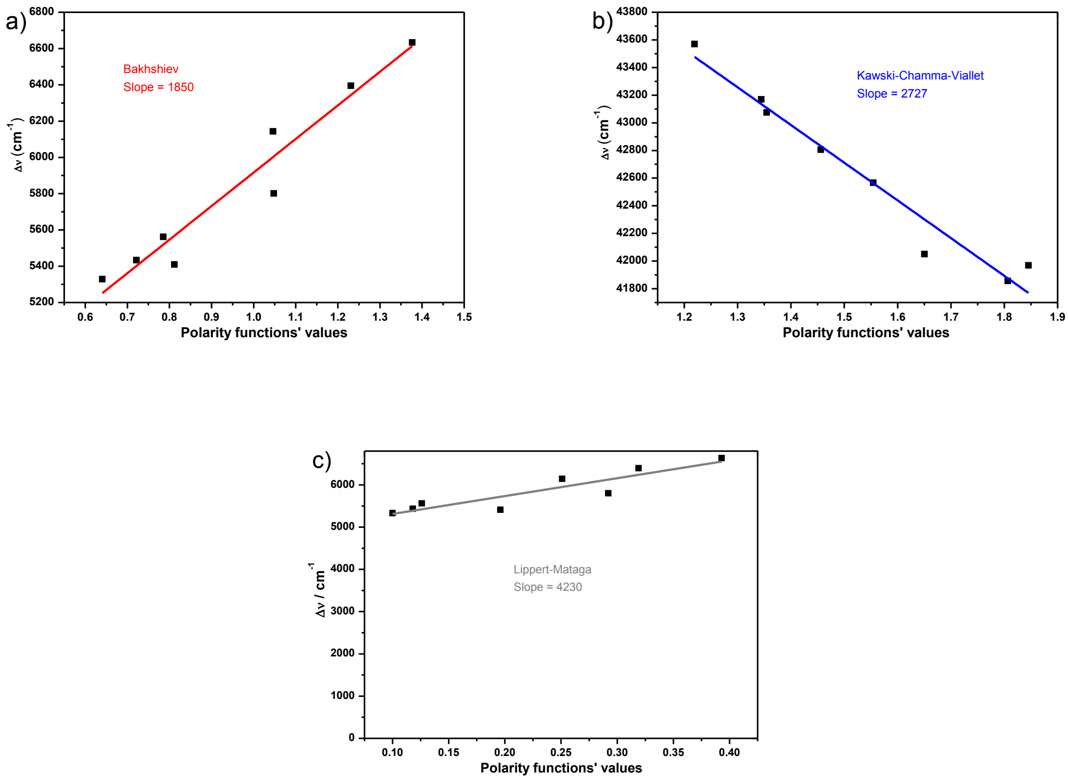

*Figure 2.26 Solvent polarity functions of **C10-PBT**.*

The slope of **(1)** and **(2)** represents m^1 and m^2, which used in **(7)** allowed to determined the ground state dipole moments of **C10-PBT** (μ_g = 2.68 Debye). Then the slope of **(9)** gives m^3 which reported in **(11)** along with the values of μ_g allows to calculate the excited state dipole moment of **C10-PBT** (μ_e = 17.66 Debye).

Chapter 3 Synthesis and Characterization of Liquid Crystal Fluorescent Dyad and Triad

In this chapter, we will study a family of triad and dyad architectures based on the fluorescent benzothiadiazole-based derivative studied in the previous chapter as central emissive core and benzo[4,5]thieno[2,3-d]thiophene (BTBT) derivatives as side groups. In fact, the BTBT derivatives exhibit pretty good charge transport abilities and very good mesomorphic properties with a mobility of 3 cm^2 V^{-1} S^{-1} measured by OFET[174]. So, the objective of this work is to try to obtain multi-lamellar liquid crystal materials with high charge carrier mobility and high fluorescent properties simultaneously, for applications such as light emitting transistors, for instance. More precisely, the chemical structures of these expected luminescent liquid crystalline dyad and triad are given in Figure 3.1.

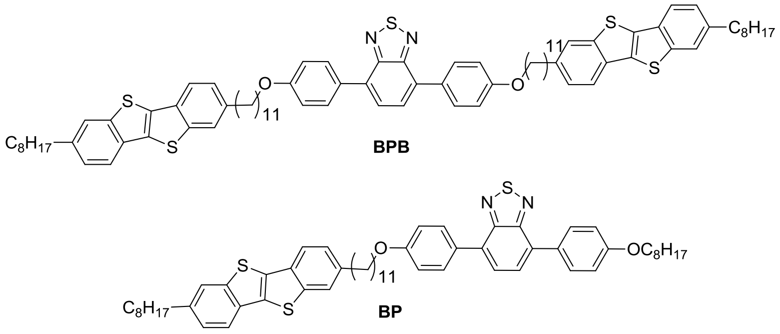

BPB

BP

Figure 3.1 Chemical structures of the linear dyad and triad architectures based on fluorescent benzothiadiazole derivative and BTBT units.

In particular, we will describe and discuss the synthesis, the photophysical and electronic properties as well as the mesomorphic and self-organization of these molecules. In addition, charge transport properties will be investigated.

3.1 Synthesis

3.1.1 Synthesis of precursory building blocks

For the synthesis of the triad and dyad architectures, two precursors are prepared: a 4,4'-(benzo[c][1,2,5]thiadiazole-4,7-diyl)diphenol (BTP) and a benzo[4,5]thieno[2,3-d]thiophene (BTBT) derivatives.

3.1.1.1 Synthesis of 4,4'-(benzo[c][1,2,5]thiadiazole-4,7-diyl)diphenol (BTP)

The synthesis of the precursory BTP building block **3B** is given in *Figure 3.2*. It is prepared according to adapted procedures described in the literature[175]. This synthetic route for the preparation of compound **3B** consists in three steps. The first step, to prepare the compound **2E**, has been already described in the Chapter 2. The second step concerns the preparation of the dimethoxy derivative compound **3A** obtained by classical Suzuki cross-coupling between **2E** and the 4-methoxybenzene boronic acid (commercially available). After a demethylation reaction with via bromic acid solution, the target dihydroxy building block **3B** was obtained with a good yield of 70%.

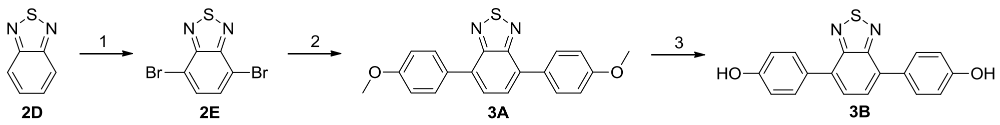

Figure 3.2 Synthetic route of benzothiadiazole-based precursor ***3B****. Conditions: 1) bromine, HBr (48%), reflux, 6h, 60%; 2) 4-methoxybenzene boronic acid, KF, Cs_2CO_3, toluene, H_2O, rt, 12h, 70%; 3) tetrabutylammonium bromide, HBr (33%), 100 °C, 24h, 70%.*

3.1.1.2 Synthesis of benzo[4,5]thieno[2,3-d]thiophene (BTBT)

The synthesis of the precursory BTBT building block **3J** is shown in *Figure 3.3*. It is prepared through a multi-step synthetic route adapted from the literature [176, 177].

The BTBT aromatic core **3D** was synthesized in one step process from commercially available 2-chlorobenzaldehyde and sodium hydrosulfide hydrate, following literature procedures to produce a large amount of material. The next step is a Friedel–Crafts acylation of BTBT with an equimolar ratio of octyl acid chloride at room temperature to obtain a mono-addition leading to the product **3E** with high yields. Then, the ketone was reduced by using aluminum chloride and lithium aluminum hydride to produce **3F** in a quasi-quantitative yield of 96%. Then, the two previous steps were repeated with 11-bromoundecanoic acid chloride, firstly prepared from 11-bromoundecanoic acid and oxalyl chloride, to obtain the intermediary **3I**, and finally the building block **3J** in high yield.

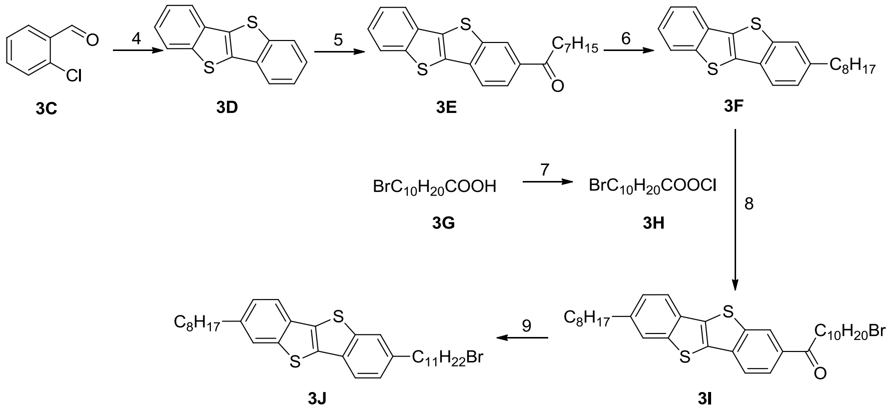

Figure 3.3 Synthetic route of the BTBT building block ***3J****. Conditions: 4) $NaSH\cdot xH_2O$, ammonium chloride solution, 80 °C 1 h then 155 °C for 3 days,30%; 5) octyl acid chloride, $AlCl_3$, DCM, RT, overnight, 80%; 6) $LiAlH_4$, $AlCl_3$, Et_2O, DCM, RT, overnight, 96%; 7) $SOCl_2$, RT, overnight, 99%; 8) $AlCl_3$, -78 °C 1 hour, RT overnight, 70%; 9) $LiAlH_4$, $AlCl_3$, Et_2O, DCM, RT, overnight, 94%*

3.1.2 Synthesis of triad BPB

The synthetic route to prepare the BTP/BTBT based triad is given in *Figure 3.4*. The synthesis of the triad **BPB** was carried out by the Williamson reaction between the benzothiadiazole derivative **3B** and two equivalents of benzo[4,5]thieno[2,3-d]thiophene halide **3J**. The first trials of this reaction with conventional conditions (in DMF or ethanol, reflux, under N_2/24h) didn't work well with yields lower than 20%. For this reason, we performed this reaction in microwave reactor leading to an increase of the yield around 60% and a reaction time of 20 minutes. This compound was purified (Soxhlet, column chromatography, recrystallization) and characterized at high temperature using high boiling point chlorinated solvent due to the low solubility in most of the organic solvents. The ^{1}H NMR and ^{13}C NMR characterization of triad **BPB** was proceeded in chlorobenzene solution at 80 °C.

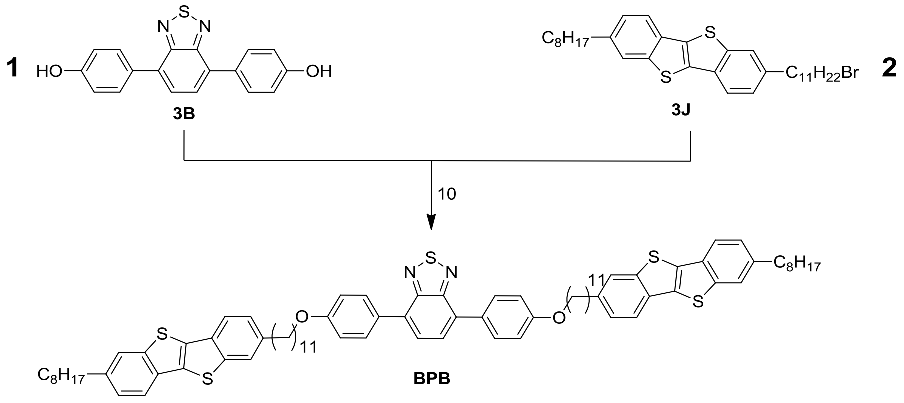

*Figure 3.4 Synthetic route of the triad **BPB**. 10) Microwave reactor, Cs_2CO_3, EtOH, 120 °C, 20 min, 60%.*

3.1.3 Synthesis of dyad BP

The synthesis of dyad **BP** is shown in *Figure 3.5*. The dyad **BP** can be obtained from the same benzothiadiazole derivative **3B** and benzo[4,5]thieno[2,3-d]thiophene halide **3J** in two steps. Firstly, the intermediate compound **3K** was obtained through a classical Williamson etherification reaction with an equimolar ratio between **3B** and **3J** with, an acceptable yield of 30%. Then, the dyad **BP** was produced by grafting the n-octyl bromide via another Williamson reaction. It is worth to mention that the dyad **BP** is well soluble in the usual chlorinated solvents such as chloroform, dichlorobenzene, and it can be easily purified and characterized by the conventional methods.

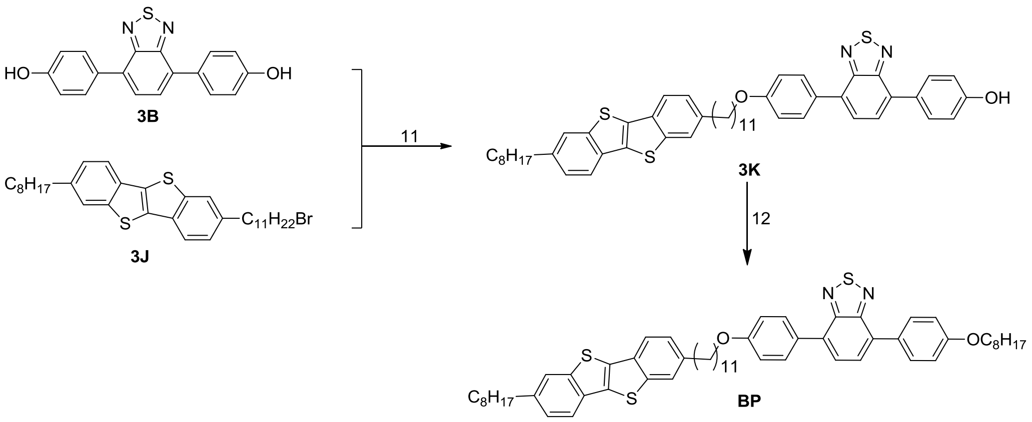

*Figure 3.5 Synthetic route of the dyad **BP**. 11) K_2CO_3, DMF, 120 °C , overnight, 30%; 12) Microwave reactor, Cs_2CO_3, EtOH, 120 °C, 20 min, 65%.*

The NMR spectra of **BPB** and **BP** are given in *Figure 3.6*. For these compounds, the proton peak from hydroxyl at 4.9 ppm disappeared after Williamson etherification reaction, indicating the success of the grafting of the BTBT units.

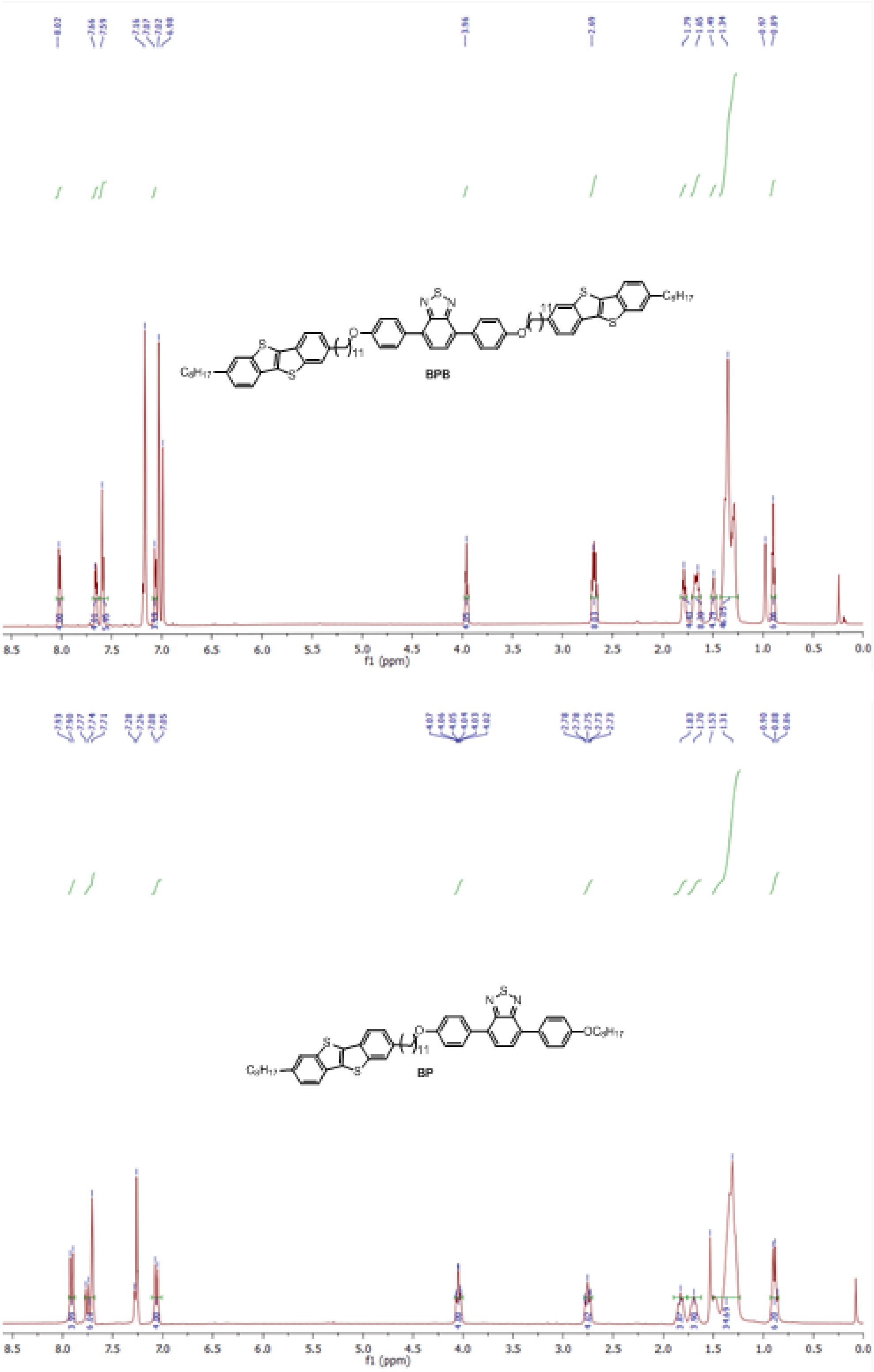

Figure 3.6 The NMR spectrum of the ***BPB*** *and* ***BP****.*

3.2 Photophysical properties (absorption and emission)

The absorption and emission properties of this family of dyad and triad combining different calamitic units were studied in diluted chloroform solutions (ca. 10^{-5} M). In this condition, all these molecules are adequately isolated therefore the aggregation and the intermolecular interactions can be neglected.

3.2.1 Photophysical properties of building block molecules

The *Figure 3.7* shows the absorption and emission spectra in solution of BTBT and BTP units, individually. Note that the model BTBT unit is a dioctyl-BTBT which is commercially available and that the **C10-PBT** has been already described in the Chapter 2.

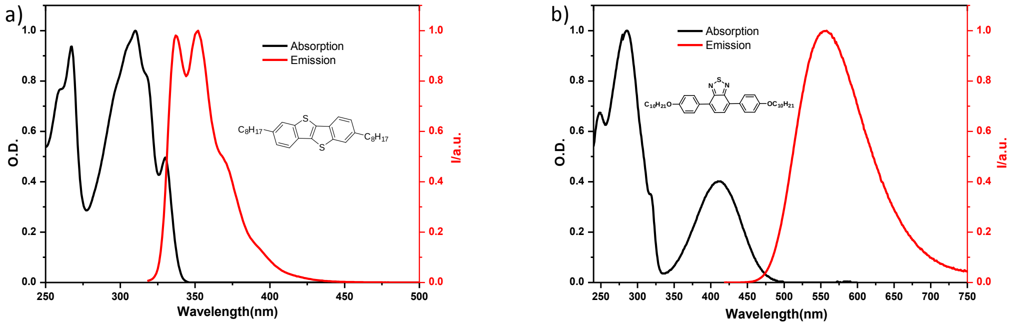

Figure 3.7 UV/Vis absorption and emission spectra of a) BTBT and b) C10-PBT units in DCM.

In the case of the model BTBT (*Figure 3.7 a*), the characteristic absorption peaks can be observed at 267 nm and 310 nm, while the fluorescence spectrum exhibit the peaks at 337 nm and 351 nm. These absorption and emission spectra indicate that there is no aggregation of the BTBT moieties in these experimental conditions [178].

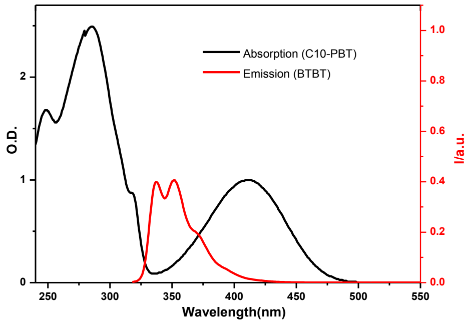

*Figure 3.8 UV/Vis absorption spectrum of **C10-PBT** and emission spectra of **BTBT**.*

The *Figure 3.8* indicates that there is overlap between the emission of the donor (BTBT) and the absorption of the acceptor suggesting a possible Förster resonance energy transfer (FRET) between

BTBT and BTP. However, this overlap is not optimal, and the energy transfer between these units will not be very efficient.

3.2.2 Absorption and Emission of triad BPB

The absorption and emission spectra of triad **BPB** were carried out in solution and are given in *Figure 3.9*. Not surprisingly, the absorption spectrum of **BPB** is the sum of the isolated BTBT and BTP building blocks taken separately.

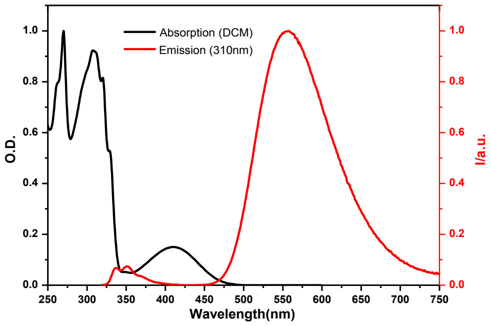

*Figure 3.9 UV/Vis absorption and emission spectra of triad **BPB** in DCM (excitation wavelength 310 nm).*

More precisely, at wavelengths shorter than 350 nm, the absorption band is due to the BTBT unit combined with the π-π* band of the BTP moiety, while in the visible region of the spectrum it is due to the intramolecular CT band of the BTP unit with a maximum peak located at 410 nm. The maxima of the absorption from the BTBT present the same values as individual BTBT (see in *Figure 3.7 a*), indicating the absence of interaction in the ground state or aggregation in the solution of the BTBT units. In addition, the CT band of BPB at 410 nm is also exactly at the same position that the one of individual BTP. Overall, this perfect overlapping between the spectrum of the triad and the spectra of the individual BTBT and BTP moieties evidences the absence of aggregation between the two moieties in solution in the ground state.

Concerning the emission properties, this compound is strongly fluorescent (green) in DCM solution. The emission spectrum excited at 310 nm is mainly dominated by the emission of BTP moiety as shown by the presence of the intense peak at 556 nm, attributed to the BTP unit (*Figure 3.9*). In addition of the BTP emission, when excited at 280 nm, a relatively weak signals at 350 nm is also visible, corresponding to the residual emission of BTBT due to the uncomplete energy transfer.

When exciting at 410 nm, the same emission spectrum as BTP is also observed and the PLQY is found to be around 59%. This value being lower than the PLQY of BTP moiety alone in DCM (77%), we can conclude that there is formation of donor-acceptor pairs in the excited state that quenches the fluorescence (*Figure 3.10*). Based on PLQY values, we can estimate that there is 23.4% of donor-acceptor pair in the excited state.

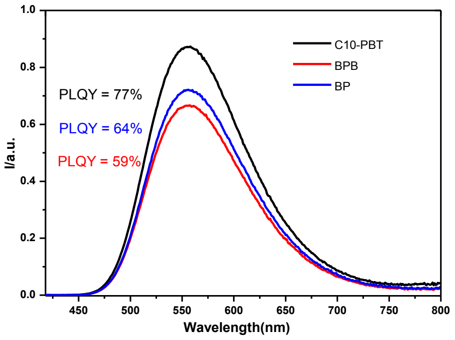

Figure 3.10 Emission spectra of C10-PBT, ***BPB*** *and* ***BP*** *in DCM (excitation wavelength 410 nm).*

3.2.3 Absorption and Emission of dyad BP

We also studied the photophysical properties of dyad **BP** and absorption and emission spectra in solution are given in *Figure 3.11*.

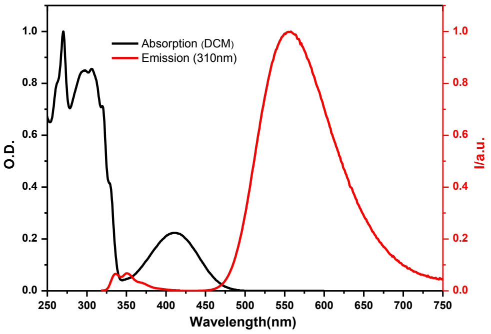

Figure 3.11 UV/Vis absorption and emission spectra of dyad ***BP*** *in DCM (excitation wavelength 310 nm).*

As already described for the triad **BPB**, the absorption spectrum of **BP** is also the sum of the isolated BTBT and BTP absorption spectra and it is quite similar to that of **BPB**. Evidently, as the BTBT/BTP ratio is here of 1/1 in comparison with the triad BPB, we can observe a stronger contribution of the π-π* (280 nm) and CT (410nm) bands of the BTP unit in the absorption spectrum of **BP** as illustrated in *Figure 3.11*.

Similarly with what we observed for the triad **BPB**, the absorption maxima of the BTBT (270 nm) and BTP CT band (410 nm) in the dyad **BP** spectrum are also exactly at the same position that the same maxima of individual BTBT and BTP units (*Figure 3.12*). These observations evidence the absence of aggregation between the two moieties of the dyad **BP** in solution in the ground state.

Concerning the emission properties, the dyad **BP** is also strongly fluorescent (green) in DCM solution. The emission spectrum excited at 310 nm is mainly dominated by the emission of BTP moiety as shown by the presence of the peak at 556 nm (*Figure 3.10*). Similarly with triad **BPB**, in addition of the BTP unit emission, when exciting at 280 nm, a relatively weak signals at 350 nm is also observed, corresponding to the residual emission of BTBT due to uncomplete energy transfer. When exciting at 410 nm, the same emission spectrum as BTP is also observed and the PLQY can be measured to be about 64%. This value being lower than the PLQY of BTP moiety alone in DCM (77%), we can conclude that there is formation of donor-acceptor pairs in the excited state that quenches one part of the fluorescence (*Figure 3.10*). Based on PLQY values, we can estimate that there is 16.8% of donor-acceptor pair in the excited state. Not surprisingly, the presence of half BTBT units in the case of the dyad **BP** in comparison with the triad **BPB** is consistent with the lower number of donor-acceptor pair in the excited state and the higher PLQY observed.

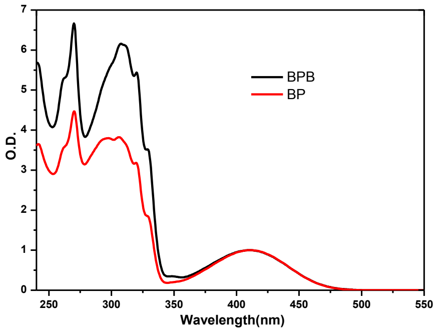

*Figure 3.12 UV/Vis absorption spectra of **BPB** and **BP**.*

3.3 Mesomorphic properties

The mesomorphic properties of the dyad **BP** and triad **BPB** were studied by differential scanning calorimetry (DSC) on heating and cooling cycles and polarized optical microscopy (POM). All the samples for POM were prepared on cleaned or octadecyltrichlorosilance (OTS) treated glass sides, and all the photographs were captured upon cooling from isotropic phases.

3.3.1 DSC and POM of triad BPB

The POM studies were both performed on clean glass substrates (*Figure 3.13 a-d*) and on OTS treated glass substrates (*Figure 3.13 e-h*). Under POM with crossed polarizers, the compound triad **BPB** appeared as a birefringent yellowish powder. On heating, the yellow powder melted at around 196 °C to give a fluid phase with no birefringence associated to the isotropic phase. Then, on cooling from the former isotropic state, a birefringent phase reappeared at around 194 °C showing schlieren texture characteristic of a nematic phase (*Figure 3.13 a*). On further cooling, a fan-shape texture was observed at 180 °C on clean glass substrate (*Figure 3.12 b*) as well as a homeotropic texture on OTS treated glass substrates (*Figure 3.13 f*). These both observations are characteristic of an untilted lamellar smectic A mesophase. The transition from the lamellar mesophase to crystal phase was clearly observed at around 177 °C (*Figure 3.13 c*) and the crystal phase texture was then maintained unchanged until 30 °C (*Figure 3.13 d*).

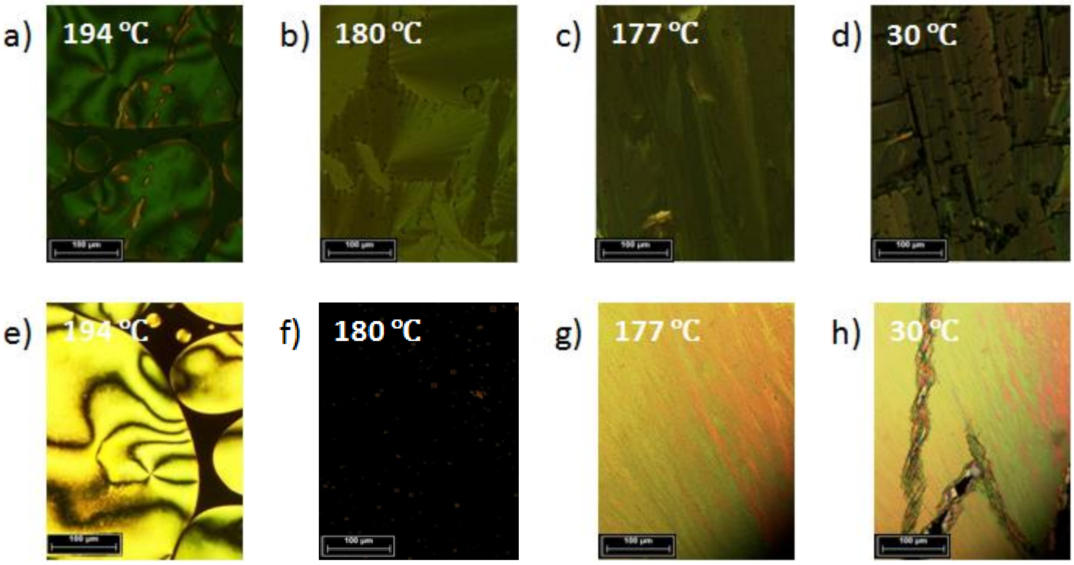

*Figure 3.13 POM microphotographs (under crossed polarizers) of **BPB**. POM microphotographs obtained upon cooling: a-d) the optical textures of BPB at 194 °C, 180 °C, 177 °C and 30 °C respectively, on clean glass substrates; e-h) the optical textures of BPB at 194 °C, 180 °C, 177 °C and 30 °C respectively on OTS treated glass substrates.*

The DSC thermogram of **BPB** corresponds to the typical thermal behavior of low molecular weight liquid crystal molecules, which contains endothermic transitions at high temperature and corresponds to crystalline phase/mesophase or mesophase/isotropic phase transitions, consistent with POM observations. The DSC traces of **BPB** are given in *Figure 3.14* and the phase transition temperatures and enthalpy changes data are summarized in *Table 3.1*.

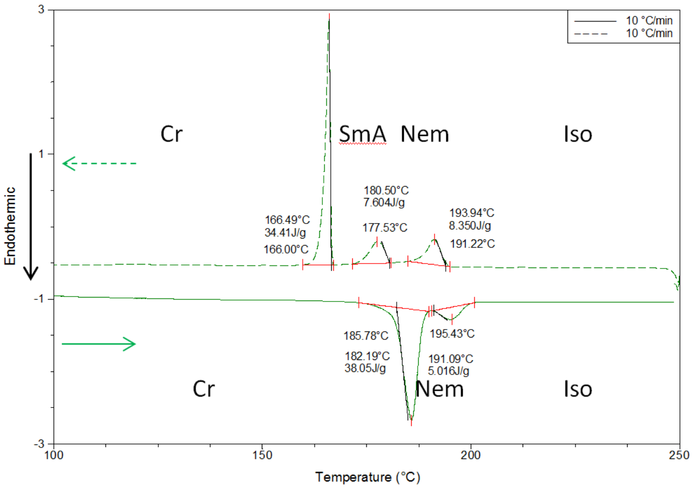

*Figure 3.14 DSC thermogram of **BPB**.*

On heating recorded with a rate of 10 °C/min, the DSC thermogram of **BPB** shows two endothermic peaks (*Figure 3.14, Table 3.1*). Based on POM observations, the first strong and broad peak observed at around 182 °C (ΔH = 38.1 Jg^{-1}) can be attributed to the transition from crystal phase to nematic liquid crystal phase (Cr→Nem). On further heating, the second weak peak at 191 °C (ΔH = 5.0 Jg^{-1}) corresponds to the transition from the nematic phase to the isotropic liquid phase. On cooling, the DSC trace shows three peaks at 194 °C (ΔH = 8.4 Jg^{-1}), 180 °C (ΔH = 7.6 Jg^{-1}) and 166 °C (ΔH = 34.4 Jg^{-1}) which can be associated respectively to the Iso→Nem, Nem→SmA and SmA→Cr transitions.

It can be noticed that the SmA mesophase is only observed on cooling (monotropic mesophase) and can exist due to the large hysteresis between the temperature of crystallization (166 °C) and of melting (182 °C).

The thermal behavoirs of **BPB** are summerized in *Table 3.1*.

		T (°C)	**ΔH(J g^{-1})**	**Transition**	**T (°C)**	**ΔH(J g^{-1})**	**Transition**	**T (°C)**	**ΔH(J g^{-1})**	**Transition**
BPB	**Heating**	182	38.1	Cr→Nem	--	--	--	191	5.0	Nem →Iso
	Cooling	166	34.4	SmA→Cr	180	7.6	Nem→SmA	194	8.4	Iso→Nem

Crystalline phase (Cr), Smectic A phase (SmA), Nemetic phase (Nem), Isotropic liquid phase (Iso).

*Table 3.1 Phase transition temperatures and enthalpy changes of **BPB**.*

3.3.2 DSC and POM of dyad BP

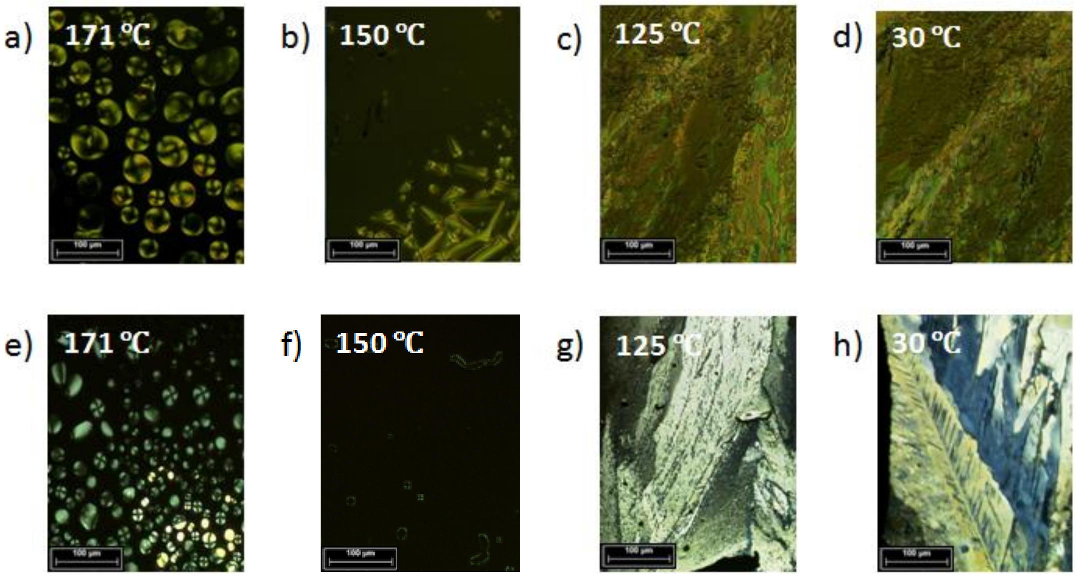

*Figure 3.15 POM microphotographs (under crossed polarizer) of **BP**. POM microphotographs obtained upon cooling: a-d) the optical textures of **BP** at 173 °C, 150 °C, 125 °C and 30 °C respectively on clean glass substrates; e-h) the optical textures of **BP** at 171 °C, 150 °C, 125 °C and 30 °C respectively on OTS treated glass substrates.*

The dyad **BP** was also studied by POM on clean glass substrates, and the observed optical textures are given in *Figure 3.15 a-d*. Under crossed polarizers upon cooling from isotropic phase a birefringent schlieren texture appeared at 171°C suggesting the presence of a nematic phase (*Figure*

3.15 a). On further cooling, a fan-shape focal-conic texture was observed at 150 °C (*Figure 3.15 b*) which corresponding to the transition from nematic phase to a more ordered lamellar mesophase. When cooled to 125 °C, another phase transition to a crystal phase quickly appeared (*Figure 3.15 c*). Then, the crystalline optical texture was maintained unchanged until room temperature as shown in *Figure 3.15 d*.

In order to investigate more precisely the mesophase nature, the same study was performed on OTS treated glass substrates (*Figure 3.14 e-h*). On cooling, the first transition appears at 171 °C and the POM images also show a schlieren texture. Then at 150 °C, a mainly homeotropic texture was observed with some very small residual birefringent domains corresponding to the presence of an untitled lamellar smectic A-like mesophase with an homeotropic orientation. On cooling then to room temperature, the sudden reappearance of a birefregent texture at 125 °C clearly suggests the formation of the crystal phase (*Figure 3.15 g*). On further cooling, on OTS substrates, the birefringent crystalline texture was also maintained unchanged until room temperature, as shown in *Figure 3.15 h*.

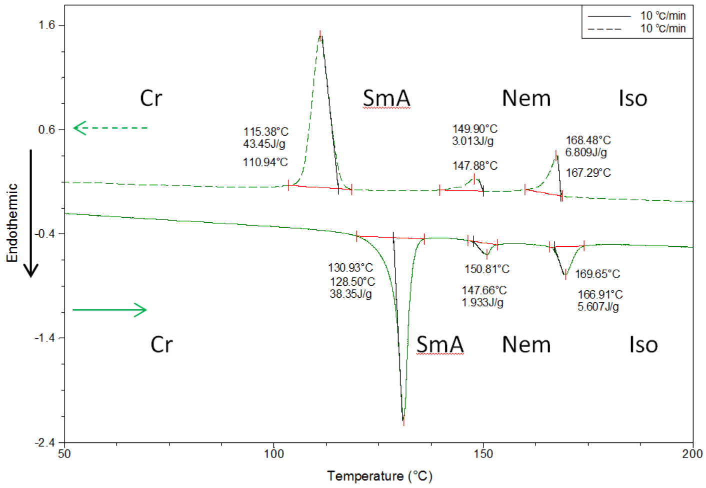

Figure 3.16 DSC thermogram of ***BP****.*

The DSC traces of BP on second heating and second cooling recorded with a rate of 10 °C/min present several transitions (*Figure 3.16*). On heating until 200 °C, three endothermic peaks are observed: at 131 °C (ΔH = 38.4 Jg^{-1}), 148 °C (ΔH = 1.9 Jg^{-1}) and 167 °C (ΔH = 5.6 Jg^{-1}). Regarding the DSC trace on cooling from the isotropic state, the first transition at 168 °C associated to a small enthalpy (ΔH = 6.8 Jg^{-1}) is consistent with the appearance of the birefrigent texture of nematic phase observed by POM. Upon further cooling, at 150 °C, the second transition with a smaller enthalpy (ΔH = 3.0 Jg^{-1}) is attributed to the transition to the smectic A phase. At 115 °C, the third transition with a higher enthalpy (ΔH = 43.5 Jg^{-1}) is observed and corresponds to the phase transition from smectic A phase to crystal phase. It is worth mentioning that the temperature of phase transition by DSC is not exactly as that observed by POM. This maybe due to the difference of cooling rates between the two methods.

		T (°C)	ΔH(J g^{-1})	Transition	T (°C)	ΔH(J g^{-1})	Transition	T (°C)	ΔH(J g^{-1})	Transition
BP	**Heating**	131	38.4	Cr→SmA	148	1.9	SmA→Nem	167	5.6	Nem →Iso
	Cooling	115	43.5	SmA→Cr	150	3.0	Nem→SmA	168	6.8	Iso→Nem

Crystalline phase (Cr), Smectic A phase (SmA), Nemetic phase (Nem), Isotropic liquid phase (Iso).

Table 3.2 Phase transition temperatures and enthalpy changes of ***BP****.*

Based on DSC and POM studies, the polymorphism can be refined and the following phase sequence Iso→Nem→SmA→Cr can be proposed (on cooling). A summary of the mesomorphic properties of **BP** is presented in *Table 3.2*.

3.4 Self-organization study (X-ray diffraction and Atomic force microscopy)

In this paragraph, the **BPB** and **BP** are analyzed by temperature dependent X-ray diffraction (XRD) and Atomic force microscopy (AFM) to study their self-organization properties. The XRD measurements were carried out in collaboration with Dr. B. Heinrich at Institut de Physique et de Chimie des Matériaux de Strasbourg (IPCMS).

3.4.1 XRD of BPB

The *Figure 3.17* gives the X-ray patterns of the **BPB** recorded on cooling from the isotropic state at 185 °C, at 175 °C and at 20 °C.

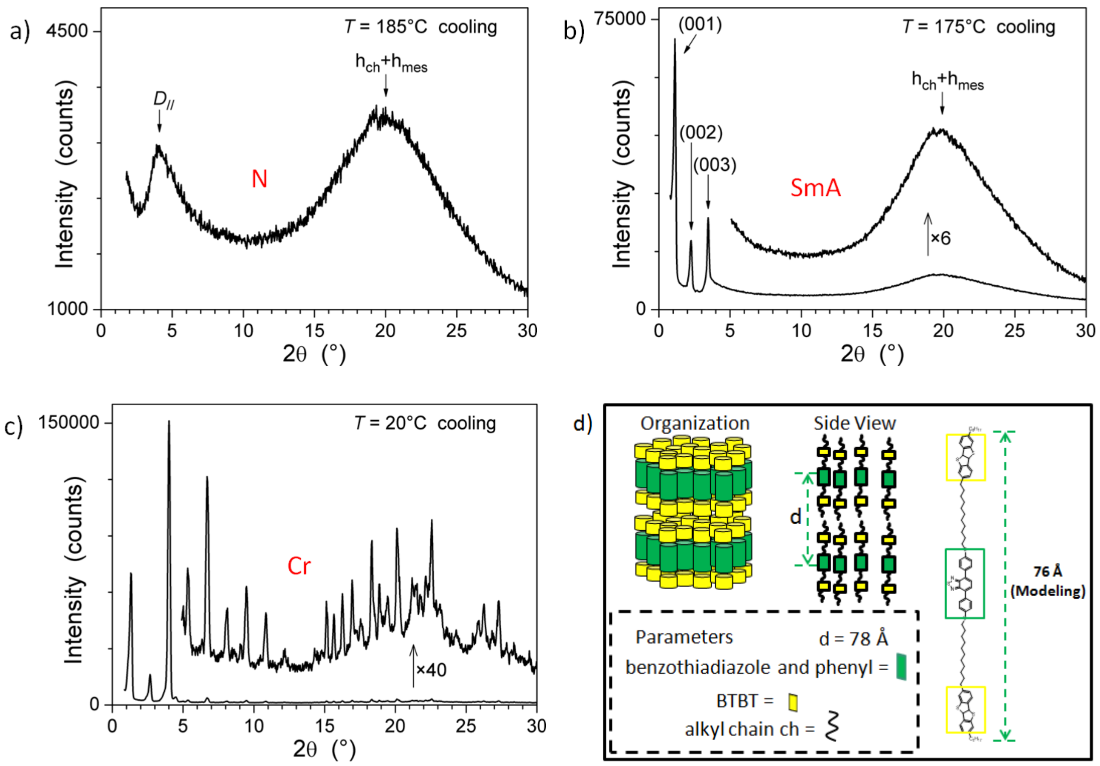

Figure 3.17 X-ray diffraction patterns of triad ***BPB****: a) 185 °C on cooling; b) 120 °C on cooling; c) 20 °C on cooling; d) Schematic representation of the multi-segregated lamellae and a molecular modeling.*

The pattern at 185 °C, typical of nematic phase, presents a broadened reflection in the small-angle region and a diffuse halo in the wide-angle region (*Figure 3.17 a*). The average distance d evaluated from the broadened reflection in the small-angle region can be calculated at 21.6 Å ($D_{//}$) in using the Bragg's law: $\lambda = 2d \sin \theta$, where λ is the wavelength of incident X-ray and θ is the angle incidence. This value corresponds to the average distance between layers of lamellar sibotactic domains of undifferentiated calamitic units. In the wide-angle region, the very broad halo centered at 4.5 Å ($h_{ch}+h_{mes}$) indicates the molten state of the alkyl chains and the average distance of the aromatic cores in the non well defined layers.

On further cooling above the transition at 180 °C detected by DSC, we can observe in the X-ray pattern a significant self-organization enhancement of the lamellar arrangement characterized by the presence of three sharp reflections with a d-spacing ratio of 3:2:1 in the small-angle region and a diffuse halos in the wide-angle region (*Figure 3.17 b*). The small-angle reflections can be assigned to (001), (002) and (003) reflections and indicate clearly that the molecules are arranged in a lamellar fashion with a long correlation distance. The repeat distances d associated with these reflections can be calculated at 78 Å. These results are typical of a lamellar mesophase SmA-like, consisting on an alternate superposition of one layer of fluorescent derivatives and one bilayer of BTBT. That description is also consistent with the homotropic texture (black texture) observed between OTS glass slides by POM under crossed polarizers at 180 °C.

On further cooling from the SmA phase, the pattern at 20°C shows a variety of sharp reflections suggesting a three-dimensional crystal lattice and the crystallization of **BPB** (*Figure 3.17 c*). At this temperature, there is still a very slight disorder in the structure due to residual diffusion scattering of partially melted alkyl chain features that can be observed in addition to sharp reflections in the wide-angle region.

Based on previous observations, a schematic representation of the **BPB** molecular arrangement is presented in *Figure 3.17 d*. The organization of **BPB** can be described as a multi-lamellar structure consisting of alternating superposition of BTBT and fluorescent derivative sublayers.

3.4.2 XRD of BP

The typical X-ray patterns of **BP** recorded on cooling from the isotropic state at 160 °C, at 140 °C and at 20 °C are given in *Figure 3.18.*

Similary with the triad **BPB**, the X-ray pattern recorded at 160 °C on cooling for the dyad **BP** (*Figure 3.18 a*) presents a broadened reflection in the small-angle region and a diffuse halo in the wide-angle region centered at 4.5 Å ($h_{ch} + h_{mes}$). This pattern is characteristic of a nematic mesophase presenting a very local lamellar organization with an interlamellar distance around 23.3 Å ($D_{//}$) between layers of undifferentiated calamitic units.

The X-ray pattern at 140 °C shows a significant self-organization enhancement of the lamellar arrangement as evidence by the presence of two small-angle reflections (*Figure 3.18 b*). These two sharp reflections with a d-spacing ratio of 2:1 correspond to (001) and (002) reflections and are characteristic of a disordered layered mesophase SmA-like with a lamellar periodicity d = 55 Å. This is consistent with the homotropic texture (black) observed by POM between OTS slides under crossed polarizers at the same temperature. The molecular arrangement of this SmA mesophase consists on an alternate superposition of one layer of fluorescent derivatives and one layer of BTBT.

The X-ray pattern recorded upon further cooling to room temperature in the crystalline phase of dyad **BP** (*Figure 3.18 c*) presents also several equidistant reflections in the small angle region indicating the lamellar organization of the crystal. However, the observation of broadened small-angle reflections and several very broad reflections in the wide-angle region indicates the presence of a small size of crystallites with a high degree of structural disorder and consequently, a low crystallinity of the material.

A schematic representation of **BP** molecular arrangement is given in *Figure 3.18 d.* The organization is typical of a multi-segregated lamellar structure consisting of an alternate superposition of BTBT and fluorescent derivative sublayers.

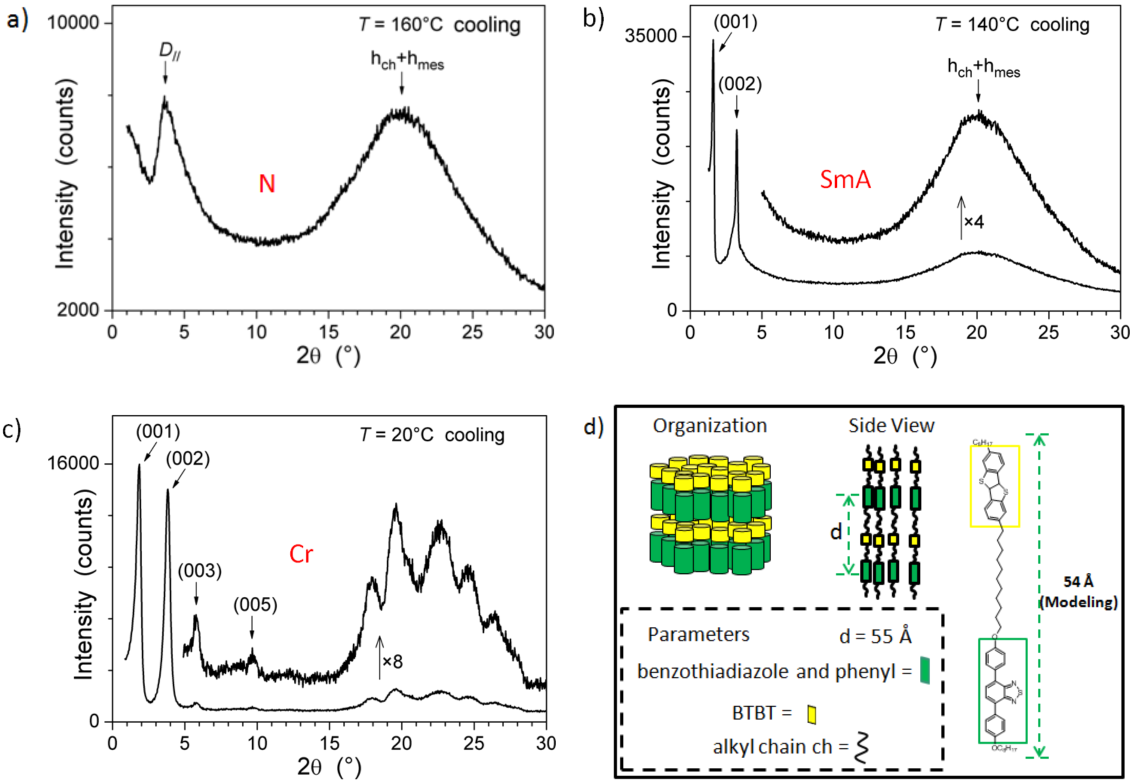

*Figure 3.18 X-ray diffraction patterns of triad **BP**: a) 160 °C on heating; b) 140 °C on cooling; c) 20 °C on cooling; d) Schematic representation of the multi-segregated lamellae and a molecular modeling.*

3.4.3 AFM of BPB and BP

The thin film morphologies on surfaces of the **BPB** and **BP** were studied by tapping mode Atomic Force Microscopy (AFM). These measurements were carried out at the Institut des NanoSciences de Paris (INSP) in collaboration with Dr. E. Lacaze and Ms. Xiao Liu (PhD IPCM/INSP).

The **BPB** film was prepared on a OTS treated silicon wafer by melt processing [171] and the typical AFM image of the **BPB** film is shown in *Figure 3.19*. As shown in *Figure 3.19 a* and *Figure 3.19 b*, the AFM topography and 3D images show a nanostructured film with steps indicating an extended flat sheet oriented parallel to the surface of the substrate. The height of the terraces determined from the topographical images is approximately 7 nm, or multiples of 7 nm, as shown in *Figure 3.19 c* and *Figure 3.19 d*. This is in good agreement with the lamellar periodicity (d = 78 Å) previously measured by small angle X-ray diffraction in bulk.

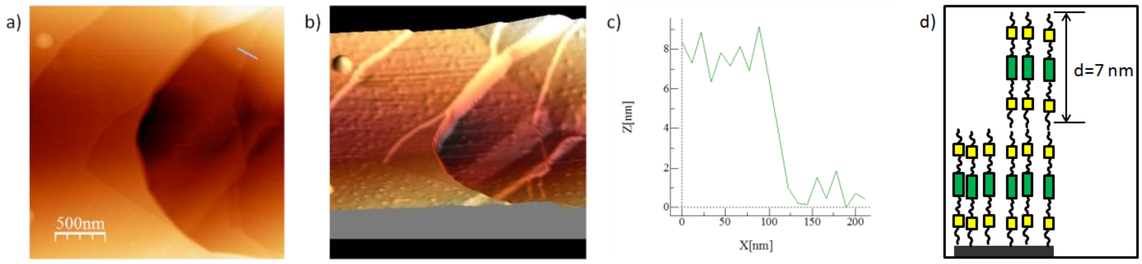

*Figure 3.19 The AFM images of **BPB** thin film on OTS substrate: a) Topography; b) 3D image of terrace structure; c) Terrace step profile of film determined from topography image; d) Schematic representation of film terrace structure of **BPB**.*

A film of **BP** was also prepared by melt-processing between OTS substrate and cover glass. The AFM study of this sample shows that a nanostructured film with terraces could be also observed (*Figure 3.20 a* and *Figure 3.20 b*). The heights of the terraces determined from topography images were about 5.5 nm, as shown in *Figure 3.20 c*. These values are well consistent with inter lamellar distance ***d*** around 55 Å measured from X-ray patterns of **BP** in SmA mesophase (*Figure 3.18*).

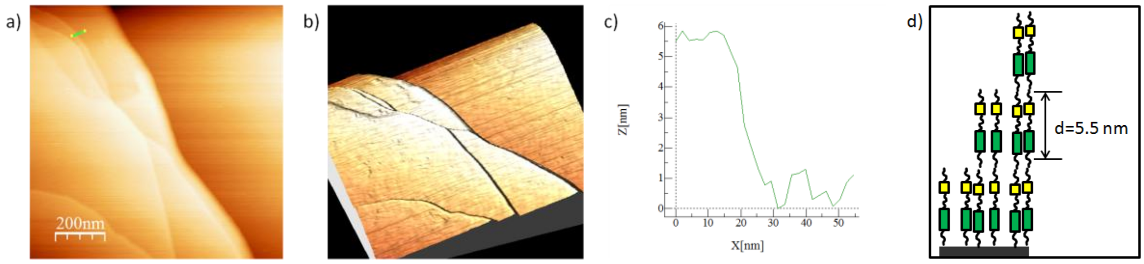

*Figure 3.20 The AFM images of **BP** thin film on OTS substrate: a) Topography; b) 3D image of terrace structure; c) Terrace step profile of film determined from topography image; d) Schematic representation of film terrace structure of **BP**.*

These observations indicate that well defined multi-lamellar organizations of triad **BPB** and dyad **BP** can be obtained in thin films after melt-processing and that for both derivatives, layers can be oriented parallel to the substrate.

3.5 Charge Transport Properties

The charge transport properties of **BPB** and **BP** material were studied by temperature-dependent time-of-flight (TOF) technique in the crystal phase. These measurements were carried out at Kyushu University (OPERA, Japan), in collaboration with the Prof. J.-C. Ribierre. The devices fabrication is described in the experimental part Paragraph 3.7.3.

The bulk charge transport properties of **BPB** and **BP** were characterized following the same procedure as described in the previous chapter for **C10-PBT**: 9 μm thick **BPB** or **BP** films (sandwiched between two ITO electrodes) were excited by laser nanosecond pulses at 337 nm, where the sample strongly absorbs light. The *Figure 3.21* shows typical transient photocurrents obtained in the crystal phase of **BPB** and **BP** for hole and electron transport at 85 °C and 100 °C, respectively.

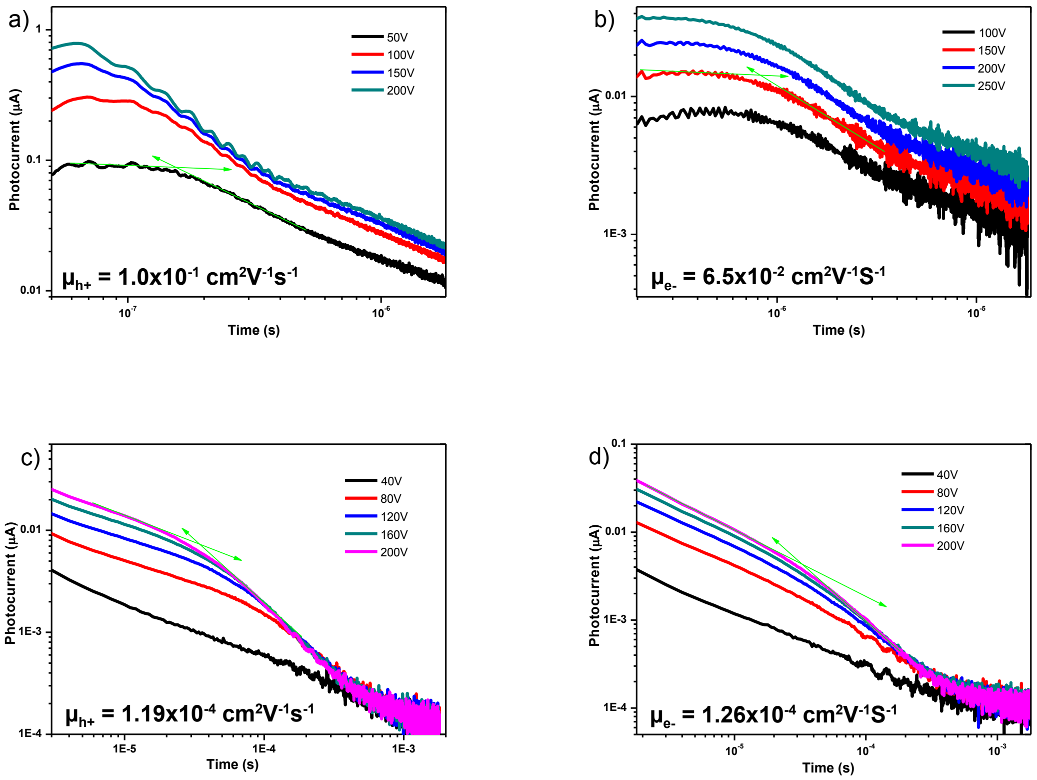

*Figure 3.21 Transient photocurrent curves recorded on cooling in a bulk sample in the crystal phase a) hole mobility of **BPB** at 85 °C; b) electron mobility of **BPB** at 85 °C; c) hole mobility of **BP** at 100 °C; d) electron mobility of **BP** at 100 °C.*

As mentioned in Chapter 2, the hole/electron mobility (μ) is calculated using the standard equation $\mu = d / \tau E$. From this equation, high mobilities of 1.0 x 10^{-1} cm^{2} V^{-1} s^{-1} for holes and 6.5 x 10^{-2} cm^{2} V^{-1} s^{-1} for electrons were extracted for the triad **BPB**. Regarding the dyad **BP**, lower hole (1.2 x 10^{-4} cm^{2} V^{-1} s^{-1}) and electron (1.26 x 10^{-4} cm^{2} V^{-1} s^{-1}) mobilities were calculated that they are balanced. This difference of mobility values about two or three orders of magnitude is consistent with the lower crystallinity of dyad **BP** in the crystalline state observed by X-ray diffraction on cooling from the isotropic state (broadened reflections in the small and wide-angle regions of X-ray pattern). The presence of many grain boundaries and structural disorder in bulk generates many traps for charge carriers, highly detrimental for the charge transport properties.

3.6 Conclusions

In this chapter, a novel set of materials consisting of linear triad **BPB** and dyad **BP**, based on benzothiadiazoldiphenyl (BTP) and benzothienothiophene (BTBT) derivatives, were designed, synthesized and characterized.

The photophysical properties study indicated that these compounds can present high luminescence properties, with a yellow-green emission and PLQYs in solution as high as 59% and 64% for **BPB** and **BP**, respectively.

These compounds also exhibit liquid crystalline properties on heating and cooling as demonstrated by DSC and POM. The structural study indicated that these materials present a multi-lamellar organization consisting of alternating layers of BTP and BTBT units, and that this arrangement remains at room temperature, as evidenced by XRD.

The film morphology studied by AFM showed clearly the presence of nanostructured thin films with terraces structures and evidences that it is possible to orient layers of these fluorescent complex molecular architectures parallel to the substrate surface. This is a promising property in the domain of organic transistors where 2D orientation is one of the key parameters for the fabrication of high performance transistors.

Finally, the charge transport properties were investigated by time-of-flight measurements. As a preliminary results, a relatively high hole transport mobility of 1×10^{-1} cm^2 V^{-1} s^{-1} and electron transport mobility of 6.5×10^{-2} cm^2 V^{-1} s^{-1} in crystal state was obtained for the triad **BPB**. Regarding the dyad **BP**, lower but balanced mobilities ($\mu_{h+} = 1.19 \times 10^{-4}$ cm^2 V^{-1} s^{-1} and $\mu_{e-} = 1.26 \times 10^{-4}$ cm^2 V^{-1} s^{-1}) in crystal state were obtained due to the lower material crystallinity, as evidenced by XRD.

To conclude, this family of self-organized, orientable and highly fluorescent semiconductors was prepared by this design strategy. Both molecules can be considered as interesting and promising candidates in the field of organic electronics and photonics, for example, for the fabrication of organic light-emitting devices such as light-emitting diodes or transistors (OLEDs/OLETs).

3.7 Experimental

3.7.1 Materials and methods

Some starting materials have been mentioned in Chapter 2 and other starting materials were needed to synthesize this new set: 4-methoxybenzene boronic acid, potassium fluoride, caesium carbonate, tetrabutylammonium bromide, hydrobromic acid (33% in HOAc), sodium hydroxide, hydrochloric acid, sodium hydrosulfide hydrate, ammonium chloride, aluminum chloride, octyl acid chloride, lithium aluminum hydride, 11-bromoundecanoic acid, thionyl chloride, sodium chloride, 1-bromooctane, 1-methyl-2-pyrrolidone and potassium iodide were purchased from Aldrich, Alfa and Acros or TCI and used without any further purification. The solvents ethyl ethanoate, chloroform, cyclohexane were purchased from VWR Chemicals. The solvents for recrystallization and precipitation were purchased from Aldrich or distilled before using and column chromatography was performed on silica gel.

^{1}H- and ^{13}C NMR spectra were recorded on Bruker AC 300, 400 and 600 spectrometers (300 MHz, 400 MHz and 600 MHz) using the signal of Tetramethylsilane (TMS) or the carbon signal of the deuterated solvents as internal standard, and the chemical shift are reported in ppm. Abbreviations used for splitting patterns are s = singlet, d = doublet, t = triplet, q = quintet, m = multiplet. The UV/vis spectra were taken on a spectrometer of Varian Cary 300 scan spectrometer, using 100 mm quarts cuvette, and the fluorescence spectrum was recorded on a Varian Cary Eclipse spectrofluorimeter. The PLQY measurements in films were performed using an integrating sphere system coupled with a photonic multichannel analyser (Hamamatsu Photonics C9920-02, PMA-11) under a flowing nitrogen atmosphere. DSC measurement was performed on an Instrument DSC Q2000 V24.4 Build 116, using the Module DSC Standard Cell RC. Phase transitions (POM) were examined by a Leica microscope of Linkam TMS 94 with a Linkam LTS temperature-controlled hot stage and Nikon LWD 0.65 camera. The elementary analysis was examined in the Service de Microanalyse ICSN-CNRS (France) and in Service Central d'Analyse isa (France). The SAXS measurement was carried out in the Institut de Physique et de Chimie des Matériaux de Strasbourg (IPCMS) and the patterns were obtained with a transmission Guinier-like geometry. A linear focalized monochromatic Cu Kα1 beam (λ = 1.5405 Å) was obtained using a sealed-tube generator (600 W) equipped with a bent quartz monochromator. In all cases, the crude powder was filled in Lindemann capillaries of 1 mm diameter and 10 μm wall-thickness. The diffraction patterns were recorded with a curved Inel CPS120 counter gas-filled detector linked to a data acquisition computer (periodicities up to 90 Å) and on image plates scanned by STORM 820 from Molecular Dynamics with 50 μm resolution (periodicities up to 120 Å). The sample temperature was controlled within ± 0.01 °C and typical exposure times were of 6 h.

3.7.2 Synthesis

3.7.2.1 Synthesis of precursory building blocks (terthiophene and perylene building blocks)

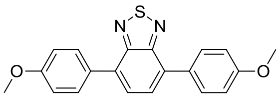

Chemical Formula: $C_{20}H_{16}N_2O_2S$
Molecular Weight: 348.418
3A

4,7-bis(4-methoxyphenyl)benzo[c][1,2,5]thiadiazole (3A): To a mixture of **2E** (750 mg, 2.54 mmol), 4-methoxybenzene boronic acid (850 mg, 5.59 mmol), KF (12 mg, 2 mmol) and $Pd(PPh_3)_4$ (19 mg, 0.08 mmol) in a degassed mixture of toluene (40 mL) and H_2O (7 mL), Cs_2CO_3 (2.48 g, 7.62 mmol) was added. The reaction mixture was heated to reflux and this temperature was maintained for 12 h under intensive stirring. After being cooled to room temperature, EtOAc (3 × 50 mL) was added. The organic layer was separated, washed with water and dried over anhydrous $MgSO_4$. After evaporation of the solvent in vacuo, a black yellow solid was obtained which was purified by chromatography (chlorofum : petroleum ether = 2 : 1) to produce pure product as yellow solid (622 mg). Yield, 70%. NMR δH (ppm) (300 MHz, $CDCl_3$) 7.95 (d, 4H), 7.73 (s, 2H), 7.10 (d, 4H), 3.90 (s, 6H).

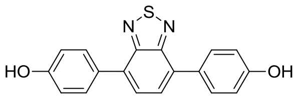

Chemical Formula: $C_{18}H_{12}N_2O_2S$
Molecular Weight: 320.365
3B

4,4'-(benzo[c][1,2,5]thiadiazole-4,7-diyl)diphenol(3B): **3A** (300 mg, 0.86 mmol) and tetrabutylammonium bromide (277 mg, 0.86 mmol) were added to a 50 mL flask, and HBr (33% in HOAc, 10 mL) was added. The mixture was heated for 24 h at 100 °C, then cooled to room temperature, water (100 mL) was added. The mixture was extracted with ethyl acetate (3 × 100 mL), and then organic solution was neutralized with NaOH (aq) and dilute HCl (aq) in sequence. The organic solution was collected, dried over anhydrous $MgSO_4$, then the solvent was evaporated in vacuo, the residue was purified by chromatography (petroleum ether:ethyl acetate = 3:1) to produce pure product as yellow solid (193 mg). Yield, 70%. NMR δH (ppm) (300 MHz, $CDCl_3$) 7.90 (d, 4H), 7.72 (s, 2H), 7.03 (d, 4H), 4.90 (s, 2H).

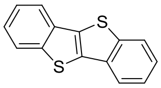

Chemical Formula: $C_{14}H_8S_2$
Molecular Weight: 240.343
3D

Benzo[b]benzo[4,5]thieno[2,3-d]thiophene (3D): To a solution of 3C (5 g, 36 mmol) in 100 mL

NMP was added sodium hydrosulfide hydrate (NaSH•xH_2O, 4.6 g, 92 mmol) at 80 °C and stirred for one hour. Then, the temperature was increased to 155 °C. The mixture was stirred for 3 days at the same temperature, and then it was poured into saturated aqueous ammonium chloride solution (50 mL) and cooled with an ice-bath. The resulting precipitate was collected by filtration and and washed with water and acetone. The precipitate was dissolved in chloroform. The solution was extracted with a large quantity of chloroform. The combined extract was washed with water, dried over anhydrous $MgSO_4$ and concentrated under reduce pressure to get a crude BTBT, which was further purified by recrystallization from chloroform to pure BTBT as a white solid (1.26 g). Yield, 30%. NMR δH (ppm) (300 MHz, $CDCl_3$) 7.95-7.87 (qdq, 4H), 7.51-7.37 (m, 4H).

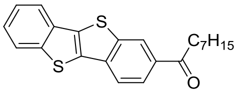

Chemical Formula: $C_{22}H_{22}OS_2$
Molecular Weight: 366.539
3E

1-(benzo[b]benzo[4,5]thieno[2,3-d]thiophen-2-yl)octan-1-one (3E): Under argon, **3D** (4.4 g, 18.3 mmol) was disolved in anhydrous DCM (220 mL) at room temperature, followed by an addition of aluminum chloride (6.1 g, 45.75 mmol) at -10 °C. The solution was cooled down to -78 °C and octyl acid chloride (4 ml, 20.14 mmol) was dropwise added, the mixture being stirred for 1h. After one more night at room temperature, the reaction mixture was cooled down to 0 ºC, quenched with ice water (30 mL), and diluted with cold methanol to give a precipitate. The precipitate was filtered and an extraction followed with chloroform. The organic phase was washed with brine, dried over anhydrous $MgSO_4$ and concentrated under reduced pressure to give a crude product, which was further purified by silica gel column chromatography (chloroform /cyclohexane, 3/1 as eluent). A white solid was obtained after being dried under vacuum (5.1 g). Yield, 77%. NMR δH (ppm) (300 MHz, $CDCl_3$) 8.59 (dd, 2H), 8.07-7.91 (m, 4H), 7.52-7.42 (m, 2H), 3.06 (t, 2H), 1.80 (t, 2H), 1.43-1.31 (m, 8H), 0.90 (t, 3H).

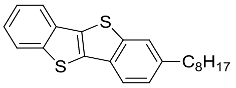

Chemical Formula: $C_{22}H_{24}S_2$
Molecular Weight: 352.556
3F

2-octylbenzo[b]benzo[4,5]thieno[2,3-d]thiophene (3F): In an atmosphere of argon, lithium aluminium hydride (34 ml, 1M in Et_2O, 34.5 mmol) was added to a suspension of aluminum chloride (4.6 g, 34.5 mmol, in anhydrous Et_2O) at ambient temperature. To this mixture, a solution of **3E** (5 g, 13.6 mmol) in 400.0 mL dried DCM was slowly added dropply and then stirred at room temperature overnight. The reaction was quenched by ice water at 0°C before 1 M HCl was added until an acidic pH (≤ 7) was achieved. The mixture was extracted with chloroform. The organic phase was washed with water (3 × 100 mL), dried over $MgSO_4$ and concentrated under vacuum to give a white solid (4.6

g). Yield, 96%. NMR δH (ppm) (300 MHz, $CDCl_3$) 7.92-7.72 (m, 4H), 7.47-7.27 (m, 3H), 2.76 (t, 2H), 1.70 (t, 2H), 1.34-1.28 (m, 10H), 0.89 (t, 3H).

$BrC_{10}H_{20}COOCl$

Chemical Formula: $C_{11}H_{20}BrClO_2$
Molecular Weight: 299.632
3H

11-bromoundecanoic hypochlorous anhydride (3H): 11-bromoundecanoic acid (10 g, 37.7 mmol) and thionyl chloride (8.97 g, 75.4 mmol) were mixed into a round flask under argon, and then the mixture was stirred overnight at room temperature. The excess thionyl chloride and other impurities were removed under reduce pressure, and then a brown liquid (10.51 g) was isolated for next step without further purification.

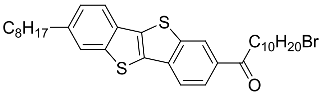

Chemical Formula: $C_{33}H_{43}BrOS_2$
Molecular Weight: 599.728
3I

11-bromo-1-(7-octylbenzo[b]benzo[4,5]thieno[2,3-d]thiophen-2-yl)undecan-1-one (3I): To a solution of **3F** (4.6 g, 13 mmol) in anhydrous DCM (250 mL) was added aluminum chloride (1.7 g, 13 mmol) at -10 °C under argon. After 20 minutes, the reaction was cooled down to -78 °C, followed by a dropwise addition of **3H** (4 g, 13 mmol). After one hour, the reaction was stirred at ambient temperature overnight. The mixture was quenched by ice-water at 0 °C, and then was extracted with DCM. The organic phase was washed with water (3 × 50 mL), dried over $MgSO_4$ and concentrated under reduced pressure. The crude product was purified through two successive silica gel column chromatography using DCM/cyclohexane (1/1) and DCM/ethyl acetate (4/1) as eluents respectively, to obtain a white solid (5.5 g). Yield, 87 %. NMR δH (ppm) (300 MHz, $CDCl_3$) 8.53 (d, 1H), 8.06 (d, 1H), 7.92-7.66 (m, 3H), 7.30 (dd, 1H), 3.41 (t, 2H), 3.05 (t, 2H), 2.85-2.60 (m, 2H), 1.82 (dt, 6H), 1.29 (m, 24H), 0.88 (t, 3H).

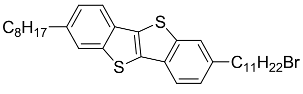

Chemical Formula: $C_{33}H_{45}BrS_2$
Molecular Weight: 585.744
3J

2-(11-bromoundecyl)-7-octylbenzo[b]benzo[4,5]thieno[2,3-d]thiophene (3J): A suspension of aluminum chloride (3.68 g, 27.6 mmol) in dried Et_2O (50 mL) was prepared at room temperature under argon, followed by the dropwise addition of lithium aluminium hydride (23 mL, 1M in Et_2O). A solution of **3I** (5.5 g, 9.2 mmol) in 500.0 mL anhydrous DCM was added to the precedent mixture by dropping funnel, and then the mixture was stirred one night. The reaction was quenched by ice-water at 0 °C, and the pH was adjusted by HCl (1M in water) until acidic state. The crude product was extracted with chloroform. The organic phase was washed with brine (3 × 100 mL), dried over $MgSO_4$ and concentrated under reduced pressure to get a white solid (5 g). Yield, 94%. NMR δH (ppm) (300 MHz, $CDCl_3$) 7.92-7.61 (m, 4H), 7.29 (d, 1H), 7.25 (d, 1H), 3.40 (t, 2H), 2.76 (t, 4H), 1.83 (dd, 2H), 1.68 (dd, 2H), 1.30 (m, 24H), 0.89 (t, 3H).

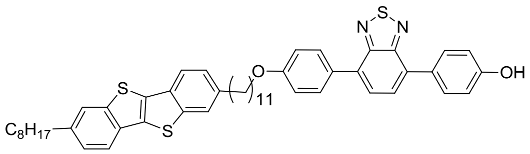

Chemical Formula: $C_{51}H_{58}N_2O_2S_3$
Molecular Weight: 825.198
3K

4-(7-(4-((11-(7-octyl-4b,9b-dihydrobenzo[b]benzo[4,5]thieno[2,3-d]thiophen-2 yl)undecyl)oxy)phenyl)benzo[c][1,2,5]thiadiazol-4-yl)phenol (3K): 3B (60 mg, 0.19 mmol) and 3J (60 mg, 0.1 mmol) were disolved in anhydrous DMF (10 mL), and K_2CO_3 (52 mg, 0.38 mmol) was added. The mixture was heated at 120 °C overenight. Then the mixture was cooled to room temperature. The crude product was extracted with DCM and EtOAc. The organic phase was washed with water (3 × 50 mL), dried over $MgSO_4$ and concentrated under reduced pressure. The crude product was purified through a silica gel column chromatography using DCM as eluent, to obtain a yellow solid (25 mg). Yield, 30 %. NMR δH (ppm) (300 MHz, $CDCl_3$) 7.92-7.87 (m, 4H), 7.77-7.71 (m, 6H), 7.08-6.99 (q, 4H), 4.97 (s, 1H), 4.04 (t, 2H), 2.75 (t, 4H), 1.82 (m, 2H), 1.69 (m, 4H), 1.69 (m, 24H), 0.88 (t, 3H).

3.7.2.2 Synthesis of BPB

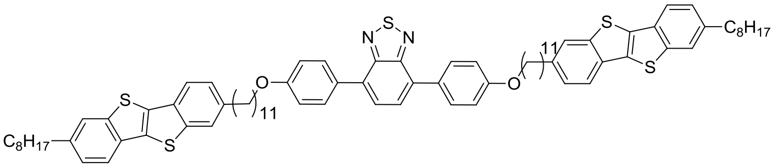

Chemical Formula: $C_{84}H_{104}N_2O_2S_5$
Molecular Weight: 1330.03
BPB

BPB: In a 25 mL microwave reactor vial, 3B (36 mg, 0.11 mmol) and 3J (200 mg, 0.34 mmol) were disolved in anhydrous DMF (10 mL), and Cs_2CO_3 (76 mg, 0.55 mmol) was added. The mixture was heated at 120 °C for 20 min. Then the crude product was washed with DCM, CHCl3 and EtOAc (3 × 50 mL, respectively). After recrystallization with $CHCl_3$ two times, the target molecule was prepared as a yellow solid (90 mg). Yield, 60 %. NMR δH (ppm) (600 MHz, chlorobenzene-d5, 80 °C) 7.99-7.98 (d, 4H), 7.63-7.61 (d, 4H), 7.57-7.56 (d, 6H), 7.04-7.02 (d, 4H), 3.94 (t, 4H), 2.66 (t, 8H), 1.77 (m, 4H), 1.65 (m, 8H), 1.47 (m, 4H), 1.32 (m, 44H), 0.88 (t, 6H). δC (ppm) (150 MHz, chlorobenzene-d5, 80 °C) 159.81, 154.63, 142.85, 140.16, 140.14, 132.94, 132.48, 132.42, 131.43, 131.61, 130.66, 130.16, 127.13, 123.42, 123.40, 121.13, 114.90, 68.29, 36.17, 32.02, 31.61, 29.75, 29.68, 29.63, 29.62, 29.59, 29.50, 29.40, 13.99. Elementary analysis: Calcd for C84H104N2O2S5: C 75.63, H 7.86, N 2.10; Found C 75.35, H 7.61, N 1.83.

3.7.2.3 Synthesis of BP

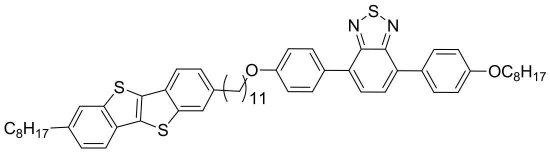

Chemical Formula: $C_{59}H_{74}N_2O_2S_3$
Molecular Weight: 937.41
BP

BP: In a 25 mL microwave reactor vial, **3K** (25 mg, 0.03 mmol) and 1-bromooctane (58 mg, 0.3 mmol) were disolved in anhydrous DMF (10 mL), and Cs_2CO_3 (98 mg, 0.3 mmol) was added. The mixture was heated at 120 °C for 20 min. After cooled to room temperature, the crude product was extracted with DCM. The organic phase was washed with water (3 × 50 mL), dried over $MgSO_4$ and concentrated under reduced pressure. The crude product was purified through a silica gel column chromatography using DCM as eluent, to obtain a yellow solid (18 mg). Yield, 65%. NMR δH (ppm) (400 MHz, $CDCl_3$) 7.93-7.90 (d, 4H), 7.77-7.71 (m, 6H), 7.08-7.06 (d, 4H), 4.07-4.02 (m, 4H), 2.78-2.73 (d, 4H), 1.83 (t, 4H), 1.70 (t, 4H), 1.31 (m, 34H), 0.88 (t, 6H). δC (ppm) (100 MHz, $CDCl_3$) 159.22, 154.12, 142.22, 139.82, 132.55, 132.37, 131.21, 130.27, 129.72, 127.38, 125.88, 123.36, 121.00, 114.59, 68.08, 36.15, 31.73, 31.62, 29.50, 29.25, 26.01, 22.61, 14.05. Elementary analysis: Calcd for $C_{59}H_{74}N_2O_2S_3$: C 75.43, H 7.94, N 2.98; Found C 75.31, H 7.63, N 2.89.

3.7.3 TOF configurations

In this chapter, the TOF measurement performed were in the basic configuration, CGL was not used. The standard liquid crystal cell was purchased from Instec Inc. with gap thickness of 9 μm and a transparent electrodes of indium tin oxide (ITO). Compounds **BPB** and **BP** powder were placed near the hole of the cell and heated to an isotropic state. The sample then flows into the cell by capillary force and the film is cooled down before using.

The sample was mounted in the TOF setup using hot stage (Instec HCS302). Sample was excited by nanosecond pulses from N_2 laser at 337 nm, where the sample strongly absorbs light and a repetition rate of 1.8 Hz. The excitation of the sample results in a transient photocurrent signal that is amplified and then recorded by a Tektronix TDS 5034 350 MHz digital oscillosco

Chapter 4 Narrow Bandgap Molecules Based on Naphthalene and Thiophene

Narrow bandgap molecules and polymers, absorbing in the near-IR range and presenting a bandgap typically smaller than 1.6 eV, are particularly attractive in organic electronic devices such as organic photovoltaics (OPVs), photodetectors (PDs), and organic field effect transistors (OFETs) [179, 180, 181]. Due to their small energy gaps, this class of materials possesses some very interesting physical properties. For instance, they can cover a broader spectrum of solar irradiation or they can allow an easier charge injection in devices [4]. As a result, the photophysics and charge transport of such materials are rather unique in organic semiconductors.

In this chapter, we will study two different naphthalene based molecules. These molecules will be designed based on acceptor units such as naphthalene diimide, benzothiadiazole and cyano groups, and donor thiophene units (*Figure 4.1*). These donor/acceptor derivatives are promising narrow bandgap candidates for n-type and/or ambipolar behavior and to be use as semiconducting layers in organic field effect transistor devices. We will describe and discuss the synthesis, photophysical and electronic properties of these compounds. Furthermore, the thermal behavior and the preliminary charge transport properties will be also studied.

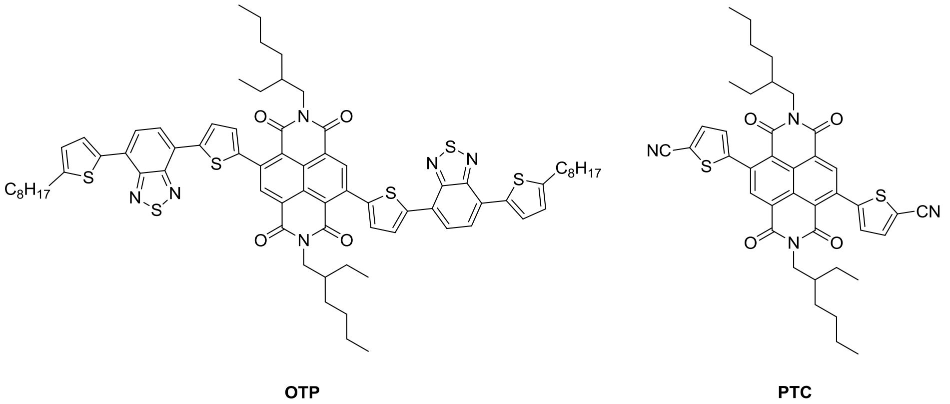

Figure 4.1 Chemical structures of narrow bandgap moleculars based on donor/acceptor π-conjugated systems.

4.1 Synthesis

4.1.1 Synthesis of precursory building blocks

For the synthesis of the two target molecules of this chapter, two building blocks are needed : the 4-(5-octylthiophen-2-yl)-7-(5-(tributylstannyl)thiophen-2-yl)benzo[c][1,2,5]thiadiazole (**4C**) and the 4,9-dibromo-2,7-bis(2-ethylhexyl)benzo[lmn][3,8]phenanthroline-1,3,6,8(2H,7H)-tetraone (**4F**). The *Figure 4.2* shows the synthetic routes of these two precursory building blocks. The compound **4C** was prepared from the starting materials **2E** already described in Chapter 2. This latter (**2E**) was first coupled with stannane octylthiophene by a Stille reaction to give the intermediate derivative **4A.** Another thiophene unit was then coupled on **4A** by Stille reaction to lead to the benzothiadiazole derivative **4B** end-capped by two thiophene units. Then, **4B** was converted into the stannane derivative **4C** by the reaction of the tributyltin chloride on the lithiated intermediate of **4B**.

In the meantime, the commercially available naphthalenetetracarboxylic dianhydride **4D** was converted into its dibromide derivative **4E** by treatment with dibromoisocyanuric acid as brominating reagent. Then, branched chains were grafted on the naphthalene core by addition of 2-ethylhexylamine on **4E** through an imidification reaction catalyzed by the acid medium, leading to the naphthalene diimide derivative **4F.**

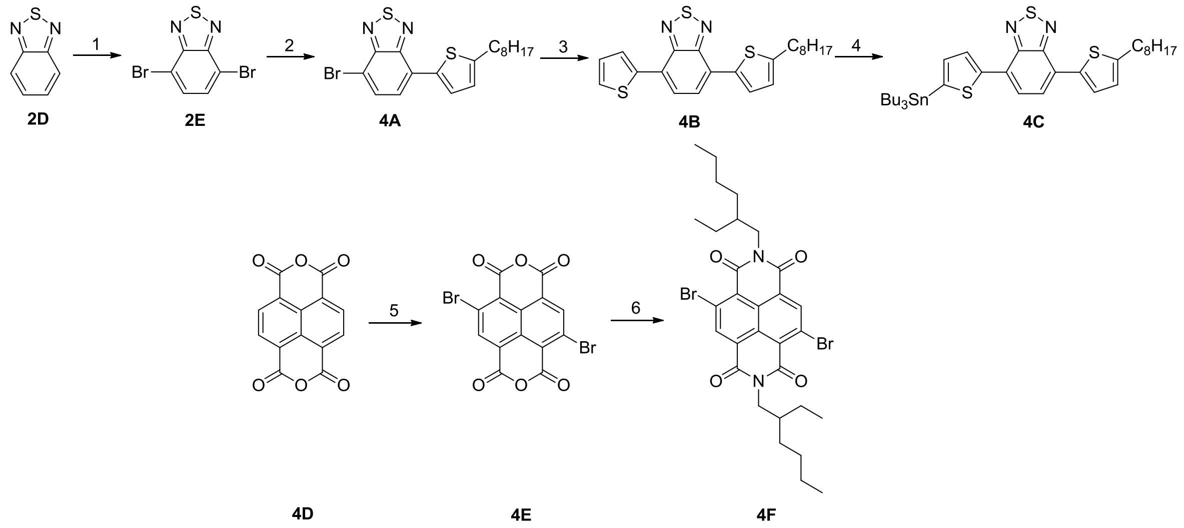

Figure 4.2 Synthetic route of building blocks. Conditions: 1) bromine, HBr (48%), reflux, 6h, 60%.; 2) tributyl-(5-octyl-thiophen-2-yl)-stannane, Pd(PPh_3)$_4$, DMF, 130 °C, overnight, 66%; 3) tributyl(thiophen-2-yl)stannane, Pd(PPh_3)$_4$, toluene, 80 °C, overnight, 75%; 4) n-butyllithium, $SnBu_3Cl$, THF, -78 °C/rt, overnight, 97% ; 5) dibromoisocyanuric acid, fuming sulphuric acid , rt, 5h, 100%; 6) 2-ethylhexylamine, 1-propionic acid, o-xylene, 130 °C, 2 h, 30%.

4.1.2 Synthesis of OTP

The synthetic route of **OTP** based on a naphthalene diimide core and benzothiadiazole moieties is given in *Figure 4.3*. This compound was prepared by a palladium-catalysed Stille coupling between the precursory building blocks **4F** and **4C** with an acceptable yield around 18%. Due to the existence of the branched chain, the **OTP** is well soluble in the usual chlorinated solvents such as dichloromethane. It can be purified on a silica-gel packed column and eluted with a 1:2 (Hex/DCM) mixture and characterized by the usual methods (NMR, Elementary analysis).

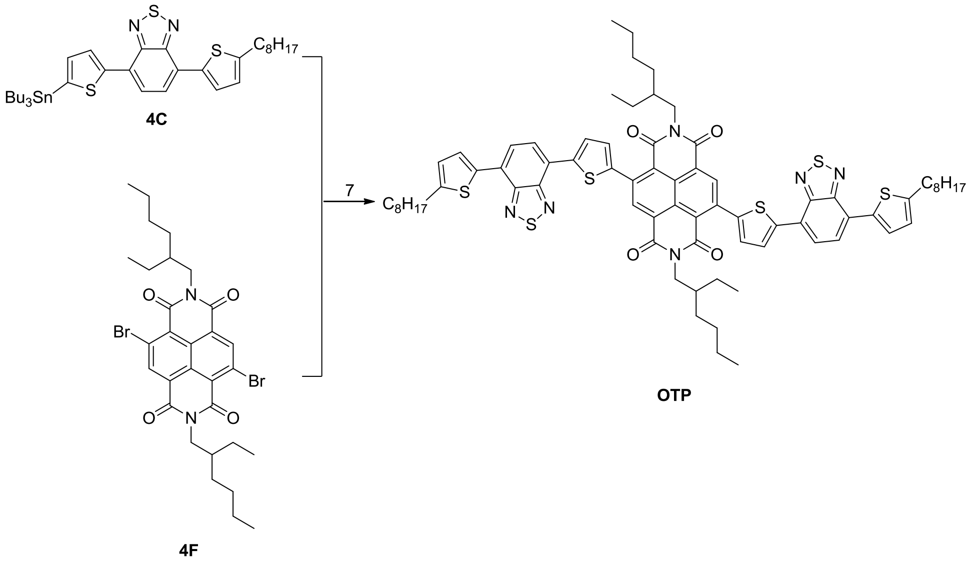

Figure 4.3 Synthetic route of ***OTP****. Conditions: 7) Pd(PPh$_3$)$_4$, DMF, 115 °C, overnight, 18%.*

4.1.3 Synthesis of PTC

The synthesis of **PTC** composed of a with naphthalene diimide core end-capped by two cyanothiophene groups is described in *Figure 4.4*. The first step of this synthesis consists on the coupling of the precursory building block **4F** with a stannane thiophene derivative through a Stille coupling reaction, leading to the intermediate compound **4G**. Then, a bromination reaction was performed with two equivalent of NBS to obtain the dibrominated derivative **4H**. Finally, the two bromide of **4H** was converted to nitrile groups to give the compound **PTC** with a good yield of 72%. This compound is well soluble in the usual organic solvents, it can be purified by chromatography on silica gel (dicholoromathe) and characterized by the usual methods (NMR, Elementary analysis, HRMS).

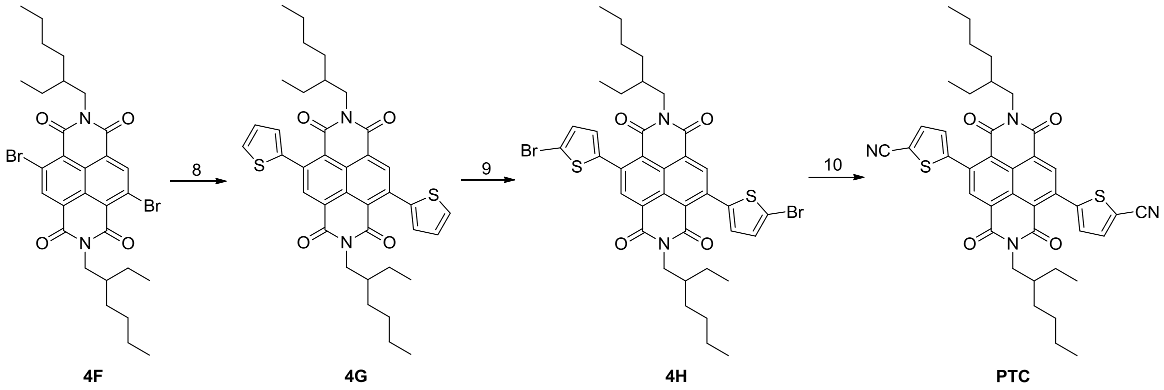

Figure 4.4 Synthetic route of ***PTC****. Conditions: 8) tributyl(thiophen-2-yl)stannane, Pd(PPh$_3$)$_4$, toluene, 105 °C, 24 h, 95%; 9) acetic acid, NBS, CHCl$_3$, 0 °C/rt, 12 h, 76%; 10) copper(I)cyanide, DMF, 140 °C, 24 h, 72%.*

The NMR spectra of the **OTP** and **PTC** are given in *Figure 4.5*. For **OTP**, the peak of protons from naphthalene diimide core shifted from 8.96 ppm to 8.89 ppm after Stille coupling reaction. A suitable ratio between the protons on thiophene rings and the protons on the phenyl rings demonstrates the success of the coupling. For **PTC**, the convertion of bromide to nitrile groups is confirmed as well by the shift of the thiophene protons from 7.17 ppm to 7.74 ppm.

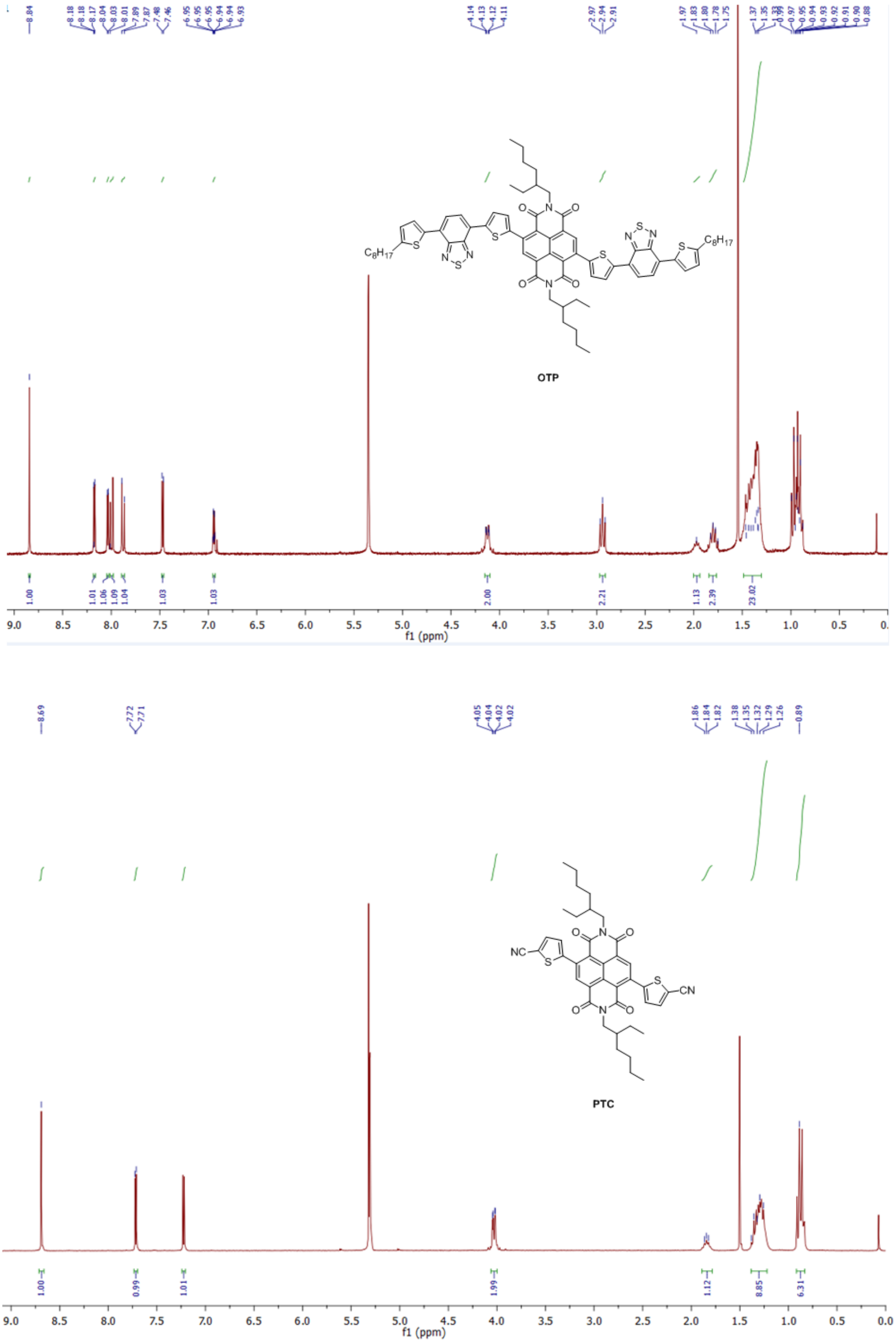

*Figure 4.5 The NMR spectrum of the **OTP** and **PTC**.*

4.2 Photophysical properties (absorption and emission)

The absorption and emission properties of this family were studied in diluted solutions (ca. 10^{-5} M). In this condition, these molecules can be considered as adequately isolated, i.e. the aggregation and the intermolecular interactions can be neglected.

4.2.1 Absorption of OTP

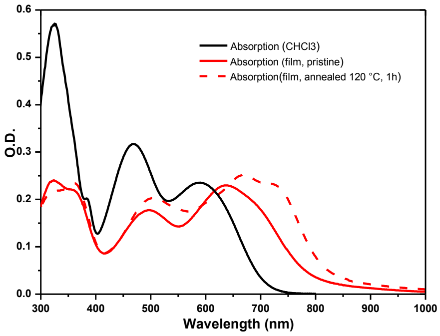

Figure 4.6 UV-Vis absorption spectra of ***OTP*** *in solution (CHCl$_3$) and film.*

The UV-Visible spectra of **OTP** in solution and in solid state are given in *Figure 4.6*. In solution, the absorption band at wavelengths shorter than 400 nm is due to the π-π* transition, while in the 400-700 nm region of the spectrum we can observe two strong intramolecular charge transfer bands from the donors to naphthalene diimide acceptor core.

In solid state, the absorption spectrum of the pristine spin-coated film shows also the π-π* transition in the 300-400 nm range and two intramolecular charge transfer bands in the 450-800 nm range. However, all these bands are broadened and red shifted as compared to that measured in solution. These observations indicate strong molecular π-π stacking interactions between the π-conjugated systems. After annealing of the film at 120 °C (1h), we can observe a broadening and a red shift of the ICT bands as compared to that in the pristine film, indicating an important change in the molecular packing.

After annealing, the absorption spectrum extends over the near-IR range and covers all the visible spectrum, which could be very attractive for photovoltaic applications. Note that no emission spectra were observed either in solution or in solid state due to very weak emission properties of this compound.

4.2.2 Absorption and emission of PTC

The absorption and emission spectra of **PTC** in dichloromethane solution were carried out and are given in *Figure 4.7*. More precisely, in solution the **PTC** molecules show three absorption bands: several π-π* transition in the 230-400 nm range and an intramolecular charge transfer band in the 400-

500 nm range. It is worth to mention here, that the absorption spectrum of this compound doesn't cover a large range of visible spectrum and stops at 500 nm. This seems to indicate a relatively large energy gap between the HOMO and LUMO levels, and that PTC could be outside the range of so-called 'narrow-bandgap' materials. For the emission properties, this compound exhibits a weak fluorescence in chloroform solution with the maximum emission peak at 550 nm.

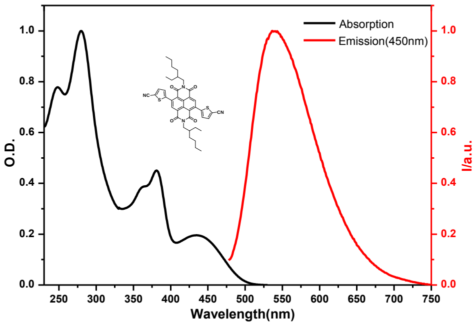

*Figure 4.7 UV/Vis absorption and Emission spectra of **PTC** in solution.*

4.3 Electronic properties and HOMO/LUMO energy levels

4.3.1 OTP

The electrochemical behaviors of the **OTP** was first studied by cyclic voltammetry (CV). The experimental conditions and optimized test parameters used are identical to those already described for **C10-PBT** in Paragraph 2.5.

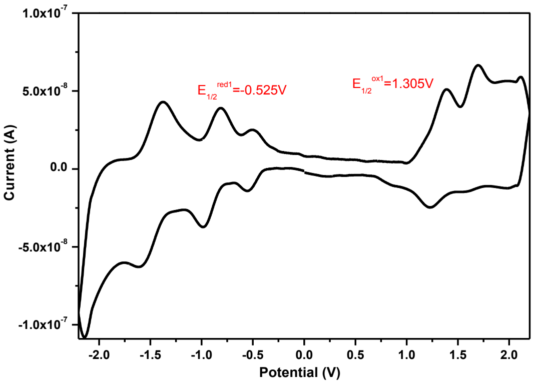

*Figure 4.8 Cyclic voltammetry of **OTP** in $CHCl_3$, 0.5M n-Bu_4NPF_6, at a scan rate of 0.05V/s, room temperature.*

The voltamogramme of OTP is given in *Figure 4.8* and shows on one hand three separated reversible reduction waves at -1.49 V, -0.895 V and -0.525 V (vs Ag/AgCl) corresponding to the formation of the radical anion, dianion and trianion characteristic of the acceptor moieties, even if due to the obligation to use $CHCl_3$ as solvent (not usual in CV) the shape of the waves are curious and optimized conditions should be tested. On the other hand, we observe two reversible one-electron oxidation waves corresponding to the donnor moiety radical cation at 1.305 V and 1.63 V (vs Ag/AgCl). Based on these redox potential values and as more described in Chapter 2, the HOMO and LUMO energies of OTP were estimated as E^{HOMO} = -5.68 eV and E^{LUMO} = -3.85 eV, giving an electrochemical bandgap of E_g = 1.83 eV (see *Figure 4.8*). This band gap is consistent with the gap about 1.75 eV accordance to that obtained experimentally by extrapolation of the onset of the lowest-energy absorption observed by UV-Vis spectroscopy in solution (see *Figure 4.9*).

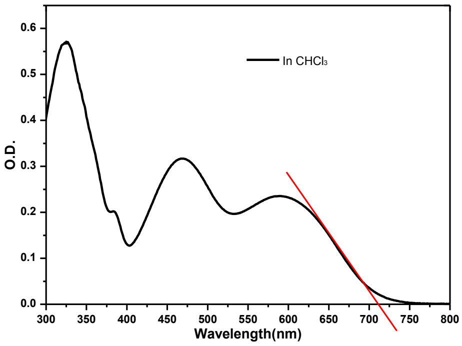

Figure 4.9 Determination of band gap from UV-vis spectrum of ***OTP****.*

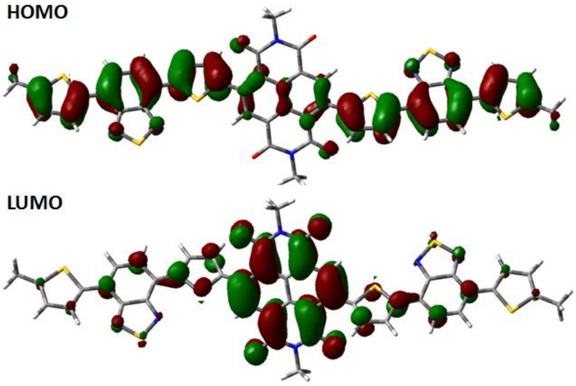

Figure 4.10 The HOMO and LUMO of ***OTP*** *calculated at the B3LYP/6-31G* level. The alkyl chains have been replaced with methyl groups for simplicity.*

The electronic properties of **OTP** in the ground-state were also investigated by density functional theory (DFT) at the B3LYP/6-31G* level, the alkyl chains were also replaced with methyl groups to simplify the calculation. The *Figure 4.10* shows clearly that the electronic spatial distribution of the HOMO is mainly distributed over the benzothiadiathole and donor unit thiophene, while the LUMO distribution is completely localized over the naphthalene diimide core. The calculated HOMO/LUMO energy values of the optimized structures are listed in *Table 4.1.* As we can see, the modulation of the bandgap by introduction of other π-donor/acceptor moieties to the naphthalene diimide core was possible, approaching the ranges of regular low bandgap polymeric materials.

	CV	**B3LYP/6-31G***
HOMO (eV)	-5.68	-5.196
LUMO (eV)	-3.85	-3.29
E_g	1.83	1.90

*Table 4.1 Comparison of the HOMO/LUMO energy values of **OTP** obtained by cyclic voltammetry and by DFT B3LYP/6-31G*.*

The HOMO energy level of **OTP** in solid state (spin coated thin films) was also investigated by photoelectron spectroscopy (see *Figure 4.11*) at OPERA labratory (Japan) and the value of -5.7 eV was measured, which is not so different from the value determined by cyclic voltammetry.

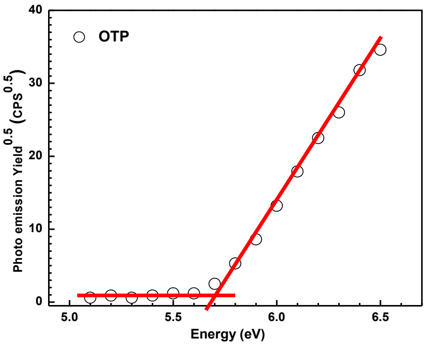

*Figure 4.11 Photoelectron spectroscopy of **OTP** (spin coated thin film).*

4.3.2 PTC

The electronic propertied of PTC in the ground-state were investigated by DFT calculations at the B3LYP/6-31G* level and the calculated HOMO/LUMO energy levels are given in *Table 4.2*. As we can see in *Figure 4.12*, the electronic spatial distribution of the HOMO distribution is mainly localized over the naphthalene and thiophene moieties, while the LUMO distribution is competely distributed over the naphthalene moiety. The result suggests a charge-transfer character for the A-D-A-D-A type compound. From the HOMO/LUMO energy levels in *Table 4.2*, we can estimate a bandgap around 2.76 eV for PTC derivative. This relatively high value is quite large in comparison with the typical narrow bandgap materials. However, the LUMO value around -3.92 eV is low enough to expect an n-type behavior in field effect transistor for instance.

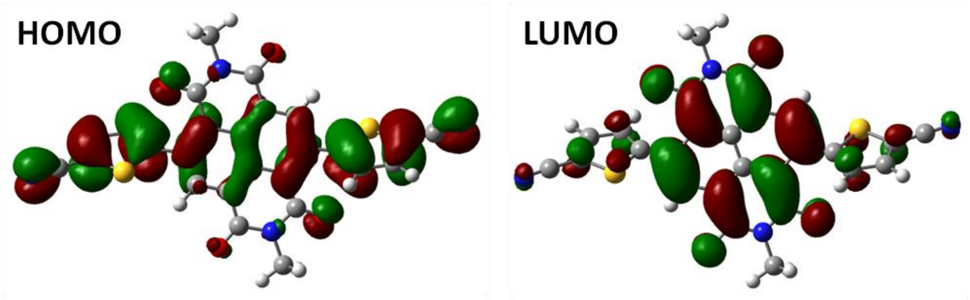

Figure 4.12 The HOMO and LUMO of PTC calculated at the B3LYP/6-31G level. The alkyl chains have been replaced with methyl groups in the calculation.*

Comound	**E^{HOMO} (eV)**	**E^{LUMO} (eV)**	**E_g^{Cal} (eV)**
PTC	-6.68	-3.92	2.76

Table 4.2 Summary of DFT derived HOMO and LUMO energies of PTC.

The HOMO energy level of **PTC** in solid state (thin film) was also investigated by photoelectron spectroscopy. As shown in *Figure 4.13*, the value of HOMO level was estimated at -6.5 eV, which is close to the calculated value -6.68 eV. This deep HOMO is consitent with the large bandgap of the material and typical of ‘n-type’ materials.

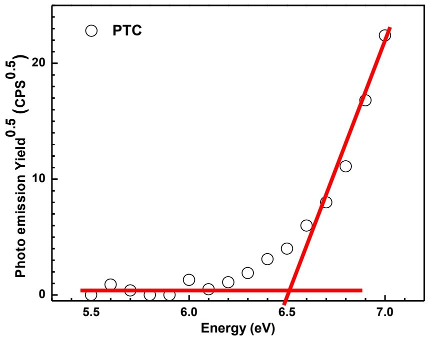

*Figure 4.13 Photoelectron spectroscopy of **PTC** (spin coated thin film).*

4.4 Thermal behavior

The thermal behaviors of the **OTP** and **PTC** were investigated by differential scanning calorimetry (DSC) on heating and cooling. The thermograms are given in *Figure 4.13*.

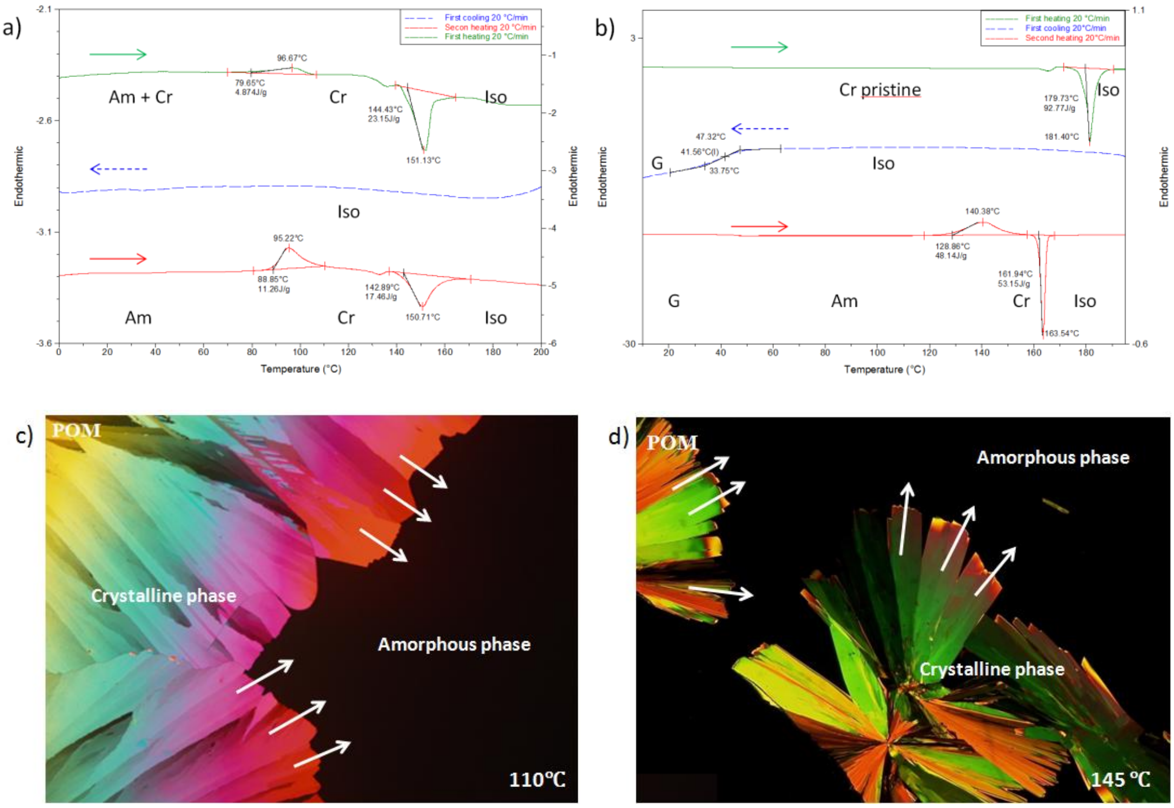

Figure 4.14 DSC thermograms of a) ***OTP*** *and b)* ***PTC****; c) and d) POM microphotographs (under crossed polarizer) of the "cold crystallization" occurring on heating from the amorphous state between the exo- and endothermic transitions for* ***OTP*** *and* ***PTC****, respectively.*

The DSC traces of **OTP** recorded on first heating, first cooling and second heating are given in *Figure 4.14 a*. On first heating, we can meanly observe an unusual exothermic peak around 80 °C (ΔH = 4.9 Jg^{-1}) and an endothermic peak at 144 °C (ΔH = 23.1 Jg^{-1}). The first exothermic transition at 80 °C is typical of a 'cold crystallization', indicating that the material is not well crystallized in its pristine state and presents an amorphous character. The following endothermic transition at 144 °C corresponds to the classical melting point of the material leading to the isotropic liquid state. On cooling from the isotropic state, the DSC trace presents no transition until -40 °C leading to an amorphous state at room temperature. On second heating, we observe again the exothermic peak around 88 °C (ΔH = 11.3 Jg^{-1}) previously observed on first heating corresponding to the 'cold crystallization' of the 'frozen' amorphous phase obtained on first cooling from liquid state. On further heating, the same endothermic peak that on the first heating is observed at 143 °C (ΔH = 17.5 Jg^{-1}), associated to the melting of the crystal phase obtained by 'cold crystallization'. Note that, this thermal behavior was observed whatever the heating and cooling rates (from 20 °C/min to 1°C/min). This 'cold crystallization' was evidenced by POM. As shown in *Figure 4.14 c*, we can observe a slow growing of polycrystalline domains on heating from an amorphous thin film previously prepared by cooling the materials from its isotropic state to room temperature between glass and cover glass.

The DSC traces of **PTC** recorded on first heating, first cooling and second heating are given in *Figure 4.14 b*. On first heating, the DSC trace shows a large endothermic peak at 180 °C (ΔH = 92.77 Jg^{-1}), corresponding to the melting point of material and the transition from the crystalline to the isotropic liquid phase. On cooling, similar to **OPT**, no peak was detected whatever the rate of cooling and only a clear glass transition (Tg) was detected at around 50°C, indicating the amorphous state (glassy state) of the material at room temperature. On second heating, we observe a broad exothermic peak around 129 °C associated with a large transition enthalpy (ΔH = 48.1 Jg^{-1}). As previously described for **OPT**, this exothermic peak is typical of the 'cold crystallization' of the 'frozen' amorphous phase obtained on cooling from isotropic liquid state. Here also, this phenomenon was evidenced by POM as shown in *Figure 4.14 d*. Then, on further heating, the endothermic peak at 162 °C (ΔH = 53.1 Jg^{-1}) is observed corresponding to the melting of the crystal phase obtained by 'cold crystallization'. We can notice that the large difference of transition temperatures and transition enthalpies of the melting point on the first and second heating seems indicate that the pristine crystalline and 'cold crystallized' phases don't present the same crystalline structures.

As described in this paragraph, the thermal study showed that these two compounds don't crystallize properly on cooling from the isotropic state and present easily an amorphous character at room temperature. This behavior is not surprising and can be explained by the presence of branched alkyl chains on the perylene cores. These ramified substituents are very good for the solubility of organic derivatives but they are detrimental for their self-organization properties, in introducing a large disorder.

The DSC thermal analysis results are listed in *Table 4.3*.

Compound	**Tg(°C)**	**Transition***	**T(°C)**	**ΔH($J g^{-1}$)**	**Transition***	**T(°C)**	**ΔH($J g^{-1}$)**	**Transition***
OTP	--	--	88	11.3	Am → Cr	143	17.5	Cr →Iso
PTC	50	G → Am	129	48.1	Am → Cr	162	53.1	Cr →Iso
Glassy state (G), Amorphous phase (Am), Crystalline phase (Cr), Isotropic liquid phase (Iso). *on second heating.								

*Table 4.3. Phase transition temperatures and enthalpy changes of **OTP** and **PTC**.*

4.5 Thin film morphology study (Atomic force microscopy)

The thin film morphology on surfaces of the **OTP** was studied by tapping mode Atomic Force Microscopy (AFM). These measurements were carried out at the Institut des NanoSciences de Paris (INSP) in collaboration with Dr. E. Lacaze and Ms. Xiao Liu (PhD IPCM/INSP).

The **OTP** films were prepared by spin-coating from a chloroform solution of material (1% w/w, 3000 rpm) onto OTS-treated silicon wafer substrate. The thickness is around 85 nm as determined by profilometer. The film samples were studied before and after annealing (100 °C for 1 hours in vacuum). The typical topography and phase images are given in *Figure 4.15*.

The as-prepared film presents a very rough surface with large size of uneven and there was no specific grains (*Figure 4.15 a* and *b*). After annealing at 100 °C, a smoother and uniform surface can be observed. Indicating a change in the thin film morphology. This observation is consistent with the existence of the exothermic transition observed by DSC at 90 °C, associated to the cold crystallization of the material. This transition should induce a better crystallinity of the film and should unpact its charge transport properties.

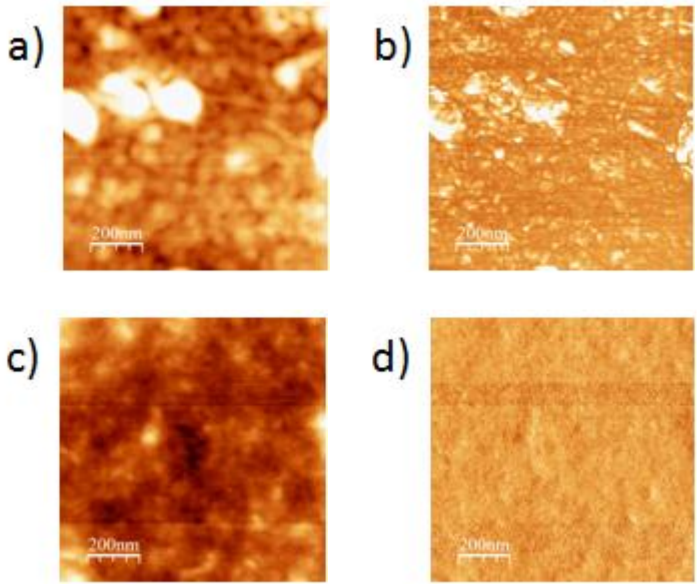

*Figure 4.15 The AFM images of **OTP** thin film on OTS substrate: a) Topography (as prepared); b) Phase (as prepared); c) Topography (after annealed); d) Phase (after annealed).*

4.6 Charge Transport Properties Study (OFET)

4.6.1 Charge Transport Properties Study of OTP

The charge transport properties of **OTP** were investigated in OFET configurations. These measurements were carried out at Kyushu University (OPERA, Japan), in collaboration with the Prof. J.-C. Ribierre and the Dr. Piotr Sleczkowski. The details about the transistor fabrication and measurement parameters are given in Paragraph 4.8.3.

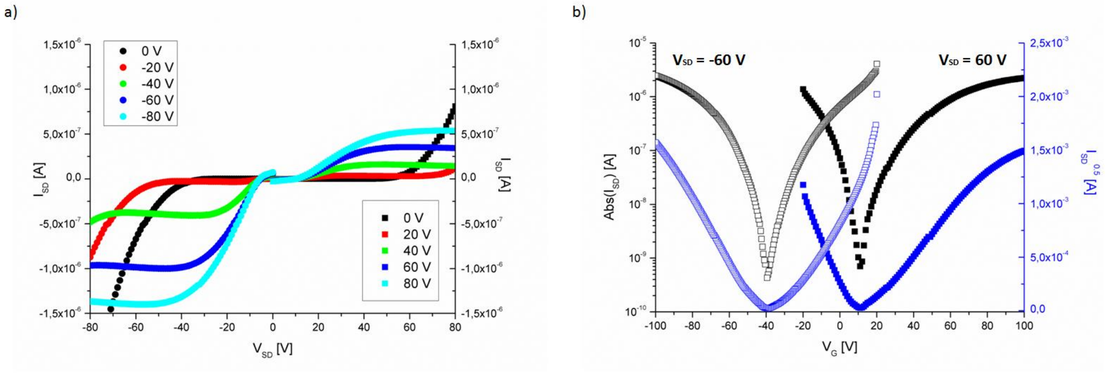

*Figure 4.16 Output and transfer characteristics for holes and electrons of **OTP** (OFET).*

The thin films of **OTP** were spin-coated on OTS treated transistors in bottom contact (BC) and bottom gate (BG) configuration. The typical output and transfer characteristics of transistors are shown in *Figure 4.16*. In this configuration, an ambipolar charge transport was observed and a hole mobility of 4.7 x 10^{-4} cm^2 V^{-1} s^{-1} and electron mobility of 2.3 x 10^{-4} cm^2 V^{-1} s^{-1} were measured.

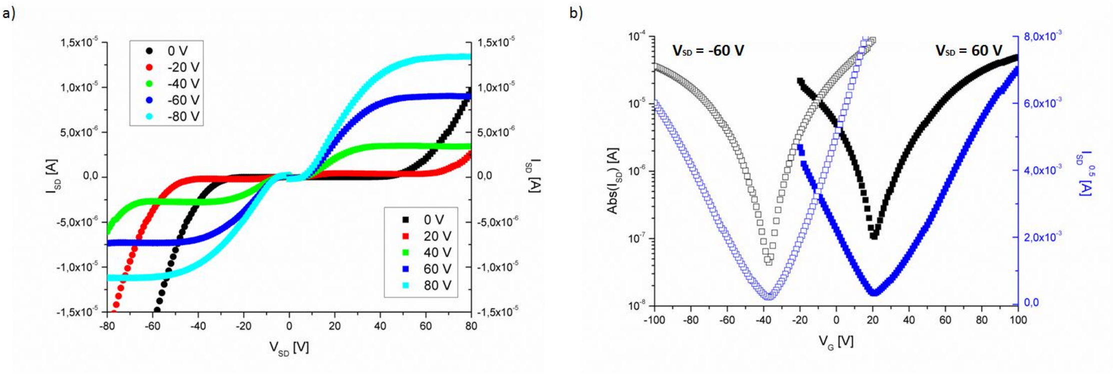

Figure 4.17 Output and transfer characteristics for holes and electrons of ***OTP****(OFET) after annealing.*

We also investigated the influence of thermal treatment on the charge transport properties. Thus, the same OFET was then annealed at 80 °C during 1 hours under nitrogen (*Figure 4.17*). After annealing, the material shows also an ambipolar transport with improved mobility 3.4 x 10^{-3} and 6.1 x 10^{-3} cm^2 V^{-1} s^{-1} for the holes and electrons respectively.

Mobilities, threshold voltage (V) and on/off current ratio ($I_{on}/_{off}$) deduced from the device characteristics of **OTP** are summarized in *Table 4.4*.

Annealing	**Hole mobility($cm^2V^{-1}s^{-1}$)**	**Electron mobility($cm^2V^{-1}s^{-1}$)**	**Threshold voltage (V) p-type**	**Threshold voltage (V) n-type**	**I_{on}/I_{off} ratio p-type**	**I_{on}/I_{off} ratio n-type**
N	$4.7x10^{-4}$	$2.3x10^{-4}$	-45	20	10^5	10^3
Y	$3.4x10^{-3}$	$6.1x10^{-3}$	-40	27	10^3	10^3

Table 4.4 OFET performances of OTP.

The ambipolar charge transport properties observed for OTP in our transistor are typical of narrow bandgap materials. It can be explained by the proper alignment of HOMO and LUMO energy levels of the compounds with the work function W_f of gold electrodes ($W_{f/Au}$ = 5.1 eV). In the present case, the energy barriers between the W_f of the electrodes and the LUMO or LUMO levels of the material (1.3 or 0.6 eV respectively) are small enough to allow the injection of both holes and electrons in the material as displayed in *Figure 4.18*.

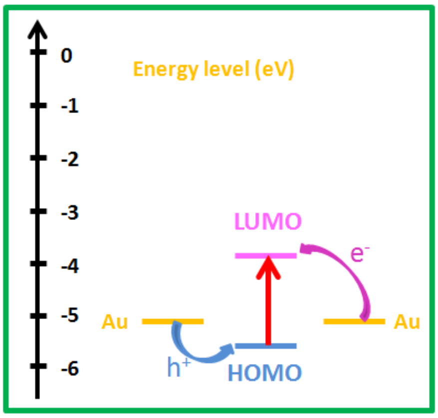

Figure 4.18 Schematic representations of HOMO/LUMO energy levels of ***OTP****, the work function of gold electrodes and both injection of holes and electrons in the material.*

4.6.2 Charge Transport Properties Study of PTC

The charge transport properties of **PTC** was investigated in OFET configurations as well. These measurements were carried out at Institut des NanoSciences de Paris (Sorbonne University), in collaboration with Ms Xiao Liu (PhD IPCM/INSP).

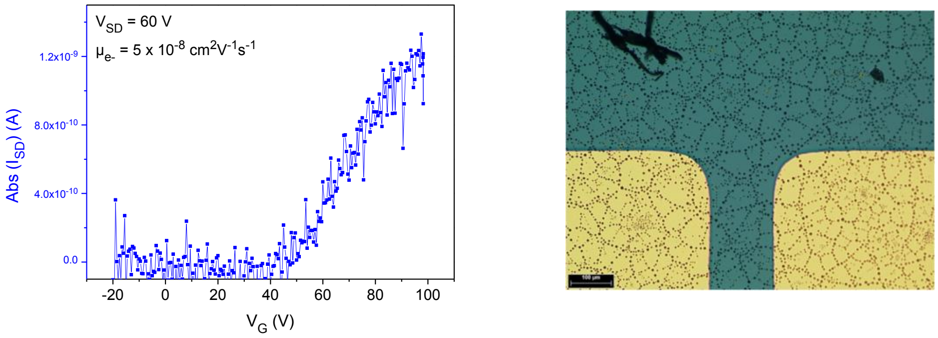

Figure 4.19 a) Transfer characteristics for holes of ***PTC*** *(OFET). b) Microscope image of dewetted* ***PTC*** *thin film observed on heating until 130°C.*

As a preliminary measurement, **PTC** was spin-coated on a transistor in bottom contact (BC) and bottom gate (BG) configuration. A typical transfer characteristic of a transistor with the as-prepared film is given in *Figure 4.19 a*. Only a very weak electron transport was observed with an electron mobility of 5 x 10^{-8} cm^2 V^{-1} s^{-1}. This very low mobility can be explained by the amorphous character of the thin film of **PTC**. Indeed, when observed under polarized optical microscope, the thin film obtained after spin-coating shows no-birefringence, evidencing the absence of order with the layer. As described in Paragraph 4.4, we tried to induce the ‘cold crystallization’ of the thin film to improve the film crystallinity by annealing the sample at 130 °C. Unfortunately, we observed a rapid dewetting of the film during the process as showed in *Figure 4.19 b*.

4.7 Conclusion

In this chapter, two ‘narrow bandgap’ molecules based on central naphthalene diimide core were designed, synthesized and characterized.

The photophysical study of these molecules showed that they both present an intermolecular charge transfer character evidenced by the presence of broad absorption bands at low energy and characteristic of D-A systems. In addition one of these molecules presents a very broad absorption spectrum extended into the near infrared range in solid state. The electronic propriety study of the latter evidences a narrow energy bandgap of 1.8 eV, while the second molecule presents a larger bandgap (2.7 eV) with a very deep HOMO level (-6.7 eV).

The thermal behavior of compounds was investigated by DSC and this study showed that these derivatives don’t crystallize properly on cooling from the isotropic state, and present easily an amorphous character at room temperature due to their chemical structures incorporating branched alkyl chains.

Finally, the charge transport properties of these compounds were investigated in field-effect transistor configuration. The measurement with the molecule presenting a narrow bandgap of 1.8 eV showed a balanced ambipolar transport with a relatively high hole and electron mobility about 3.4 x 10^{-3} cm^2 V^{-1} s^{-1} and 6.1 x 10^{-3} cm^2 V^{-1} s^{-1}, respectively. The second material presents only an electron transport, which is consistent with its deep HOMO energy level making only possible the electron injection.

To conclude, these ‘narrow bandgap’ molecules can be considered as interesting and promising candidates in the field of optoelectronics as for example for the fabrication of ambipolar or n-type organic field effect transistors (OFETs), and for OPV applications such as non-fullerene solar cells.

4.8 Experimental

4.8.1 Materials and methods

Some starting materials have been mentioned in second and third chapter. But other starting materials were needed to synthesize this new family: thus, tributyl-(5-octyl-thiophen-2-yl)-stannane, tributyl(thiophen-2-yl)stannane, 2,2,6,6-tetramethylpiperidine, n-butyllithium, $SnBu_3Cl$, naphthalene dianhydride, fuming sulphuric acid, dibromoisocyanuric acid, hydrochloric acid, 1-propionic acid, o-xylene, 2-ethylhexylamine, copper(I)cyanide were purchased from Aldrich, Alfa and Acros or TCI and used without any further purification. The solvents for recrystallization and precipitation were purchased from Aldrich or distilled before using. The solvents for spectroscopic studies were of spectroscopic grade. Column chromatography was performed on silica gel.

^{1}H- and ^{13}C NMR spectra were recorded on a Bruker AC 300 spectrometers (300 MHz) using the signal of Tetramethylsilane (TMS) or the carbon signal of the deuterated solvents as internal standard, and the chemical shift are reported in ppm. Abbreviations used for splitting patterns are s = singlet, d = doublet, t = triplet, q = quintet, m = multiplet. The UV/vis spectra were taken on a spectrometer of Varian Cary 300 scan spectrometer, using 100 mm quarts cuvette, and the fluorescence spectrum was recorded on a Varian Cary Eclipse spectrofluorimeter. DSC measurement was performed on an Instrument DSC Q2000 V24.4 Build 116, using the Module DSC Standard Cell RC. Phase transitions (POM) were examined by a Leica microscope of Linkam TMS 94 with a Linkam LTS temperature-controlled hot stage and Nikon LWD 0.65 camera. The elementary analysis was performed at the Service de Microanalyse ICSN-CNRS (France) and at Service Central d'Analyse isa (France). AFM images were recorded on a Digital Instrument, DI3100 in tapping mode to analyze the surface density of the samples at INSP-Sorbonne University (France).

4.8.2 Synthesis

4.8.2.1 Synthesis of building blocks

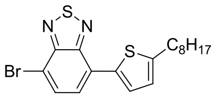

Chemical Formula: $C_{18}H_{21}BrN_2S_2$
Molecular Weight: 409.407
4A

4-bromo-7-(5-octylthiophen-2-yl)benzo[c][1,2,5]thiadiazole (4A): **2E** (10 g, 34 mmol), tributyl-(5-octyl-thiophen-2-yl)-stannane (13.2 g, 27 mmol) were dissolved in dry, de-gassed DMF (200 mL) and under an inert atmosphere. To this mixture Pd(PPh$_3$)$_4$ (0.98 g, 0.8 mmol) was added via cannula and the reaction heated to 100 °C whilst stirring overnight. The reaction is then cooled to room temperature, washed with water and extracted with dichloromethane. The organic phase is dried with MgSO$_4$, filtered and the solvent evaporated under reduced pressure. The crude product is dry-loaded on a silica-gel packed column and eluted with a 3:1 (Hex/DCM) mixture. The desired product is recovered in the second fraction which after evaporation and recrystallisation in EtOH yielded bright fluorescent yellow needle-like crystals (Yield 66%). NMR δH (ppm)(300MHz, CDCl$_3$) 7.93 (d, 1H), 7.82 (d, 1H), 7.64 (d, 1H), 6.87 (dd, 1.0 Hz, 1H), 2.87 (t, 2H), 1.73 (t, 2H), 1.32 (m, 10H), 0.95-0.80 (t, 3H).

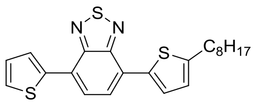

Chemical Formula: $C_{22}H_{24}N_2S_3$
Molecular Weight: 412.634
4B

4-(5-octylthiophen-2-yl)-7-(thiophen-2-yl)benzo[c][1,2,5]thiadiazole (4B): **4A** (4 g, 9.8 mmol) was dissolved in dry, de-gassed toluene (90 mL) together with tributyl(thiophen-2-yl)stannane (4.4 g, 12.0 mmol) under an inert atmosphere. The Pd(PPh$_3$)$_4$ (0.28 g, 0.24 mmol) is added via cannula and the reaction is left to stir at 80°C overnight. The mixture is cooled to room temperature, washed with water and extracted with dichloromethane. The organic phase is dried with $MgSO_4$, filtered and the solvent evaporated under reduced pressure. The crude product is dry-loaded on a silica-gel packed column and eluted with a 3:1 (Hex/DCM) mixture. The product is recovered in the second fraction which after evaporation gives the desired product as a bright red-orange powder (3 g, 75% yield). NMR δH (ppm)(300 MHz, $CDCl_3$) 8.10 (d, 1H),7.94 (d, 1H), 7.86 (d, 1H), 7.80(d, 1H), 7.44 (d, 1H), 7.20 (m, 1H), 6.88 (d, 1H), 2.89-2.86 (t, 2H), 1.78-1.70 (m, 2H), 1.42-1.28 (m, 12H), 0.89-0.86 (t, 3H).

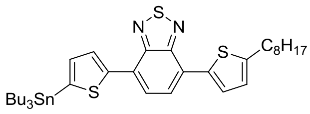

Chemical Formula: $C_{34}H_{50}N_2S_3Sn$
Molecular Weight: 701.679
4C

4-(5-octylthiophen-2-yl)-7-(5-(tributylstannyl)thiophen-2-yl)benzo[c][1,2,5]thiadiazole (4C): 2,2,6,6-Tetramethylpiperidine (0.49 mL, 2.9 mmol) was dissolved in dry THF (15 mL) and cooled to -78°C in a dry ice/acetone bath under an inert atmosphere. Once cooled, n-butyllithium (1.2 mL, 2.9 mmol, 2.5 M in hexanes) is added dropwide to the solution and left to warm to room temperature whilst stirring for 20 minutes. The solution is cooled to -78°C and a solution of **4B** (1 g, 2.4 mmol) in dry THF (10 mL) is added dropwise via syringe changing the colour of the mixture to a deep purple colour and left to stir for 1 hr at room temperature. The mixture is cooled once again and $SnBu_3Cl$ (0.79 mL, 2.9 mmol) are added via syringe turning the solution back to a red/orange colour. The reaction was left to warm to room temperature whilst stirring under and inert atmosphere overnight. The reaction mixture is washed with a 20 % solution of NH_4Cl, water and extracted with dichloromethane. The organic phase is dried with $MgSO_4$, filtered and the solvent evaporated under reduced pressure to give the product as a dark red oil (1.65 g, 97% yield). NMR δH (ppm)(300MHz, CD_2Cl_2) 8.24 (d, 1H), 7.95 (d, 1H), 7.90-7.69 (m, 2H), 7.29 (d, 1H), 6.88 (d, 1H), 2.89 (t, 2H), 1.87-1.54 (m, 6H), 1.51-1.11 (m, 24H), 1.07-0.79 (m, 12H).

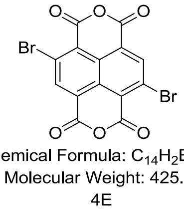

Chemical Formula: $C_{14}H_2Br_2O_6$
Molecular Weight: 425.970
4E

4,9-dibromoisochromeno[6,5,4-def]isochromene-1,3,6,8-tetraone (4E): Naphthalene dianhydride (1.35 g, 5 mmol) is dissolved in fuming sulphuric acid (50 mL) at room temperature. To this mixture, dibromoisocyanuric acid (1.45 g, 5 mmol) dissolved also in fuming sulphuric acid (25 mL) is added slowly over a period of 4h via addition funnel. After addition the mixture is left stirring for another hour at room temperature. The reaction mixture is then poured carefully onto ice (250 g) to produce a bright yellow precipitate. Distilled water (1 L) is added and the crude mixture left to stand for 30 min, after which it is filtered through a Buchner funnel under vacuum, washed with dilute HCl (5%, 250 mL) and water. The precipitate is left to dry under vacuum overnight to give a bright yellow powder which was used without further purification as reported in the literature. (2.15 g, 100% yield). NMR δH (ppm)(300M Hz, $CDCl_3$) 8.89 (s, 2H).

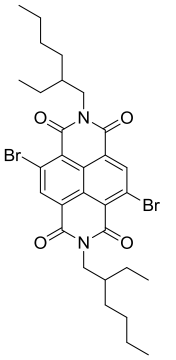

Chemical Formula: $C_{30}H_{36}Br_2N_2O_4$
Molecular Weight: 648.426
4F

4,9-dibromo-2,7-bis(2-ethylhexyl)benzo[lmn][3,8]phenanthroline-1,3,6,8(2H,7H)-tetraone (4F) : 4E (3 g, 7 mmol) was added together with 1-propionic acid (9 mL) in o-xylene (30 mL) and stirred at room temperature. 2-ethylhexylamine (2.88 mL, 17.7 mmol) are added and the reaction is heated to 130 °C whilst stirring for 2h. The solvent is removed under reduced pressure and the resulting red-orange solid is precipitated using a 1:1 (methanol/water) mixture. The solids are filtered and washed with hot methanol (twice) followed by hot cyclohexane, leaving a light yellow solid. The solid is recrystallised from dichloromethane/methanol to give the desired product as fine pale yellow crystals (1.38 g, 30% yield). NMR δH (ppm)(300MHz, CD_2Cl_2) 8.96 (s, 2H), 4.11 (d, 4H), 1.90 (m, 2H), 1.46 – 1.18 (m, 16H), 0.90 (q, 12H).

4.8.2.2 Synthesis of OTP

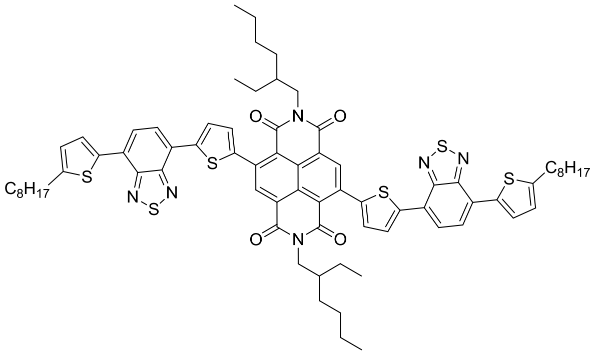

Chemical Formula: $C_{74}H_{82}N_6O_4S_6$
Molecular Weight: 1311.871
OTP

OTP: 4C (400 mg, 0.57 mmol), **4F** (154 mg, 0.239 mmol) were dissolved in dry, de-gassed DMF (15 mL) and under an inert atmosphere. To this mixture $Pd(PPh_3)_4$ (28 mg, 0.024 mmol) was added and the reaction heated to 115 °C whilst stirring overnight. The reaction is then cooled to room temperature, washed with water and extracted with dichloromethane. The organic phase is dried with MgSO$_4$, filtered and the solvent evaporated under reduced pressure. The crude product is dry-loaded on a silica-gel packed column and eluted with a 1:2 (Hex/DCM) mixture. The desired product is recovered in the second fraction. After evaporation, the product was obtained as a black solid (140 mg, 18% yield). NMR δH (ppm)(300MHz, CDCl$_3$) 8.89 (s, 2H), 8.16 (d, 2H), 8.00 (d, 2H), 7.95 (d, 2H), 7.83 (d, 2H), 7.46 (d, 2H), 6.90 (d, 2H), 4.11 (d, 4H), 2.87 (m, 4H), 1.96 (m, 2H), 1.74 (m, 4H), 1.24-1.40 (m, 10H), 0.89 (q, 12H). δC (ppm)(75MHz, CDCl$_3$) 162.64, 162.37, 152.66, 152.62, 148.53, 142.63, 142.08, 139.78, 136.78, 136.62, 129.99, 128.03, 127.69, 127.43, 126.98, 126.01, 125.49, 125.00, 122.95. Elementary analysis: Calcd for C74H82N6O4S6: C 67.75, H 6.30, N 6.41; Found : C 67.34, H 6.46, N 6.19.

4.8.2.3 Synthesis of PTC

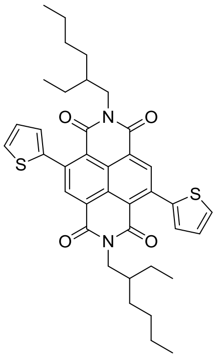

Chemical Formula: $C_{38}H_{42}N_2O_4S_2$
Molecular Weight: 654.881
4G

2,7-bis(2-ethylhexyl)-4,9-di(thiophen-2-yl)benzo[lmn][3,8]phenanthroline-1,3,6,8(2H,7H)-tetraone (4G): Tributyl(thiophen-2-yl)stannane (186 mg, 0.5 mmol) and **4E** (130 mg, 0.2 mmol) were dissolved into anhydrous toluene (15 mL) in a round-bottom flask under an argon atmosphere, and a catalytic amount Pd(PPh$_3$)$_4$ (12 mg, 0.01 mmol) was added into the flask. Then the solution was reated for 24 h at the temperature of 105 °C. After cooling down, the mixture was washed with water and dichloromethane. The organic extracts were dried over MgSO$_4$. The solvent was evaporated, and the crude product was purified via column chromatography using dichloromethane by volume as the eluent to afford **4G** as a red solid. Yield, 95%. NMR δH (ppm)(300MHz, Acetone) 8.62 (s, 2H), 7.74 (d, 2H), 7.42 (d, 2H), 7.22 (t, 2H), 4.05 (d, 4H), 1.67(m, 2H), 1.67(m, 2H) , 1.28-1.42 (m, 16H) , 0.89(t, 12H).

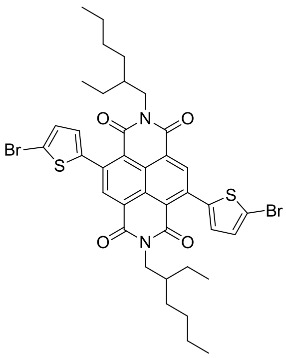

Chemical Formula: $C_{38}H_{40}Br_2N_2O_4S_2$
Molecular Weight: 812.673
4H

4,9-bis(5-bromothiophen-2-yl)-2,7-bis(2-ethylhexyl)benzo[lmn][3,8]phenanthroline-1,3,6,8(2H,7H)-tetraone (4H): A solution of **4G** (130 mg, 0.2 mmol) in 15 ml dry chloroform and 15 ml acetic acid was cooled to 0 °C for 20 minutes. NBS (140 mg, 0.8 mmol) was added in one portion. Then the mixture was allowed to warm to the room temperature and stirred for 12 h. The mixture was then poured into water, extracted with chloroform and then dried with $MgSO_4$. Evaporation off the solvent, the residue was purified by chromatography on silica gel ($CHCl_3$) to give a dark red solid of **4H**. Yield, 76%. NMR δH (ppm)(300MHz, CD_2Cl_2) 8.72 (s, 2H), 7.17 (s, 2H), 7.10 (s, 2H), 4.10 (d, 4H), 1.90(m, 2H), 1.29-1.40 (m, 16H) , 0.89(q, 12H).

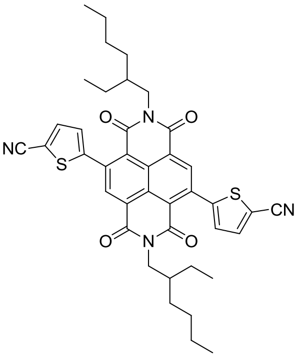

Chemical Formula: $C_{40}H_{40}N_4O_4S_2$
Molecular Weight: 704.900
PTC

PTC: A mixture of **4H** (170 mg, 0.2 mmol) and copper(I)cyanide (450 mg, 0.5 mmol) in dry DMF was heated under argon for 24 h at 140 °C. After cooling to the room temperature, the mixture was poured into icy water and then extracted with $CHCl_3$, washed with water for three times, $MgSO_4$ was added to dry the organic phase. Evaporation off the solvent, the residue was purified by chromatography on silica gel (dicholoromathe) to give an orange solid of **PTC**. Yield, 72%. NMR δH (ppm)(300MHz, CD_2Cl_2) 8.73 (s, 2H), 7.74 (d, 2H), 7.24 (d, 2H), 4.03 (q, 4H), 1.86 (m, 2H), 1.24-1.40 (m, 16H), 0.89 (q, 12H). δC (ppm)(75MHz, CD_2Cl_2) 162.59, 162.52, 148.63, 138.34, 138.02, 136.52, 128.63, 128.37, 126.52, 125.24, 114.30, 111.92, 45.25, 38.46, 31.17, 29.07, 24.51, 23.65, 14.40, 10.91. Elementary analysis: Calcd for $C_{40}H_{40}N_4O_4S_2$: C 68.16, H 5.72, N 7.95; Found C 67.63, H 5.56, N 7.90. HRMS: $C_{40}H_{40}N_4O_4S_2+Na^+$: 727.2383, Found: 727.2408.

4.8.3 OFET sample preparation and configurations

The **OTP** films were prepared by spin-coating from a chloroform solution of material (0.25% w/w. 3000 rpm) on OTS treated substrate. The thickness of films varies from 50 to 70 nm as evaluated by profilometer. The samples were studied after annealing (80 °C for 1 hour in vacuum).

The substrates were sonicated in acetone and isopropanol and then placed in a piranha solution to remove the residues of organic materials and to induce OH groups in the vicinity of the surface. After rinsing the substrates again in isopropanol and tried by nitrogen flow. Then they were cleaned in a UV cleaner during 20 minutes. For the preparation of the OTS-treated substrates, the silanization was carried out in a 3 mm OTS (Octadecyltrichlorosilane) solution of dry hexane for 90 min. All solvents were purchased from Sigma Aldrich and were used without further purification.

The transistors used are Fraunhofer chips (bottom gate/top contact) with n-doped silicon and an oxide layer of $<$ 30 nm, source/drain (30 nm Au). 4 type of transistor : L = 2.5 µm, W = 10 nm; L = 5 µm, W = 10 nm; L = 10 µm, W = 10 nm; L = 20 µm, W = 10 nm.

OFET characteristics were measured using a double channel source meter unit (Keithley 2600) and all the tests were realized in glove-box. All the field effect mobilities were calculated on the saturation regime.

Conclusions and Perspectives

Conclusions

In this work, we designed, synthesized, and characterized new self-organized semiconducting materials based on donor/acceptor architectures presenting high luminescence or narrow bandgap properties, that combine different types of electron donor and electron acceptor moieties in liquid crystal molecules or narrow bandgap molecular structures. We expected these materials to be considered as promising candidates in the field of organic electronics and photonics.

More precisely, we first synthesized a family consisting of two liquid crystalline fluorescent calamitic (D-A-D) derivatives **C10-PBT** and **C6-PBT** based on O-alkylphenyl donor groups and a benzothiadiazole acceptor central core.

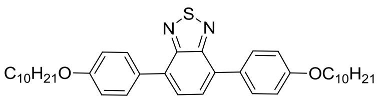

C10-PBT

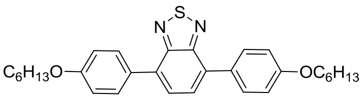

C6-PBT

After developing an efficient chemical strategy, we determined and discussed the photophysical properties, thermal behaviors, self-organizations as well as the charge transport properties of these new molecules. The photophysical study showed that these materials can present very high luminescence properties with high PLQYs in solution and in film. It must be noticed that both molecules are liquid crystalline (SmA, Nem), as demonstrated by DSC and POM, and that these materials present a lamellar organization consisting of aromatic core and alkyl chain separate sublayers. We also performed AFM measurements on thin films evidencing that it is possible to orient these fluorescent molecules perpendicular to the substrate surface. As a preliminary results, a hole mobility about 3 x 10^{-3} $cm^2V^{-1}s^{-1}$ in crystal state was observed in OFET configuration for **C10-PBT**. TOF measurements in the liquid crystal SmA phase of the same compound show an ambipolar charge transport with a hole and electron mobility about 3.8 x 10^{-5} $cm^2 V^{-1} s^{-1}$ and 2.8 x 10^{-4} $cm^2 V^{-1} s^{-1}$, respectively.

Then, we synthesized a second series consisting of linear dyad and triad architectures based on the fluorescent benzothiadiazole-based derivative and benzo[4,5]thieno[2,3-d]thiophene (BTBT) derivatives.

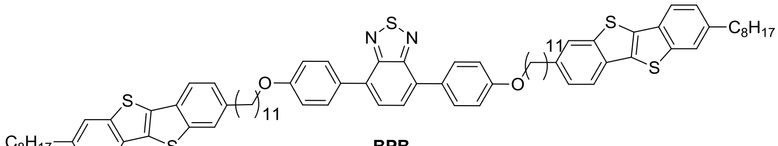

BPB

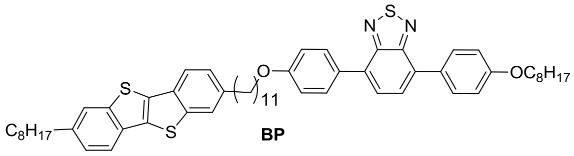

BP

After developing an efficient chemical strategy, we determined and discussed the photopysical properties, thermal behaviors, self-organizations as well as the charge transport properties of these molecules. Both of them revealed liquid crystal properties with multi-lamellar structures consisting of an alternate superposition of one layers of fluorescent derivatives and one or two layers of BTBT. The film morphology study showed clearly the presence of nanostructured thin films with terraces structures and evidences that it is possible to orient layers of these fluorescent complex molecular architectures parallel to the substrate surface. Finally, TOF measurements exhibit a relatively high hole transport mobility of 1 x 10^{-1} cm^2 V^{-1} s^{-1} and electron transport mobility of 6.5 x 10^{-2} cm^2 V^{-1} s^{-1} in crystal state for **BPB** derivative.

We finally designed and synthesized a family of ‘narrow bandgap’ molecules based on central naphthalene diimide core.

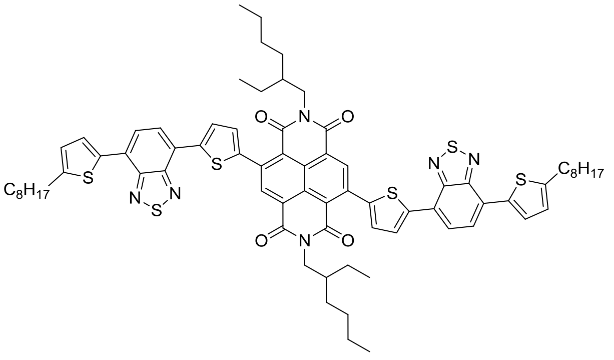

OTP

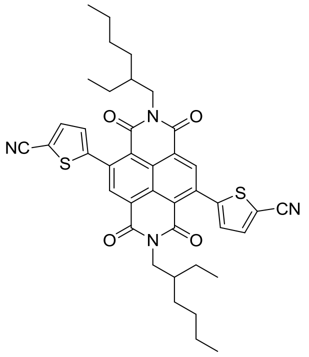

PTC

The photophysical study of these molecules showed that they both present an intermolecular charge transfer and one of the molecule **OTP** presents a very broad absorption spectrum extended into the near infrared range in solid state. The electronic propriety study of **OTP** evidences a narrow energy bandgap of 1.8 eV, while the **PTC** presents a larger bandgap (2.7 eV) with a very deep HOMO level (-6.7 eV). The thermal behavior of compounds showed that these derivatives have a tendency to form disordered thin films detrimental for charge conduction for instance. Finally, the charge transport properties of these compounds were investigated in field-effect transistor configuration. The measurement with **OTP** showed a well balanced ambipolar transport with a hole and electron mobility about 3.4 x 10^{-3} cm^2 V^{-1} s^{-1} and 6.1 x 10^{-3} cm^2 V^{-1} s^{-1}, respectively. The **PTC** presents only an electron transport, which is consistent with its deep HOMO energy level making only possible the electron injection.

Perspectives

Based on the above work, we make the following outlook.

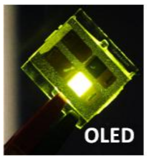

First, based on the high luminescence and charge transport properties of the liquid crystalline fluorescent calamitic compounds (**C10-PBT**/**C6-PBT**) and linear dyad and triad architectures (**BPB**/**BP**) in solid state, these molecules should be incorporated in emissive devices such as light emitting diodes and/or transitors (OLEDs or OLETs). Some first trials are currently carried out in collaboration with the group of Prof. C. Adachi at Kyushu University.

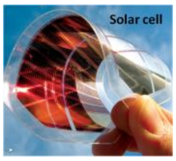

Second, the narrow bandgap derivative OTP, covering all the visible range of visible spectrum and presenting relatively high mobility, is a very good candidate for the fabrication of OPV devices (non-fullerene solar cells) or the elaboration of phototransistors.

Third, the thermal study of PTC showed that this compound have a tendency to form disordered thin films, detrimental for charge transport properties, due to the presence of branched alkyl chains on the perylene cores. In this context, in replacing the ramified aliphatic substituents by linear chains, we should significantly improve the molecular packing and the crystallinity of thin films, leading to higher n-type conduction for this material.

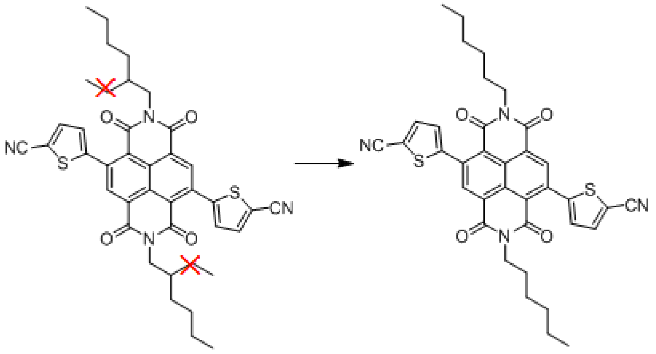

Finally, based on the molecular structure of the linear triad BPB, an exciting new challenge would be to design and synthesize a new series of more complex triad derivatives, combining three different π-conjugated units in a unique molecular architecture; one p-type unit for hole transport, one central emissive unit for light-emission and one n-type unit for electron transport. This architecture could form complex multi-lamellar structures, presenting a spontaneous nanosegregation of p-type, emissive, and n-type entities. This should lead to well-distinct conductive channels (for each type of charge carriers) and emissive layers, and would be an ideal structure to limit charge recombination processes in bulk in classical monolithic OLET, for example.

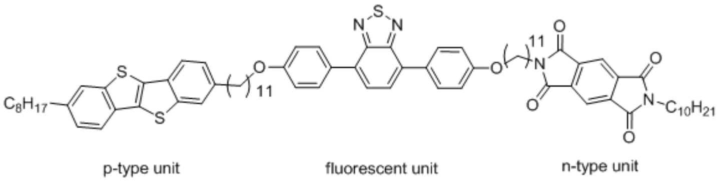

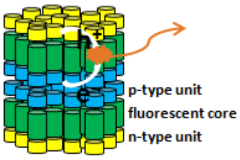

References

References

1. C. L. Wang, H. L. Dong, L. Jiang, W. P. Hu, Organic semiconductor crystals. *Chem. Soc. Rev.* **2018**, *47*, 422.
2. D. D. Eley, Phthalocyanines as Semiconductors. *Nature* **1948**, *162*, 819.
3. H. Shirakawa, E. J. Louis, A. G. MacDiarmid, C. K. Chiang, A. J. Heeger, Synthesis of Electrically Conducting Organic Polymers : Halogen Derivatives of Polyacetylene, $(CH)_X$. *J.C.S. CHEM. COMM.* **1977**, 578.
4. L. Dou, Y. S. Liu, Z. R. Hong, G. Li, Y. Yang, Low-Bandgap Near-IR Conjugated Polymers/Molecules for Organic Electronics. *Chem. Rev.* **2015**, *115*, 12633.
5. S. Günes, H. Neugebauer, N. S. Sariciftci, Conjugated Polymer-Based Organic Solar Cells. *Chem. Rev.* **2007**, *107*, 1324.
6. G. L. Patrick, Organic chemistry Second Edition, **2004**, ISBN 1 85996 264 5.
7. W. J. Mu, S. Sun, J. Zhang, M. Y. Jiao, W. T. Wang, Y. W. Liu, X. N. Sun, L. Jiang, B. Z. Chen, T. Qi, Advantage of arch-shaped structure on transistor performances over linearshaped structure in dibenzothienopyrrole semiconductors. *Organic Electronics* **2018**, *61*, 78.
8. Y. Y. Hu, D. X. Cao, A. T. Lill, L. Jiang, C. A. Di, X. K. Gao, H. Sirringhaus, T. Q. Nguyen, Effect of Alkyl-Chain Length on Charge Transport Properties of Organic Semiconductors and Organic Field-Effect Transistors. *Adv. Electron. Mater.* **2018**, *4*, 1800175.
9. Z. R. Yi, Y. Y. Jiang, L. Xu, C. Zhong, J. Yang, Q. J. Wang, J. W. Xiao, X. M. Liao, S. Wang, Y. L. Guo, W. P. Hu, Y. Q. Liu, Triple Acceptors in a Polymeric Architecture for Balanced Ambipolar Transistors and High-Gain Inverters. *Adv. Mater.* **2018**, *30*, 1801951.
10. S. R. Forrest, The path to ubiquitous and low-cost organic electronic appliances on plastic. *Nature* **2004**, *428*, 911.
11. C. L. Wang, H. L. Dong, W. P. Hu, Y. Q. Liu, D. B. Zhu, Semiconducting π-Conjugated Systems in Field-Effect Transistors: A Material Odyssey of Organic Electronics. *Chem. Rev.* **2012**, *112*, 2208.
12. C. W. Tang, S. A. VanSlyke, Organic electroluminescent diodes. *Applied Physics Letters.* **1987**, *51*, 913.
13. J. H. Burroughes, D. D. C. Bradley, A. R. Brown, R. N. Marks, K. Mackay, R. H. Friend, P. L. Burns, A. B. Holmes, Light-emitting diodes based on conjugated polymers. *Nature* **1990**, *347*, 539.
14. N. Aizawa, T. Yasuda, Design of Thermally Activated Delayed Fluorescence Materials for Organic Light-Emitting Diodes. *AAPPS Bulletin* **2016**, *26*, 9.
15. D. M. Zink, L. Bergmann, D. Ambrosek, M. Wallesch, D. Volz, M. Mydlak, Singlet harvesting copper-based emitters: a modular approach towards next-generation OLED technology. *Transl. Mater. Res.* **2014**, *1*, 015003.
16. D. Volz, M. Wallesch, C. Fléchon, M. Danz, A. Verma, J. M. Navarro, D. M. Zink, S. Bräse, T. Baumann, From iridium and platinum to copper and carbon: new avenues for more sustainability in organic light-emitting diodes. *Green Chem.* **2015**, *17*, 1988.
17. C. Cebrián, M. Mauro, Recent advances in phosphorescent platinum complexes for organic light-emitting diodes. *Beilstein J. Org. Chem.* **2018**, *14*, 1459.
18. H. U. Kim, H. J. Park, J. H. Jang, W. Song, I. H. Jung, J. Y. Leeb, Do-Hoon Hwang, Green phosphorescent homoleptic iridium(III) complexes for highly efficient organic light-emitting diodes. *Dyes and Pigments* **2018,** *156*, 395.
19. J-H. Jang, H. J. Park, J. Y. Park, H. U. Kim, D-H. Hwang, Orange phosphorescent Ir(III) complexes consisting of substituted 2-phenylbenzothiazole for solution-processed organic light-emitting diodes. *Organic Electronics* **2018**, *60*, 31.
20. T-T. Bui, F. Goubard, M. Ibrahim-Ouali, D. Gigmes, F. Dumur, Recent advances on organic blue thermally activated delayed fluorescence (TADF) emitters for organic light-emitting diodes (OLEDs). *Beilstein J. Org. Chem.* **2018**, *14*, 282.
21. a) J. J. Guo, Z. J. Zhao, B. Z. Tang, Purely Organic Materials with Aggregation-Induced Delayed Fluorescence for

Efficient Nondoped OLEDs. *Adv. Optical Mater.* **2018**, *6*, 1800264.

b) H. Uoyama, K. Goushi, K. Shizu, H. Nomura, C. Adachi, Highly efficient organic light-emitting diodes from delayed fluorescence. *Nature,* **2012**, *492*, 234.

22. H. Borchert, Elementary processes and limiting factors in hybrid polymer/nanoparticle solar cells. *Energy Environ. Sci.,* **2010**, *3*, 1682.
23. Y. M. Sun, G. C.Welch, W. L. Leong, C. J. Takacs, G. C. Bazan, A. J. Heeger, Solution-processed small-molecule solar cells with 6.7% efficiency. *Nature Materials*, **2012**, *11*, 44.
24. C. Sekine, Y. Tsubata, T. Yamada, M. Kitano, S. Doi, Recent progress of high performance polymer OLED and OPV materials for organic printed electronics. Sci. Technol. *Adv. Mater.* **2014**, *15*, 034203.
25. A. Tsumura, H. Koezuka, T. Ando, Macromolecular electronic device: field-effect transistor with a polythiophene thin film. *Appl. Phys. Lett.* **1986**, *18*, 49.
26. L. Bürgi, M. Turbiez, R. Pfeiffer, F. Bienewald, H. Kirner, C. Winnewisser, High-Mobility Ambipolar Near-Infrared Light-Emitting Polymer Field-Effect Transistors. *Adv. Mater.* **2008**, *20*, 2217.
27. H. J. Chen, Y. L. Guo, G. Yu, Y. Zhao, J. Zhang, D. Gao, H. T. Liu, Y. Q. Liu, Highly π -Extended Copolymers with Diketopyrrolopyrrole Moieties for High-Performance Field-Effect Transistors. *Adv. Mater.* **2012**, *24*, 4618.
28. T. Lei, Y. Cao, Y. L. Fan, C. J. Liu, S. C. Yuan, J. Pei, High-Performance Air-Stable Organic Field-Effect Transistors: Isoindigo-Based Conjugated Polymers. *J. Am. Chem. Soc.* **2011**, *133*, 6099.
29. J. Yang, J. Y. Chen, Y. L. Sun, L. X. Shi, Y. L.Guo, S. Wang, Y. Q. Liu, Design and Synthesis of Novel Conjugated Polymers for Applications in Organic Field-effect Transistors. *ACTA POLYMERICA SINICA* **2017**.
30. C. Luo, A. K. K. Kyaw, L. A. Perez, S. Patel, M. Wang, B. Grimm, G. C. Bazan, E. J. Kramer, A. J. Heeger, General Strategy for Self-Assembly of Highly Oriented Nanocrystalline Semiconducting Polymers with High Mobility. *Nano Lett.* **2014**, *14*, 2764.
31. Z. Y. Zhao, Z. Y. Yin, H. J. Chen, L. P. Zheng, C. G. Zhu, L. Zhang, S. T. Tan, H. L. Wang, Y. L. Guo, Q. X. Tang, Y. Q. Liu, High-Performance, Air-Stable Field-Effect Transistors Based on Heteroatom-Substituted Naphthalenediimide-Benzothiadiazole Copolymers Exhibiting Ultrahigh Electron Mobility up to 8.5 cm V^{-1} s^{-1}. *Adv. Mater.* **2017**, *29*, 1602410.
32. J. Lee, A. Han, H. Yu, T. J. Shin, C. Yang, J. H. Oh, Boosting the ambipolar performance of solution-processable polymer semiconductors via hybrid side-chain engineering. *J. Am. Chem. Soc.* **2013**, *135*, 9540.
33. S. F. Nelson, Y.-Y. Lin, D. J. Gundlach, T. N. Jackson, Temperature-independent transport in high-mobility pentacene transistors. *Appl. Phys. Lett.* **1998**, *72*, 1854.
34. H. Iino, J. Hanna, Liquid crystalline organic semiconductors for organic transistor applications. *Polymer Journal* **2017**, *49*, 23.
35. H. Ebata, T. Izawa, E. Miyazaki, K. Takimiya, M. Ikeda, H. Kuwabara, T. Yui, Highly soluble [1]Benzothieno[3,2-b]benzothiophene (BTBT) derivatives for high-performance, solution-processed organic field-effect transistors. *J. Am. Chem. Soc.* **2007**, *129*, 15732.
36. S. Tatemichi, M. Ichikawa, T. Koyama, Y. Taniguchi, High mobility n-type thin-film transistors based on N,N-ditridecyl perylene diimide with thermal treatments. *Appl. Phys. Lett.* **2006**, *89*, 112108 .
37. C. D. Sheraw, T. N. Jackson, D. L. Eaton, J. E. Anthony, Functionalized pentacene active layer organic thin-film transistors. *Adv. Mater.* **2003**, *15*, 2009.
38. B. Wilson, A. S. El-Nawawy, W. D. Ollis, Eight- and higher-membered ring compounds. Part X. Di-, tri-, and tetra-thiosalicylides. *J. Chem. Soc.* **1952**, 3163.
39. N. Karl, Charge carrier transport in organic semiconductors. *Synthetic Metals* **2003**, *133–134*, 649.
40. V. Coropceanu, J. Cornil, D. A. Da Silva Filho, Y. Olivier, R. Silbey, J. Brédas, Charge Transport in Organic Semiconductors. *Chem. Rev.* **2007**, *107*, 926.
41. G. Horowitz, P. Delannoy, Charge Transport in Semiconducting Oligothiophenes. In Wiley-VCH Verlag GmbH,

1998, 283.

42. H. Klauk, Organic thin-film transistors. *Chem. Soc. Rev.* **2010**, *39*, 2643.
43. G. Horowitz, M. E. Hajlaoui, R. Hajlaoui, Temperature and gate voltage dependence of hole mobility in polycrystalline oligothiophene thin film transistors. *J. Appl. Phys.* **2000**, *87*, 4456.
44. A. Facchetti, π-Conjugated Polymers for Organic Electronics and Photovoltaic Cell Applications, *Chem. Mater.* **2011**, *23*, 733.
45. H. E. Katz, Z. Bao, The Physical Chemistry of Organic Field-Effect Transistors. *J. Phys. Chem. B* **1999**, *104*, 671.
46. R. G. Kepler, Charge Carrier Production and Mobility in Anthracene Crystals. *Physical Review* **1960**, *119*, 1226.
47. O. H. LeBlanc, Hole and Electron Drift Mobilities in Anthracene. *J. Chem. Phys.* **1960**, *33*, 626.
48. D. Demus, J. W. Goodby, G. W. Gray, H. W. Spiess, V. Vill, Handbook of Liquid Crystals, Viley VCH, **1988**, ISBN 3-527-29502-X, 2-17.
49. S. Friberg, Lyotropic Liquid Crystals, Naturwissenschaften, **1977**, *64*, 612.
50. C. Tschierske, Amphotropic liquid crystals, Current Opinion in Colloid & Interface Science, **2002**, 7, 355.
51. J. Hanna, A. Ohno, H. Iino, Charge carrier transport in liquid crystals, *Thin Solid Films* **2014**, *554*, 58.
52. Smectic liquid crystals --- textures and structures, ISBN 0-249-44168-3.
53. S. M. Kelly, M. O'Neill, liquid crystals for electro-optic applications, Handbook of Advanced Electronic and Photonic Materials and Devices, Volume 7: Liquid Crystals, Display and Laser Materials, **2000**, 1-66.
54. W. Kuczyński, H. Stegemeyer, Ferroelectric properties of smectic C liquid crystals with induced helical structure. *Chem. Phys. Lett.* **1980**, *70*, 123.
55. M. Funahashi, Development of Liquid-Crystalline Semiconductors with High Carrier Mobilities and Their Application to Thin-film Transistors. *Polymer Journal* **2009**, *41*, 459.
56. Y. Shirota, Photo- and electroactive amorphous molecular materials—molecular design, syntheses, reactions, properties, and applications. *J. Mater. Chem.* **2005**, *15*, 75.
57. T. Kato, N. Mizoshita, K. Kishimoto, Functional Liquid-Crystalline Assemblies: Self-Organized Soft Materials. *Angew. Chem., Int. Ed.* **2005**, *45*, 38.
58. H. Iino, J. Hanna, Liquid crystalline organic semiconductors for organic transistor applications. *Polymer Journal* **2017**, *49*, 23.
59. H. E. Katz, J. G. Laquindanum, A. J. Lovinger, Synthesis, solubility, and field-effect mobility of elongated and oxa-substituted α,ω-dialkyl thiophene oligomers. extenstion of 'polar intermediate' synthetic strategy and solution deposition on transistor substrates. *Chem. Mater.* **1998**, *10*, 633.
60. F. Garnier, R. Hajlaoui, A. E. Kassmin, G. Horowitz, L. Laigre, W. Prozio, M. Aramanini, F. Provasoli, Dihexylquaterthiophene, a two-dimensional liquid crystal-like organic semiconductor with high transport properties. *Chem. Mater.* **1998**, *10*, 3334.
61. A. J. J. M. Van Breemen, P. T. Herwig, C. H. T. Chlon, J. Sweelssen, H. F. M. Schoo, S. Setayesh, W. M. Hardeman, C. A. Martin, D. M. de Leeuw, J. J. P. Valeton, C. W. M. Bastiaansen, D. J. Broer, A. R. Popa-Merticaru, S. C. J. Meskers, Large area liquid crystal monodomain field-effect transistors. *J. Am. Chem. Soc.* **2005**, *128*, 2336.
62. M. Funahashi, F. Zhang, N. Tamaoki, High ambipolar mobility in a highly ordered smectic phase of a dialkylphenylterthiophene derivative that can be applied to solution-processed organic field-effect transistors. *Adv. Mater.* **2007**, *19*, 353.
63. K. Oikawa, H. Monobe, K. Nakayama, T. Kimoto, K. Tsuchiya, B. Heinrich, D. Guillon, Y. Shimizu, M. Yokoyama, High carrier mobility of organic field-effect transistors with a thiophene–naphthalene mesomorphic semiconductor. *Adv. Mater.* **2007**, *19*, 1864.
64. W. Pisula, A. Menon, M. Stepputat, I. Liebewirth, U. Kolb, A. Tracz, H. Sirringhaus, T. Pakula, K. Müllen, A zone casting technique for device fabrication of field-effect transistors based on discotic hexa-peri-hexabenzocoronene. *Adv. Mater.* **2005**, *17*, 684.

65. H. Meng, F. Sun, M. B. Goldfinger, G. D. Jaycox, Z. Li, W. J. Marshall, G. S. Blackman, High-performance, stable organic thin-film field-effect transistors based on Bis-5’-alkylthiophen-2’-yl-2,6-anthracene semiconductors. *J. Am. Chem. Soc.* **2005**, *127*, 2406.
66. H. Ebata, T. Izawa, E. Miyazaki, K. Takimiya, M. Ikeda, H.Kuwabara, T. Yui, Highly soluble [1]Benzothieno[3,2-b]benzothiophene (BTBT) derivatives for high-performance, solution-processed organic field-effect transistors. *J. Am. Chem. Soc.* **2007**, *129*, 15732.
67. Y. Hirai, H. Monobe, N. Mizoshita, M. Moriyama, K. Hanabusa, Y. Shimizu, T. Kato, Enhanced Hole-Transporting Behavior of Discotic Liquid-Crystalline Physical Gels, *Adv. Funct. Mater.* **2008**, *18*, 1668.
68. T. Yasuda, H. Ooi, J. Morita, Y. Akama, K. Minoura, M. Funahashi, T. Shimomura, T. Kato, π-Conjugated Oligothiophene-Based Polycatenar Liquid Crystals: Self-Organization and Photoconductive, Luminescent, and Redox Properties. *Adv. Funct. Mater.* **2009**, *19*, 411.
69. Y. Molard, F. Dorson, V. Circu, T. Roisnel, F. Artzner, S. Cordier, Clustomesogens: Liquid Crystal Materials Containing Transition-Metal Clusters. *Angew. Chem. Int. Ed.* **2010**, *49*, 3351.
70. A. Perez, J. L. Serrano, T. Sierra, A. Ballesteros, D. de Saa, J. Barluenga,Control of Self-Assembly of a 3-Hexen-1,5-diyne Derivative: Toward Soft Materials with an Aggregation-Induced Enhancement in Emission. *J. Am. Chem. Soc.* **2011**, *133*, 8110.
71. T. Christ, B. Glusen, A. Greiner, A. Kettner, R. Sander, V. Stumpflen, V. Tsukruk, Wendorff, Columnar discotics for light emitting diodes. *Adv. Mater.* **1997**, *9*, 48.
72. H. Hayasaka, T. Miyashita, K. Tamura, K. Akagi, Helically π-Stacked Conjugated Polymers Bearing Photoresponsive and Chiral Moieties in Side Chains: Reversible Photoisomerization-Enforced Switching Between Emission and Quenching of Circularly Polarized Fluorescence. *Adv. Func. Mater.* **2010**, *20*, 1243.
73. B. A. San Jose, S. Matsushita, Y. Moroishi, K. Akagi, Disubstituted Liquid Crystalline Polyacetylene Derivatives That Exhibit Linearly Polarized Blue and Green Emissions. *Macromolecules* **2011**, *44*, 6288.
74. G. Lussem, J. H. Wendorff, Liquid crystalline materials for light-emitting diodes. *Polym. Adv. Technol.* **1998**, *7*, 443.
75. K. S. Whitehead, M. Grell, D. D. C. Bradley, M. Inbasekaran, E. P. Woo., Polarized emission from liquid crystal polymers, *Synth. Met.* **2000**, *111 112*, 181.
76. C. Weder, C. Sarwa, A. Montali, C. Bastiaansen, P. Smith, Incorporation of Photoluminescent Polarizers into Liquid Crystal Displays, *Science* **1998**, *279*, 835.
77. S. H. Chen, H. Shi, B. M. Conger, J. C. Mastrangelo, T. Tsutsui, Novel vitrifiable liquid crystals as optical materials, *Adv. Mater.* **1996**, *12*, 998.
78. W. Z. Yuan, Z. Q. Yu, Y. H. Tang, J. W. Y. Lam, N. Xie, P. Lu, E. Q. Chen, B. Z. Tang, High Solid-State Efficiency Fluorescent Main Chain Liquid Crystalline Polytriazoles with Aggregation-Induced Emission Characteristics. *Macromolecules*, **2011**, *44*, 9618.
79. H. Wang, F. Zhang, B. Bai, P. Zhang, J. Shi, D. Yu, Y. Zhao, Y. Wang, M. Li, Synthesis, liquid crystalline properties and fluorescence of polycatenar 1,3,4-oxadiazole derivatives. *Liq. Cryst.* **2008**, *35*, 905.
80. J. B. Birks, Photophysics of Aromatic Molecules: Wiley: London, **1970**.
81. C. H.Ting, J. T. Chen, C. S. Hsu, Synthesis and Thermal and Photoluminescence Properties of Liquid Crystalline Polyacetylenes Containing 4-Alkanyloxyphenyl trans-4-Alkylcyclohexanoate Side Groups. *Macromolecules* **2002**, *35*, 1180.
82. S. A. Jenekhe, J. A. Osaheni, Excimers and Exciplexes of Conjugated Polymers. *Science* **1994**, *265*, 765.
83. J. Han, Z. Q. Xi, F. L. Wang, L. H. Bu, Y. M. Wang, Synthesis, liquid crystalline and photoluminscent properties of 1,3,4-oxadiazole derivatives: From calamitic monomers, H-Shaped dimers to calix[4]arene-based tetramers. *Dyes and Pigments*, **2018**, *154*, 234.
84. H. Y. Feng, X. T. Geng, J. R. Lin, H. Y. Guo, F. F.Yang, Novel fluorescent liquid crystals: synthesis, mesomorphism

and fluorescence of triphenylene-Bodipy derivatives based on 1,3,5-triazine core. *Liquid Crystals*, **2018**, 1470.

85. M. Muccini, A bright future for organic field-effect transistors, Nature Materials, 2006, 5, 605.
86. A. Hepp, H. Heil, W. Weise, Light-emitting field-effect transistor based on a tetracene thin film. *Phys Rev Lett*, **2003**, *91*, 157406.
87. S. Cho, K. Kim, T. Kim, H. Park, J. M. Kim, S. H. Lee, Y. S. Kang, K. Chang, C. Kim, High-Contrast Imaging of Cholesterol Crystals in Rabbit Arteries Ex Vivo Using LED-Based Polarization Microscopy. *Sensors* **2018**, *18*, 1258.
88. Y. Xiao, D. Kreher, F. Mathevet, A. J. Attias, Engineering, synthesis and characterization of New π-conjugated (macro) molecular architectures for Organic Optoelectronics, thesis of PhD, Laboratoire de Chimie des Polymères (LCP), Institut Parisien de Chimie Moléculaire-UPMC (CNRS-UMR 8232), **2014**.
89. F. Lincker, A.-J. Attias, F. Mathevet, B. Heinrich, B. Donnio, J.-L. Fave, P. Rannou, R. Demadrille, Influence of polymorphism on charge transport properties in isomers of fluorenone-based liquid crystalline semiconductors. *Chem. Commun.* **2012**, 48, 3209.
90. D. John A. The Analytical Chemistry Handbook. New York: McGraw Hill, Inc. **1995**: 15.1–15.5. ISBN 0-07-016197-6.
91. Pungor, Erno. A Practical Guide to Instrumental Analysis. Florida: Boca Raton. **1995**: 181–191.
92. Skoog, Douglas A., F. James Holler and Timothy Nieman. Principles of Instrumental Analysis 5. New York. **1998**: 805–808. ISBN 0-03-002078-6.
93. Website http://lipidlibrary.aocs.org/Biochemistry/content.cfm?ItemNumber=40884
94. Website https://textilestudycenter.com/x-ray-diffraction-method/
95. L. T. Dou, J. B. You, Z. R. Hong, Z. Xu, G. Li, R. A. Street, Y. Yang, 25th Anniversary Article: A Decade of Organic/Polymeric Photo-voltaic Research. *Adv. Mater.* **2013**, *25*, 6642.
96. J. M. Szarko, B. S. Rolczynski, S. J. Lou, T. Xu, J. Strzalka, T. J. Marks, L. P. Yu, L. X. Chen, Photovoltaic Function and Exciton/Charge Transfer Dynamics in a Highly Efficient Semiconducting Copolymer. *Adv. Funct. Mater.* **2014**, *24*, 10.
97. F. Wudl, M. Kobayashi, A. J. Heeger, Poly(isothianaphthene). *J. Org. Chem.* **1984**, *49*, 3382.
98. M. H. Hao, X. D. Li, Y. Zhao, Z. H. Chen, J. F. Fang, L. Wang, C. L. Yang, Influence of side chains on low optical bandgap copolymers based on 2,1,3-benzoxadiazole for polymer solar cells. *Organic Electronics* **2018**, *61*, 261.
99. G. Alves, E. F. Oliveira, A. Batagin-Neto, F. C. Lavarda, Molecular modeling of low bandgap diblock co-oligomers with π-bridges for applications in photovoltaics. *Computational Materials Science* **2018**, 152, 12.
100. G. L. Gibson, T. M. McCormick, D. S. Seferos, Atomistic Band Gap Engineering in Donor−Acceptor Polymers. *J. Am. Chem. Soc.* **2012**, *134*, 539.
101. Y. J. Cheng, S. H. Yang, C. S. Hsu, Synthesis of Conjugated Polymers for Organic Solar Cell Applications. *Chem. Rev.* **2009**, *109*, 5868.
102. Z. H. Zhou, T. Maruyama, T. Kanbara, T. Ikeda, K. Ichimura, T. Yamamoto, K. Tokuda, Unique optical and electrochemical properties of π-conjugated electrically conducting copolymers consisting of electron-withdrawing pyridine units and electron-donating thiophene units. J. Chem. Soc. *Chem. Commun.* **1991**, 1210.
103. E. E. Havinga, W. Hoeve, H. Wynberg, Alternate donor-acceptor small-band-gap semiconducting polymers; Polysquaraines and polycroconaines. *Synth. Met.* **1993**, *55*, 299.
104. L. Lu, T. Zheng, Q. Wu, A. M. Schneider, D. Zhao, L. Yu, Recent Advances in Bulk Heterojunction Polymer Solar Cells. *Chem. Rev.* **2015**, *115*, 12666.
105. C. Zhang, X. Z. Zhu, Thieno[3,4-b]thiophene-Based Novel Small-Molecule Optoelectronic Materials, *Acc. Chem. Res.* **2017**, *50*, 1342.
106. L. Y. Bian, E. W. Zhu, J. Tang, W. H. Tang, F. J. Zhang, Recent progress in the design of narrow bandgap conjugated polymers for high-efficiency organic solar cells. Progress in Polymer *Science* **2012**, *37*, 1292.
107. B. P. Rand, D. P. Burk, S. R. Forrest, Offset energies at organic semiconductor heterojunctions and their influence on

the open-circuit voltage of thin-film solar cells. *Phys. Rev. B* **2007**, *75*, 115327.

108. K. Vandewal, K. Tvingstedt, A. Gadisa, O. Inganäs, J. V. Manca, On the origin of the open-circuit voltage of polymer−fullerene solar cells. *Nat. Mater.* **2009**, *8*, 904.
109. Y. J. Cheng, S. H. Yang, C. S. Hsu, Synthesis of Conjugated Polymers for Organic Solar Cell Applications. *Chem. Rev.* **2009**, *109*, 5868.
110. J. D. Yuen, F. Wudl, Strong acceptors in donor−acceptor polymers for high performance thin film transistors. *Energy Environ. Sci.* **2013**, *6*, 392.
111. Y. F. Li, Molecular Design of Photovoltaic Materials for Polymer Solar Cells: Toward Suitable Electronic Energy Levels and Broad Absorption, *Acc. Chem. Res.* **2012**, *45*, 723.
112. Y. Liang, Y. Wu, D. Feng, S. T. Tsai, H. J. Son, G. Li, L. Yu, Development of New Semiconducting Polymers for High Performance Solar Cells. *J. Am. Chem. Soc.* **2009**, *131*, 56.
113. H. Zang, Y. Liang, L. Yu, B. Hu, Intra-Molecular Donor−Acceptor Interaction Effects on Charge Dissociation, Charge Transport, and Charge Collection in Bulk-Heterojunction Organic Solar Cells. *Adv. Energy Mater.* **2011**, *1*, 923.
114. J. D. Chen, C. Cui, Y. Q. Li, L. Zhou, Q. D. Ou, C. Li, Y. Li, J. X. Tang, Single-Junction Polymer Solar Cells Exceeding 10% Power Conversion Efficiency. *Adv. Mater.* **2015**, *27*, 1035.
115. Z. Zhu, D. Waller, R. Gaudiana, M. Morana, D. Mühlbacher, M. Scharber, C. Brabec, Panchromatic Conjugated Polymers Containing Alternating Donor/Acceptor Units for Photovoltaic Applications. *Macromolecules* **2007**, *40*, 1981.
116. M. Morana, H. Azimi, G. Dennler, H. J. Egelhaaf, M. Scharber, K. Forberich, J. Hauch, R. Gaudiana, D. Waller, Z. Zhu, Nanomorphology and Charge Generation in Bulk Heterojunctions Based on Dithiophene Polymers with Different Bridging Atoms. *Adv. Funct. Mater.* **2010**, *20*, 1180.
117. L. Dou, C. C. Chen, K. Yoshimura, K. Ohya, W. H. Chang, J. Gao, Y. Liu, E. Richard, Y. Yang, Synthesis of 5H-Dithieno[3,2-b:2’,3’-d]pyran as an Electron-Rich Building Block for Donor-Acceptor Type Polymers. *Macromolecules* **2013**, *46*, 3384.
118. M. M. Wienk, M. Turbiez, J. Gilot, R. A. J. Janssen, Narrow-Bandgap Diketo-Pyrrolo-Pyrrole Polymer Solar Cells: The Effect of Processing on the Performance. *Adv. Mater.* **2008**, *20*, 2556.
119. L. Dou, J. You, J. Yang, C. C. Chen, Y. He, S. Murase, T. Moriarty, K. Emery, G. Li, Y. Yang, Tandem polymer solar cells featuring a spectrally matched polymer. *Nat. Photonics* **2012**, *6*, 180.
120. R. S. Ashraf, I. Meager, M. Nikolka, M. Kirkus, M. Planells, B. Schroeder, S. Holliday, M. Hurhangee, C. Nielsen, H. Sirringhaus, Chalcogenophene Comonomer Comparison in Small Band Gap Diketopyrrolopyrrole-Based Conjugated Polymers for High-Performing Field-Effect Transistors and Organic Solar Cells. *J. Am. Chem. Soc.* **2015**, *137*, 1314.
121. E. Wang, Z. Ma, Z. Zhang, K. Vandewal, P. Henriksson, O. Inganäs, F. Zhang, M. R. Andersson, An Easily Accessible Isoindigo-Based Polymer for High-Performance Polymer Solar Cells. *J. Am. Chem. Soc.* **2011**, *133*, 14244.
122. G. W. P. Van Pruissen, F. Gholamrezaie, M. M. Wienk, R. A. J. Janssen, Synthesis and properties of small band gap thienoisoindigo basedconjugated polymers. *J. Mater. Chem.* **2012**, *22*, 20387.
123. Y. Koizumi, M. Ide, A. Saeki, C. Vijayakumar, B. Balan, M. Kawamoto, S. Seki, Thienoisoindigo-based low-band gap polymers for organic electronic devices. *Polym. Chem* **2013**, *4*, 484.
124. G. K. Dutta, A. R. Han, J. Lee, Y. Kim, J. H. Oh, C. Yang, Visible-Near Infrared Absorbing Polymers Containing Thienoisoindigo and Electron-Rich Units for Organic Transistors with Tunable Polarity. *Adv. Funct. Mater.* **2013**, *23*, 5317.
125. Y. S. Chen, X. J. Wan, G. K. Long, High Performance Photovoltaic Applications Using Solution-Processed Small Molecules. *Acc. Chem. Res.* **2013**, *46*, 2645.
126. J. Roncali, P. Leriche, P. Blanchard, Molecular Materials for Organic Photovoltaics: Small is Beautiful. *Adv. Mater.* **2014**, *26*, 3821.
127. W. Ni, X. J. Wan, M. M. Li, Y. C. Wang, Y. S. Chen, A−D−A small molecules for solution-processed organic

photovoltaic cells. *Chem. Commun.* **2015**, *51*, 4936.

128. W. X. Liu, J. N. Yao, C. L. Zhan, A Novel BODIPY-Based Low-Band-Gap Small-Molecule Acceptor for Efficient Non-fullerene Polymer Solar Cells. *Chin. J. Chem.* **2017**, *35*, 1813.
129. D. B. Yang, H. Sasabe, T. Sano, J. Kido, Low-Band-Gap Small Molecule for Efficient Organic Solar Cells with a Low Energy Loss below 0.6 eV and a High Open-Circuit Voltage of over 0.9 V. *ACS Energy Lett.* **2017**, *2*, 2021.
130. A. A. Raheem, S. Kamaraj, V. Sannasia, C. Praveen, New D–π-A push–pull chromophores as low band gap molecular semiconductors for organic small molecule solar cell applications. *Org. Chem. Front.* **2018**, *5*, 777.
131. B. Tieke, A. R. Rabindranath, K. Zhang, Y. Zhu, Conjugated polymers containing diketopyrrolopyrrole units in the main chain. *Beilstein J. Org. Chem.* **2010**, *6*, 830.
132. Y. N. Li, P. Sonar, L. Murphy, W. Hong, High mobility diketopyrrolopyrrole (DPP)-based organic semiconductor materials for organic thin film transistors and photovoltaics. *Energy Environ. Sci.* **2013**, *6*, 1684.
133. A. B. Tamayo, B. Walker, T. Q. Nguyen, A Low Band Gap, Solution Processable Oligothiophene with a Diketopyrrolopyrrole Core for Use in Organic Solar Cells. *J. Phys. Chem. C* **2008**, *112*, 11545.
134. A. B. Tamayo, X. D. Dang, B. Walker, J. Seo, T. Kent, T. Q. Nguyen, A low band gap, solution processable oligothiophene with a dialkylated diketopyrrolopyrrole chromophore for use in bulk heterojunction solar cells. *Appl. Phys. Lett.* **2009**, *94*, 103301.
135. P. Deng, Q. Zhang, Recent developments on isoindigo-based conjugated polymers. *Polym. Chem.* **2014**, *5*, 3298.
136. A. Yassin, P. Leriche, M. Allain, J. Roncali, Donor−acceptor−donor (D−A−D) molecules based on isoindigo as active material for organic solar cells. *New J. Chem.* **2013**, *37*, 502.
137. T. Wang, Y. H. Chen, X. C. Bao, Z. K. Du, J. Guo, N. Wang, M. L. Sun, R. Q. Yang, A new isoindigo-based molecule with ideal energy levels for solution-processable organic solar cells. *Dyes Pigm.* **2013**, *98*, 11.
138. Y. H. Chen, Z. K. Du, W. C. Chen, L. L. Han, Q. Liu, M. L. Sun, R. Q. Yang, Near-infrared response thienoisoindigo-based small molecule for solution-processed bulk-heterojunction solar cells. *Synth. Met.* **2014**, *187*, 24.
139. O. Vybornyi, Y. Jiang, F. Baert, D. Demeter, J. Roncali, P. Blanchard, C. Cabanetos, Solution-processable thienoisoindigo-based molecular donors for organic solar cells with high open-circuit voltage. *Dyes Pigm.* **2015**, *115*, 17.
140. L. Beverina, P. Salice, Squaraine Compounds: Tailored Design and Synthesis towards a Variety of Material Science Applications. Eur. *J. Org. Chem.* **2010**, 1207.
141. D. B. Yang, Q. Q. Yang, L. Yang, Q. Luo, Y. Chen, Y. Q. Zhu, Y. Huang, Z. Y. Lu, S. L. Zhao, A narrow bandgap asymmetrical squaraine for high-performance solution-processed small molecule organic solar cells. *Chem. Commun.* **2014**, *50*, 9346.
142. Y. Cakmak, E. U. Akkaya, Phenylethynyl-BODIPY Oligomers: Bright Dyes and Fluorescent Building Blocks. *Org. Lett.* **2009**, *11*, 85.
143. A. Loudet, K. Burgess, BODIPY Dyes and Their Derivatives: Syntheses and Spectroscopic Properties. *Chem. Rev.* **2007**, *107*, 4891.
144. H. Lu, J. Mack, Y. C. Yang, Z. Shen, Structural modification strategies for the rational design of red/NIR region BODIPYs. *Chem. Soc. Rev.* **2014**, *43*, 4778.
145. W. X. Liu, A. L. Tang, J. W. Chen, Y. S. Wu, C. L. Zhan, J. N. Yao, Photocurrent Enhancement of BODIPY-Based Solution-Processed Small-Molecule Solar Cells by Dimerization via the Meso Position. *ACS Appl. Mater. Interfaces* **2014**, *6*, 22496.
146. A. M. Poe, A. M. Della Pelle, A. V. Subrahmanyam, W. White, G. Wantz, S. Thayumanavan, Small molecule BODIPY dyes as non-fullerene acceptors in bulk heterojunction organic photovoltaics. *Chem. Commun.* **2014**, *50*, 2913.
147. J. Zaumseil, H. Sirringhaus, Electron and Ambipolar Transport in Organic Field-Effect Transistors. *Chem. Rev.* **2007**, *107*, 1296.

148. J. D. Yuen, F. Wudl, Strong acceptors in donor−acceptor polymers for high performance thin film transistors. *Energy Environ. Sci.* **2013**, *6*, 392.

149. Y. Zhao, Y. Guo, Y. Liu, 25th anniversary article: recent advances in n-type and ambipolar organic field-effect transistors. *Adv. Mater.* **2013**, *25*, 5372.

150. C. B. Nielsen, M. Turbiez, I. McCulloch, Recent Advances in the Development of Semiconducting DPP-Containing Polymers for Transistor Applications. *Adv. Mater.* **2013**, *25*, 1859.

151. J. Li, Y. Zhao, H. S. Tan, Y. Guo, C. A. Di, G. Yu, B. S. Ong, A stable solution-processed polymer semiconductor with record high-mobility for printed transistors. *Sci. Rep.* **2012**, *2*, 754.

152. P. Sonar, S. P. Singh, Y. Li, M. S. Soh, A. Dodabalapur, A Diketopyrrolopyrrole-Benzothiadiazole Based Copolymer for High-Mobility Ambipolar Organic Thin-Film Transistors. *Adv. Mater.* **2010**, *22*, 5409.

153. J. Lee, A. R. Han, H. Yu, T. J. Shin, C. Yang, J. H. Oh, Boosting the Ambipolar Performance of Solution-Processable Polymer Semiconductors via Hybrid Side-Chain Engineering. *J. Am. Chem. Soc.* **2013**, *135*, 9540.

154. T. Lei, J. H. Dou, Z. J. Ma, C. H. Yao, C. J. Liu, J. Y. Wang, J. Pei, Ambipolar Polymer Field-Effect Transistors Based on Fluorinated Isoindigo: High Performance and Improved Ambient Stability. *J. Am. Chem. Soc.* **2012**, *134*, 20025.

155. J. Fan, J. D. Yuen, M. Wang, J. Seifter, J. H. Seo, A. R. Mohebbi, D. Zakhidov, A. Heeger, F. Wudl, High-Performance Ambipolar Transistors and Inverters from an Ultranarrow bandgap Polymer. *Adv. Mater.* **2012**, *24*, 2186.

156. M. Tantiwiwat, A. Tamayo, N. Luu, X. D. Dang, T. Q. Nguyen, Oligothiophene Derivatives Functionalized with a Diketopyrrolopyrrolo Core for Solution-Processed Field Effect Transistors: Effect of Alkyl Substituents and Thermal Annealing. *J. Phys. Chem. C* **2008**, *112*, 17402.

157. W. Kang, M. Jung, W. Cha, S. Jang, Y. Yoon, H. Kim, H. J. Son, D. K. Lee, B. Kim, J. H. Cho, High Crystalline Dithienosilole-Cored Small Molecule Semiconductor for Ambipolar Transistor and Nonvolatile Memory. *ACS Appl. Mater. Interfaces* **2014**, *6*, 6589.

158. A. Riano, P. M. Burrezo, M. J. Mancheno, A. Timalsina, J. Smith, A. Facchetti, T. J. Marks, J. T. L. Navarrete, J. L. Segura, J. Casado, The unusual electronic structure of ambipolar dicyanovinyl-substituted diketopyrrolopyrrole derivatives. *J. Mater. Chem. C* **2014**, *2*, 6376.

159. M. J. Kim, Y. W. Lee, Y. Lee, H. Y. Woo, J. H. Cho, Solvent-vapor-annealed A–D–A-type semicrystalline conjugated small molecules for flexible ambipolar field-effect transistors, *J. Mater.Chem.C* **2018**, *6*, 5698.

160. D. L. Zeng, I. Tahar-Djebbar, Y. M. Xiao, F. Kameche, N. Kayunkid, M. Brinkmann, D. Guillon, B. Heinrich, B. Donnio, D. A. Ivanov, E. Lacaze, David Kreher, F. Mathevet, A. J. Attias, Intertwined Lamello-Columnar Coassemblies in Liquid-Crystalline Side-Chain π-Conjugated Polymers: Toward a New Class of Nanostructured Supramolecular Organic Semiconductors, *Macromolecules*, **2014**, *47*, 1715.

161. Y. Xiao, D. Kreher, F. Mathevet, A. J. Attias, Engineering, synthesis and characterization of New π-conjugated (macro) molecular architectures for Organic Optoelectronics, thesis of PhD, Laboratoire de Chimie des Polymères (LCP), Institut Parisien de Chimie Moléculaire-UPMC (CNRS-UMR 8232), **2014**.

162. A. Castiglione, D. Kreher, F. Mathevet, A. J. Attias, Liquid crystalline macromolecular architectures based on regioregular poly(3-alkylthiophene) as backbone and calamitic mesogens as side-groups: towards ambipolar materials, thesis of PhD, Laboratoire de Chimie des Polymères (LCP), Institut Parisien de Chimie Moléculaire-UPMC (CNRS-UMR 8232), **2013**.

163. XL. Su, D. Kreher, F. Mathevet, A. J. Attias, Engineering, Synthesis, and Characterization of New Multi-lamellar Liquid Crystalline Molecular Architectures based on Discotic and Calamitic π-Conjugated Mesogens, thesis of PhD, Laboratoire de Chimie des Polymères (LCP), Institut Parisien de Chimie Moléculaire-UPMC (CNRS-UMR 8232), **2016**.

164. J. P. Heiskanen, V. Paola, N. M. Saari, T. I. Hukka, T. Kastinen, K. Kaunisto, H. J. Lemmetyinen, O. E. O. Hormi, Synthesis of Benzothiadiazole Derivatives by Applying C-C Cross-Couplings. *J. Org. Chem.* **2016**, *81*, 1535.

165. a) M. R. Elmorsy, R. Sua, A. A. Fadda, H.A. Etman, E. H. Tawfik, A. El-Shafeia, Molecular engineering and synthesis

of novel metal-free organic sensitizers with D-π-A-π-A architecture for DSSC applications: The effect of the anchoring group. *Dyes and Pigments* **2018**, *158*, 121.

b) Z. Xu, H. M. Du, M. J. Yin, B. Z. Wang, J. S. Zhao, Y. Xie, Benzothiadiazole, hexylthiophen and alkoxy benzene based solution processable copolymer: Effect of the electron withdrawing substituents (fluorine atoms) on electrochemical, optical and electrochromic properties. *Organic Electronics* **2018**, *61*, 1.

166. a) D. X. Huang, M. Prehm, H. F. Gao, X. H. Cheng, Y. S. Liu, C. Tschierske, Synthesis and self-assembly of luminescent hexacatenar molecules incorporating a 4,7-diphenyl-2,1,3-benzothiadiazole core. *RSC Adv.* **2016**, *6*, 21387.

     b) M. P. Aldred, A. J. Eastwood, S. P. Kitney, G. J. Richards, P. Vlachos, S. M. Kelly, M. O'Neill, Synthesis and mesomorphic behaviour of novel light-emitting liquid crystals. *Liquid Crystals*, **2005**, *32*, 1251.
167. S.R. Manohara, V. Udaya Kumar, Shivakumaraiah, L. Gerward, Estimation of ground and excited-state dipole moments of 1, 2-diazines by solvatochromic method and quantum-chemical calculation, *Journal of Molecular Liquids* **2013**, *181*, 97.
168. D. D. Thiaré, A. Khonté, A. Diopb, L. Cissé, A. Coly, A. Tine, F. Delattre, Determination of ground and excited state dipole moments of amino-benzimidazole by solvatochromic shift methods and theoretical calculations, *Journal of Molecular Liquids* **2015**, *211*, 640.
169. M. Kuwata, S. R. Zorn, S. T. Martin, Using Elemental Ratios to Predict the Density of Organic Material Composed of Carbon, Hydrogen, and Oxygen, *Environ. Sci. Technol.* **2012**, *46*, 787.
170. A. D'Aléo, M. H. Sazzad, D. H. Kim, E. Y. Choi, J. W. Wu, G. Canard, F. Fages, J. C. Ribierre, C. Adachi, Boron difluoride hemicurcuminoid as an efficient far red to near-infrared emitter: toward OLEDs and laser dyes. *Chem. Commun.* **2017**, *2*, 2.
171. J. C. Maunoury, J. R. Howse, M. L. Turner, Melt-Processing of Conjugated Liquid Crystals: A Simple Route to Fabricate OFETs. *Adv. Mater.* **2007**, *19*, 805.
172. H. Scher, E.W. Montroll, Anomalous transit-time dispersion in amorphous solids. *Phys. Rev.* **1975**, *12*, 2455.
173. G. S. Girolami, A Simple "Back of the Envelope" Method for Estimating the Densities and Molecular Volumes of Liquids and Solids. *J. Chem. Educ.* **1994**, *71*, 962.
174. H. Iino, J. Hanna, Availability of Liquid Crystallinity in Solution Processing for Polycrystalline Thin Films. *Adv. Mater.* **2011**, *23*, 1748.
175. D. X. Huang, M. Prehm, H. F. Gao, X. H. Cheng, Y. S. Liu, C. Tschierske, Synthesis and self-assembly of luminescent hexacatenar molecules incorporating a 4,7-diphenyl-2,1,3-benzothiadiazole core. *RSC Adv.* **2016**, *6*, 21387.
176. C. M. S. Combe, L. Biniek, B. C. Schroeder, I. McCulloch, Synthesis of [1]benzothieno[3,2-b][1]benzothiophene pendant and norbornene random co-polymers via ring opening metathesis. *J. Mater. Chem. C* **2014**, *2*, 538.
177. M. Saito, I. Osaka, E. Miyazaki, K. Takimiya, H. Kuwabara and M. Ikeda, One-step synthesis of [1]benzothieno[3,2-b][1]benzothiophene from o-chlorobenzaldehyde. *Tetrahedron Lett.* **2011**, *52*, 285.
178. K. Niimi, S. Shinamura, I. Osaka, E. Miyazaki, K. Takimiya, Dianthra[2,3-b:2',3'-f]thieno[3,2-b]thiophene (DATT): Synthesis, Characterization, and FET Characteristics of New π-Extended Heteroarene with Eight Fused Aromatic Rings. *J. Am. Chem. Soc.* **2011**, *133*, 8732.
179. Li, G.; Zhu, R.; Yang, Y. Polymer solar cells. *Nat. Photonics* **2012**, *6*, 153.
180. Janssen, R. A. J.; Nelson, J. Factors Limiting Device Efficiency in Organic Photovoltaics. *Adv. Mater.* **2013**, *25*, 1847.
181. Zhao, Y.; Guo, Y.; Liu, Y. 25th anniversary article: recent advances in n-type and ambipolar organic field-effect transistors. *Adv.Mater.* **2013**, *25*, 5372.